Università degli Studi di Cagliari
Dipartimento di Fisica

Scuola di Dottorato di Ricerca in Fisica
XXX Ciclo

UNDERSTANDING THERMAL TRANSPORT
IN NANOSCALE SYSTEMS BY ATOMISTIC SIMULATIONS

FROM NANOSTRUCTURED SEMICONDUCTORS TO ORGANIC MOLECULES

Settore scientifico disciplinare di afferenza: FIS/03

Presentata da:
Riccardo Dettori

Coordinatore Dottorato:
Prof. Alessandro de Falco

Supervisor:
Prof. Luciano Colombo

Esame finale anno accademico 2016–2017
Tesi discussa nella sessione d'esame Febbraio-Marzo 2018

UNDERSTANDING THERMAL TRANSPORT IN NANOSCALE COMPLEX SYSTEMS BY ATOMISTIC SIMULATIONS

FROM NANOSTRUCTURED SEMICONDUCTORS TO ORGANIC MOLECULES

Riccardo Dettori:
Understanding thermal transport in nanoscale complex systems by atomistic simulations

It's all about the journey, not the destination

Dedicated to my parents.

ABSTRACT

Thermal transport represents an open issue for experimental and theoretical investigation in the field of nanoscale physics. Several challenges strictly depend on understanding the details related to how heat is transported at the nanoscale, how heat carriers behave when the size involved are that small and how to better exploit such features. In this scenario, the role of the present work is twofold: first, theoretical methods and atomistic simulations are adopted to investigate thermal transport is adopted and a very detail-oriented assessment have been performed; secondly, it is studied a panoply of different materials exhibiting interesting features related to thermal transport. The first aspect aims at highlighting the advantages and disadvantages of each approach, in order to delineate how these techniques can complement each other to give the best performances, reliable trends and especially detailed information about thermal conductivity and its related properties in nanostructured systems. The purpose of second element, istead, is to characterize nanostructured material in order to provide a thorough description of the nanoscale features which can influence thermal transport. Semiconductors are widely adopted to devise nanostructured materials: the first part of this thesis is focused on nanostructures based on silicon and germanium. The idea of nanoengineering a material involves the usage of interfaces, reduced dimensionality, substitutional defects and alloys, and the creation of nanovoids: these components have been deeply addressed in the present investigation aiming at possible applications in the field of renewable energies (e.g. thermoelectric conversion), and in the field of information technology (e.g. thermal rectification, thermal dissipation, etc.).

In the context of complex material for technological application, organic molecules are rising due to their improved performances in several application areas: LEDs, photovovoltaic cells, thermoelectric applications, etc. The second part of this thesis aims at shredding light on the mechanisms of energy relaxation and thermal dissipation in organic and hydrogen-bonded system. Fur-

thermore, organic molecules present several interesting characteristics when arranged in a glassy configuration: here a detailed investigation to understand the role of molecular orientation in organic glasses thermal transport is also provided.

ACKNOWLEDGMENTS

Riccardo Dettori gratefully acknowledges Sardinia Regional Government for the financial support of her PhD scholarship (P.O.R. Sardegna F.S.E. Operational Programme of the Autonomous Region of Sardinia, European Social Fund 2007-2013 - Axis IV Human Resources, Objective l.3, Line of Activity l.3.1.)

CONTENTS

LIST OF FIGURES

LIST OF TABLES

ACRONYMS

Si	silicon
Ge	germanium
1D	one dimensional
MFP	mean free path
GF	Green's function
DFT	Density Functional Theory
DFPT	Density Functional Perturbation Theory
BTE	Boltzmann Transport Equation
TBR	Thermal Boundary Resistance
AMM	Acoustic Mismatch Model
DMM	Diffuse Mismatch Model
MD	Molecular Dynamics
EDIP	Environment Dipendent Interatomic Potential
CVFF	Consistent-Valent Force Field
COMPASS	Condensed-phase Optimized Molecular Potentials for Atomistic Simulation Studies
RTA	relaxation time approximation
SMA	single mode approximation
GK	Green-Kubo

PBC	periodic boundary conditions
EMD	Equilibrium Molecular Dynamics
c-Si	crystalline silicon
NEMD	Non-Equilibrium Molecular Dynamics
AEMD	Approach-to-Equilibrium Molecular Dynamics
GLE	Generalized Langevin Equation
PS	porous silicon
OPS	ordered porous silicon
RPS	random porous silicon
NW	nanowire
PSNW	porous silicon nanowire
GB	grain boundaries
MoD	morphological defect
pc-Si	polycrystalline silicon
TE	Thermoelectric Effect
SL	superlattice
PR	period ratio
HT	heterojunction
HB	hydrogen-bonded
vDOS	vibrational density of dtates
ITR	interface thermal resistance
TPD	N,N'-Bis(3-methylphenyl)-N,N'-bis(phenyl)-benzidine

vdW van der Waals

XRD X-Ray diffraction

OLED organic light-emitting device

DOF degrees of freedom

Part I

INTRODUCTION

1

INTRODUCTION

During the last two decades, the investigation on thermal transport at the nanoscale has been strongly stimulated by practical interests in thermal management in microelectronics. Indeed, thermal management is a key factor in many fields of science and technology. The design of next generation integrated circuits is one of the main driving argument when dealing with thermal transport. The performances of ultra-large scale integrated circuits are indeed critically affected by temperature. In fact, the number of components inside a single chip has rigorously followed Moore's law [1]. Nowadays, field-effect-transistors have typical channel length of 10 nm and 5-nm devices are projected for 2020, meaning that typical integrated circuit chips have billions of transistors, as shown in Fig. 1.1. Furthermore, the progressive increase of CPU operating frequency beyond a few GHz stopped when typical dissipated power reached 100 W/cm^2. Such levels of thermal and electronic power impact negatively when dealing with performances and scalability. In this perspective, a fundamental role is not only played by the power supply required: data centers and great infrastructures consume an additional $50\% - 100\%$ of additional energy for cooling, as shown in Fig. 1.2, which so far represents the most important factor limiting their performance, not the hardware itself. Present growth trends embody one of the greatest challenge of our time: technologically developed regions such as the U. S., Western Europe, and Japan currently account for 58% of the world computers, but only 15% of the world population. On top of that, the amount of equivalent CO_2 emissions generated to supply such energy demand, represent $\sim 42\%$ of worldwide emissions [2].

The above scenario outline the two main issues related to energy production and heat dissipation: first of all, the necessity to provide a continuous energy supply, limiting greenhouse gas emissions, and secondly the exigency

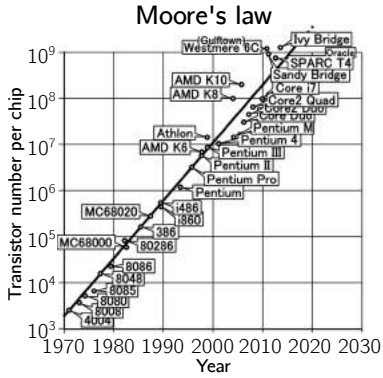

Figure 1.1. Moore's law still holds true after 50 years. The number of transistor per chip increases exponentially, meaning that the productive process is able to manufacture ever smaller components.

of efficient dissipation and adequate thermal management, which involves the capability of cooling. The latter aspect encompass many technological applications involving nano- and opto-mechanics [3], quantum technologies [4, 5], and medical applications [6]. In this context, assumes a key role the possibility of "nanostructuring", i.e. the possibility of engineering the system at the nanoscale, by reducing dimensionality, introducing interfaces or tailoring point and/or extended defects.

1.1 THE ROLE OF NANOSTRUCTURES

The most fundamental approach to understand heat is represented by Joseph Fourier's work [7], whose most important theory, the Fourier law, states that $\mathbf{j} = -\kappa\nabla T$ where $\mathbf{j}$ is the heat flux and ∇T is the temperature gradient. This law implies basically two things: heat flows in the opposite direction of a temperature gradient and the relation between the two is linear with proportionality constant κ, i.e. *thermal conductivity*. Such quantity is measured $Wm^{-1}K^{-1}$ and is the property of a material ability to conduct heat. Thermal conductivity is an *intrinsic* property, which means that it depends on many charateristics of a material, notably its structure and temperature.

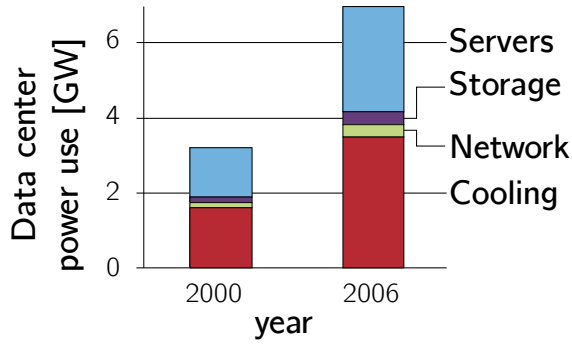

Figure 1.2. Data center power use in the U. S. doubled in six years, with an extremely large portion devoted to cooling.

In solid state systems, heat is carried by lattice vibration and electrons. In insulators and semiconductors, the concentration of free electrons is very low (even in doped semiconductors) resulting in an electronic thermal conductivity negligible with respect to lattice thermal conductivity. Quantized lattice vibrations in condensed phase, responsible for thermal conduction, are called *phonons*. Depending on the type of these vibrations, we can have longitudinal and transverse modes. Acoustic and optical phonons refer to the case where neighboring atoms oscillate in phase or out of phase, respectively. Electron transport in devices often generates optical phonon. Since these phonon have low group velocities, they have to decay to acoustic phonons so that heat is transported. When one area of the sample is hot, the interaction between neighboring atoms causes the random vibrations to propagate in the material. Huge efforts have been addressed to achieve control on phonons especially at the nanoscale, a research topic usually referred to as *nanophononics*, fueled by the importance assumed by phonons.

Consequences of nanoscaling

Spatial confinement of phonons occurs when the system size reaches the nanoscale [8, 9]. Furthermore, when the size is of the same order of magnitude as the phonon mean free path (MFP) heat conduction experiences enhancement of boundary scattering in the ballistic regime [10]. These two features can strongly affect the phonon dispersion and modify phonon properties such as phonon group velocity, polarization, density of states [11], and

affect phonon interaction with electrons, point defects, other phonons, etc. Such modification may turn out to be desirable for some applications while detrimental for others. Thus, nanostructures offer a new way of controlling phonon transport via tuning its dispersion relation, i.e., via *phonon engineering*. Modern manufacturing techniques offer the possibility to fabricate structures that are confined to 2 (thin films), 1 (nanowires), or 0 (nanodots) dimensions with sizes in the $1-100$ nm range. The possibility of controlling phonons and their interaction with electrons and photons, produced a growing interest by the scientific community, resulting in a very broad range of technological applications [12, 13].

1.1.1 *Low-dimensional thermoelectrics*

Among the many implications which feed the field of nanophononics, one of the most important is represented by the thermoelectric conversion, especially for its potential impact in the landscape of the renewable energy. In the perspective of the above mentioned energy supply, the possibility to convert low-grade thermal energy, generally a waste product of several kind of processes, to reusable electricity delineates an appealing and intriguing challenge. The efficiency of the thermoelectric process is related to a dimensionless parameter called *figure of merit*

$$ZT = \frac{\sigma S^2 T}{\kappa} \tag{1.1}$$

where T is the absolute temperature, S is the Seebeck coefficient and σ and κ are the electrical and thermal conductivities of the material, respectively [14–16]. Here κ contains both the electronic κ_e and the lattice contribution κ_l. Figure 1.3a shows the behavior of ZT and its related quantities for different class of solid materials, reported as a function of the number of charge carriers . Thermoelectric conversion is a physical phenomenon known since the end of 18th century and which involves basically all kind of materials. However, so far thermoelectric conversion has covered only niche applications due to the very low efficiency: to reach a power generation of 25%, thus comparable to traditional heat engines, a $ZT = 3.0$ is required when temperature gradients involved are $\Delta T = 400$ K. Dealing with smaller and more "human" temper-

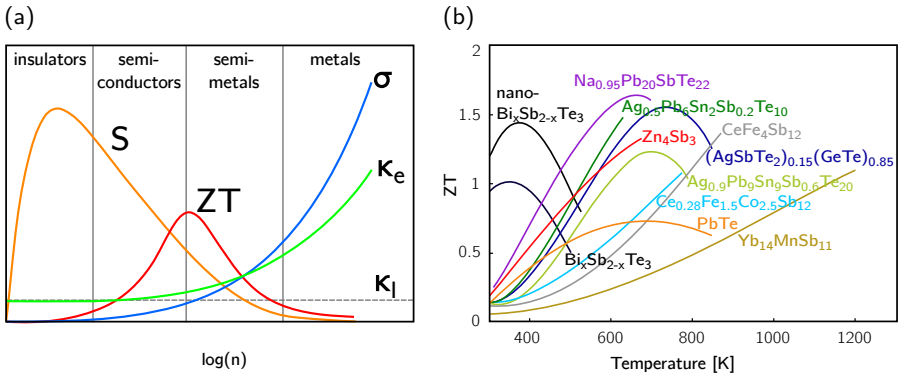

Figure 1.3. **a**: Mutual dependence of ZT on its components S, σ, κ_e and κ_l as a function of charge carriers n. **b**: Values of ZT obtained for different materials in the last 20 years, as a function of absolute T. [18].

ature values, for example $\Delta T = 20$ K, the thermoelectric efficiency drops to values of about $5-6\%$ [17]. For bulk materials, figure of merit is usually very low and hardly reaches values of 0.4.

As reported in Fig. 1.3b, which shows the figure of merit peaks for several thermoelectric materials at a given temperature, higher ZT values are obtained by devising composite systems, introducing impurities in pristine structures: as a matter of facts, the key approach to maximize ZT is to minimize the material thermal conductivity without appreciably affecting the electronic transport properties. In this respect, alloyed semiconductors, such as Bi_2Te_3, $Bi_xSb_{2x}Te_3$, PbTe and $Si_{0.8}Ge_{0.2}$ have been shown to be promising materials [19, 20]. Scattering of short-wavelength phonons on impurity atoms is responsible for the decrease of κ while thermal transport by mid- and long-wavelength phonons remains unperturbed by atomistic defects [19]. Noticeable high figure of merits have been obtained for materials which components are rare-earth or other heavy elements [21]. Such materials however, exhibit several disadvantages: they are expensive, not easy to synthesize and to scale, and their environmental impact is not negligible. In this perspective, nanostructuring a material represents the direction of near-future thermoelectric research: Dresselhaus *et al.* showed that electrons in low-dimensional semiconductors such

Nanostructured thermoelectrics

as quantum wells and wires have an improved thermoelectric power factor and $ZT > 2-3$ can be achieved [22].

One of the most popular and effective approach consists in using nanofabrication techniques so as to increase phonon scattering by internal interfaces. Superlattices consists in a succession of quantum wells and quantum barriers [23, 24]: quantum confinement of electrons eliminates some states that electrons can occupy, but electronic density of states and electronic transport properties are not markedly altered. On the contrary, phonon can appreciably suffer the presence of the barriers, resulting in a remarkable reduction of lattice thermal conductivity. Such nanostructures can reach $ZT > 1$. A natural extension of quantum wells and superlattices are quantum wires [25–27]. Theoretical studies predict a large enhancement of ZT inside quantum wires due to additional electron confinement.

In the perspective of pursuing ever higher ZT values, a full understanding of the nanoscale features becomes the paramount concern. The development of a new generation of thermoelectric materials builds on a profound comprehension of how point defects, grain boundaries, interfaces and surface scattering influence the thermal properties [28–33].

1.1.2 *Why simulating nanostructures*

Although significant progress has been made over the last years, heat transport mechanisms at the nanoscale suffer from limited available theoretical and experimental descriptions. The experimental difficulties begin with the severely limited capabilities for measuring thermal transport in increasingly small systems. Among the different measurement approaches, the 3ω method is a widely adopted procedure in the case of bulk materials and thin films [34–37], although it has been used also to investigate thermal transport in nanowires.

The 3ω method

The process involves a periodically heating of a metal heater applied to a sample: the following temperature oscillations are measured. If an AC current is used to heat it, the temperature and consequently the resistance (as long as it is temperature dependent) of the sample will change at 2ω, since the heating power varies as the square of the current. This periodic resistance changes at 2ω and, combined with the current at frequency ω, leads to a

voltage modulation with triple the driving frequency. The temperature amplitude, phase and the thermal properties are extracted from the 3ω component of the voltage along the bridge. While the 3ω method initially could only measure the out-of-plane thermal conductivity in dielectric films [38, 39], recent extensions using multiple bridges of varying width were able to measure the thermal conductivity anisotropy in superlattices [40], polymide [41], and the in-plane conductivity of thin silicon films [42]. The drawback stands in the high electrical and thermal conductivity that are required for the sample and, moreover, in the difficulty of evaluating the thermal boundaries at the contacts [43].

The 3ω can be applied also as a scanning technique by adopting a Scanning Thermal Microscope. It consists of a scanning tip with an electrical conductivity which is temperature-dependent. The tip scans the sample while an AC current is driven through it to heat it. This heat will be transferred to the sample, according to its local thermal conductivity. The consequence is a voltage signal with a frequency 3ω in response, due to the resistance of the tip, which can be measured. Despite its higher spatial resolution with respect to the standard 3ω method, scan speed is very slow and is very sensitive to mechanical vibrations and thus requires a much more complex setup to properly measure. Furthermore, the thermal contact between the tip and the sample is essential, resulting in a high dependence on the thermal contacts.

Optical techniques

A rather different approach is represented by optical techniques, which involve a laser used both as a heater and as a thermometer [43]. By using a micro-Raman technique [44, 45], the temperature change induced by the laser incidence can be related to the shift of the phonon frequency, which varies linearly with the temperature. The sample is suspended in vacuum while the ends are placed on the substrate, which serves as a thermal bath. The laser spot can scan the temperature profile in the sample, and therefore both the thermal conductivity and the thermal contact resistance can be obtained. Although it helps in overcoming the limits of the 3ω method, the problem lies in the fact that the modeling of the absorbed laser power is a non-trivial issue especially for very thin nanowires and films.

Theoretical approaches

In order to rationalize and integrate this experimental scenario, the theoretical approach acquire a central position. Computer performances have skyrocketed in the last 10 years and this has opened the possibility to perform

large scale investigations. Several theoretical approaches have been proposed: self-consistent and variational approaches to solve the Boltzmann Transport Equation (BTE) with Density Functional Theory (DFT) allowed to overcome the limits of single-mode relaxation time and the local near-to-equilibrium approximations [46], providing more accurate calculations of the intrinsic thermal conductivity of crystals [47, 48], and a more fundamental knowledge about the role of collective excitations in non-diffusive heat transport of low-dimensional nanostructures [49, 50]. However, the use of DFT is still limited to periodic systems making it unsuitable for nanostructured and disordered systems.

The Landauer approach [51] with phonon Green's function (GF) is also widely used in thermal transport calculations [52–56]: usually it is used with harmonic force constant matrices and it incorporates the Bose-Einstein statistics for phonons. As a consequence, this approach is particularly suitable to treat ballistic transport at relatively low temperatures and it allows to deal with semi-infinite open systems [28]. The drawback is represented by the underlying assumption of harmonic forces, which make this technique inadequate to the study of thermal properties at high temperature, where anharmonic effects come at play. Moreover, its high complexity and computational costs limited its use to small systems such as molecular junctions [54, 55].

In addition, a fundamental understanding of phonon scattering at boundaries and interfaces is still missing. The effect of interfaces on heat flux is known as TBR, also known as Kapitza resistance [57]. Theoretical models to quantitatively investigate quantitatively the TBR are available such as Acoustic Mismatch Model (AMM) and Diffuse Mismatch Model (DMM) [39, 58]. However, these models make *a priori* assumptions of the scattering processes (for example, scattering is considered to be elastic in both methods). Moreover, the DMM considers only diffuse scattering at the interface, while this aspect is neglected in AMM, where only specular scattering is assumed. This often results in incorrect predictions of thermal resistances.

The importance of being "Classical"

For these and other reasons, an approach involving a different description of the system of interest can be helpful, in order to be able to calculate thermal conductivity in such complex systems not addressable with the above introduced techniques. This approach is based on classical MD [59, 60], which stands as a useful complementary method to assess material properties. Due to its real space representation, MD directly provides the atomic trajectories

at well defined thermodynamic conditions, allowing to compute heat fluxes, local temperatures and a large number of other observables. MD runs can deal with system as large as $\mathcal{O}(10^7)$ for simulation times up to several tens of nanoseconds, constituting the ideal framework to investigate nanostructured materials. The disadvantage of this approach stands in the reliability of MD simulations, strictly related to the accuracy and the validity of the adopted interatomic potentials, which sometimes turn out to be inaccurate in reproducing the phonon spectrum. Furthermore, since MD is based on the integration of Newton's equation of motions, it is unable to reproduce quantum features as, for example, phonon populations (Bose-Einstein distribution) making its thermal transport predictions strictly valid only at high temperature, i.e. for temperatures higher than the Debye temperature Θ_D.

1.2 PLAN OF THIS WORK

This thesis is addressed to different goals: several theoretical approaches, lying in the MD framework, have been adopted to investigate heat transport in various material systems, characterized by different level of disorder, different states of aggregation and also different chemical nature. The panoply of methods here reported somehow complement each other: equilibrium methods based on statistical mechanics theorems are characterized by slow convergence, but are suitable for investigating separately thermal transport along different directions; non-equilibrium direct methods require long simulation times especially to perform an appropriate heat flux average, however they represent a perfect approach when addressing thermal rectification and all those measurement involving heat current inside a material; finally, methods based on the transient response to an excitation are characterized by a relatively light computational workload and, furthermore, a number of useful informations can be extracted during the approach to the equilibrium configuration. Techniques here proposed involving a temperature or an excitation decay, thus those that explore the transient regime, have been originally implemented in this work and the results obtained are the product of their first applications. In Chapter 2 is reported a detailed overview of theoretical methods used in atomistic simulations to probe thermal transport in all its details. The theoret-

ical development is accompanied by different examples related to the systems studied in the next chapters.

Different issues and features, which are state-of-the-art problems in nanoscale thermal transport as above explained, have been here explored. For example, nanoporous silicon, either in its bulk version or with reduced dimensionality, has been investigated for its intriguing applications in the field of thermal insulation and for thermoelectric applications. Thermoelectric applications have also stimulated extensive simulations in silicon-germanium nanostructures, in order to reduce the thermal conductivity and achieve high thermoelectric figures of merit. Possible thermal rectification without interfaces is demanded by applications in nanophonics and by the possibility of devising the building blocks for logic gates controlled by phonons. The investigation of thermal transport in organic glasses is encouraged by their promising performances in optoelectronics and in the field of photovoltaics.

The topics covered in the present work are quite diverse, however the very nature of the materials here investigated offers a natural division of this thesis in two main part: the first one concerning thermal transport in inorganic systems, nanostructured semiconductor for which model potentials such as Tersoff and Environment Dipendent Interatomic Potential (EDIP) are required, and the second part dealing with hydrogen bonded and organic molecules, which instead necessitate empirical force field of first and second generation, such as CVFF and the Condensed-phase Optimized Molecular Potentials for Atomistic Simulation Studies (COMPASS) force field. In particular, in Chapter 3 nanostructured silicon is taken into account: a profound analysis of the role of defects in c-Si is presented, addressing the role of point defects and extended defects as well. Indeed, a model for thermal conductivity in nanoporous silicon is derived from atomistic results. Then, the interplay between localized porosity and extended grain boundaries is critically addressed for nanoporous polycrystalline silicon: the model for κ previously introduced is reinterpreted by considering the "gray" and the "non-gray" approaches, i.e. without or with spectral resolution. Finally, also the interaction between defects and dimensionality has been studied: the thermal conductivity model for nanoporous silicon is extended to the case of nanoporous nanowires, by fitting atomistic results and providing physical insight about the investigated system.

Si and Ge structures are instead presented in Chapter 4. Here, the role of the interface is considered in two different flavors: in the first place, heat transfer in Ge/Si and Ge/Si_xGe_{1-x} superlattices is studied to highlight the effect of different silicon concentrations in SiGe alloys as a phonon barrier and the period ratio (defined as the ratio between the germanium layer and SiGe layer thicknesses) as well. Then, a closer look to the interface between the two different materials itself is given: a different formulation to calculate the interface thermal resistance is introduced, based on a non-equilibrium thermodynamics approach.

The final chapter of the first part is Chapter 5: here the two classes of impurities (substitutional or voids) previously introduced are used to realize rectifying materials avoiding discontinuities and interfaces, thus by designing graded geometries. The role of system length, temperature offset and defect concentration is taken into account

In the second part of the thesis, Chapter 6 is devoted to the study of energy relaxation in organic molecules and hydrogen bonded liquids in general. A spectrally resolved thermostat, which only transfers kinetic energy to a confined region of the vibrational spectrum is introduced. Thus, the thermostatting occurs only for a subset of the system degrees of freedom (DOF), exciting the oxygen-deuterium (in the case of deuterated methanol) or the oxygen-hydrogen (in the case of water) stretching mode in order to mimic a pump and probe vibrational spectroscopy experiment. The goal is to study how the spectral excitation is relaxed thanks to the coupling between the excited modes and the unperturbed ones.

Next, in Chapter 7, different kind of organic glasses are realized. Typical glass former with more or less symmetric shape are considered, in order to provide a consistent picture about the role of anisotropy in thermal conduction. Two classes of system, isotropic and anisotropic, are investigated and thermal conductivity calculations are performed together with detailed characterization of the morphological features and molecular orientation.

Finally, in Appendix A a brief explanation about the MD scheme underlying this thesis is given, while Appendix B offers a quick overview about the interatomic potentials extensively adopted in this work.

2

MODELING THERMAL TRANSPORT

Contents

In this chapter, the two main methods for investigating thermal transport are described. In particular, in the following section the so-called *phonon picture* is briefly explained in its main features. The phonon picture relies on a reciprocal space description of the system and thus it requires the definition of a wave vector, which is the typical situation found in perfect crystals. However, when translational invariance is no longer satisfied. it is necessary to switch to an *atomistic picture* which is built on a real space description and thus only involves the knowledge of atomic positions and velocities.

2.1 BOLTZMANN TRANSPORT EQUATION

Lattice dynamics describes the vibrations of the atoms in a crystal: in fact, in dielectric crystals lattice vibrations are the main heat carriers. In this context, lattice dynamics provides the mathematical framework to describe, exactly, the interatomic forces. In its most basic form, lattice dynamics describes the crystal potential energy as a function of separation between the atoms

$$V = \frac{1}{2} \sum_{i,j}^{N} \phi_{i,j}(r_{i,j}) \tag{2.1}$$

where $\phi_{i,j}(r_{i,j})$ is some function that depends on the distance between atoms i and j.

Phonons investigation, and their related properties, represents a complicated task. Methods from first principles can, in principle, provide accurate predictions on the material properties without using any fitting parameter, relying only in the chemical composition of the system under investigation. However, the increasing precision and sophistication of the adopted numerical method require a deep understanding of the physical phenomena. Currently, one of the most used approach is the DFT [61, 62] which allows to evaluate any ground state property. The electronic many-body problem is reduced to a single particle problem where all the informations are stored in the electronic density. Many physical properties, such as phonons scattering, electron-phonon interactions or polarizability, depend upon a system response to some form of perturbation. In these cases the system responses may be calculated by DFT with the addition of some perturbing potential and by using the so called Density Functional Perturbation Theory (DFPT) [63], which is a powerful theoretical tool to address such properties. Lattice dynamics approaches to thermal transport rely either on the harmonic approximation (harmonic Kubo [64] or GF approaches [52]), or account for anharmonic terms in a perturbative manner, which is the case of the BTE.

Phonons interaction

The main idea behind BTE is to divide phonons interactions in two distinxt terms: the first part accounts for the interaction with external forces, while the second one is related to microscopic interactions between the particles. These collisions continuously "create" and "destroy" phonons, thus the idea is to study phonon distribution as a function of time. In equilibrium condition, at a temperature T, the phonon system is characterized by the Bose-Einstein thermal equilibrium distribution:

$$n^0_{\mathbf{k},s} = \frac{1}{\exp\left(\frac{\hbar\omega_{\mathbf{k},s}}{k_B T}\right) - 1} \tag{2.2}$$

Here $\mathbf{k}, s$ indicates the phonon wave vector $\mathbf{k}$ in a specific phonon branch s, while $\omega_{\mathbf{k},s}$ is the phonon frequency. Starting from this condition of equilibrium, if a temperature gradient is applied, the phonon population leaves its equilibrium condition reaching an out-of-equilibrium one: a corresponding flux of heat, collinear to the gradient, is thus generated.

The most general version of the BTE [65] reads as

$$-v_{\mathbf{k},s}\nabla T\frac{\partial n_{\mathbf{k},s}}{\partial T}+\left.\frac{\partial n_{\mathbf{k},s}}{\partial t}\right|_{scatt}=0 \tag{2.3}$$

where $v_{\mathbf{k},s}$ is the group velocity and $n_{\mathbf{k},s}$ is the occupation factor of the specific mode, which includes all deviations from equilibrium phonon distribution. The two terms in Eq. (2.3) describe diffusion processes, i.e. a system of non interacting phonons, and scattering processes respectively, which form is unknown to date, since a theory for phonon cross section for scattering of phonons in real space is still missing. In a perfect harmonic crystals with no defects, no impurities and no boundaries, phonon MFP is infinite and so the thermal conductivity. However, this is not the case and real materials have finite thermal conductivity. This can be explained by the fact that real materials are not perfectly harmonic and that phonons actually scatter via a variety of mechanisms, including phonon-phonon interactions (vibrational anharmonicities), defect scattering, surface scattering, electron-phonon interactions. Discarding for one moment effects due to defects and to surfaces (i.e. considering perfect and bulk crystals) and electron-phonon interactions (i.e. considering only semiconductors), phonon-phonon interactions can be classified into two distinct type of interactions. The first, called *normal* process (N-process), involves the collision of two phonons, $\mathbf{k}_1$ and $\mathbf{k}_2$, that combine to form a third phonon, $\mathbf{k}_3$, via the following relation

$$\omega_3=\omega_1+\omega_2 \tag{2.4}$$

In this type of interaction, crystal momentum is conserved. If this was the only type of phonon interaction, then there would be nothing impeding the transport of energy, resulting in an infinite thermal conductivity. The second type of phonon interaction, called *Umklapp* process (U-process), combines two phonons in such a way that crystal momentum is not conserved. This can be described according to the relation

$$\mathbf{k}_1+\mathbf{k}_2=\mathbf{k}_3+\mathbf{G} \tag{2.5}$$

where $\mathbf{G}$ is a reciprocal lattice vector. U-processes lead to finite thermal conductivities and are described by the anharmonic terms [66, 67].

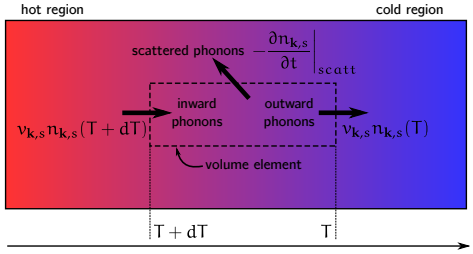

Figure 2.1. An applied thermal gradient generates a heat flux, determined by the net variation of the phonon population within each volume element, due to the different phonon population at the hot and cold ends of the volume element and to scattered phonons.

Dealing with BTE, the main challenge is to determine and calculate an expression for the scattering term. The general approach for solving Eq. (2.3) involves dealing with small perturbation from the equilibrium: typically, when considering small temperatures gradient, for example the situation depicted in Fig. 2.1, it is assumed that the modes occupation factor withstands small deviations with respect to the equilibrium value. This allow to recast Eq. (2.3) in a linearized form. In fact, exploiting the relaxation time approximation (RTA) or single mode approximation (SMA), a single lifetime can be adopted to describe the overall effect of the scattering processes for each mode, assuming the equilibrium for the remaining phonon modes

Linearizing BTE

$$\left.\frac{\partial n_{\mathbf{k},s}}{\partial t}\right|_{scatt} = \frac{n_{\mathbf{k},s} - n^0_{\mathbf{k},s}}{\tau_{\mathbf{k},s}} \tag{2.6}$$

where $\tau_{\mathbf{k},s}$ is the lifetime and $n^0_{\mathbf{k},s}$ again is the equilibrium occupation factor and is given by Eq. (2.2). Hence, it is assumed that fluctuations $n_{\mathbf{k},s} - n^0_{\mathbf{k},s}$ are small and not temperature dependent. Adopting this strategy, BTE can be solved in terms of $n_{\mathbf{k},s}$. The heat flux due to phonons motion, i.e. due to the fluctuations of the distribution functions with respect to equilibrium, is given by

$$\mathbf{j} = \frac{1}{N_{\mathbf{k}} V} \sum_{\mathbf{k},s} \hbar \omega_{\mathbf{k},s} v_{\mathbf{k},s} n_{\mathbf{k},s} \tag{2.7}$$

Considering Fourier law

$$\mathbf{j}(x,y,z) = -\kappa \nabla T(x,y,z) \tag{2.8}$$

where $\mathbf{j}$ is the heat flux vector, κ is the system thermal conductivity and $T(x,y,z)$ is the local temperature, thermal conductivity can be obtained as [68, 69]

$$\kappa = \frac{1}{N_{\mathbf{k}} V} \sum_{\mathbf{k},s} c_{\mathbf{k},s} \mathbf{v}_{\mathbf{k},s}^2 \tau_{\mathbf{k},s} \tag{2.9}$$

where $N_{\mathbf{k}}$ is the number of considered $\mathbf{k}$-point for the calculation.

Phonon frequencies and phonon eigenmodes are obtained by diagonalizing the dynamical matrix [68]

$$D_{\alpha\beta}(\mathbf{bb'}|\mathbf{k}) = \frac{1}{\sqrt{m_b m_{b'}}} \sum_{l'} \Phi_{\alpha\beta}(\mathbf{ob},\mathbf{l'b'}) \exp(i\mathbf{kl'}) \tag{2.10}$$

where $\Phi_{\alpha\beta}(\mathbf{ob},\mathbf{l'b'})$ are the harmonic force constant defined as the second order derivatives of potential energy W with respect to atomic displacements u, which are assumed to be small, with respect to the equilibrium positions $(0b)$, l is the l-th unit cell lattice vector, b represents an atom in the l-th cell with mass m_b, and α and β are Cartesian coordinates, Quantum heat capacity for phonon mode $c_{\mathbf{k},s}$ is given by

$$c_{\mathbf{k},s} = k_B \frac{\left(\frac{\hbar\omega_{\mathbf{k},s}}{k_B T}\right)^2 \exp\left(\frac{\hbar\omega_{\mathbf{k},s}}{k_B T}\right)}{\left[\exp\left(\frac{\hbar\omega_{\mathbf{k},s}}{k_B T}\right) - 1\right]^2} \tag{2.11}$$

Group velocities are defined according to $v_{\mathbf{k},s} = d\omega_{\mathbf{k},s}/d\mathbf{k}$. In RTA approximation, first order perturbation theory is adopted

$$v_{\mathbf{k},s} = \frac{1}{2\omega_{\mathbf{k},s}} \left\langle \mathbf{k},s \left| \frac{dD(\mathbf{k})}{d\mathbf{k}} \right| \mathbf{k},s \right\rangle \tag{2.12}$$

Moreover, phonon lifetime are computed according to the Fermi golden rule and considering only the lowest order term, that is the contribution from three-phonon processes (*quasi-harmonic approximation*) [68–70]

$$\begin{aligned}\tau_{\mathbf{k},s}^{-1} =& \frac{\pi\hbar}{4N_{\mathbf{k}}} \sum_{\mathbf{k}',s'} \sum_{\mathbf{k}'',s''} \delta_{\mathbf{G},\mathbf{k}+\mathbf{k}'+\mathbf{k}''} \frac{|V_3(\mathbf{k}s,\mathbf{k}'s',\mathbf{k}''s'')|^2}{\omega_{\mathbf{k},s}\omega_{\mathbf{k}',s'}\omega_{\mathbf{k}'',s''}} \times \\ &\times [\frac{1}{2}(1+n^0_{\mathbf{k}',s'}+n^0_{\mathbf{k}'',s''})\delta(\omega_{\mathbf{k},s}-\omega_{\mathbf{k}',s'}-\omega_{\mathbf{k}'',s''}) + \\ &+(n^0_{\mathbf{k}',s'}+n^0_{\mathbf{k}'',s''})\delta(\omega_{\mathbf{k},s}+\omega_{\mathbf{k}',s'}-\omega_{\mathbf{k}'',s''})]\end{aligned} \tag{2.13}$$

where phonon modes $(\mathbf{k},s),(\mathbf{k}',s')$ e $(\mathbf{k}'',s'')$ are coupled by the matrix element

$$\begin{aligned}V_3(\mathbf{k}s,\mathbf{k}'s',\mathbf{k}''s'') =& \sum_{\mathbf{l}',\mathbf{l}''} \sum_{\mathbf{b},\mathbf{b}',\mathbf{b}''} \sum_{\alpha,\beta,\gamma} \Psi_{\alpha,\beta,\gamma}(\mathbf{ob},\mathbf{l}'\mathbf{b}',\mathbf{l}''\mathbf{b}'') \exp(i\mathbf{k}'\mathbf{l}') \times \\ &\times \exp(i\mathbf{k}''\mathbf{l}'') \frac{e_\alpha(\mathbf{b}|\mathbf{k}s)e_\beta(\mathbf{b}'|\mathbf{k}'s')e_\gamma(\mathbf{b}''|\mathbf{k}''s'')}{\sqrt{m_{\mathbf{b}}m_{\mathbf{b}'}m_{\mathbf{b}''}}}\end{aligned} \tag{2.14}$$

$\Psi_{\alpha,\beta,\gamma}(\mathbf{ob},\mathbf{l}'\mathbf{b}',\mathbf{l}''\mathbf{b}'')$ are the third order force constants, defined as the third order derivatives of potential energy with respect to small atomic displacements around the equilibrium position.

The SMA assumes that each phonon population thermalizes independently from the other ones and the thermal conductivity can be written in terms individual phonon properties, which is equivalent to say that a given amount of heat current is perfectly dissipated every time that a single phonon is scattered. This assumption is in contradiction to the fact that the normal N-processes (Eq. (2.4)) are momentum-conserving. As a consequence, this approximation fails in describing heat flux exchange among the various phonon modes, providing an approximate treatment of the heat transport theory. SMA is a reliable to describe thermal transport in 3D crystal structures at temperatures above the room temperature where phonon population is restored isothermally thanks to the high number of scattering.

Beyond the SMA

In order to correct the inadequacy of the SMA at low temperatures Callaway combined the procedure of Klemens [71] and Ziman [46] splitting the relaxation process in two steps. His idea relies on the assumption that, since N

scattering rates are very large, an out-of-equilibrium distribution will mostly decay first into a drifting distribution, and from this state it will relax towards the static equilibrium (the Bose-Einstein distribution) thanks to the other resistive scattering events. With this model Callaway correctly describe the germanium experimental data at low temperatures [72].

In more recent years different approaches have been developed for solving exactly the BTE [47, 48]. The exact solution becomes mandatory when studying systems, such as 2D systems [49, 73, 74] where the high abundance of N-processes makes the SMA completely unreliable.

2.2 MOLECULAR DYNAMICS

The above described approach represents a powerful and reliable tool when dealing with thermal transport in crystalline systems. However, the drawback is represented by the fact that in case of defected or nanostructured systems (such the ones proposed in Chpt. 3, 4 and 5), the description of the system would require either a very large unit cell or the whole system itself, making the reciprocal space analysis useless. Moreover, solving the BTE within the empirical potential framework, i.e, by computing interatomic force constant empirical potential, often results in thermal conductivity values in open disagreement with experimental ones [75], Thus, it is always preferable to adopt an ab initio or, better, a self consistent approach which, however, strongly limit the class of addressable systems. Whenever the system of interest lacks of translational invariance, atomic vibrations cannot be any longer described as collective modes but it is possible to exploit a direct approach, which require the calculation of atomic trajectories in real space. To this aim, a force field describing atomic interactions is needed; such a force field can be developed at very different levels of sophistication, varying from fully-quantum ab initio techniques [76, 77] (the most fundamental methods), to quantum semi-empirical [78] schemes (a compromise between accurate but expensive ab initio methods and light but somewhat inaccurate empirical ones), to fully classical empirical potentials [79] (taking full profit from their low numerical complexity but suffering in terms of accuracy and transferability). Newton equations of motion are numerically solved for all interacting particles by taking under control

the thermodynamical ensemble, for any given state of temperature. volume and pressure (or strain). Some physical quantities can be calculated on-the-fly during the simulation as ensemble averages over the atomic trajectories, according to standard statistical mechanics, while others (e.g. transport coefficients) require the knowledge of the entire trajectory before being computed. The method is known as MD and shows an extremely high degree of applicability, regardless of state aggregation, lattice disorder and thermodynamical configuration. A detailed description of the MD framework is reported in Appx. A. In this section, MD simulations will be taken under consideration in all their different flavors: Equilibrium Molecular Dynamics (EMD) (or Green-Kubo (GK) method), which relies on the linear-response theory and fluctuation-dissipation theorem, and Non-Equilibrium Molecular Dynamics (NEMD), which address κ through the Fourier law, have been adopted to perform the calculations and the investigations reported in this thesis. Moreover, here will be illustrated the importance of the transient regime, which analyze the system during its approach to the equilibrium, and a spectrally resolved method, which influences only selected regions of the vibrational spectrum. Both these system have been developed and implemented for the first time during the investigation here proposed.

2.2.1 *Equilibrium Molecular Dynamics*

From a system of interacting atoms subjected to a time-independent perturbation ∇n, it is possible to obtain the corresponding time-dependent response $\mathcal{J}(t)$. At the first order, a transport coefficient η can be defined as the ratio between the system response and the perturbation observed ideally for an infinite time

$$\eta \sim \lim_{t\to\infty} \frac{\mathcal{J}(t)}{\nabla n} \tag{2.15}$$

The fluctuation-dissipation theorem, in a *steady state response regime*, proves that [80, 81]

$$\eta \sim \lim_{t\to\infty} \int_0^t \langle \xi(t')\xi(0)\rangle \, dt' \tag{2.16}$$

stating that any transport coefficient is related to the *time auto-correlation function* of a physical quantity $\xi(t)$. The *GK relations* give the exact mathematical expression for transport coefficients of several transport mechanisms and, if the perturbation is a thermal gradient, Eq. (2.16) becomes the GK formula for thermal conductivity [80, 82–84], which is obtained from the *auto-correlation function of the heat flux*

$$\kappa_{\lambda\mu}^{GK}(T) = \frac{1}{3Vk_BT^2}\lim_{t\to\infty}\int_0^t \langle j_\lambda(t')j_\mu(0)\rangle_T dt' \tag{2.17}$$

where $\langle\dots\rangle_T$ is the ensemble average taken at constant temperature T, V is the system volume, and $\kappa_{\lambda\mu}^{GK}$ denotes the $\lambda\mu$-component ($\lambda,\mu = x,y,z$).

The aim of the EMD approach is to implement the GK solution in a MD simulation, a non-trivial task for two main reasons: the convergence (in time and system size) of the auto-correlation function $\langle j_\lambda(t')j_\mu(0)\rangle$, which however strongly depends on the nature of the system investigated, and the actual calculation of $\mathbf{j}(t)$, which depends on the microscopic theory of heat flux.

Microscopic theory of heat flux

Problems in the calculation of $\mathbf{j}(t)$ arise when using empirical many-body potentials, which are the foundation of classical MD. Singe-atom energies

$$E_i(t) = \frac{1}{2}m_i v_i^2(t) + U_i(t) \tag{2.18}$$

where m_i are atomic masses and $U_i(t)$ is the on-site potential energy at time t, are needed to calculate the heat current during an EMD run, according to the microscopic definition

$$\mathbf{j}(t) = \frac{d}{dt}\sum_i \mathbf{r}_i(t)E_i(r) = \sum_i\left[\mathbf{v}_i(t)E_i(t) + \mathbf{r}_i(t)\frac{d}{dt}E_i\right]. \tag{2.19}$$

On the second right hand side of this equation two contributions can be identified: $\mathbf{j}^{conv}(t) = \sum_i \mathbf{v}_i(t)E_i(t)$ is the *kinetic contribution* (also called the convective term), which is negligibly small in solid-state materials [85], and

$$\mathbf{j}^{pot}(t) = \sum_i \mathbf{r}_i(t)\frac{d}{dt}E_i = \sum_i \mathbf{r}_i(t)\left[\mathbf{F}_i(t)\cdot\mathbf{v}_i(t)\right] + \sum_i \mathbf{r}_i(t)\frac{dU_i(t)}{dt} \tag{2.20}$$

the *potential contribution*, where $\mathbf{F}_i(t)$ is the net force acting on the i-th atom at time t. In what follows, the kinetic term will be discarded.

A many-body potential U can be decomposed in terms of single site contributions U_i [86]

$$U = \sum_i U_i(\{\mathbf{r}_{j\neq i}\}) \tag{2.21}$$

where the pair potential between particles i and j, only depends on the distance r_{ij} between the particles. Hence for any particle pair (i,j) a pairwise force can be defined

$$\begin{aligned} \mathbf{F_i} &= \sum_{j\neq i} \mathbf{F}_{ij}, \\ \mathbf{F_{ij}} &= \frac{\partial U_{ij}}{\partial \mathbf{r}_{ij}} = \frac{\partial U_i}{\partial \mathbf{r}_{ij}} - \frac{\partial U_j}{\partial \mathbf{r}_{ji}} = -\mathbf{F}_{ji} \end{aligned} \tag{2.22}$$

where F_{ij} is the force on particle i due to particle j and the convention $r_{ij} \equiv r_j - r_i$ for the relative position between two particles is adopted. If periodic boundary conditions (PBC) are applied in a given direction, the minimum image convention is used to all the relative positions in that direction (see Appx. A). Equation (2.22) allows to cast the potential contribution in its most general form

$$\mathbf{j}^{pot}(t) = \sum_i \sum_{j\neq i} \mathbf{r}_{ij}(t) \left[\frac{\partial U_j(t)}{\partial \mathbf{r}_{ij}} \cdot \mathbf{v}_i(t) \right] \tag{2.23}$$

which is known also as the Hardy formula [87]. This relation for the heat current applies to any many-body potential, because the condition that the many-body bond energy U_{ij} (or the site potential U_i) is only a function of the set of vectors $\{r_{ij}\}_{j\neq i}$, is satisfied by any empirical potential: any other position difference vector can be expressed as the difference of two vectors in this set. Practical implementations have been worked out for the most popular empirical potentials [86], including the Stillinger-Weber [88], the Tersoff [89], and the Brenner [90] potentials.

Classical MD simulations are based on model potentials which have simplified analytical forms and, furthermore, their parameters are obtained by fitting macroscopic quantities (e.g. structural, mechanical properties) which

are not necessarily connected to third-order (or higher) derivatives of the energy with respect to the atomic displacements. This results in a poor description of anharmonic forces and, consequently, in not always accurate thermal conductivity values. These considerations hold whenever model potentials are adopted instead of computing the interactions self-consistently, as already stated above for BTE. However, model-potential MD is suitable in obtaining trends like (thermal conductivity vs. temperature or vs. system size or vs. chemical composition), since it can deal with very large and complex systems, and thus this methodology is better suited for getting physical insight, rather than reliable absolute numbers. An alternative is represented by the combination of the GK approach and the *ab-initio* MD, which provide a much accurate description of the interatomic interactions. Although this has been done only recently [91–93], since this implementation has always been considered unfeasible due to the ill definiteness of quantum mechanical energy densities and currents at the atomic scale, its application is in any case confined to small scale systems and hence homogeneous and/or scale invariant systems.

The issue of convergence

The computation of $\kappa_{\lambda\mu}^{GK}$ requires a well-converged auto-correlation function, which is related to very nature of the system itself. For example, considering bulk c-Si containing 1728 atoms as a test system, Fig. 2.2a shows how at least 10^6 time steps are required for the heat current autocorrelation function to reach a converged value. This calculation, performed adopting the Stillinger-Weber potential [88], shows how the slow convergence of the autocorrelation function is reflected on the thermal conductivity behavior, which converges rather slowly. The obtained value of ~ 197 W m^{-1}K^{-1} is appreciably larger than the experimental one of ~ 150 W m^{-1}K^{-1}: such a disagreement is not due to any failure of the GK formulation or any inaccuracy in its implementation, rather it is due to the limited accuracy of the adopted interaction potential in providing the vibrational spectrum of c-Si, and to the purity of the simulated sample, which is ideally elemental with no defects, impurities and surfaces. However, the slow-convergence issue is not always a limiting factor, as obtained for a sample of liquid methanol containing 216 molecules: as shown in Fig. 2.2b, the converged value κ is definitively reached within the first 500000 time steps. Moreover, for c-Si a time step of $\delta t = 2.0$ fs was adopted, while for methanol $\delta t = 0.5$ fs; only 25% of simulation time of the crystalline sample was required for the liquid one. It is possible to conclude

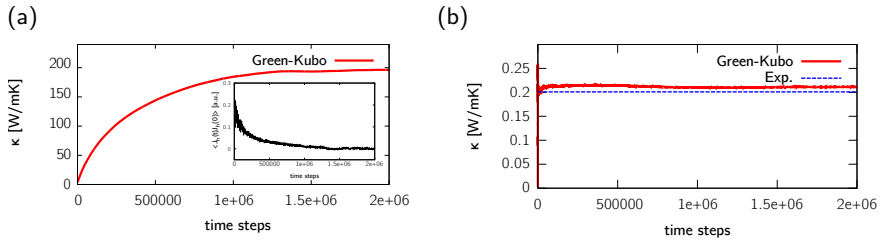

Figure 2.2. **a**: Thermal conductivity convergence for a bulk c-Si sample containing 1728 atoms during a GK run performed at T = 500 K. In the inset is shown the convergence of the auto-correlation function for the heat flux, which is used to compute κ. **b**: Thermal conductivity convergence for a methanol sample containing 216 molecules: in contrast with the behavior obtained for c-Si, thermal conductivity reaches a converged value within the first 500000 time steps. The final conductivity value is in very good agreement with the experimental one [94].

that a drawback of the EMD approach is that extremely long simulations are needed, representing an exceedingly large computational effort for larger system sizes. However, the EMD method is not completely disadvantageous: when dealing with systems with no long-range order, such as liquid methanol (see Chpt. 6) or organic glasses (see Chpt. 7), considerably shorter simulations are sufficient to correctly converge the heat flux autocorrelation function. Furthermore, it represents a powerful tool to distinguish the contribution of different directions to thermal transport, when addressing the role of anisotropies or peculiar structural geometries (see Chpt. 7).

2.2.2 *Non-Equilibrium Molecular Dynamics*

In contrast to the GK formalism, simulations performed according to NEMD methods compute κ in analogy to what happens in an experimental set up, when a perturbation is applied to the system in order to observe its response in terms of flux to study transport phenomena. Studying heat transport requires the fulfillment of two fundamental hypothesis:

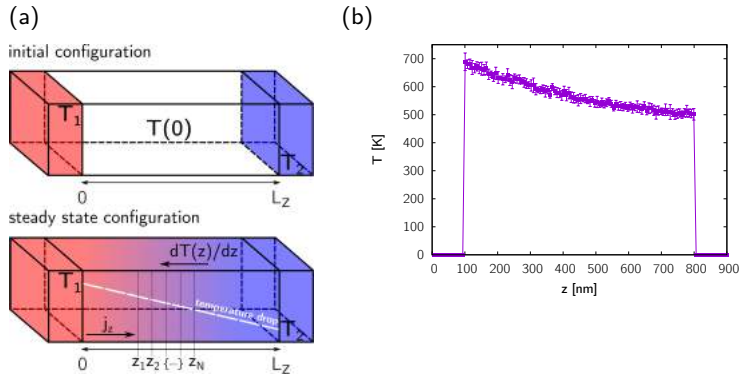

Figure 2.3. **a**: Top, setup of a NEMD simulation. Bottom, the resulting temperature drop (dashed white line), once that a steady state condition has been established. Both the resulting heat flux j_z and thermal gradient $dT(z)/dz$ are shown. The color palette is chosen according to temperature gradient from the hot reservoir, T_1, and the cold one, T_2. **b**: Calculated temperature profile along the simulation cell, according to the procedure here described. NB: although in a uniform and isotropic material the established temperature profile between the thermostats is a straight line, in this case it deviates from linearity since the system is non-homogeneous, due to an increasing content of germanium along the z direction (see Chpt. 5).

1. it is necessary that the non-equilibrium condition corresponds to the *steady state*, which results in a stationary configuration and the perturbation, in this case a temperature gradient, does not change in time. The steady state requires a transient time, during which the system is setting up its own response and which duration depends on the actual perturbation and, of course, on the very physics of the system under investigation. The stationary configuration allows to perform time-averaging of the response physical quantity, namely the heat flux;

2. it is necessary that the system obeys to the Fourier law (Eq. (2.8)), which is a transport equation and it is valid locally and at any time as

well, provided that the only heat transport mechanism is the conduction (no convection or chemical reactions inside the system)

The most common approach for NEMD simulations relies on choosing a direction for heat flux propagation (in this case the z direction). First of all, the system is thermostatted at a suitable temperature $T(0)$ and then the two ends of the simulation cell are coupled to two thermostats at temperature T_1 and T_2, with $T_2 \leqslant T(0) \leqslant T_1$, as shown in Fig. 2.3a.

In achieving the stationary condition, the two thermostats act as a hot and cold reservoir and the PBC are only applied in the plane normal to the heat flux direction. The simulation cell is then aged by keeping the two reservoir at constant temperature, in order to provide a heat source and a sink, while the equations of motion in the central region are integrating according to the NVE ensemble, i.e. without any thermostatting. After a sufficient time, a temperature gradient is established along the sample, as shown in Fig. 2.3b.

A very useful quantity to calculate during NEMD simulations is the local temperature profile $T(z,t)$: the kinetic energy of each atom in the system is averaged over a suitable set of thin material slabs at positions $\{z_1, z_2, \ldots, z_N\}$. The width of these slabs should be large enough to allow a proper kinetic temperature calculation, and it is usually defined include at least $\simeq 10^2$ atoms. This allows to define a spatial dependent kinetic temperature, as reported in Fig. 2.3c, which is further averaged over time periods much shorter than the total duration of the NEMD simulation. In Fig. 2.4a is reported the kinetic temperature as a function of time of several slabs defined in a nanostructured system of Si and Ge (an alloy with z-dependent stoichiometry, see Chpt. 5) with $L_z = 69.46$ nm: the two reservoir are kept at $T_1 = 700$ K and $T_2 = 500$ K. Here the initial temperature of the central region was set at $T(0) = 0$ K: this allows for an effective visualization of the establishment of the steady state regime and the corresponding temperature drop across the sample, but usually it requires very long simulations time. Figure 2.4c instead shows the same situation but with $T(0) = (T_1 + T_2)/2 = 600$ K. This choice can be useful to save simulation time, since it allows to reach the steady state at least 300 ps earlier, as demonstrated also by the exchanged energy between the thermostat and the system in Fig. 2.4b and d, respectively.

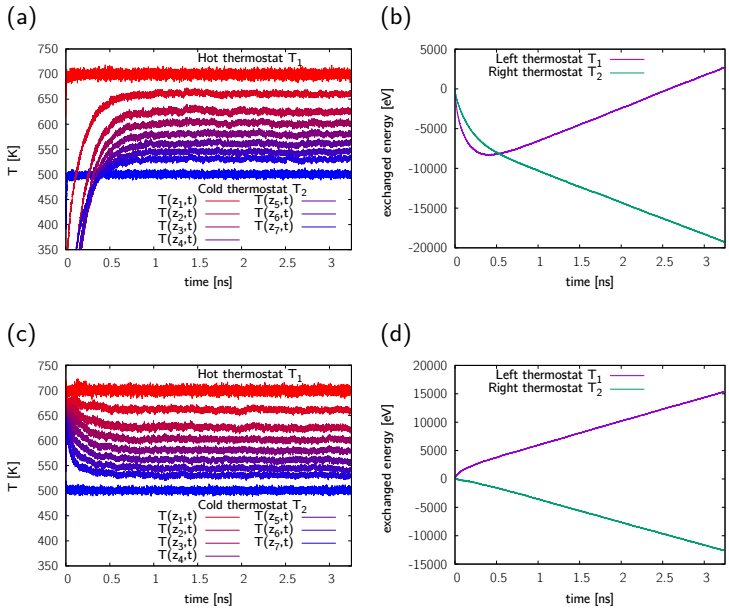

Figure 2.4. **a**: Kinetic temperatures for the hot and cold thermostats and for seven different slabs inside the central region, with different z_i, for a NEMD run where $T(0) = 0$ K. **b**: The work done by the two thermostats, i.e. the energy exchanged with the central region, for a NEMD run where $T(0) = 0$ K. **c** and **d**: The same quantities shown in **a** and **b**, but relative to a NEMD run where $T(0) = (T_1 + T_2)/2 = 600$ K, with $T_1 = 700$ K and $T_2 = 500$ K.

As a matter of facts, establishing the temperature gradient in the simulation cell could represent a bottleneck of NEMD as for its resulting computational workload: the lower the material thermal conductivity, the longer the simulation time. Furthermore, an additional time is required once reached the steady state in order to accumulate data for computing with enough accuracy the heat flux, as explained below. This is a non-trivial drawback of the method, especially when dealing with large simulation cells.

Calculation of κ

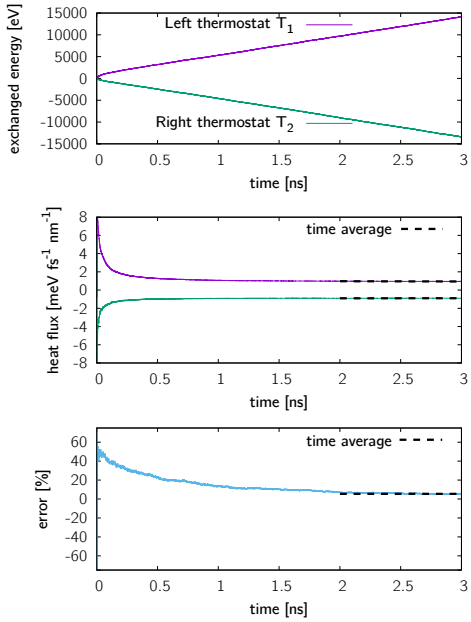

Figure 2.5. Top: Injected (violet) and extracted (green) energy in a silicon-germanium graded system subjected to a temperature offset of 200 K [95]. Middle: Heat flux coming out from/going into the hot/cold thermostat obtained by performing the time derivative of the injected/extracted energy and dividing by the cross section. Bottom: Relative difference between the extracted and the injected heat flux. Dashed black lines represent the time average of all the corresponding quantities

During the stationary condition, thermal conductivity is computed according to the one dimensional Fourier law (see also Eq. (2.8))

$$\kappa_{\mathrm{NEMD}}(T) = \frac{\langle j_z(T)\rangle}{\Delta T/L_z} \tag{2.24}$$

where $\langle \dots \rangle$ indicates time averages taken over a suitable time interval and the temperature gradient ∇T has been replaced with the ratio between the temperature offset and the distance between the two thermostatted regions. The temperature drop ΔT within the core region is evaluated directly from the local kinetic temperature profile $T(z,t)$ already mentioned, which is also

shown in Fig. 2.3c, while heat flux j_z is computed as explained in Sec. 2.2.1 or, alternatively, by considering the work done by the thermostats. The latter option is more straightforward because is directly calculated by the MD code for any thermostat implemented, without ambiguities for the calculation of the heat flux. The instantaneous energies injected/extracted by the hot/cold reservoir into/from the system, hereafter indicated as $\mathcal{L}^{in}$ and $\mathcal{L}^{out}$ respectively, are computed from the beginning of the simulation, as shown in Fig. 2.4b and d. Their time derivatives, divided by the cross section of the simulation cell

$$j_z^{in,out} = \frac{1}{\Sigma}\frac{\partial \mathcal{L}^{in,out}}{\partial t} \tag{2.25}$$

have opposite sign and correspond to the fluxes coming from/going into the central region from the two thermostats (see Fig.2.5).

A steady state condition is proclaimed only when $|j_z^{in}| = |j_z^{out}|$ within the accepted numerical error. This procedure requires additional simulation time after the steady state is settled. Once reached such a condition, the heat current is calculated as the average $(|j_z^{in}| + |j_z^{out}|)/2$. Deviations from the asymptotic relative difference $(|j_z^{in}| - |j_z^{out}|)/|j_z^{in}|$ are used for estimating the error on the heat current. Thus, the computation of the thermostat work provides also a quick and useful way to check the progress in reaching the stationary condition, i.e. whether if the two curves plotted in Fig. 2.4b and d have the same slope.

NEMD method provides also a useful tool to investigate several phenomena related to thermal transport, e.g. interface thermal resistance or thermal rectification, as extensively explained in Sec. 5.1.

Reverse Non-Equilibrium Molecular Dynamics

For sake of completeness, in what follows it will be discussed an alternative formulation of the non-equilibrium MD method. The advantage of this approach relies on the fact that there is no need to compute the heat flux: the main idea of the *reverse* NEMD (also known as the Müller-Plathe method [96, 97]) is imposing through the system a given energy current and then evaluating the ΔT temperature drop once the steady state regime has been established.

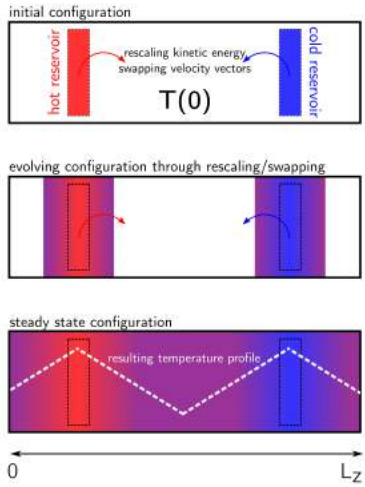

Figure 2.6. Top: Within an equilibrated system a hot and cold reservoir regions are identified; there, atomic kinetic energies are rescaled or atomic velocities are swapped. Middle: The resulting energy (heat) flux generates a time-evolving temperature distribution. Bottom: Eventually, a steady state condition is established, characterized by a time-independent temperature profile.

The simulation starts from a system with imposed PBC and previously thermalized at an initial temperature $T(0)$. Then, two different regions in the systems are defined in order to provide the "hot" and "cold" thermostat: the kinetic energy of the atoms there contained is rescaled by a fixed amount Δe_{kin} during a time interval Δt [97], according to the scheme illustrated in Fig. 2.6. This results in a net energy flux in the system of

$$j = \frac{\Delta e_{kin}}{2\Sigma\Delta t} \tag{2.26}$$

where Σ is the cross section of the simulation cell.

A periodic temperature profile is thus established, which is used to obtain the temperature gradient. A similar procedure requires to select the coldest atom, with velocity $v_{coldest}$, from the hot thermostat and the hottest atom,

with velocity $v_{hottest}$, from cold reservoir, and to swap their velocities [96]. A energy flux is obtained by iterating this $v_{hottest} \longleftrightarrow v_{coldest}$ over a time interval Δt

$$j = \frac{1}{2} m \frac{\sum_{swaps} (v^2_{hottest} - v^2_{coldest})}{2 \Sigma \Delta t} \tag{2.27}$$

where m is the atomic mass and the sum runs over the number of swaps performed. Also in this case the steady state can be proclaimed by detecting a constant temperature profile or by evaluating the work done in the reservoir regions, and thermal conductivity is calculated with the same Eq. (2.24).

2.2.3 *Approach-to-Equilibrium Molecular Dynamics*

Equilibrium and non-equilibrium methods portrayed so far suffer from several drawbacks which often limit their applications to atomistic models large enough to properly describe a given complex nanostructure. In particular, both require very long simulation times in order to converge or to establish the steady-state. A rather different approach involves simulations in the transient regime which stands between the equilibrium state and a non-equilibrium configuration. The AEMD method is based on the solution of the one dimensional heat equation and starts by imposing an out-of-equilibrium condition and then studying the evolution of the system [98–101]. A step-like temperature profile with an initial offset $T_1 - T_2$, i.e. the Heaviside function, is imposed along the z direction

$$T(z, 0) = H(z) = \begin{cases} T_1 & \text{if } \ 0 < z < L_z/2 \\ T_2 & \text{if } \ L_z/2 < z < L_z \end{cases} \tag{2.28}$$

where L_z is the sample length.

This configuration, depicted in Fig. 2.7, plays a central role in solving the heat equation when conduction is the only transport mechanism and when no heat source or sink is present

$$\frac{\partial T}{\partial t} = \bar{\kappa} \frac{\partial^2 T}{\partial z^2} \tag{2.29}$$

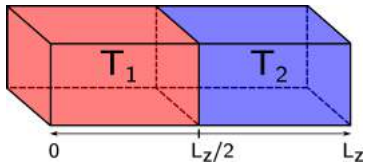

Figure 2.7. Sketch of the step-like temperature profile imposed in the simulation cell, with PBC along the three directions. The hot ($0 < z < L_z/2$) and cold ($L_z/2 < z < L_z$) regions are initially set at temperature T_1 and T_2, respectively, with $T_1 > T_2$.

By separating the variables $T(z,t) = Z(z)\Theta(t)$, and applying the PBC

$$\begin{aligned} Z(0) &= Z(L_z) \\ \left.\frac{\partial Z}{\partial z}\right|_{z=0} &= \left.\frac{\partial Z}{\partial z}\right|_{z=L_z} \end{aligned} \tag{2.30}$$

Equation (2.29) is readily solved and the most general solution is expressed in terms of Fourier series and reads as

$$T(z,t) = A_0 + \sum_{n=1}^{\infty} [A_n \cos(\alpha_n z) + B_n \sin(\alpha_n z)] e^{-\alpha_n^2 \bar{\kappa} t} \tag{2.31}$$

where $\alpha_n = 2\pi n/L_z$, $\bar{\kappa}$ is thermal diffusivity and the coefficients A_0, A_n and B_n depend only on the initial condition $T(z,0) = H(z)$ through the following expressions

$$\begin{aligned} A_0 &= \frac{1}{L_z}\int_0^{L_z} H(z)\,dz \\ A_n &= \frac{2}{L_z}\int_0^{L_z} H(z)\cos(\alpha_n z)\,dz \\ B_n &= \frac{2}{L_z}\int_0^{L_z} H(z)\sin(\alpha_n z)\,dz \end{aligned} \tag{2.32}$$

Thus, the analytic solution $T(z,t)$ depends on the geometry of the problem, on initial conditions and on thermal diffusivity which is related to thermal conductivity through $\bar{\kappa} = \kappa/\rho c_v$.

According to the aforementioned initial conditions, it is easy to prove that $A_n = 0 \; \forall n > 0$ and the solution given in Eq. (2.31) becomes

$$T(z,t) = A_0 + \sum_{n=1}^{\infty} B_n \sin(\alpha_n z)\, e^{-\alpha_n^2 \bar{\kappa} t} \tag{2.33}$$

where

$$\begin{aligned} A_0 &= \frac{T_1 + T_2}{2} \\ B_n &= \frac{T_1 - T_2}{\alpha_n \pi}[1 - \cos(\alpha_n \pi)] \end{aligned} \tag{2.34}$$

Implementing AEMD in a simulation

This protocol can be easily implemented in a MD simulation: once that the left and right regions of the simulation cell have been initially thermostatted at temperature T_1 and T_2 respectively, in order to impose the temperature profile according to Eq. (2.28), the system is then aged in a microcanonical run and the initial step-like temperature profile is progressively smoothed by thermal conduction. It is therefore possible to define the average temperatures $\langle T_1 \rangle$ and $\langle T_2 \rangle$ in the two semi-cells

$$\begin{aligned} \langle T_1(t) \rangle &= \int_0^{L/2} T(z,t)\,dz \\ \langle T_2(t) \rangle &= \int_{L/2}^{L} T(z,t)\,dz \end{aligned} \tag{2.35}$$

which will vary in time toward approaching a uniform temperature (i.e. equilibrium) configuration. During such a transient regime the time-dependent difference in average temperatures $\Delta T(t) = \langle T_1 \rangle - \langle T_2 \rangle$ is defined by exploiting Eq. (2.33) and displays as

$$\Delta T(t) = \sum_{n=1}^{\infty} C_n e^{-\alpha_n^2 \bar{\kappa} t} \tag{2.36}$$

where the coefficients C_n include informations on the geometry and on the initial conditions

$$C_n = 8(T_1 - T_2)\frac{[\cos(\alpha_n L_z/2) - 1]^2}{\alpha_n^2 L_z^2} \tag{2.37}$$

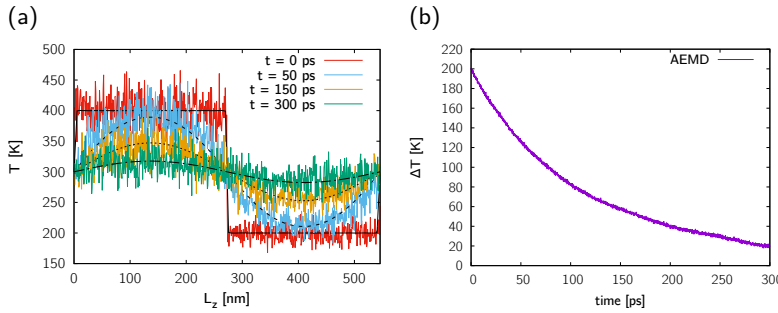

Figure 2.8. **a**: Time evolution of the temperature profile across a crystalline silicon sample with $L_z = 545.71$ nm and a section $\Sigma = 2.18 \times 2.18$ nm^2; black smooth lines represent the analytic solutions of Eq. (2.29), while the colored noisy lines are obtained by computing the temperature on-the-fly across the simulation cell. **b**: Average temperature difference computed during the NVE run.

Equation (2.36) is the core of the AEMD method and of its implementation in a simulation: temperature difference is computed on-the-fly during the NVE run, as shown in Fig. 2.8b, and the collected data is then fitted with the analytic solution in order to obtain the system thermal diffusivity $\bar{\kappa}$. The corresponding thermal conductivity is eventually evaluated as $\kappa = \bar{\kappa}\rho c_v$. For $T > \Theta_D$ we have $c_v = 3Nk_B/V$ and quantum corrections, taking into account the deviations from the Maxwell-Boltzmann distribution below the Debye temperature [66, 101], are usually inserted by renormalizing c_v by a factor $\bar{q}$ defined, in turn, as the ratio between the actual temperature and the Debye temperature. In particular, for c-Si at 600 K we get $\bar{q} = 0.947$.

Figure 2.8a shows also what happens during the transient regime by comparing the analytical solution of the heat equation and the numerical result obtained by AEMD simulation: the time evolution of the temperature profile across a crystalline silicon sample with L_z=545.71 nm and $\Sigma = 2.18 \times 2.18$ nm^2 reveals how the step-like initial profile smooths towards equilibrium, i.e. a constant temperature along the whole simulation cell. This picture provides robust evidence that the transient regime is rather well captured by an AEMD run.

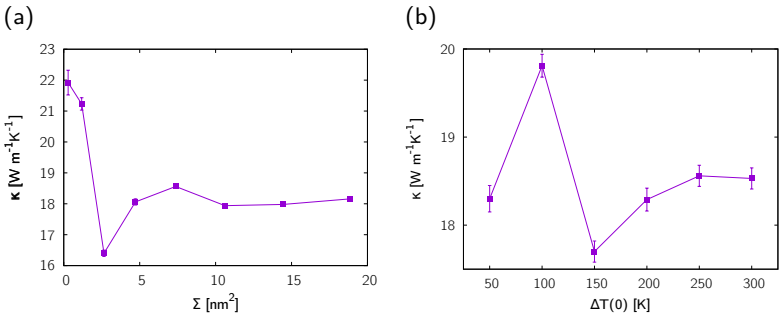

Figure 2.9. **a**: Calculated κ for c-Si samples with $L_z = 108.61$ nm, but different cross sections Σ. The initial temperature difference between the hot and cold regions is $\Delta T(0) = 200$ K. **b**: Calculated κ for a crystalline silicon sample with $L_z = 108.61$ nm and $\Sigma = 3.80 \times 3.80$ nm^2 as function of the initial temperature difference between the hot and cold regions [98].

In order to prove the reliability of the method, systematic calculations of thermal conductivity have been performed under several conditions. In particular, Fig. 2.9 shows the dependence of the thermal conductivity upon the cross section of the sample and the initial temperature offset imposed in the simulation cell: a weak dependence in the former case is observed and thermal conductivity results independent for $\Sigma > 4.72$ nm^2, while in the latter case data seem scattered and no trend is observed. However, a good choice for silicon and solid state systems is generally $T = 200$ K, although this results depends on the system investigated [98].

An important feature of AEMD method lies in the transient regime itself: the system need to be aged for a time comparatively much shorter than in a typical EMD or NEMD setup, a feature that has indeed favored large-scale applications up to $\mathcal{O}(10^7)$. This allowed to investigate system with an experiment-like structural complexity [102, 103] and dimensions [104] as well. Moreover, there is no need to compute thermal fluxes and to define "local"temperatures, which could, in principle, constitute important conceptual barriers.

2.2.4 *Size effects*

It is well known that in MD calculations κ depends on the actual length L of the simulated sample [97, 105]. In particular, when L is shorter than the average phonon MFP a ballistic-like transport where $\kappa = \kappa(L)$ is expected. By increasing L the probability that phonons are scattered before reaching the cell boundaries increases, eventually driving to a diffusive regime where κ is independent of the sample length. In NEMD hot and cold reservoirs (placed at the opposite boundaries of the simulation cell) are used to guarantee a temperature gradient. When phonons enter into the reservoir regions they lose their orientation since the local temperature is there kept constant by stochastic thermostats. Therefore, the system/reservoir boundary acts as an (artificial) diffusive interface. On the other hand, in EMD the dimensions of the simulation cell dictates the actual sampling of the phonon population: the smaller L, the less complete is such a sampling. This results into a $\kappa(L)$ dependence which, however, is comparatively weaker than in the NEMD case. In AEMD the scenario is more complex: an explicit phonon scattering source as in NEMD is missing; nevertheless a strong κ size dependence (up to the μm range) similar to NEMD is always observed. As pointed-out in reference [106] the different $\kappa(L)$ dependence between EMD and NEMD is mainly due to the distinct phonon population either equilibrium or non-equilibrium. The actual AEMD phonon population corresponds to a non-equilibrium condition which, in addition to the presence of PBC, results in an effective size effect similar to the NEMD one. In particular, in AEMD method the phonon scattering takes place at the sample boundaries, which actually show different temperatures due to the presence of PBC. Due to this similarities among NEMD and AEMD, the analysis of the $\kappa(L)$ dependence here adopted is the same as the one followed by reference [105] for NEMD.

Accordingly, the κ dependence on L is described by the following equation

$$\kappa(L) = \sum_{\mathbf{k},s} c_{\mathbf{k},s} \mathbf{v}_{\mathbf{k},s}^2 \tau_{\infty,\mathbf{k},s} \left[1 + \frac{2|\mathbf{v}|_{\mathbf{k},s} \tau_{\infty,\mathbf{k},s}}{L} \right]^{-1} \tag{2.38}$$

where the sum takes into account all the phonon modes labeled by their momentum $\mathbf{k}$ and polarization s. The terms $c_{\mathbf{k},s}$, $\mathbf{v}_{\mathbf{k},s}$ and $\tau_{\mathbf{k},s}$ are, respectively,

the heat capacity, the group velocity and the relaxation time (for intrinsic phonon-phonon bulk-like scattering) of each vibrational mode. According to Eq. (2.38) it is possible to write $1/\kappa = f(1/L)$, i.e. it is possible to define a f-function converging to the inverse bulk value of thermal conductivity $1/\kappa_\infty$ when L is large enough to mimic an infinite sample. Accordingly, it is possible to estimate κ_∞ by considering the Taylor expansion

$$\frac{1}{\kappa_\infty} = f(0) - \frac{f'(0)}{L} + \frac{f''(0)}{2L^2} + \dots \tag{2.39}$$

where apices indicate the order of derivation of the f−function. The resulting usual way of predicting κ_∞ consists in: (i) truncating Eq. (2.39) at the first order term and (ii) plotting $1/\kappa$ versus $1/L$ for a suitable range of sample lengths; κ_∞ is then obtained by extrapolating with a linear fit the data down to the $1/L \to 0$ limit.

Thus, the presence of size effects is ubiquitous in MD simulations, especially when dealing with thermal transport. For this reason in the following chapters, particular care was paid to deeply investigate the role of a finite simulation cell and to possibly overcome this limitation.

2.2.5 *Generalized Langevin Equation Thermostat*

In the framework of classical MD simulations, Ceriotti et al. developed a novel approach based on the GLE to obtain dynamical trajectories whose properties are devised to achieve specific sampling features [107–112], such for example an improved convergence during the advanced sampling of the DOF withing a system or an implementation of quantum heat baths both in equilibrium and out-of-equilibrium MD simulations. The most common approaches to constant temperature MD are those based on the introduction of an extended Lagrangian such as Nosé thermostat [113, 114]. This approach provides the correct Boltzmann distribution. However, it does not satisfy the ergodic hypotheses in some cases, such as harmonic systems. Several different extensions of the Nosé-Hoover method have been introduced, for example the Nosé-Hoover chains [115], which addresses the ergodicity issue but with increased complexity in the algorithm. An alternative approach is to adopt stochastic

MD methods. The first stochastic approach to sample the canonical ensemble is represented by the Andersen thermostat [116]. It couples the system to a heat bath via stochastic forces that modify the kinetic energy of the atoms or molecules. The number of collisions per unit of time is chosen randomly, following a Poisson distribution. Between two subsequent collisions the system evolves with constant energy. When a "collision" between the heat bath and the system occurs, the momentum of the atoms are taken according to a Boltzmann distribution at temperature T. The disadvantage of this thermostat is that it can be used only for time-independent properties. Dynamical properties, such as the diffusion, suffer of bad prediction when computed using Andersen thermostat [117].

The most common form of stochastic MD is represented by the implementation of Langevin dynamics [118]. The Langevin thermostat is local and ergodicity can be proven to be always fulfilled [119]. However, since the friction and noise terms alter significantly the Hamiltonian dynamics, it cannot be used to compute dynamical properties, unless an extremely small friction is used. Moreover, the effect of the friction and noise terms on the sampling efficiency is non trivial. The Langevin equation has been extensively adopted in MD simulations as an efficient tool to obtain trajectories which sample the constant-temperature, canonical ensemble. It is based on the assumption of instantaneous system-bath interactions, which stands for the random force being uncorrelated at different times. The Langevin equations that describe the Brownian motion of a particle with position x and momentum p, subject to a potential $V(x)$, can be written as:

$$\begin{aligned} \dot{x} &= p(t)/m \\ \dot{p} &= -V'(x) - \gamma p + \sqrt{2m\gamma/\beta}\,\xi(t) \end{aligned} \tag{2.40}$$

where $\beta = 1/k_B T$ is the inverse temperature, while the friction coefficient γ determines the interaction between the system and the Langevin heat bath and the fluctuations of the total energy. $\xi(t)$ is a Gaussian-distributed random force, delta-correlated, such that $\langle \xi(t)\xi(0)\rangle = \delta(t)$, and with zero mean, $\langle \xi \rangle = 0$. The delta-correlation of the stochastic forces implies that past events have no influence on the present state of the system, i.e. the dynamics is Markovian.

Stochastic thermostats are a good choice for modeling the interactions with an external heat bath because of their random nature which results in a good ergodic behavior. Generalizing Eq. (2.40) results in a non-Marcovian stochastic equation, allowing to improve and extend the performances of MD simulations. A Generalized Langevin Equation can be casted in a non-Markovian form by introducing history dependent terms [120]

Introducing a non-Markovian dynamics

$$\begin{aligned}\dot{x} &= p(t)/m \\ \dot{p} &= -V'(x) - \int_{-\infty}^{t} K(t-s)p(s)ds + \zeta(t)\end{aligned} \tag{2.41}$$

where the friction coefficient was replaced by an integral over time of the momentum weighted by a memory kernel $K(t)$ that describes dissipation and must be related to the time correlation of the noisy force via the fluctuation-dissipation theorem [121, 122]

$$H(t) = \langle \zeta(t)\zeta(0)\rangle = mk_B TK(t) \tag{2.42}$$

in order to be consistent with constant temperature thermodynamics conditions.

The numerical integration of this equation is a hard task, especially for the computation of the friction integral in Eq. (2.41), since it would require the complete storage of the past trajectory of the momenta. According to the Mori-Zwanzig theory [120, 123], it is possible to recast a non-Markovian problem in an extended phase-space, supplementing the physical variables with a set of n auxiliary momenta $\mathbf{s}$, linearly coupled to the physical momentum and among themselves. It has been proven that a Markovian dynamics in an extended phase-space is a practical method to simplify the treatment of non-Markovian problems [123–125]. The resulting Markovian Langevin equation can be written as

$$\begin{pmatrix}\dot{p}\\ \dot{\mathbf{s}}\end{pmatrix} = \begin{pmatrix}-V'(x)\\ 0\end{pmatrix} - \begin{pmatrix}a_{pp} & \mathbf{a}_p^T\\ \bar{\mathbf{a}}_p & \mathbf{A}\end{pmatrix}\begin{pmatrix}p\\ \mathbf{s}\end{pmatrix} + \begin{pmatrix}b_{pp} & \mathbf{b}_p^T\\ \bar{\mathbf{b}}_p & \mathbf{B}\end{pmatrix}\boldsymbol{\xi}. \tag{2.43}$$

Here, $\boldsymbol{\xi}$ is a vector of $n+1$ uncorrelated Gaussian random numbers with $\langle \xi_i(t)\xi_j(0)\rangle = \delta_{ij}\delta(t)$. All momenta are linearly coupled via the"drift matrix"

$$\mathbf{A}_p = \begin{pmatrix}a_{pp} & \mathbf{a}_p^T\\ \bar{\mathbf{a}}_p & \mathbf{A}\end{pmatrix} \tag{2.44}$$

while the noise components are coupled via the "diffusion matrix"

$$\mathbf{B}_p = \begin{pmatrix} b_{pp} & \mathbf{b}_p^T \\ \bar{\mathbf{b}}_p & \mathbf{B} \end{pmatrix} \tag{2.45}$$

Given the phase-space vector $\mathbf{x} = (x, p, \mathbf{s})$, it is useful to distinguish between a matrix acting on the full vector $\mathbf{x}$ and one connecting subsets of its components. Thus $\mathbf{A}_p$ and $\mathbf{B}_p$ are defined according to the compact notation introduced in Ref. [109], in order to refer to the portions of the matrices which describe the coupling between different parts of the state vector. Considering the extended phase-space vector $\mathbf{x} = (q, p, \mathbf{s})$, it is possible to distinguish between a matrix acting on the full $\mathbf{x}$ and one connecting subsets of its component, according to the scheme

$$\begin{array}{c|ccc} & q & p & \mathbf{s} \\ q & m_{qq} & m_{qp} & \mathbf{m}_q^T \\ p & \bar{m}_{qp} & m_{pp} & \mathbf{m}_p^T \\ \mathbf{s} & \bar{\mathbf{m}}_q & \bar{\mathbf{m}}_p & \mathbf{M} \end{array} \quad \left.\begin{array}{l} \\ \\ \} \mathbf{M}_p \end{array}\right\} \mathbf{M}_{qp} \tag{2.46}$$

In this context, referring to Eq. (2.43), the vectors $\mathbf{a}_p$, $\bar{\mathbf{a}}_p$, $\mathbf{b}_p$, $\bar{\mathbf{b}}_p$ represent the coupling between the p and $\mathbf{s}$ variables; a_{pp} and b_{pp} act only on the momentum p and the submatrices $\mathbf{A}$ and $\mathbf{B}$ account for the coupling between the additional momenta. Integrating out the $\mathbf{s}$ DOF in Eq. (2.43), a non-Markovian equation of motion for the physical variables (x, p) is recovered and it was shown [107] that the memory kernel is related to the drift and diffusion matrices via

$$K(t) = 2a_{pp}\delta(t) - \mathbf{a}_p^T e^{-|t|\mathbf{A}} \bar{\mathbf{a}}_p \tag{2.47}$$

as well as the noise correlation is:

$$H(t) = d_{pp}\delta(t) + \mathbf{a}_p^T e^{-|t|\mathbf{A}} [\mathbf{Z}\mathbf{a}_p - \mathbf{d}_p] \tag{2.48}$$

where $\mathbf{D}_p = \mathbf{B}_p \mathbf{B}_p^T$ and $\mathbf{Z} = \int_0^\infty e^{-\mathbf{A}t} \mathbf{D} e^{-\mathbf{A}^T t} dt$. The details of the integration of the auxiliary momenta $\mathbf{s}$ are reported in Ref. [107].

The elements of the matrices $\mathbf{A}_p$ and $\mathbf{B}_p$ control the memory functions of the equation, thus determining the dynamics and the stationary distribution of the system. It is then possible to introduce the conditions for canonical, constant-temperature sampling. A further matrix is introduced $\mathbf{C}_p = \langle (p, \mathbf{s})^T (p, \mathbf{s}) \rangle$, which is the static covariance matrix and is related to the drift and diffusion matrices by

Canonical sampling

$$\mathbf{A}_p \mathbf{C}_p + \mathbf{C}_p \mathbf{A}_p^T = \mathbf{B}_p \mathbf{B}_p^T \tag{2.49}$$

Parts of $\mathbf{C}_p$ enter the expression for the Fourier transform of the memory kernels of Eqs.(2.47) and (2.48)

$$\begin{aligned} K(\omega) &= 2a_{pp} - 2\mathbf{a}_p^T \frac{\mathbf{A}}{\mathbf{A}^2 + \omega^2} \bar{\mathbf{a}}_p \\ H(\omega) &= K(\omega) \left(c_{pp} - \mathbf{a}_p^T \frac{\mathbf{A}}{\mathbf{A}^2 + \omega^2} \mathbf{c}_p \right) + \\ &\quad + 2\omega^2 \left(\mathbf{a}_p^T \frac{\mathbf{A}}{\mathbf{A}^2 + \omega^2} \mathbf{c}_p \right) \left(1 + \mathbf{a}_p^T \frac{\mathbf{A}}{\mathbf{A}^2 + \omega^2} \bar{\mathbf{a}}_p \right) \end{aligned} \tag{2.50}$$

Equations (2.50) show that, in order to satisfy the fluctuation-dissipation theorem [120], which requires $H(\omega) = k_B T K(\omega)$, it is necessary to choose $c_{pp} = K_B T$ and $\mathbf{c}_p = 0$. Since the kernels, and therefore the dynamics of (q, p), do not depend on the $\mathbf{C}$ block in $\mathbf{C}_p$, $\mathbf{C}_p = k_B T$ can be chosen which lead to a fluctuation-dissipation theorem in the form

$$\mathbf{D}_p = \mathbf{B}_p \mathbf{B}_p^T = k_B T (\mathbf{A}_p + \mathbf{A}_p^T) \tag{2.51}$$

Together with Eq. (2.49), the fluctuation-dissipation theorem fixes $\mathbf{D}_p$ once $\mathbf{A}_p$ is given. However different interesting features can be investigated if the fluctuation-dissipation theorem is violated: in particular, the possibility of implementing the GLE thermostat in its "hot-spot" version will be explored in Chapter 6.

The above method has been originally developed by the group of Ceriotti, Bussi and Parrinello and a detailed derivation of the GLE thermostat, together with benchmarks and different applications, can be found in Refs. [107–111].

Part II

NANOSTRUCTURED SEMICONDUCTORS

3

NANOSTRUCTURED SILICON

Contents

Among many other intriguing properties, porous silicon (PS) is characterized by a thermal conductivity κ up to three orders of magnitude smaller than in c-Si [126] and by the ease of increasing the concentration of charge carriers by gas adsorption [127, 128]. These features make it very promising for thermoelectric conversion [129]. As already stated in the Introduction, thermoelectric materials can convert a thermal gradient into electricity. They represent one of the most appealing clean energy sources, as they allow transforming waste heat, normally regarded as a source of loss, into useful energy that can be easily harvested and stored. Unfortunately, the low efficiency of these materials has prevented their widespread use, confining them to niche applications. Therefore, the design of new materials whose lattice thermal conductivity is more largely affected than the electrical conductivity by some additional structural features is one of the most active research lines in thermoelectricity. PS is also a perfect candidate for thermal insulation [130, 131] and, therefore, is under extensive investigation as a key energy material.

In this section, an detailed investigation about the role of porosity in thermal transport is given. Moreover, it will be taken into account the interplay with other morphological defects (MoDs), such as grain boundaries, and reduced dimensionality, as occurs in porous nanowires (NWs).

3.1 POROUS SILICON

Several experimental studies have been performed, reporting a wide range of κ values, depending either on doping and on fabrication techniques [132]. The lowest values $0.04 \leqslant \kappa \leqslant 1.2$ W m^{-1} K^{-1} have been achieved for p- and p^{+}-doped silicon in disordered porous samples with porosity varying from 40% to 80% [133–135]. Tang et al. [136] instead focused on the thermoelectric properties of samples with cylindrical pores arranged in a hexagonal pattern, reporting that κ is reduced by a factor 100 with respect to c-Si, reaching a figure of merit of ZT~ 0.4. From a theoretical point of view, Lee et al. [131, 137] used a combination of classical MD and ab initio DFT to study the thermoelectric properties of nano-PS, characterized by periodically arranged circular and square pores, estimating $0.6 \leqslant \kappa \leqslant 2.5$ W m^{-1} K^{-1}, and ZT$=$ 0.4. He et al. [126] performed MD and lattice dynamics calculations in thin films with cylindrical pores, showing that κ could be reduced up to a factor 20 with respect to bulk c-Si.

Although the above scenario offers quite a number of reliable determinations of κ in many PS samples differing by morphology, a general picture is still missing in that the correlation between heat transport properties and some overall feature related to porosity is still unclear. This is detrimental to understanding possible general structure-property trends. In particular, comparatively little attention has been so far given to characterize by atomistic simulations thermal transport in samples with disordered porosity, a configuration closer to the experimental situation. As a matter of fact, it is very unlikely to obtain a real sample with an ordered array of pores especially when using etching fabrication processes which do not allow to control the spatial and shape distribution of voids. Another important feature is that etching introduces oxide layers on the pore surfaces. This section is addressed to investigate some aspects of the above introduce open problems: atomistic simulations are used to inform an effective model describing on a general basis the relationship between κ and interface density (i.e. the ratio between porosity and average pore diameter). The model here developed, including and extending the previous Eucken model valid only for macroporous composites [138, 139], is applied to both ordered and random nano-PS structures, providing a robust rationale to understand and predict κ values, once the system morphology has been given.

3.1.1 *Nanopores generation*

A bulk c-Si matrix has been modeled by a simulation cell with length L_z varying in the range $24 \leqslant L_z \leqslant 136$ nm (see below) and fixed 13.6×13.6 nm^2 section in the xy-plane. The resulting number of atoms varied therefore from 0.2×10^6 to 1.3×10^6, corresponding to simulation cells large enough to reproduce all the main structural features of PS. Two different kinds of systems were investigated: ordered porous silicon (OPS), where the porosity is created by arranging a periodical array of spherical pores, and random porous silicon (RPS), with randomly distributed, sized and shaped pores.

In general, the porosity

$$\varphi \equiv \frac{V_{pores}}{V_{system}} \tag{3.1}$$

is defined as the ratio between the total volume V_{pores} of the regions where Si atoms have been removed and the system volume V_{system} [140]. The porosity itself does not provide any relevant information on the system morphology since, at least for OPS, it depends on two parameters, namely: the number of the pores N_p, and the pore diameter d_p, i.e. $\varphi = \varphi(N_p, d_p)$.In principle, the same given porosity φ can be obtained by creating a large number of small pores or by just few larger ones. Three examples of OPS are shown in Fig. 3.1a, characterized by the same porosity φ=0.14, but different pore size d_p. As extensively explained in the next section, the quantity that identifies accurately the porous system and its inner surfaces is the *interface density* Ψ. In particular, it will be shown that the overall thermal conductivity monotonically depends on Ψ.

Ordered porous silicon

As for OPS, spherical pores with diameter d_p were arranged in a simple cubic lattice or in a tetragonal lattice: the array of pores was created by assigning the positions of the center of the pores and then by removing the atoms contained in the sphere with radius $d_p/2$ (see Fig. 3.1a).

As for RPS, educated guesses were added to the above procedure in order to enforce a twofold character of the resulting spatial distribution of pores, namely: randomness and uniformity. Such distribution is achieved by defining contiguous subregions in the simulation cell: inside each region atoms are randomly selected and a surrounding sphere is drawn by considering an average

Random porous silicon

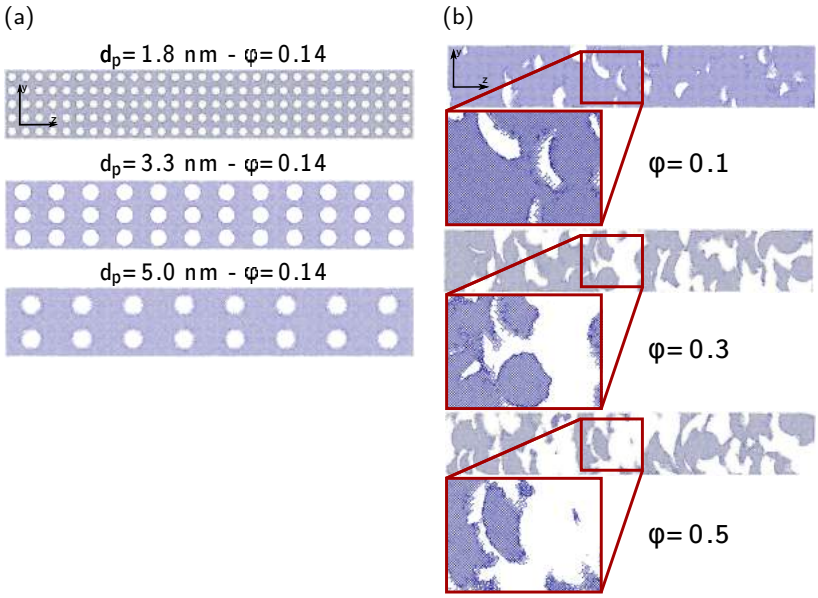

Figure 3.1. **a**: OPS samples with same porosity $\varphi = 0.14$, but different pore diameter d_p. Pictures show a 1.36 nm-thick longitudinal section. Heat flux is generated along the z-direction (see text). **b**: RPS samples with different porosity φ. The zoomed frames provide additional details on the atomic scale structure. Pictures show a 1.36 nm-thick longitudinal section and, therefore, matter is not discontinuous. Heat flux is generated along the z-direction (see text).

diameter of 4.0 nm, sampled from a Gaussian distribution with a standard deviation of 1.5 nm. All atoms lying inside the sphere are removed and further iterations, where additional small pores are created or small portion of material restored, are then carried out until the desired porosity is obtained within a certain tolerance. Such procedure is repeated for every subregion defined in the system. The uniform distribution of pores is not only intended to mimic a typical experimental condition [132], but it is also required by the assumption underlying the AEMD method adopted here to calculate κ [98–100]. Both structures were carefully equilibrated by simulated annealing up to 900K, fol-

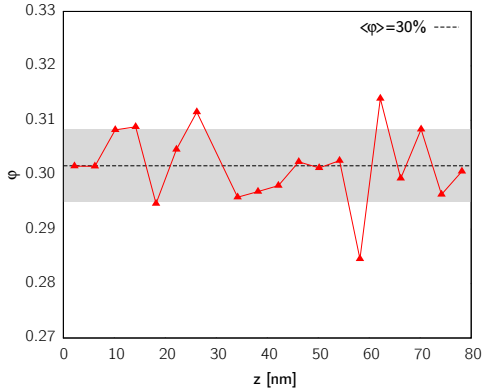

Figure 3.2. Red triangles: local porosity of a typical RPS sample calculated along the z-direction. Horizontal solid line: average porosity. Shaded area: standard deviation for porosity.

lowed by a further equilibration at room temperature for a total simulation time of 0.6 ns. This procedure allows inner surfaces to fully relax towards a highly-defected structure, very similar to amorphous silicon. In Fig. 3.2 are reported the calculated φ along the z direction of a typical RPS, showing that the deviation around the pre-set value of φ=0.30 is indeed very small.

Finally, when dealing with disordered structures like RPS (which are shown in Fig. 3.1b) configurational averaging is requested in order to provide quantitative information. Therefore, for each value of porosity the thermal conductivity was averaged over four different samples (with fixed size and porosity).

The equations of motion have been integrated by the velocity-Verlet algorithm with a time step as short as 2 fs and simulations have been performed using the LAMMPS [141] package and the EDIP potential [142]. This interaction scheme has been adopted since it is accurate in describing noncrystalline forms of silicon, as indeed required for the present investigations. More importantly, it has been elsewhere established its accuracy in predicting the thermal transport properties of disordered silicon forms, like, e.g., amorphous and nanocrystalline ones [98]. See Appx. B for a detailed discussion about this interatomic potential. Finally, the reliability of the present simulation protocol is also proved by the good agreement found for the AEMD thermal conduc-

L_z [nm]	N_p	κ [W m^{-1} K^{-1}]			
		$\varphi = 0.15$	$\varphi = 0.25$	$\varphi = 0.35$	$\varphi = 0.45$
		$d_p = 3.0$ nm	$d_p = 3.5$ nm	$d_p = 3.9$ nm	$d_p = 4.3$ nm
54.3	99	3.91	2.12	1.09	0.65
81.5	153	4.26	2.26	1.28	0.73
108.6	198	4.67	2.37	1.20	0.70
135.8	252	4.77	2.48	1.31	0.75
∞ (extrapolated)		5.6±0.2	2.8±0.1	1.5±0.1	0.8±0.1

Table 3.1: Thermal conductivity κ for various OPS samples, differing in porosity φ, pore diameter d_p, pore number N_p and size L_z. These data are also reported in Fig. 3.3a.

tivity of c-Si with the BTE prediction of Refs. [105, 126, 143] based on the same EDIP potential, although the actual value (i.e., $\kappa = 294$ W m^{1}K^1) is somewhat larger than the experimental one.

3.1.2 *Size dependence in porous systems*

As already explained in 2.2.4, MD simulations performed on cells with finite length L_z it occurs that $\kappa = \kappa(L_z)$ due to a fraction of the heat carriers having a MFP longer than L_z [97, 105].

By adopting the usual $1/\kappa(L_z)$ procedure [97, 105], size effects in OPS were investigated by considering four values of porosity in the range $0.15 \leqslant \varphi \leqslant 0.45$ and by calculating $\kappa(L_z)$ for systems with $54.3 \leqslant L_z \leqslant 135.8$ nm. The results are shown in Fig. 3.3a and are also reported numerically in Table 3.1. A linear $1/\kappa$ vs. $1/L_z$ trend is found, although its slope is comparatively much smaller than in c-Si [98], providing evidence that, for the system dimensions here considered, size only marginally affects thermal conductivity predictions. Consistently with previous findings [126, 144], this suggests that pores indeed act as very efficient scatterers for heat carriers, causing a considerable reduction of their MFP.

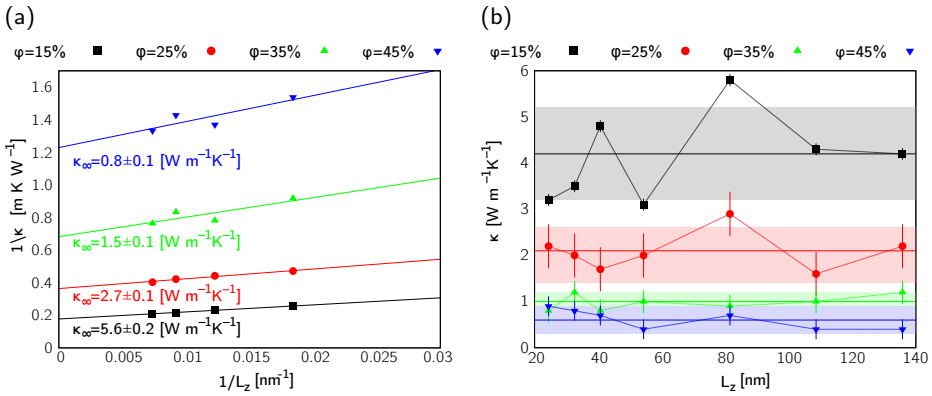

Figure 3.3. **a**: Inverse thermal conductivity $1/\kappa$ vs. inverse cell size $1/L_z$ for OPS samples with different porosity. **b**:Thermal conductivity κ as a function of cell size L_z for RPS system with different porosity. The horizontal solid lines (shaded area) represent the average values (standard deviation).

As for RPS, a larger range of system sizes was explored, corresponding to $24.4 \leqslant L_z \leqslant 135.8$ nm. The results are summarized in Table 3.2: interestingly enough, a really weak dependence of κ on L_z is observed (even at very low porosity), as confirmed by Fig. 3.3b. The conclusion is straightforward: a random distribution of unequally shaped and sized voids fully inhibits the long range features of any vibrational modes, regardless the actual value of φ.

Based on the benchmark calculations described in this section, it is possible to argue that in PS the estimation of the thermal conductivity by AEMD is only marginally affected (OPS), or even not at all affected (RPS), by the selected length L_z of the simulation cell. Therefore,the following investigations is focused to just one reference system size, namely $L_z = 81.6$ nm. This offers the best compromise between numerical convenience and accuracy (as shown in Figs. 3.3a and 3.3b)

L_z [nm]	κ [W m^{-1} K^{-1}]			
	$\varphi = 0.15$	$\varphi = 0.25$	$\varphi = 0.35$	$\varphi = 0.45$
24.4	3.2±0.1	2.2±0.5	0.8±0.2	0.9±0.3
32.6	3.5±0.1	2.0±0.5	1.2±0.2	0.8±0.3
40.7	4.8±0.1	1.7±0.5	0.8±0.2	0.7±0.3
54.3	3.1±0.1	2.0±0.5	1.0±0.2	0.4±0.3
81.5	5.8±0.1	2.9±0.5	0.9±0.2	0.7±0.3
108.6	4.3±0.1	1.6±0.5	1.0±0.2	0.4±0.3
135.8	4.6±0.1	2.2±0.5	1.2±0.2	0.4±0.3
$\langle\kappa\rangle$	4.2±0.1	2.1±0.5	1.0±0.2	0.6±0.3

Table 3.2: Thermal conductivity κ for various RPS samples, differing in porosity φ and size L_z. These data are also reported in Fig. 3.3b. The indicated errors reflect a configurational average over 4 different samples. The average thermal conductivity $\langle\kappa\rangle$ is reported for any porosity.

3.1.3 κ *vs. porosity - ordered systems*

As mentioned before, in OPS φ only depends on N_p and d_p. Therefore, the porosity can be varied either by fixing the number of pores and by varying their diameter or, conversely, by distributing a different number of equally sized pores.

The first option was exploited by generating seven different samples with $0.03 \leqslant \varphi \leqslant 0.34$, each containing as many as $N_p = 750$ identical pores (with suitable dimension to accommodate any assigned porosity) arranged in a simple cubic lattice. The second option, instead, was exploited by generating a new set of seven different samples, where an increasing number of pores was placed on a tetragonal lattice so to span the $0.02 \leqslant \varphi \leqslant 0.27$ porosity range. In this case all pores have the same dimension d_p=3.3 nm. For this second case-study, the procedure was also repeated by choosing d_p=5.0 nm. The results for the two procedures are summarized, respectively, in Table 3.3 and in Tables 3.4 and 3.5.

φ	d_p [nm]	κ [W m^{-1} K^{-1}]
0.03	1.0	8.67
0.06	1.3	6.24
0.09	1.6	4.93
0.14	1.8	2.70
0.22	2.0	1.71
0.31	2.3	0.87
0.34	2.4	0.73

Table 3.3: Thermal conductivity κ for various OPS samples with increasing porosity φ and pore diameter d_p. The number of pores is fixed at $N_p = 750$.

The common feature is that the thermal conductivity of OPS is greatly reduced with respect to the bulk crystalline value. However, samples obtained by following the first procedure have, on average, a much smaller κ, precisely: as small as 50% or 30% of the corresponding one for samples obtained by the second procedure with $d_p = 3.3$ nm or $d_p = 5.0$ nm, respectively. Although these results are expected and qualitatively explained by the presence of several internal interfaces (at each matrix/pore boundary) which provide an efficient phonon scattering mechanism, a more quantitative picture is definitely needed in order to elaborate a rationale for the observed trends.

3.1.4 *Effective thermal conductivity in porous media*

There have been many attempts to provide a general law $\kappa = \kappa(\varphi)$. The most widely referenced model was originally proposed by Eucken, based on an effective medium approximation for two-phase porous media [138, 139, 145–147]. There, the first- and second-phase are, respectively, the material forming the host matrix and the embedded voids. By assuming that the second phase

φ	N_p	κ [W m^{-1} K^{-1}]
0.02	18	22.22
0.05	36	11.01
0.09	72	6.15
0.14	108	4.61
0.18	144	3.75
0.23	180	3.22
0.27	216	2.96

Table 3.4: Thermal conductivity κ for various OPS samples with increasing porosity φ and number of pores N_p. The pore diameter is fixed at $d_p = 3.3$ nm.

is organized in spheres and that the distance between the spheres is much larger than d_p, the Eucken model leads to the relation

$$\kappa_{eff}(\varphi) = \kappa_{bulk}\frac{1-\varphi}{1+\frac{\varphi}{2}} \tag{3.2}$$

that accounts for the reduction of the thermal conductivity κ_{bulk} of the first-phase material, caused by the presence of the pores. Eq. (3.2) accurately describes the thermal conduction properties of composites with macropores, i.e. when the MFP of the vibrational modes of the pristine (first phase) material is smaller than the typical pore size. Conversely, in porous materials the situation is just the opposite. Furthermore, Eq. (3.2) is basically scale-invariant, as typical of effective medium theories. Therefore, it does not carry any information about the dependence of thermal conduction on structural details like, e.g., the pore size (as indeed reported experimentally [148, 149]). Any model aimed at improving the Eucken one must fully exploit the above two features, namely: the actual presence of pores (common to both macro- and nano-porous systems) and their nanoscale features (which additionally affect, through atomic-scale details).

As for the first issue, the standard picture is that the diffusion of microscopic heat carriers is affected by pores as well as by their mutual scattering. A differ-

φ	N_p	κ [W m^{-1} K^{-1}]
0.03	8	24.62
0.05	12	12.17
0.07	16	9.54
0.12	28	7.06
0.14	32	6.64
0.17	40	5.98
0.21	48	5.16

Table 3.5: Thermal conductivity κ for various OPS samples with increasing porosity φ and number of pores N_p. The pore diameter is fixed at $d_p = 5.0$ nm.

ent maximum MFP for the carriers is therefore associated to each scattering mechanism, respectively: Λ_{pores} and Λ_{bulk}. While for systems obeying Eq. (3.2) it is easily found that $1/\Lambda_{pores} = 2\Lambda_{bulk}/\varphi$, the evaluation of Λ_{bulk} requires an anharmonic lattice dynamics calculation. This second scattering mechanism is the dominant one in the pristine material (i.e. in the first phase matrix with no voids). Applying Matthiessen rule [46, 66] Λ_{eff} reads as

Accounting for nanoscale features

$$\frac{1}{\Lambda_{eff}} = \frac{1}{\Lambda_{bulk}} + \frac{1}{\Lambda_{pores}} \tag{3.3}$$

which is the effective distance traveled by heat carriers when both the above mechanisms limiting their diffusion are properly taken into account.

As for nanoscale features, it is convenient to consider the interface density Ψ easily defined as

$$\Psi = \frac{N_{interface}}{V_{system}} 4\pi (d_p/2)^2 = \frac{6\varphi}{d_p} \tag{3.4}$$

A new scattering length $\Lambda_{interface}$ (associated to interface-specific scattering events) is accordingly defined, that can be written in the following form

$$\Lambda_{interfaces} = \frac{1}{N_{coll}} = \frac{4}{\Psi} = \frac{2d_p}{3\varphi} \tag{3.5}$$

where

$$N_{coll} = \frac{\pi d_p^2}{4} \frac{N_{pores}}{V_{system}} \tag{3.6}$$

is the number of interface scattering events per unit length. The factor $\pi d_p^2/4$ is the cross section for scattering at spherical pore of diameter d_p. By adding this new scattering contribution to Eq. (3.3), Λ_{eff} for a porous system can be written as

$$\Lambda_{eff} = \left[\frac{1}{\Lambda_{bulk}} + \frac{1}{\Lambda_{bulk}} \frac{\varphi}{2} + \frac{\Psi}{4} \right]^{-1} = \frac{\Lambda_{bulk}}{1 + \frac{\varphi}{2} + \frac{3\Lambda_{bulk}}{2d_p}\varphi} \tag{3.7}$$

In order to proceed further, it is necessary to recall that the thermal conductivity of an homogeneous (i.e. containing no voids) material with heat capacity $\mathcal{C}_v$ is usually approximated as [66]

$$\kappa \sim \frac{1}{3} \mathcal{C}_v v_g \Lambda \tag{3.8}$$

where only the dominant heat carrier with MFP equal to Λ and propagating with speed v_g is considered. When considering a (nano)porous material, the heat capacity can be usefully replaced with an effective value $\mathcal{C}_{v,eff} = (1 - \varphi)\mathcal{C}_{v,bulk}$ (where $\mathcal{C}_{v,bulk}$ is the specific heat of the first-phase material), since the heat capacity of the pores is negligible [150]. Furthermore, phonon group velocity is mostly determined by short-range interactions and it is correct to assume that is not that much affected by the presence of the pores; this is confirmed by MD simulations and lattice dynamics calculations [126].In conclusion, under these assumptions and by combining Eqs. (3.7) and (3.8) the following relation is obtained

$$\kappa_{eff}(\varphi) = \kappa_{bulk} \frac{1 - \varphi}{1 + \frac{\varphi}{2} + \frac{3\Lambda_{bulk}}{2d_p}\varphi} \tag{3.9}$$

Effective thermal conductivity

which provides a simple, but very informative general expression for the effective thermal conductivity in a porous material. Interestingly enough, Eq. (3.9) not only contains informations about the pristine matrix (through κ_{bulk} and

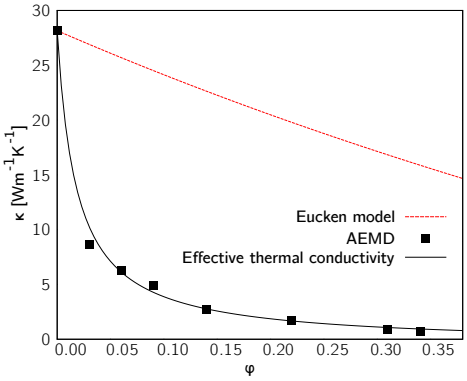

Figure 3.4. Thermal conductivity κ as a function of porosity φ in OPS samples with fixed number of pores. Black solid line: effective model provided by Eq. (3.9). Red dashed line: standard Eucken model provided by Eq. (3.2). Dots are typically as large as the standard deviation on κ_{eff}.

Λ_{bulk} terms) and the overall porosity φ, but it also properly takes into account the actual morphology of the pores through the d_p parameter. This feature represents a major step forward since it makes Eq. (3.9) able to describe porous systems, at variance with Eq. (3.2) which is limited to macroporous composites. Nevertheless, the functional form of $\kappa_{eff}(\varphi)$ is the same of the Eucken model: in fact it is worth noting that for $d_p \gg \Lambda_{bulk}$ it reduces back to the Eucken model. The factor $\beta = \dfrac{3\Lambda_{bulk}}{2d_p}$ can be enclosed in a single parameter to be fit on the results of AEMD simulations.

In Fig. 3.4 are reported the κ values obtained by AEMD (black squares) for OPS with fixed pores; the solid black curve represent the effective thermal conductivity relation given in Eq. (3.9) that has been used to fit the data and the red dashed curve is the Eucken model. Fig. 3.4 clearly stands for the major improvement of the present model to the conventional Eucken one. The value for the β parameter obtained by fitting the AEMD data is 55.3 ± 4.4. As d_p is known for each point in the plot, β can be used to calculate the values for Λ_{bulk}. This order-of-magnitude estimate predicts $40 \lesssim \Lambda_{bulk} \lesssim 90$ nm, in nice agreement with Ref. [105] where the dominant contribution to thermal

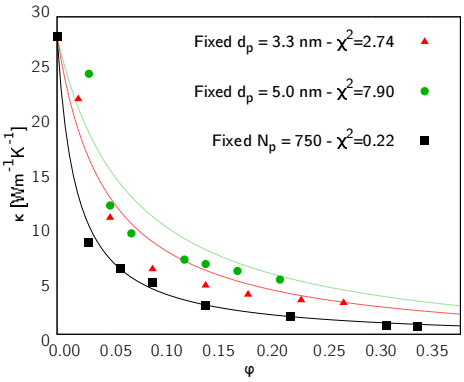

Figure 3.5. Thermal conductivity κ as a function of porosity φ in OPS samples with either fixed number of pores N_p (black squares) and fixed pore diameter d_p=3.3 nm (red triangles) and d_p=5.0 nm (green dots). Solid lines: effective model provided by Eq.(3.9).

conductivity in c-Si is calculated to come from phonons with MFP as long as ~10^2 nm.

In Fig. 3.5 is shown a comparison between the two different classes of OPS here investigated, namely: those with fixed N_p (black symbols) and those with fixed d_p (red and green samples). For both $d_p = 3.3$ nm and $d_p = 5.5$ nm, the agreement between calculated AEMD data and Eq.(11) is definitely less good than by keeping N_p fixed. This can be explained considering the local morphology of the samples: the structural relaxations at the pore/matrix interface result in the formation of an amorphous or highly-defected spherical shell surrounding the pore. The amount of defected matter increases with growing pore diameter, as shown in Fig. 3.6.

It is worth remarking that the Eucken model for $\kappa_{eff}(\varphi)$ has been derived by assuming a two phase composite structure, while the observed defected/amorphous shell is in fact a third phase: in the case of OPS with fixed N_p the agreement is good because the pores are very small and there is little defected medium, while in the case of OPS with fixed d_p (both values) the actual amount of a third-phase material is too large to be neglected. This statement is validated by counting the number (per pore) of atoms forming

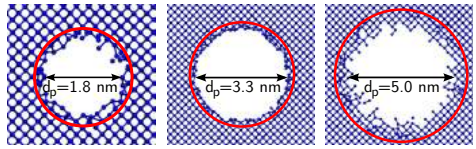

Figure 3.6. Detail of the microscopic structure nearby a typical spherical pore with increasing diameter d_p. The yellow circle identifies approximately the shell corresponding to the highly-defected region.

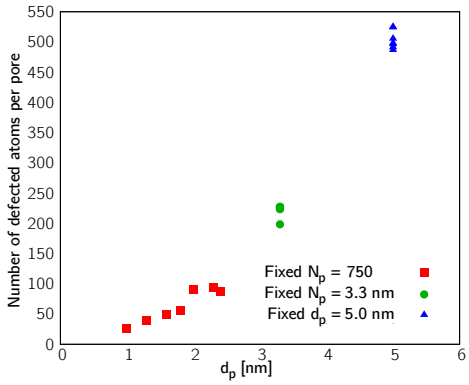

Figure 3.7. Number of defected atoms (per pore) as function of the pore diameter in OPS samples. Red squares: systems with constant number of pores. Green dots (blue triangles): systems with pore diameter fixed at $d_p = 3.3$ nm ($d_p = 5.0$ nm).

the third phase, as shown in Fig. 3.7. Defected atoms have been identified by evaluating their on-site energy, as calculated by the adopted EDIP potential: while in an ideal c-Si lattice at room temperature atoms have a configurational energy of about ~ -4.6 eV/atom, in the highly defected shells this value is raised above -4.3 eV/atom. Fig. 3.7 clearly indicates that high-energy atoms have a much smaller occurrence in OPS with fixed N_p: in this case Eq. (3.9) works at its best.

Another interesting feature of Fig. 3.5 worth of further investigation is that the larger are the pores, the worst is the agreement between calculated AEMD

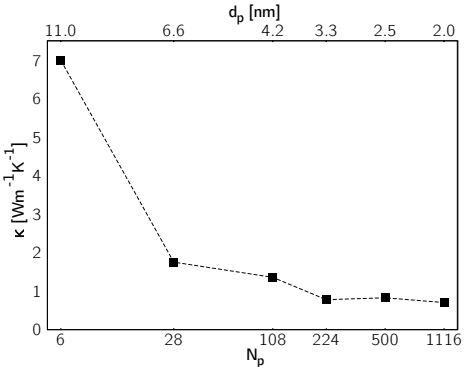

Figure 3.8. Thermal conductivity κ as function of the number of pores N_p (bottom horizontal scale) and pore diameter d_p (top horizontal scale) in OPS samples with φ =0.28.

data and the model provided by Eq. (3.9), as indicated by the reduced χ^2 of the fit reported in figure. Since $\kappa \sim (3\Lambda_{bulk}/2d_p)^{-1}$ it is obvious that, for fixed porosity, the smaller are the pores the smaller is the thermal conductivity.This is also related to the interface density $\Psi = 6\varphi/d_p$: for a given value of porosity it increases with decreasing pore diameter. In order to better point out this issue, in Fig. 3.8 is reported the thermal conductivity of six OPS with same porosity $\varphi = 0.28$, but different pore number and dimension. The corresponding values are listed in Table 3.6. The main conclusion is that, although the porosity in these system is constant, thermal transport is highly affected by an increasing interface density to which the probability of scattering is directly linked.

Interface density

3.1.5 κ *vs. porosity - random systems*

In RPS it is hard to define the position, size, and shape of each pore. Therefore, their porous structure is rather characterized by providing the distribution of the pore dimensions which, by construction, is a gaussian distribution with average value $\langle d_p \rangle = 4.0$ nm and a standard deviation of 1.5 nm, as reported above. Table 3.7 lists the results for several RPS with $0.05 \leqslant \varphi \leqslant 0.50$,

N_p	d_p [nm]	κ [W m^{-1} K^{-1}]
6	11.0	7.00
28	6.6	1.75
108	4.2	1.36
224	3.3	0.78
500	2.5	0.83
1116	2.0	0.70

Table 3.6: Thermal conductivity κ for various OPS samples with same porosity $\varphi = 0.28$, but varying number of pores N_p and pore diameter d_p.

showing, similarly to OPS, a monotonic decrease in thermal conductivity by increasing porosity. A direct comparison to experimental data is very hard, since little information is available for samples characterized at the nanoscale by a pore distribution similar to the one here investigated. However, in Ref. [151] the thermal conductivity in PS crystallites has been measured by the micro-Raman technique reporting κ-values well below 5 W m^{-1} K^{-1} for any $\varphi \geqslant 0.3$. This is a further convincing argument supporting the results here presented. Furthermore, the $\kappa = \kappa(\varphi)$ trend there reported is very similar to these findings. Furthermore, in Refs. [133, 135], it is reported a thermal conductivity for high-porosity samples lower than 2 and 1.5 W m^{-1}K^{-1}, respectively. Once again these results are in good agreement with those ones reported in Table 3.7. Finally, in Ref. [152], a direct measurement of thermal conductivity in p+-doped mesoPS is reported with $\varphi \sim 0.5$ as small as 1 W m^{-1}K^{-1} while, for a similar porosity, the rather different value of 3.9 W m^{-1}K^{-1} is reported in Ref. [153], which further indicates the large scattering of experimental data.

It is remarkable that, as shown in Fig. 3.9, the thermal conductivity values in RPS are slightly larger than in OPS with fixed N_p, indicating a reduced interface density. This is due to the fact that, since pores do not overlap, the interface density is maximum in OPS. Furthermore, AEMD results for RPS are in good agreement with Eq. (3.9). This suggests that, for samples containing a random

φ	κ [W m^{-1} K^{-1}]
0.05	9.8±0.9
0.10	5.2±0.3
0.15	4.6±0.1
0.20	2.7±0.4
0.25	2.0±0.4
0.30	1.3±0.5
0.35	0.9±0.2
0.40	0.7±0.2
0.45	0.5±0.2
0.50	0.2±0.1

Table 3.7: Thermal conductivity κ for various RPS samples with increasing porosity φ. Reported errors reflect a configurational average over four samples.

array of pores, κ is neither affected by their actual shape, nor by their spatial distribution. As a further sanity check for these calculations, the average pore diameter in RPS was evaluated from the corresponding β parameter. The result is $\langle d_p \rangle = 4.3 \pm 1.3$ nm, fully consistent with the values used during the samples generation. Incidentally, these results suggests a possible practical procedure for estimating the pore average size, indeed a relevant information hard to get through thermal transport measurements [154].

3.1.6 *Beyond the Eucken model*

All the present calculated AEMD data are in fact very accurately predicted by a model where the key structural parameter is the interface density Ψ. By generalizing Eq. (3.9) κ_{eff} can be casted in the form

$$\kappa_{eff}(\Psi) = \kappa_{bulk} \frac{1 - d_p \Psi/6}{1 + d_p \Psi/12 + \Lambda_{bulk} \Psi/4} \tag{3.10}$$

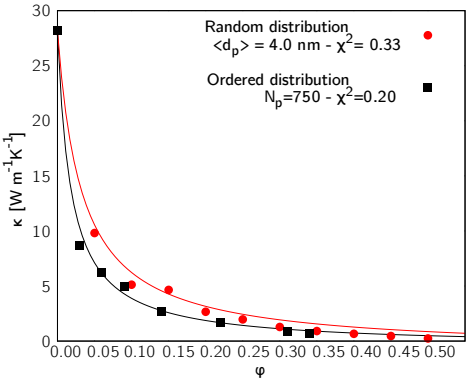

Figure 3.9. Thermal conductivity κ as function of porosity φ in random (red dots) and ordered (black squares) PS samples. Solid lines: effective model provided by Eq. (3.9). Symbols are typically as large as the standard deviation of the calculated thermal conductivity.

where Ψ now replaces all the structural parameters so far considered. It is necessary to stress that although the interface density has been previously defined for spherical pores, it is actually independent from their shape and it can be used to identify universal trends in k_{eff}. A natural consequence is that interface density, rather than the overall porosity, is a more effective quantity to fully describe thermal conductivity as a function of system conformation. As a matter of fact, samples with comparable interface density tend to have similar thermal conductivities, although having a different porosity. This is illustrated in Table 3.8 where systems with same porosity, but unlike interface density, show remarkably different thermal conductivity. On the other hand, when the interface density is similar, then so is thermal conductivity, regardless of the porosity.

In Fig. 3.10 is shown κ for the whole set of samples studied so far (namely, any OPS and RPS) as a function of interface density (left) and porosity (right). The two curves are obtained by fitting the data using Eq. (3.10) and Eq. (3.9) for Ψ and φ, respectively. The use of interface density, rather than porosity, as the main structural parameter in Eq. (3.10) gives a more accurate fit of the data, as reflected by the reduced χ^2 values, respectively: $\chi^2_\Psi = 1.2$

Ψ [nm^{-1}]	d_p [nm]	N_p	φ	κ [W m^{-1} K^{-1}]
0.153	11.0	6	0.28	7.0
0.164	3.3	72	0.09	6.2
0.840	2.0	1116	0.28	0.7

Table 3.8: Thermal conductivity κ for three PS samples differing by interface density Ψ, pore diameter d_p, pore number N_p, and porosity φ.

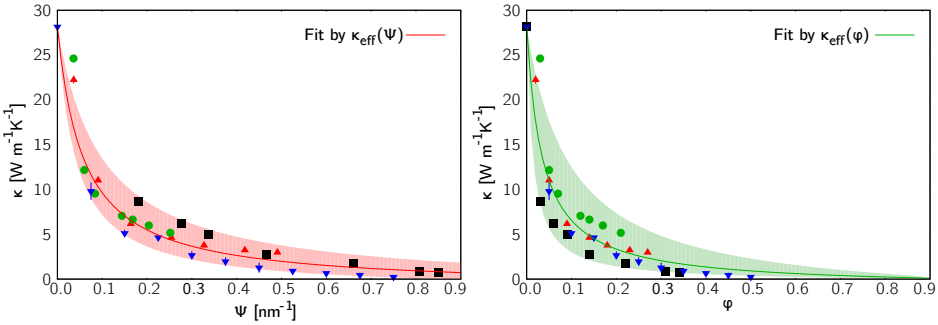

Figure 3.10. Symbols: Thermal conductivity κ as function of the interface density Ψ (left panel) and porosity φ (right panel) for all systems here investigated. Solid lines: effective model provided by Eq. (3.10) and by Eq. (3.9) for the top and bottom panel, respectively. Shaded area: the deviation of the calculated AEMD data (symbols) from such models.

and $\chi^2_\varphi = 3.5$. The shaded regions in Fig. 3.10 top and bottom represent the deviation of the calculated AEMD data from the models provided by Eq. (3.10) and by Eq. (3.9), respectively. The smaller area of the red region stands for a better agreement, i.e. for the improved accuracy of the extended Eucken model provided by Eq. (3.10) based.

The main result of the present investigation is that the thermal conductivity κ in PS does depend on porosity, as well as it is affected by the interface density Ψ, namely by the ratio between porosity and average pore diameter. Interestingly enough, Ψ is identified as the real key structural characteristic of a porous sample, fully determining its ability to transport heat. The effective

model based on the interface density fully describes the trends in thermal conductivity reduction due to the increase of the interface scattering in porous systems and provides evidence that Ψ is indeed a comparatively more effective parameter in describing trends in κ than the overall sample porosity. The agreement between the present simulation data and the effective atomistic model here developed is very good, suggesting a possible way to measure the average size of the voids in a typical experimental PS sample.

3.2 POROUS NANOWIRES

Similarly to porous materials, semiconducting NWs [155–157] are a good example of how lattice thermal conductivity is engineered without severely affecting electronic transport. In fact, a suitable distribution of voids, whose typical size is smaller than the MFP of heat carriers, but still larger than the charge carrier one, results in strong scattering of the former, with negligible effects on the electrical conductivity [102, 136]. In NW, on the other hand, heat carriers are scattered at the wire surface, while charge carriers are comparatively much less affected. Accordingly, this effect is stronger in thin NW, with a larger surface-to-volume ratio [158], and in the presence of rough surfaces [30, 159] or other kinds of modulations [160]. The possibility to bring these two features together is very appealing. From a few years on, single crystalline porous silicon nanowires (PSNWs) can be fabricated [161] and have been proposed for different applications, ranging from lithium-ion batteries [162] to solar cells [163]. However, their use as thermoelectric materials is to date still largely unexplored. The goal of the following section is filling this gap and quantifying the reduction of the thermal conductivity in PSNWs, as well as investigating its dependence on some specific features of the pore distribution, the overall porosity, the pore mean diameter and of the NW, such its diameter and length. To this purpose, a simple model describing the leading effects of all these factors is presented, followed by the comparison to MD simulations.

3.2.1 *Effective thermal conductivity in nanowires*

A first attempt at capturing both the effects of nanosized pores and the finite NW diameter can be easily constructed by adding a boundary scattering term [26, 164] to the expression for the MFP through Matthiessen rule, extending the modification to the Eucken model proposed in the previous section [102]

$$\begin{aligned}\Lambda^{-1} &= \Lambda^{-1}_{anharmonicity} + \Lambda^{-1}_{porosity} + \Lambda^{-1}_{boundaries} \\ &= \Lambda^{-1}_{bulk} + \left(\frac{1}{\Lambda_{bulk}}\frac{\phi}{2} + \frac{3\phi}{2d_p}\right) + \frac{1-p}{1+p}\frac{\alpha}{d_{NW}}\end{aligned} \tag{3.11}$$

where Λ is the MFP of heat carriers accounting for all scattering mechanisms, Λ_i is the MFP due to the i-th scattering mechanism ($i \in \{$anharmonicity, porosity, boundaries$\}$), d_p is the pore diameter, Λ_{bulk} is the MFP limited by phonon-phonon scattering in bulk material, φ is the above defined porosity, where V is volume, d_{NW} is the NW diameter, and $\beta = \alpha(1-p)/(1+p)$ accounts for the shape of the NW cross section, $\alpha = 1$ ($\alpha = 1.12$) for circular (square) cross section, [164] and the surface polish ($p = 1$ for perfectly reflecting surfaces and $p = 0$ for ideally rough surfaces).

When Eq. (3.11) is entered into the kinetic expression for the thermal conductivity $\kappa = \frac{1}{3}\mathcal{C}_{eff}v_g\Lambda_{eff}$, and taking into account the modified value of the specific heat capacity $\mathcal{C}$ due to the presence of pore $\mathcal{C}_{eff} = (1-\varphi)\mathcal{C}_{bulk}$, the model expression is obtained

$$\frac{\kappa}{\kappa_{bulk}} = \frac{1-\varphi}{1 + \frac{\varphi}{2} + \frac{3\varphi}{2d_p}\Lambda_{bulk} + \frac{\beta}{d_{NW}\Lambda_{bulk}}} \tag{3.12}$$

It is important to remark that the model given in Eq. (3.11) is addressed to the leading scattering mechanisms, i.e., it is by construction adopting the same treatment of the boundary scattering as in NWs, thus assuming the "gray" Matthiessen rule [165] for phonon MFP to be valid in the presence of anharmonic, pore, and boundary scattering. The failure of Eq. (3.12) to describe all situations here investigated (see Fig. 3.13b) leads to relax the assumption of the validity of Matthiessen rule, especially in light of previous

works where appreciable coupling between anharmonic and boundary scattering in thin films [166] and anharmonic and surface roughness scattering in ultra-scaled NWs [167] was found.

So, in order to account for the anharmonic-boundary coupling, a simple linear expression $\Lambda_{bulk} = \Lambda_{bulk,0}(1-\gamma_1\varphi)$ is adopted, where $\Lambda_{bulk,0}$ is now the bulk MFP limited by phonon-phonon scattering in bulk material and γ_1 encodes the reduction of the average anharmonic MFP due to the disturbance in the distribution function because of the presence of pores. Similarly, in order to account for the pore-boundary coupling, $\beta = \beta_0 - \gamma_2\varphi$ is set, where γ_2 describes the change in surface polish as porosity increases, and an empirical expression to adjust the coupling between porosity and surface scattering is introduced

Pore-boundary coupling

$$\Lambda^{-1}_{\varphi-d_{NW}} = \gamma_3\varphi/d^{\alpha}_{NW} \tag{3.13}$$

via a parameter γ_3 and an exponent α. When all terms are included, the final version of the model is

$$\kappa = \frac{\kappa_{bulk}(1-\varphi)}{\mathcal{Q}} \tag{3.14}$$

where

$$\begin{aligned}\mathcal{Q} = &\frac{1+\varphi/2}{1-\gamma_1\varphi} + \frac{3\varphi}{2d_p}\Lambda_{bulk,0} + \\ &+ \frac{\beta_0-\gamma_2\varphi}{d_{NW}}\Lambda_{bulk,0} + \gamma_3\frac{\varphi}{d^{\alpha}_{NW}}\Lambda_{bulk,0}\end{aligned} \tag{3.15}$$

While there have been some experimental measurements of the thermal conductivity of PSNWs [168, 169] its lack of complete characterization in terms of NW diameter and porosity renders comparison to this model difficult. Thus, the model in Eq. (3.12) is compared to the thermal conductivity from AEMD simulations [98].

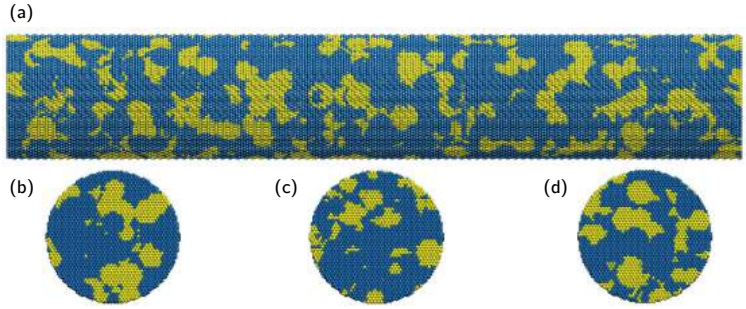

Figure 3.11. **a**: Side view of a PSNW with 0.3 porosity. Dark blue spheres represent Si atoms, while the atoms that have been removed are displayed as light yellow spheres for visualization purposes. **b**, **c**, and **d**: Cross-section views at $z = \mathrm{L}_z/4$, $\mathrm{L}_z/2$ and $3\mathrm{L}_z/4$, respectively.

3.2.2 *Nanowires structure construction*

The starting reference structure is a NW oriented along the [111] crystallographic axis, with a diameter of 15 nm and a length of 90 nm. As discussed in the following, diameters and lengths of up to 35 and 900 nm, respectively, are also considered in some selected cases. Similarly to what described in Sec. 3.1, pores are created by randomly selecting atoms and drawing a sphere around them whose diameter is sampled from a Gaussian distribution with given mean value and variance, taken to be 1.5 nm. Atoms inside the sphere are removed, creating a pore; the probability of creating a pore is adjusted to achieve a target porosity. Further iterations, where additional small pores are created or small portion of material restored, are then carried out until the desired porosity is obtained within a certain tolerance. As the AEMD method requires a uniform thermal conductivity along the transport direction, the pore generation procedure above described is applied within sequential regions of the sample, in order to guarantee a uniform porosity along the wire axis. Considered porosities are 0.05, 0.15, 0.3, and 0.5, with average pore diameters, i.e., the mean value of the Gaussian distribution, of 2, 3, and 4 nm. A typical structure is shown in Fig. 3.11.

Due to the random nature of pore formation, all the thermal conductivities here discussed have been obtained averaging over 3-4 independently generated configurations with the same target porosity and pore diameter. While this generation procedure is easily tailored on any arbitrary distribution of pore shapes and sizes, it still does not account for the oxidation at the pore surface. On the other hand, as already pointed out for PS, an amorphization of the regions closest to the pore surfaces is observed, which might mimic some characteristics of the native oxide, especially as the thermal conductivity of amorphous Si is similar to that of amorphous SiO_2 [170]. After generating the pores, metastabilities in the structure were minimized by first performing a structural relaxation followed by a heating/cooling cycle up to 900 K. This cycle was performed with periodic boundary conditions, so that unattached atoms or clusters eventually collided with the wire. After cooling back to 300 K, further thermalization proceeded for 200 ps, after which the thermostat was removed and the simulation continued for 400 ps without appreciable temperature drift, indicating successful thermalization. At this point, a step-like temperature profile was set up by velocity rescaling for 200 ps for each half, after which the AEMD procedure was allowed to proceed for 1 ns. Also in this case the EDIP potential [142] was adopted for the calculation of the energy and forces, and a time step of 2 fs was used throughout all the simulation protocol [141, 171].

3.2.3 κ *in porous nanowires*

In what follows, the AEMD results are compared to the model expressions for the thermal conductivity κ using the parameters in Table 3.9.

The parameters for Eq. (3.12) were obtained by a fit to the data in Figs. 3.12 and 3.13a only because inclusion of the points in Fig. 3.13b in the target dataset brought an insignificant improvement in Fig. 3.13b, while significantly worsening the adjustment in Figs. 3.12 and 3.13a. On the other hand, the parameters in Eq. (3.14) were chosen taking into account results in 3.13b in addition to Figs. 3.12 and 3.13a. The main result of this investigation is displayed in Fig. 3.12, where is reported the thermal conductivity, κ, of a 15 nm diameter PSNW as a function of the porosity, achieved by randomly

Parameter	Eq. (3.12)	Eq. (3.14)
$\Lambda_{bulk,0}$ [nm]	65.4	68.5
γ_1	...	1.55
β_0	0.24	0.22
γ_2	...	75.5
γ_3 [nm$^{\alpha-1}$]	...	104.0
α	...	1.11

Table 3.9: Fitted parameter values for Eqs. (3.12) and (3.14).

introducing pores of 3 nm diameter, comparing it to the fits through Eqs. (3.12) and Eq. (3.14). Notice that the value of $\Lambda_{bulk,0}$ agrees well with the one fitted for bulk PS, $40 < \Lambda_{bulk} < 110$ nm [102]. It is clear that the presence of nanovoids results in a very strong reduction of the thermal conductivity and a bare 5% of porosity is enough to decrease it approximately to half of the value of the pristine wire. The sample variation of κ is a few percent. Notice that boundary scattering alone accounts for a reduction of a factor of two for the pristine ($\varphi = 0$) NW with respect to bulk ($\kappa/\kappa_{bulk} \sim 0.5$ in Fig. 3.12), but the rather low porosity $\varphi = 0.3$ results in an additional reduction of one order of magnitude ($\kappa/\kappa_{bulk} \sim 0.05$). In the case of the highest porosity considered, $\varphi \sim 0.5$, the influence of the pore diameter was studied (inset of Fig. 3.12), comparing 2, 3, and 4 nm pores. A trend emerges, indicating that smaller pores result in slightly stronger reduction of κ. This effect was also observed in bulk PS, and it is a manifestation that at the nanoscale the interface density plays a crucial role in the behavior of κ [102]. Since Eq. (3.14) provides a good fit to the data, the "gray" Matthiessen rule for the MFP is valid when combining anharmonic and pore scattering mechanisms.

Fig. 3.13 shows the NW diameter dependence of κ for (**a**) a pristine NW and (**b**) a PSNW with $\varphi = 0.31$. The red (blue) lines correspond to the expression in Eq. (3.12) (Eq. (3.14)). So, the predictive power of the model is clearly established for the case finite diameter NWs without pores (Fig. 3.13a). The

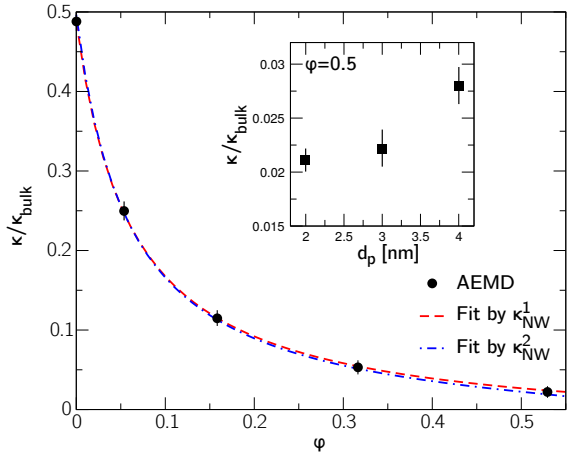

Figure 3.12. Thermal conductivity as a function of the total porosity for pores of average diameter of 3 nm in a 15 nm diameter and 90 nm long NW. The estimated values of κ are referred to the thermal conductivity of bulk c-Si, calculated in a computational cell of the same length and cross-section. The dashed red (dashed-dot blue) line corresponds to Eq. (3.12) [Eq. (3.14)] with the parameter values in Table 3.9. The symbols in the main panel indicate the thermal conductivity of each sample. Inset: dependence of κ on the pore diameter in the case of porosity $\varphi = 0.5$.

predictions of the model Eq. (3.12) are much less satisfactory for the case of the NW with finite porosity (Fig. 3.13b); while the order of magnitude of κ is correctly obtained, the model fails to reproduce the almost doubling of the conductivity as the NW diameter increases from 15 nm to 35 nm. From this, the necessity to introduce terms in the model not conforming to Matthiessen rule is evident. The failure of Matthiessen rule in ultra-scaled NWs in the presence of surface roughness and anharmonic scattering has been tentatively attributed to anharmonic scattering allowing the decay of high-energy non-propagating (due to roughness) phonons into lower energy propagating states [167]. It is conceivable that a similar mechanism might be at work in PSNWs, with the NW surface redistributing the number of vibrational modes (propagons, diffusons, and locons according to formalism introduced in Ref.[172]) expected to be

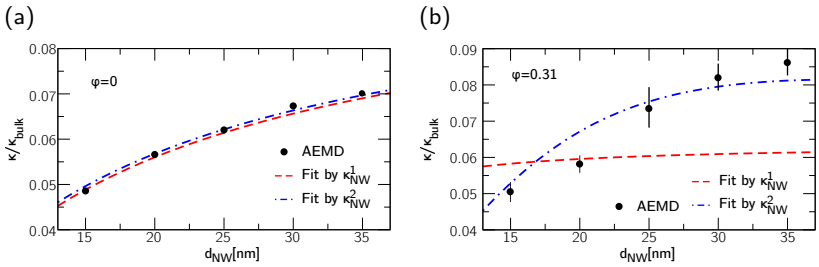

Figure 3.13. **a**: Thermal conductivity as a function of the nanowire diameter, d_{NW}, for a pristine NW. **b**: Thermal conductivity as a function of the nanowire diameter for a PSNW with porosity $\varphi = 0.31$ and pores of average diameter of 3 nm. Values are referred to the thermal conductivity of bulk c-Si. Lines have the same meaning as that in Fig. 3.12.

present in these systems with impaired translational symmetry due to the presence of pores.

Finally, as explained in Sec.2.2.4, heat carriers with a wavelength larger than the simulation cell cannot be described, a well-known fact that results in an underestimation of the thermal conductivity [97, 173]. This is why, to be consistent, the reduction of all the values of κ discussed so far has been calculated relatively to a cell of bulk Si of the same length. In general, the cell required to obtain a converged estimate of κ in Si-based systems, where phonons with MFP of up to hundreds of nm can contribute to heat transport [174], requires a very significant computational workload. The usual $\kappa^{-1}(L_z^{-1})$ procedure [175] is followed for the pristine and a porous nanowire with porosity $\varphi = 0.3$.

As seen in Fig. 3.14, for the pristine nanowire, the linear dependence of $\kappa^{-1}(L_z^{-1})$ is obtained, which allows extrapolating a value of $\kappa_\infty = 6.0$ W $m^{-1}K^{-1}$. The PSNW, on the other hand, exhibits a very poor dependence on L_z, indicating that the smallest cell size considered already accounts for the MFP of all phonons contributing to the thermal conductivity. In this case, the plot reports just the mean value of the calculated data points, because of the large uncertainty of the (small) fitted slope of $\kappa^{-1}(L_z^{-1})$. Notice that this means that the reductions of κ discussed so far would be even larger,

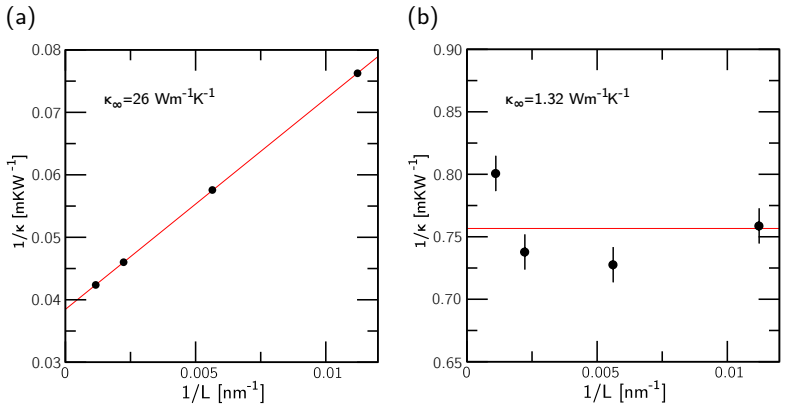

Figure 3.14. **a**: Inverse of the thermal conductivity as a function of the inverse of the nanowire length along the transport direction, L_z, for a pristine NW. A linear fit of the $\kappa^{-1}(L_z^{-1})$ allows extrapolating the value of κ_∞ for $L_z^{-1} \to 0$. **b**: Inverse of the thermal conductivity as a function of the inverse of a PSNW with porosity $\varphi = 0.3$ and pores of average diameter of 3 nm. In absence of a clear L_z dependence, just the mean value of the data points is reported.

because the thermal conductivity of the non-porous wire is being underestimated: $\kappa^{0.0}_{L_z=90\ nm}/\kappa^{0.3}_{L_z=90\ nm} \sim 10$ for the $L_z = 90$ nm cell was obtained, while for the ideally infinite-long NWs it results $\kappa_\infty 0.0/\kappa^{0.3}_\infty \sim 20$.

3.3 POROUS POLYCRYSTALLINE SILICON

The results discussed so far provide evidence that the thermal conductivity κ of a crystalline material may be significantly reduced by the introduction of MoDs such as pores. However also dislocations, internal surfaces, precipitates and other extended (2D and 3D) defects are known to strongly influence thermal transport. As already mentioned, in the development of high-performance thermoelectric materials it is of paramount importance to optimize the efficiency of scatterers, that in principle should be selected so as to decrease κ while marginally impacting the electrical conductivity σ. Possibly the most

dramatic display was provided in the case of silicon NW [30, 159], where a proper choice of nanowire wall roughness led to a more than tenfold decrease of κ while retaining σ values close to those of bulk c-Si. It is therefore not surprising that over the last few years a large number of papers have appeared proposing more sophisticated theoretical approaches to the analysis of phonon scattering. A key question they addressed was regarding the contributions of optical and acoustic phonons to the macroscopic thermal conductivity, and how they were suppressed by MoDs.

In lithographically-defined c-Si membranes it was shown that the introduction of cylindrical pores with diameters ranging from 1.9 to 10.9 μm leads to a reduction of κ depending on the pore diameter up to room temperature [147]. This is a non-trivial observation if one considers that in the gray model, the phonon MFP at room temperature in bulk silicon is around 0.2 μm [176]. A recent experiment carried out in p-type polycrystalline silicon (pc-Si) films [177] reported a decrease of κ with the hole radius, ranging from 120 nm down to 30 nm, in periodic structures with a fixed period of 300 nm. Grain sizes were widely-distributed, extending from 10 to 100 nm, thus overlapping with hole radii. Analysis led to the conclusion that thermal conductivity was controlled by volume reduction, sensibly through the heat capacity. However, a more detailed evaluation of the scattering mechanisms was not possible.

Frequency-dependent MFP

The analysis of the reduction of thermal conductivity due to grain boundariess (GBs) and porosity also motivated a revision of the standard kinetic model. Wang et al. [178] showed that below the Debye temperature Θ_D, the thermal conductivity of nanocrystalline silicon pellets obtained by spark plasma sintering followed a quadratic (rather than cubic) dependence on temperature. This suggested an ω-dependent MFP, with $\Lambda \propto \omega^{-1}$. Hua and Minnich [179] refined the model using Monte Carlo simulations, and confirmed a frequency-dependent phonon transmissivity at grain boundaries. Simulations showed that up to $\approx 60\%$ of the total heat is carried by phonons with MFP longer than the grain size. A similar temperature dependence at $T < \Theta_D$ was also reported in PS. Silicon inverse opals [180] displayed $\kappa \sim T^{1.8}$ while mesoporous nanocrystalline silicon thin films [181] reported $\kappa \sim T^2$. In the former case, the low-temperature $\kappa(T)$ was explained by invoking a quadratic frequency dependence of the scattering rate at grain boundaries due to coherent phonon reflection, while in mesoPS the quadratic increase of κ with

T was explained using the minimum thermal conductivity model derived by Cahill and Pohl in 1988 for amorphous or strongly-defective crystals [182]. No frequency-dependent transmissivity at pore surfaces was proposed.

The impact of the ω-dependence on the MFP at room temperature or above is still unclear in polycrystalline materials. According to Wang et al. [178], the spectral dependence of the MFP is of practical relevance with respect to the thermal conductivity only at low temperatures. On the other hand, Hua and Minnich [179] as well as Jiang et al. [183] have noted the importance of accounting for the frequency dependence of the MFP over the whole temperature range.

This state of affairs provides evidence that there is still an open issue about the best physically sound model to describe the effect of MoDs on the MFP of microscopic heat carriers. The question is whether it is better to treat the full phonon spectrum through effective concepts or, rather, if it is necessary to treat each single mode individually, since defects operate differently at different frequencies. Hereafter the first kind of model will be referred to as gray, while addressing each mode independently depending on its frequency as non-gray. This issue also impacts the actual usability of the adopted model. Simplified, effective models, characterized by ease of implementation and by a reduced computational workload, may enable computational analyses of materials of high structural complexity. On the contrary, a rigorous model treating each frequency mode independently may be practically applicable only to smaller systems, disallowing structurally accurate simulations of micromorphologically complex solids.

This section addresses the usability of the gray model to model phonon scattering in defective solids around and above room temperature by exploring the dependence of the thermal conductivity on the size and density of MoDs. First, single-crystalline and pc-Si films, both porous and non porous, were simulated to compute κ. These values and the derived model are compared also to experimental measurements for pc-Si films which were He^+-implanted and thermally-processed to promote the formation of pores [184]. By keeping the characteristic length scale of grains approximately fixed in both the computational and experimental investigations, the effects of the pores on phonon filtering were isolated. Silicon was chosen as the material in which to study these effect due to its well-assessed intrinsic thermal properties [42, 185–189]

and renewed interest in silicon and Si-based systems for thermoelectric applications [190–196].

3.3.1 *Theoretical background*

The standard kinetic model [66] relates the lattice thermal conductivity at temperature T to phonon MFP $\Lambda(\omega, s, T)$ and velocity $v(\omega, s)$, both quantities depending on phonon frequency ω and on polarization s

$$\kappa(T) = \frac{1}{3} \sum_s \int_0^\infty C(\omega, s, T) v(\omega, s) \Lambda(\omega, s, T) d\omega \tag{3.16}$$

where $C(\omega, s, T)$ is the spectral specific heat of the material and the sum runs over all polarizations. In addition to phonon-phonon and phonon-electron scattering, the phonon MFP is limited by the presence of defects, which have different scattering capabilities depending on ω and on a typical length scale ℓ associated with the defect itself. In single crystals, phonons are uniquely labeled by their wavevector $\mathbf{k}$ and by their polarization s, namely $\omega = \omega(\mathbf{k}, s)$. For the thermal conductivity to be described in the MFP (direct) space, it was suggested [176] that also the MFP Λ of a phonon might be labeled using the same four scalars, i.e. $\Lambda = \Lambda(\mathbf{k}, s)$. Under the (widely verified) assumption that both $\omega = \omega(\mathbf{k}, s)$ and $\Lambda = \Lambda(\mathbf{k}, s)$ be at least locally monotonic functions of k_x, k_y, and k_z , one may then invert $\Lambda(\mathbf{k}, s)$ so that $\omega = \omega(\Lambda, s)$. Thus a MFP spectral function of the thermal conductivity may be defined

$$K(\Lambda, T) = -\frac{1}{3} \sum_s C(\Lambda, s, T) v(\Lambda, s, T) \Lambda \left(\frac{d\Lambda}{d\omega} \right)^{-1} \tag{3.17}$$

where both $C(\Lambda, s, T)$ and $v(\Lambda, s, T)$ are here written as a function of the MFP. Thus

$$\kappa(T) = \int_0^\infty K(\Lambda, T) d\Lambda \tag{3.18}$$

The normalized thermal conductivity accumulation function $\alpha(\Lambda, T)$ is further defined as

$$\alpha(\Lambda_\alpha, T) = \frac{1}{\kappa} \int_0^{\Lambda_\alpha} K(\Lambda, T) d\Lambda \tag{3.19}$$

In the presence of a single morphological defect (MoD), thermal conductivity scales as

$$\kappa_{MoD}(T) = \int_0^\infty K_b(\Lambda_b, T) B_b^{MoD}(\Lambda_b, \ell_{MoD}) d\Lambda_b \tag{3.20}$$

where b refers to the MoD-free material and $B_b^{MoD}(\Lambda_b, \ell_{MoD})$ is some function of the ratio Λ_b/ℓ_{MoD} that depends on the type of defect.

In the construction of the B term, an important role is played by the way different scatterers contribute to set the MFP. Although B is in no way constrained to any specific rule of MFP combination, in practice the use of Matthiessen rule has almost no alternative, in spite of the increasing number of papers noting its limits [165, 167, 197]. Matthiessen rule assumes that in the presence of several scattering events each characterized by a scattering time τ_i, an effective scattering time τ may be defined as

$$\tau^{-1} = \sum_i \tau_i^{-1} \tag{3.21}$$

or, equivalently, it is assumed that there is no interplay among scattering mechanisms. Thus

$$\Lambda = \frac{1}{\sum_i \Lambda_i^{-1}} \tag{3.22}$$

This implementation of Matthiessen rule will be referred to as the *integral* Matthiessen rule. As known, its proposal moves from the gray hypothesis, namely that a dominant phonon mode of frequency ω_G exists, so that Eq. (3.16) reduces to its simplified kinetic form (see Eq. (3.8). It is instead well-known [46] that phonon modes are not independent, so that scattering events mix up modes both by normal and Umklapp processes.

Integral Matthiessen rule

An alternative, in order to estimate the MFP in the presence of several scattering phenomena, is to use the *spectral* Matthiessen rule. An effective specific scattering time $\tau(\omega, s)$ is defined for each phonon mode of frequency ω and polarization s as

Spectral Matthiessen rule

$$\tau(\omega, s)^{-1} = \sum_i \tau_i(\omega, s)^{-1} \tag{3.23}$$

(where $\tau_i(\omega, s)$ is the scattering time for phonon modes of frequency ω and polarization s due to the i-th scattering event) so that, since $\Lambda_i(\omega, s) = \nu(\omega, s)\tau_i(\omega, s)$,

$$\Lambda(\omega, s) = \frac{\nu(\omega, s)}{\sum_i \tau_i(\omega, s)^{-1}} = \frac{1}{\sum_i \Lambda_i(\omega, s)^{-1}} \tag{3.24}$$

It should be noted that not even the spectral Matthiessen rule provides a rigorous way to compute the effective MFP $\Lambda(\omega, s)$ as it also neglects mode mixing. Nonetheless, it does not rely upon the dominant mode assumption, so that it may be more properly and consistently used when non-gray MFP models are introduced.

Spectral function

In what follows two MFP spectral functions $K_b(\Lambda_b, T)$ will be used. For the gray model it is consistently assumed that

$$K(\Lambda_b) = \kappa_b \delta(\Lambda_b - \Lambda_{b,G}) \tag{3.25}$$

with $\Lambda_{b,G} = 205$ nm at room temperature for silicon [176]. In the gray model $\Lambda_{b,G}$ is the Λ-independent MFP of phonons that is set by scattering from extended defects [46]. For the non-gray models it will be instead adopted the MFP spectral function obtained by complementing computational data by Esfarjani et al. [198] and Jiang et al. [183].

3.3.2 *Sample preparation*

Three different prototypical silicon structures were generated, namely: (a) samples containing both a random and an ordered distribution of pores, but no GBs; (b) samples containing a GB network as well as a random distribution of pores; and (c) samples where pores are pinned at GBs. The generation of such a library of samples required two distinct procedures for pores and GBs, respectively. The pores are created according to the usual procedure, i.e. by randomly selecting a suitable number of lattice sites and removing all atoms within a distance d_p. This generates pores and, since they are randomly distributed, the probability of creating a pore is adjusted to achieve a target porosity φ, defined according to Eq. (3.1). Further iterations are carried out until the desired porosity is obtained within a certain tolerance. Similarly to

Pore generation

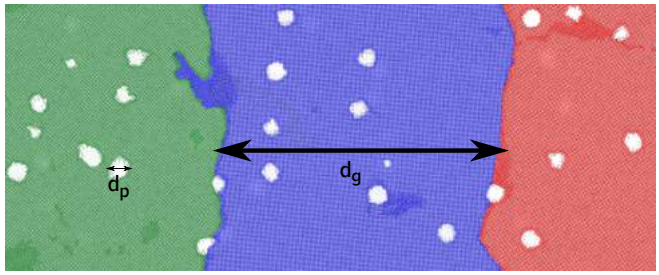

Figure 3.15. Illustration of the atomic-scale structure of a porous polycrystalline sample with randomly distributed pores. Different colors represent differently-oriented crystalline grains; darker areas identify defect-rich pockets, e.g. amorphous spots or grain boundaries. Two relevant morphological features discussed in the paper, d_p and d_g, are shown. The picture shows a 0.9-nm-thick longitudinal section, corresponding to just $\simeq 1/3$ of the overall sample thickness. The simulation cell is as thick as 2.72 nm and, therefore, matter is in fact not discontinuous, although some atoms seem to be unbound.

what explained for PS, as the AEMD simulation protocol requires a uniform mass distribution along the transport direction, the generation of pores is similarly applied within sequential regions of the sample, so as to obtain a uniform porosity. Following this procedure, samples with suitable pore density have been generated, with diameter ranging from 0.47 to 2.6 nm, resulting in an overall porosity of $\varphi = 0.005$. A similar procedure has been applied to obtain ordered pore distributions, with the only difference that the pore seeds were placed according to a cubic lattice. In this case two porosity values $\varphi = 0.028$ and $\varphi = 0.005$ have been considered. All samples required an accurate structural optimization protocol. The potential energy was at first minimized by means of conjugate gradient optimization. Next, a simulated annealing process was applied, heating the samples up to 900 K and cooling them back to room temperature for a total simulation time of 900 ps, with a final equilibration time of 400 ps at 300 K.

The generation of GBs required an ad-hoc multistep computational protocol: a crystalline sample with dimensions $L_x = 2.72$ nm, $L_y = 27.15$ nm and $L_z = 135.76$ nm (containing as many as 5×10^5 atoms) was fully amorphized

Grain generation

following a standard quenching-from-the-melt approach. Then, N_g sites were selected at random in the yz plane and around each of them a cylindrical region (passing across the full L_x dimension of the simulation box) was created in order to replace the amorphous matter with a crystalline cylinder, randomly rotated in the yz plane. The resulting structures (amorphous matrices decorated by crystalline seeds) were annealed at constant $T = 1200$ K for 3.0 ns. In this way seed grains could undergo a growth until a nanocrystalline silicon system was eventually created. The number N_g of initial seeds was chosen in order to fill the yz plane with grains of average size $d_g = 25.0$ nm. A detailed description of this protocol is reported in Refs. [199] and [103].

By combining the above two procedures a number of systems were obtained, differing in atomic scale nanostructure while keeping the same porous-polycrystalline morphology, as shown in Fig. 3.15.

Pores at grain boundaries

A third kind of porous polycrystalline sample was realized, where pores were pinned at GBs. For this purpose, pore generation was slightly modified. As already mentioned in this section, atoms in an amorphous structure are characterized by a higher configurational energy, with respect to atoms in a crystalline lattice. According to the EDIP interaction potential adopted in this work [142], the average energy for a c-Si atom is $\langle E_{c-Si} \rangle = -4.6$ eV, thus a further requirement for the generation of pores was to involve only atoms with energy greater than $\langle E_{c-Si} \rangle$. It is worth stressing that this interaction scheme has been adopted since it is accurate in describing non-crystalline forms of silicon, as well as in predicting the thermal transport properties of disordered silicon forms, e.g., amorphous and nanocrystalline ones [98, 102, 103, 200]. Porous polycrystalline samples of categories (b) and (c) are characterized by porosity values $\varphi = 0.005$, with $0.47 \leqslant dp \leqslant 2.6$ nm.

Since present thermal conductivity data for nanocrystalline porous samples are calculated for finite-size simulation cells, the actual normalizing value κ_{sc} corresponding to pristine silicon was evaluated for a system with the same length along the direction of thermal transport as nanocrystalline porous ones, similarly to previous investigations [104, 201, 202]. Since in the present case this length was as short as 162.92 nm, the corresponding conductivity of pristine silicon was set to 45.4 ± 0.2 W m^{-1}K^{-1}, as obtained by the present simulations.

3.3.3 *Single MoD in silicon*

Polycrystalline silicon

In polycrystalline materials it is quite natural to assume that GBs limit the phonon MFP to the grain size d_g so that $\Lambda_P^{-1} \equiv \Lambda_b^{-1} + \Lambda_{GB}^{-1} = \Lambda_b^{-1} + d_g^{-1}$. However, such an assumption is possibly too clear-cut. First, more than a single scattering event may be needed to fully thermalize phonons. Furthermore, phonons may be scattered with different efficiencies by grain boundaries depending on the misorientation of adjacent grains. Even in a gray model, grain boundaries may be assumed to transmit phonons with variable transmissivity $\mathcal{T}_G$ depending upon the grain pair misorientation. Both factors suggest to write

$$\Lambda_{GB} = \beta \left\langle \left(\frac{1}{\mathcal{T}_G} - 1 \right)^{-1} \right\rangle d_g \equiv \beta \gamma_G d_g \tag{3.26}$$

with $\beta (\geqslant 1)$ counting the average number of scattering events needed by phonons to recover their equilibrium distribution, while $\gamma_g (\geqslant 1)$ scaling the effective grain size by the grain boundary transmissivity. The use of β, which accounts for the difference between scattering and relaxation times, is reminiscent of the approach developed by Das Sarma and Stern for the analysis of electron scattering [203]. Therefore, within the limits of validity of the integral Matthiessen rule, the gray model leads to

$$\Lambda_{P,G}^{-1} = \Lambda_b^{-1} + (\beta \gamma_G d_g)^{-1} \tag{3.27}$$

where the subscript P labels the polycrystalline material. Thus one gets

$$B_b^{P,G} = \left(1 + \frac{\Lambda_b}{\beta \gamma_G d_g} \right)^{-1} \tag{3.28}$$

In view of Eq. (3.20) this leads immediately to

$$\begin{aligned} \kappa_{P,G} &= \kappa_b \int_0^\infty \delta(\Lambda_b - \Lambda_{b,G}) \left(1 + \frac{\Lambda_b}{\beta \gamma_G d_g} \right)^{-1} d\Lambda_b \\ &= \kappa_b \left(1 + \frac{\Lambda_{b,G}}{\beta \gamma_G d_g} \right)^{-1} \end{aligned} \tag{3.29}$$

which is the sought expression of the thermal conductivity in the gray approximation. From an alternate perspective, following Wang et al. [178] and Hua and Minnich [179] phonons may be transmitted by GBs with a transmissivity $\mathcal{T}(\omega)$

$$\mathcal{T}(\omega) = \frac{1}{\gamma\omega/\omega_{max} + 1} \tag{3.30}$$

where γ is a fitting parameter and ω_{max} is the maximum phonon frequency. Therefore, $\Lambda_{GB}(\omega) = \gamma^{-1}(\omega_{max}/\omega)\beta d_g$, namely GBs are transparent to phonons in the long-wavelength limit. Thus the non-gray model predicts, still within the limits of validity of the spectral Matthiessen rule, that

$$\Lambda_{P,NG}^{-1} = \Lambda_b^{-1} + (\gamma/\beta)(\omega/\omega_{max})d_g^{-1} \tag{3.31}$$

where the subscript NG refers to the non-gray model.

The use of Eq. (3.31) is less straightforward as the MFP depends explicitly upon ω. This implies that

$$B_b^{P,NG} = \left(1 + \frac{\gamma\omega}{\beta\omega_{max}}\frac{\Lambda_b}{d_g}\right)^{-1} \tag{3.32}$$

For the most common bulk scattering mechanisms [204]

$$\Lambda_b = A(T)\omega^{-n} \tag{3.33}$$

where n is a non-negative integer depending on the dominant scattering mechanism, and $A(T)$ is independent of ω. In the whole numerical analysis here reported, phonon-impurity scattering is assumed to dominate scattering in bulk (single-crystalline) silicon due to the high doping level. Regardless of the phonon dispersion relation, it was shown [72, 198, 204] that setting $n = 4$ in Eq. (3.33) leads to a satisfactory description of the bulk MFP. Then one may write

$$B_b^{P,NG} = \frac{\Lambda_{P,NG}}{\Lambda_b}\left[1 + \frac{\gamma/\beta}{\omega_{max}}\frac{\Lambda_b}{d_g}\left(\frac{\Lambda_b}{A}\right)^{-1/4}\right]^{-1} \tag{3.34}$$

so that

$$\kappa_{P,NG} = \int_0^\infty K_b(\Lambda_b)\left[1 + \frac{\gamma/\beta}{\omega_{max}}\frac{\Lambda_b}{d_g}\left(\frac{\Lambda_b}{A}\right)^{-1/4}\right]^{-1} d\Lambda_b \tag{3.35}$$

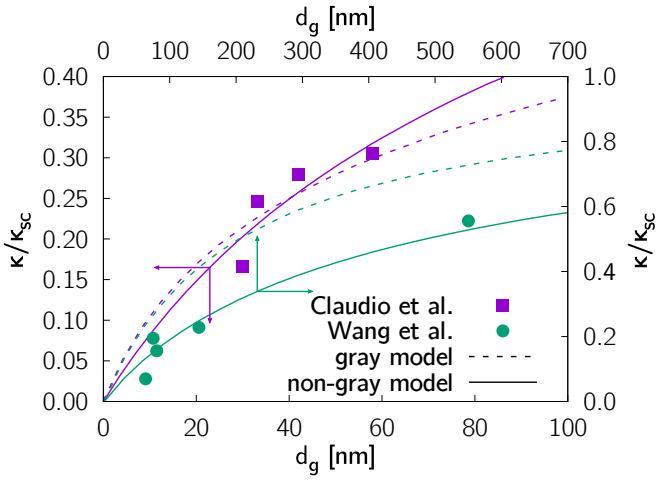

Figure 3.16. Fit of the normalized experimental values κ/κ_{sc} vs. grain size in pc-Si to the gray (dashed lines) and non-gray (full lines) models. Experimental data are from Wang et al. [178] (green circles, microcrystalline silicon) and from Claudio et al. [191] (purple squares, nanocrystalline silicon). Thermal conductivity κ_{sc} of c-Si was respectively 142 and 87.34 W $m^{-1}K^{-1}$ in the two works.

which states the dependence of the thermal conductivity in pc-Si according to the non-gray model.

Figure 3.16 displays the fits of Eqs. (3.29) and (3.35) to experimental data reported by Wang et al. [178] for microcrystalline silicon and by Claudio et al. [191] for nanocrystalline silicon.

Both models are in good agreement with data for nanocrystalline silicon, although the non-gray model fits them more closely. Instead, only the non-gray model returns an acceptable fit for microcrystalline silicon. Setting $\omega_{max} =$ 12 THz [178, 205] it results $A = (5.3 \pm 1.2) \times 10^{50}$ μm s^{-4} for both sets of data, along with γ/β values of 2.39 ± 0.07 and 0.28 ± 0.02, respectively.

Porous monocrystalline silicon

A model for the MFP in PS was already proposed in Sec. 3.1. As already stated, from Eq. (3.2), one may easily verify that the pertinent MFP Λ_{pores}

relates to porosity and boundary MFP as

$$\frac{1}{\Lambda_{pores}} = \left(\frac{\varphi}{2\Lambda_b}\right) \tag{3.36}$$

This is only the effect of macroscopic pores and results from the reduction of the filled volume in the medium.

An additional component arises for micro-/nano-pores, that relates instead to the density of scattering centers at the pore-solid interface (Eq. (3.7)). Thus the gray scattering length $\Lambda_{interfaces}$ (Eq. (3.5)) can be taken to sum up through the integral Matthiessen rule, yielding

$$\frac{1}{\Lambda_{H,G}} = \left(\frac{\varphi}{2\Lambda_b}\right) + \frac{1}{\beta\Lambda_{interfaces}} \tag{3.37}$$

where β counts the number of scattering events needed to fully thermalize phonons. Therefore

$$\frac{1}{\Lambda_{H,G}} = \frac{1}{\Lambda_b} + \left(\frac{\varphi}{2\Lambda_b} + \frac{3\varphi}{2\beta d_p}\right) \tag{3.38}$$

and

$$B_b^{H,G} = \frac{\Lambda_{H,G}}{\Lambda_b} = \left[1 + \frac{\varphi}{2}\left(1 + \frac{3\Lambda_b}{\beta d_p}\right)\right]^{-1} \tag{3.39}$$

so that finally

$$\begin{aligned} \kappa_{H,G} &= \kappa_b \int_0^\infty \delta(\Lambda_b - \Lambda_{b,G}) \left[1 + \frac{\varphi}{2}\left(1 + \frac{3\Lambda_b}{\beta d_p}\right)\right]^{-1} d\Lambda_b \\ &= \kappa_b \left[1 + \frac{\varphi}{2}\left(1 + \frac{3\Lambda_{b,G}}{\beta d_p}\right)\right]^{-1} \end{aligned} \tag{3.40}$$

which is the expression for κ in the presence of nanopores and in the gray approximation.

For the non-gray model it is necessary to account for the probability that phonons are elastically reflected at the pore surface. Actually, phonon transmissivity through a vacuum gap is exactly zero, while even at the nanoscale

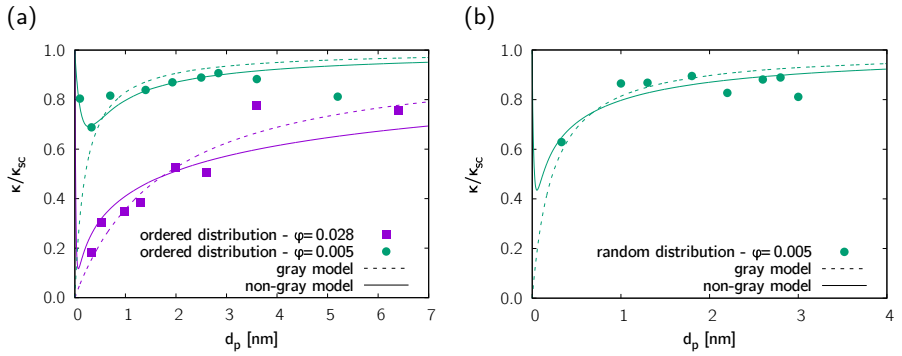

Figure 3.17. **a**: κ values obtained for OPS two different porosity values. **b**: κ values obtained for RPS. The dashed and full lines represent, respectively, the fit to gray and non-gray scattering modes of the normalized values of $\kappa(d_p)$.

the near-field thermal radiation contribution may be easily verified to be negligible [206]. Using the so-called Ziman formula [46], reflectivity $\mathcal{R}$ at pores reads

$$\mathcal{R}(\omega) = \exp\left(-\frac{16\pi^3 d_p^2 \omega^2}{v_2}\right) \tag{3.41}$$

Thus

$$B_b^{H,NG} = \frac{\Lambda_{H,NG}}{\Lambda_b} = \left\{1 + \frac{\varphi}{2} + \frac{3\varphi\Lambda_b}{2\beta d_p}\left[1 - \mathcal{R}(\omega)\right]\right\}^{-1} \tag{3.42}$$

that, using again Eq. (3.33), leads to the explicit expression for $\kappa_{H,NG}$:

$$\kappa_{H,NG} = \int_0^\infty K_b(\Lambda_b) \times \\ \times \left(1 + \frac{\varphi}{2} + \frac{3\varphi\Lambda_b}{2\beta d_p}\left\{1 - \exp\left[-\frac{16\pi^3 d_p^2}{v^2}\left(\frac{\Lambda_b}{A}\right)^{-\frac{1}{2}}\right]\right\}\right)^{-1} d\Lambda_b \tag{3.43}$$

which is the needed formula for κ in PS in the non-gray model. Note that in the gray model, where the MFP spectral function is a Dirac delta-function, Eq. (3.41) would lead only to an additional constant factor in the third term of the right-hand-side of Eq. (3.37).

Fitting of Eq. (3.40) to computed data (Fig. 3.17) reports an excellent agreement of the gray model with simulations. When pores sit on a cubic lattice one gets $\beta = 4.9 \pm 0.5$ for $\varphi = 0.028$ and $\beta = 7.6 \pm 1.4$ for $\varphi = 0.005$. Instead, for randomly distributed pores $\beta = 6.8 \pm 1.2$ for $\varphi = 0.005$. Also the non-gray (reflective) model, Eq. (3.43), shows a more than fair agreement with computational data. One gets $A = (4.6 \pm 2.0)$ μm s^{-4} independently of pore distribution and porosity. The fitting process returns β values of 12.6 ± 2.5 and 51.7 ± 11.0 for $\varphi = 0.028$ and 0.005 with ordered pore distributions; and $\beta = 46.6 \pm 12.4$ at $\varphi = 0.005$ for randomly distributed pores.

It should be noted that, despite their agreement with computational data, the two models predict a completely different behavior of $\kappa(d_p)$ for $d_p \to 0$ at constant φ. Thermal conductivity in the gray model tends to zero for vanishing pore diameters while it recovers the single-crystal value in the non-gray model, as physical intuition would actually suggest.

3.3.4 *Multiple MoDs in silicon: porous polycrystalline silicon*

Multiple defects impact thermal conductivity by introducing two classes of scattering bodies in addition to the scattering entities natively present in single-crystalline media. In the gray model one may use the integral Matthiessen rule, immediately getting from Eqs. (3.27) and (3.38) that

$$\kappa_{HP,G} = \kappa_b \frac{2\beta\gamma_G d_p d_g}{\gamma_G d_g [\beta d_p (\varphi + 2) + 3\Lambda_b \varphi] + 2 d_p \Lambda_b} \tag{3.44}$$

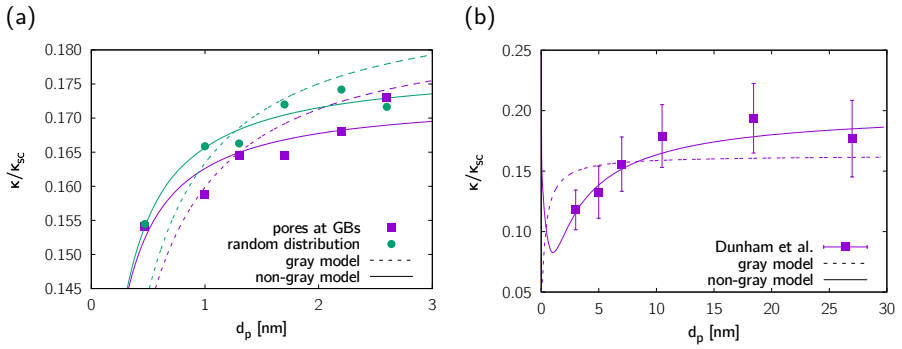

Figure 3.18. **a**: Fitting of gray (dashed lines) and non-gray (full lines) scattering models to normalized values of $\kappa(d_p)$ obtained by simulating random distributions of pores in porous pc-Si. **b**: Fitting of gray (dashed lines) and non-gray (full lines) scattering models to normalized values of $\kappa(d_p)$ measured in He^+-implanted nanocrystalline silicon [184].

Instead, in the non-gray model spectral Matthiessen rule leads to

$$\kappa_{HP,NG} = \int_0^\infty \left\{ 1 + \frac{\varphi}{2} + \frac{3\varphi\Lambda_b}{2\beta d_p} \times \right. \\ \times \left[1 - \exp\left(-\frac{16\pi^3 d_p^3}{\nu^2} \left(\frac{\Lambda_b}{A} \right)^{-\frac{1}{2}} \right) \right] \\ \left. + \frac{\gamma\Lambda_b}{\beta\omega_{max} d_g} \left(\frac{\Lambda_b}{A} \right)^{-\frac{1}{4}} \right\}^{-1} d\Lambda_b \tag{3.45}$$

In Eq. (3.45) the same β was used for both scattering mechanisms as the effectiveness of a specific type of scattering event is already accounted for by $\mathcal{R}$ for the pores and by γ/ω_{max} for the grains.

Figure 3.18 directly compares the experimental and computed thermal conductivities, both normalized to the thermal conductivity of c-Si. A value of $\kappa_{SC} = 120$ W m^{-1}K^{-1} was used, which is appropriate for sub-micrometric thin films [207]. For computer simulations a clearly better agreement is found using the non-gray model, reporting $\beta = 30.0 \pm 0.1$ and 27.4 ± 4.2 for pores

at GBs only or randomly distributed, respectively, and values of $\gamma = 4 \pm 1$ and $A = (3.00 \pm 0.99) \times 10^{51}$ μm s^{-4} in both cases. The gray model returns instead $\beta = 1.85 \pm 0.59$ and $\gamma_G = 1.00 \pm 0.36$ when pores sits at GBs only; and $\beta = 1.90 \pm 0.51$ and $\gamma_G = 1.00 \pm 0.31$ for randomly distributed pores.

Experimental data from Dunham et al. on He^+-implanted nanocrystalline thin films [208, 209] are fitted instead with $\beta = 1.0 \pm 0.5$ and $\gamma_G = 0.5 \pm 0.3$ in the gray model, and with $\beta = 1.0 \pm 0.6$, $\gamma = 7.0 \pm 3.9$, and $A = (2.29 \pm 1.31) \times 10^{46}$ μm s^{-4} in the non-gray model. Note that, since the experimental thermal conductivity was measured cross-plane, grain size used in the fitting referred to the grain height, namely $d_g = 150$ nm. It should also be remarked how the gray model predicts an almost constant κ for $d > 5$ nm, in good agreement with with gray Monte Carlo simulations reported previously [184].

Comparison of fits to both experimental and computed data suggests that non-gray models are more accurate than gray ones. This is not completely obvious, as it is reported that relevant differences between gray and non-gray models should be observed mostly at low temperatures [178]. Instead, even around room temperature and in the presence of a single MoD it is evident that, although the gray model may provide an acceptable quantitative prediction of the thermal conductivity [184, 197], a more precise analysis of morphologically-limited thermal conductivity requires relaxing the assumption of a single dominant phonon mode governing heat transport.

Comparing gray and non-gray models

However, in spite of its ability to describe the dependence of κ upon the density of the pertinent MoD, the non-gray model also raises questions when applied to porous crystals. Specifically, concerns may be raised about its physical soundness in the description of κ dependence on d_p over the whole range of pore sizes. Gray and nongray models, while mostly showing the same expected decrease of κ with decreasing d_p, dramatically differ from each other in the zero-size limit. It is worth noting that, while in porous c-Si this difference occurs at pore sizes comparable to the size of a single vacancy, in porous pc-Si the departure between the two models shows up instead for $d_p \approx 1$ nm, i.e. when pores are well-defined, extended MoDs. The gray model predicts a vanishing thermal conductivity while the non-gray model predicts a recovery of κ to the pore-free value. Such a difference is clearly explained by inspection of Eqs. (3.39) and (3.42). In both cases the MFP is dominated by phonon scattering at pores. However, the gray model considers all scattering events as

effective while the non-gray model accounts for the probability that phonons are elastically reflected at pore surfaces. In the latter case, when both d_p and ℓ_p tend to zero (as needed to keep φ constant), no collision remains effective, so that the material recovers the conductivity pertaining to the pore-free material. However, both predictions are questionable. In the gray model, the assumption that all collisions are effective (namely that in no case phonons may be elastically reflected at pore surfaces) sensibly overestimates the effectiveness of pores as scattering centers. Conversely, Eq. (3.41) provides an oversimplified description of the actual reflectivity at internal surfaces [46] that in turn underestimates scatter efficiency in the low dp limit. A more fundamental limitation of both models arises when considering non-local effects. Since for $d_p \to 0$ at fixed φ the pore density abruptly increases, one may expect lattice distortions due to pores to extend over a larger portion of the crystal, a feature that is not accounted for in either gray or non-gray models. At high porosity this should lead to an increase of positional disorder, up to a quasi-amorphization of the solid. Thus, κ may be expected to approach the Casimir limit. At low porosity, instead, pores will degenerate into a collection of sparsely distributed vacancies, imparting a negligible increase of lattice disordering and simply increasing the vacancy density. Thus, κ should almost recover its pore-free value: neither gray nor non-gray models are adequate at accounting for the effect of pores at any porosity, as neither of them properly encompasses non-local effects due to pore-related lattice disorder. Non-gray models possibly better qualify in the current case because of the relatively small φ considered in this study. One would then draw the conclusion that while the non-gray model is a more appropriate choice even at non-cryogenic temperatures, it is the use of Matthiessen rule (either integral or spectral) which determines the limits of applicability for either model. Earlier in this section, it was shown that MoD-related scattering lengths (ℓ_p and $\gamma_G d_g$) sensibly depend not only on the distribution of scattering centers within the medium but also on the medium itself. Thus, non-local descriptors accounting for the lattice distortion around MoDs are needed.

Finally, concerning the usability of more MoDs to tailor the thermal conductivity,it results that the addition of a morphological defect to an already defective material causes a further decrease of its thermal conductivity if the two sets of defects have different characteristic sizes. Experimental results

show the conductivity to drop by about 30%, with smaller decreases ($\approx$ 10%) being reported by simulations. It is possible to conclude that the use of a variety of MoDs to control a material thermal conductivity may be safely planned by the use of non-gray models and of the spectral Matthiessen rule. This result is consistent with the conclusions of previous publications [184, 208, 209] and further stresses how the introduction of pores in heavily boron-dope nanocrystalline silicon showing enhanced power factors [193, 194, 210] may lead to large thermoelectric efficiencies in a fairly geo-abundant material.

4

SILICON-GERMANIUM NANOSTRUCTURES

Contents

As extensively explained in the previous chapters, Thermoelectric Effect (TE) devices have many attractive features for heating/cooling purposes or power generation that could lead to potential applications such as waste-heat energy harvesting. The main challenge for TE devices is represented by the overall efficiency which is still too low [211]. In order to achieve high ZT values, several chemical and physical approaches have been proposed so far. One of the most popular and effective consists in using nanofabrication techniques so as to increase phonon scattering by internal interfaces. Different types of nanostructures have been explored so far, such as quantum wells [212], superlattices [24, 213], quantum wires [214], and quantum dots [215]. An overview about superlattices and the role of the interface in silicon-germanium nanostructures, is provided in this chapter.

4.1 SILICON-GERMANIUM SUPERLATTICES

This section will focus on superlattices (SLs) i.e. periodic structures made by layers of two (or more) different materials where the thickness of each layer is usually of the order of the nanometer. The idea is to use quantum-confinement effects to obtain an enhanced electronic density of states and to exploit interfaces and boundaries to scatter phonons more effectively than electrons. It is known that in SL structures phonon transport is much more

affected than the electronic counterpart, resulting in a distinct reduction of thermal conductivity [216–218]. The reduction of κ is mainly due to three mechanisms: (i) increased scattering of the lattice vibrations due to the large number of interfaces [219, 220]; (ii) increased diffuse reflection at the interface due to acoustic impedance and phonon spectrum mismatches [221]; and (iii) wave interference due to the periodic nature of the structure [222]. Several experimental studies have demonstrated a ZT increase up to 2.4 in a wide variety of SLs such as Bi_2Te_3/Sb_2Se_3 SLs and PbTe/PbTeSe quantum-dot SLs [24, 215]. However these chemically complex systems have large costs of production which strongly limit their large scale commercial use. For this reason SLs composed by conventional semiconductors such as Si and Ge, represent a promising low-cost alternative due to their relative abundance, structural simplicity and the possibility to exploit standard manufacturing processes. Several parameters in superlattice design should be optimized in order to obtain the lowest thermal conductivity. The effect of the Si/Ge SL geometrical and morphological parameters on thermal transport have been extensively explored both experimentally and theoretically. In particular, Savić et al. [223] focused on the effect of the SL dimensionality on thermal transport showing that planar SL have the lowest κ with respect to nanowire and nanodot superlattices.

Experimental results on superlattices

From an experimental point of view, Chakraborty et al. [224] studied the effect of the period thickness in strain symmetrized Si/Ge superlattices showing that κ can be reduced by a factor ~ 2 by reducing the period thickness from 16 to 7 nm. Moreover, they noticed that thermal conductivity in these systems has a minimum for period thickness of 7 nm, arguing that under this limit phonons in SL behave wave-like instead of moving ballistically [224]. Borca-Tasciuc et al. [40], instead, studied the effect of doping in Si/Ge superlattices providing evidence that κ of doped samples decreases with respect to the undoped ones.

An alternative way of reducing κ in Si/Ge based SL has been recently explored by Ferre Llin et al. [225] that proposed the substitution of the pure silicon layer with a sort of phonon barrier composed by a $Si_{0.5}Ge_{0.5}$ alloy which is a well-known phonon glass, having a $\kappa \sim 7$ times lower with respect to pure Ge. The presence of such phonon barriers should in principle strongly decrease the overall thermal conductivity. In their work a range of p-type $Ge/Si_{0.5}Ge_{0.5}$ SL was fabricated using low-energy plasma enhanced chemical vapor deposi-

The role of stoichiometry

tion. The maximum value obtained for ZT is ~ 0.08 that, although being almost 8 times greater than that of pure Ge, is too low for TE applications. The two main reasons for this are the relatively high thermal conductivity of $\kappa \sim 4-6$ W m^{-1}K^{-1} and the low electrical conductivity $\sigma \sim 2220-17600$ S m^{-1} [225] (electrical conductivity of p-doped germanium is ~ 30000 S m^{-1} [226]). Despite the fact that the overall ZT is still too low, such a SL presents the possibility of effectively tuning both the electronic and thermal transport properties by modifying several morphological and geometrical parameters.

By adopting this idea as a conceptual guideline, model potential MD simulations were carried, addressed to predict κ in several Ge/Si$_x$Ge$_{1-x}$ SL samples as a function of the alloy stoichiometry and PR, i.e. the ratio between Ge and Si$_x$Ge$_{1-x}$ layer thicknesses. In particular, the final goal is to predict the minimum Si concentration (which guarantees a small σ reduction with respect to pure Ge) providing a sizable reduction of κ and consequently an overall ZT increase. The results show that the presence of the alloy barriers greatly reduce thermal conductivity with increasing stoichiometry. Moreover, a non-monotonic dependence of the thermal conductivity on the period ratio is predicted.

4.1.1 *Pseudomorphic growth and elastic constant calculation*

Typical Ge/Si SLs samples are grown by chemical vapor deposition technique [225], which gives rise to the so-called *pseudomorphic* structure, where the substrate composition controls the in-plane lattice parameter $a_{\parallel}$, which remains unchanged in the whole structure [227]. The lattice mismatch between the substrate and the epitaxially grown Si$_x$Ge$_{1-x}$ barrier generates a strain along the growth direction leading to a lattice constant $a_{\perp}$ which, in turn, depends on the elastic properties of the alloy. According to the macroscopic theory of elasticity [228], the lattice constants of a pseudomorphic structure can be written as

$$a_{\parallel}^{alloy} = a_{\parallel}^{subs} \equiv a^{subs} \tag{4.1}$$

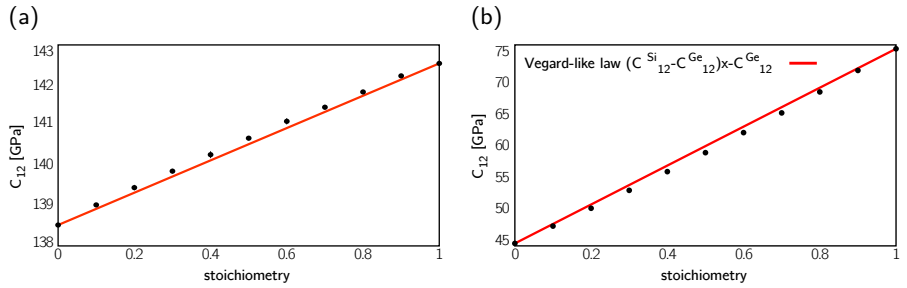

Figure 4.1. **a**: Si_xGe_{1-x} elastic constant C_{11} as a function of stoichiometry x. **b**: Si_xGe_{1-x} elastic constant C_{12} as a function of stoichiometry x. A Vegard-like law $(C^{Si} - C^{Ge})x + C^{Ge}$ accurately fits MD results

for the direction parallel to the substrate, and

$$a_{\perp}^{alloy} = a^{alloy}\left[1 - 2\left(\frac{C_12}{C_11}\right)^{alloy}\left(\frac{a^{subs}}{a^{alloy}} - 1\right)\right] \tag{4.2}$$

for the growth direction, where $a_{\parallel}^{alloy}$ and $a_{\parallel}^{subs}$ represent, respectively, the barrier and substrate in-plane lattice parameters, $a_{\perp}^{alloy}$ is the alloy out-of-plane lattice parameters and a^{alloy} is the bulk alloy lattice parameter (calculated using the Vegard law).

Pseudomorphic elastic constants

In order to prepare realistic pseudomorphically grown Ge/Si_xGe_{1-x} SLs it is necessary to estimate the C_{11} and C_{12} elastic constants provided by Tersoff potential. The calculations have been performed by computing the second derivatives of the total energy with respect to suitable deformations. Figure 4.1 shows C_{11} and C_{12} of a Si_xGe_{1-x} alloy as a function of stoichiometry. The results indicate a clear linear Vegard-like dependence of C_{11} and C_{12} in good agreement with experimental data [229]. The corresponding values for pure Si and Ge show relative deviations with respect to the experimental data of 14% and 8%, respectively for C_{11}, and 17% and 8% for C_{12}. Such a discrepancy is attributed to the Tersoff model potential as already pointed out in reference [230].

Using the above procedure several Ge/Si_xGe_{1-x} SLs having the in-plane and out-of-plane lattice constants as predicted by Eqs. (4.1) and (4.2) were

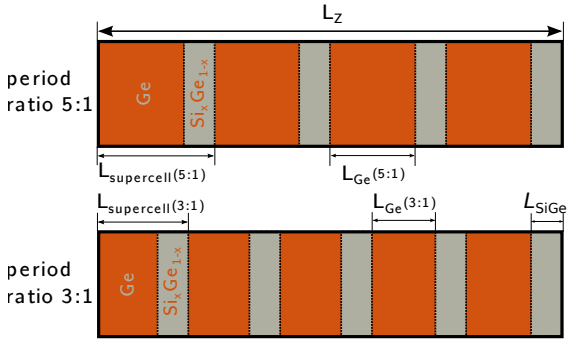

Figure 4.2. Schematic representation of the Ge/Si_xGe_{1-x} SL for two different PRs.

realized. In detail, a set of samples with varying alloy stoichiometry ($x = 0$, 10, 20, 35, 50, 70 and 100%) and the total length L_z in the range $44.3 - 803.4$ nm was generated. Correspondingly, the number of atoms varied from 1.6×10^4 to 1.54×10^6. The PR was also varied considering 1 : 1, 2 : 1, 3 : 1 and 5 : 1 superperiodic structures. Therefore, the Ge layer thickness varied from 1.13 nm for 1 : 1 PR to 5.66 nm for 5 : 1 PR, while the barrier thickness was $2a_\perp^{alloy}$, with $a_\perp^{alloy}$ depending on the stoichiometry as predicted by Eq. (4.2). Figure 4.2 shows a schematic representation of the SL samples with two different PRs.

4.1.2 κ *dependence on sample section*

In order to choose an appropriate section of the sample, a set of preliminary AEMD calculations (see Sec.2.2.3) were performed: κ was estimated as a function of the sample section in the range $0.3 - 251$ nm^2 in a $Ge/Si_{0.5}Ge_{0.5}$ SL having a fixed total length $L_z = 54.3$ nm and a 2 : 1 PR. Figure 4.3a provides evidence that for sections greater than 128 nm^2 κ does not depend on the sample geometry. For this reason, a section value of 128 nm^2, was kept in the following AEMD calculations, except the case $x = 100\%$ as explained below.

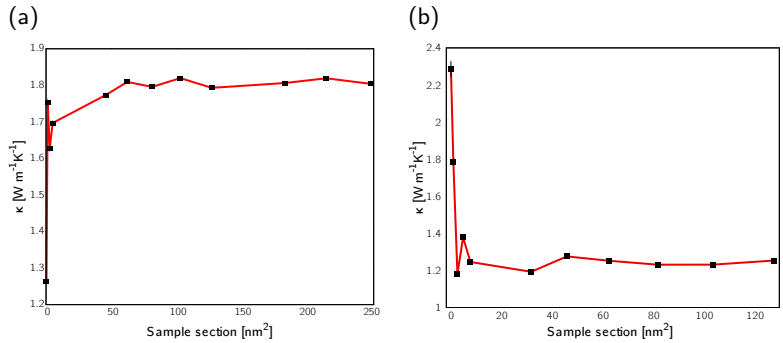

Figure 4.3. **a**: κ vs. sample section for a $Ge/Si_{0.5}Ge_{0.5}$ SL with $L_z = 54.3$ nm and $2:1$ PR. Thermal conductivity converges for sections greater than 128 nm^2. **b**: κ vs. sample section for a Ge/Si SL with $L_z = 54.3$ nm and $2:1$ PR. Thermal conductivity converges for sections greater than 8.0 nm^2.

4.1.3 κ_∞ *linear vs. quadratic extrapolation*

In order to verify size effects in a SL-like system, κ was calculated in a set of 10 samples of pure Ge/Si, with $44.3 \leqslant L_z \leqslant 803.4$ nm with period ratio $3:1$ and $5:1$. In order to minimize the computational cost while spanning the interval $44.3 - 803.4$ nm, the sample section was reduced to 8.0 nm^2. Note that such a reduction does not affect κ as shown in Fig. 4.3b.

Figure 4.4 shows $1/\kappa$ vs. $1/L_z$ for the $3:1$ and $5:1$ PRs. Both the linear (only first term of Eq. (2.39) is considered) and quadratic (both linear and quadratic terms of Eq. (2.39) are considered) extrapolations were tested. The results show that for this system the simple linear extrapolations fails in predicting κ_∞, with numerical uncertainties up to 90% which are in fact reduced by a quadratic fit down to ~ 10%. For this reason all the κ_∞ values collected in this section have been obtained by means of the quadratic extrapolation.

The resulting values for κ_∞ for the benchmark Ge/Si system are 5.44 ± 0.32 W $m^{-1}K^{-1}$ and 11.01 ± 0.32 W $m^{-1}K^{-1}$ for $3:1$ and $5:1$ PR, respectively. It is possible to conclude preliminarily that by reducing the relative thickness of the Si barrier the corresponding thermal conductivity of the SL is increased.

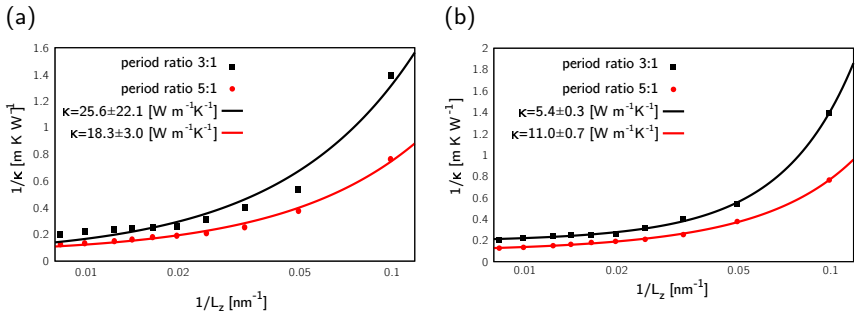

Figure 4.4. **a**: $1/\kappa$ vs. $1/L_z$ and the corresponding linear fit provided by Eq. (2.39) for a pure Ge/Si SL for the $3:1$ (black) and $5:1$ (red) PRs and $44.3 \leqslant L_z \leqslant 803.4$ nm **b**: Quadratic fit provided by Eq. (2.39) for the same set of data.

This is in good agreement with experimental results which provide $3 \leqslant \kappa \leqslant 5$ $Wm^{-1}K^{-1}$ for $1:1$ PR Ge/Si SLs [224].

4.1.4 *Thermal conductivity in Ge/Si_xGe_{1-x} superlattices*

Motivated by the experimental work of Ferre Llin et al. [225], Si_xGe_{1-x} barriers instead of pure Si layers were considered in order to explore both the role of the barrier stoichiometry and the PR.

Figure 4.5 shows $1/\kappa$ versus $1/L_z$ plot for Ge/Si_xGe_{1-x} SLs with $x = 10$, 20, 35, 50 and 70% for the $3:1$ (Fig. 4.5a) and $5:1$ (Fig. 4.5b) PR with L_z ranging from 44.7 to 269.1 nm. As previously described, κ_∞ was obtained via a quadratic extrapolation; the corresponding values are shown in Table 4.1. The value for $3:1$ PR and $x = 50\%$ is in rather good agreement with experimental value $\kappa = 5.1 \pm 0.4$ W $m^{-1}K^{-1}$ reported in reference [225]. This agreement stands for the overall quantitative reliability of the present investigation, as further confirmed by the case of bulk Ge where the experimental value of 59.5 W $m^{-1}K^{-1}$ [226] compares well with this prediction.

All the results are summarized in Fig. 4.6a where κ_∞ vs. stoichiometry is plotted for both $3:1$ and $5:1$ PR. Starting from pure Ge, a dramatic

	κ [W m^{-1} K^{-1}]	
Si%	3 : 1	5 : 1
0%	65 ± 6	
10%	17.4 ± 0.9	25.8 ± 0.8
20%	10.2 ± 0.3	15.9 ± 0.8
35%	7.2 ± 0.3	12.4 ± 0.4
50%	5.4 ± 0.1	8.7 ± 0.5
70%	4.0 ± 0.1	6.7 ± 0.3
100%	5.4 ± 0.3	11.0 ± 0.7

Table 4.1: κ_∞ quadratically extrapolated values for the Ge/Si_xGe_{1-x} SL with $x = 10$, 20, 35, 50 and 70% for the 3 : 1 and 5 : 1 PR.

decrease of κ by substituting Ge with $Si_{0.1}Ge_{0.9}$ alloy is observed. The overall κ further decreases by increasing the Si content, reaching a minimum value of 3.99 (6.69) W m^{-1}K^{-1} for 3 : 1 (5 : 1) PR. This confirms that as expected the alloy barrier acts as a strong scattering center for phonons in the SL. By increasing the stoichiometry up to 100% (pure Ge/Si SL) κ slightly increases up to 5.44 (11.01) for 3 : 1 (5 : 1) PR. This trend is similar to the one obtained for bulk Si_xGe_{1-x} alloy [103, 231], although in this case the effect is smaller (reflecting the fact that the alloy represent just a small portion of the SL).

The main result deduced from Fig. 4.6a is that the overall SL thermal conductivity can be reduced by a factor 4 by increasing the Si concentration from 10% to 70%. However, this factor could be hardly reflected in the overall ZT, since it has been shown that the electrical conductivity of the alloy decreases with increasing Si stoichiometry [232]. Therefore, in order to maximize ZT one should in principle find a compromise between the κ reduction due to the Si_xGe_{1-x} barrier and the corresponding σ reduction. Based on Fig. 4.6a and considering the values reported in literature, such an optimal concentration was identified as $10\% \leqslant x \leqslant 20\%$. This value guarantees a κ reduction with respect to pure Ge up to a factor of 6; moreover the intrinsic electrical conductivity and the electron mobility of the Si_xGe_{1-x} alloy is found to be

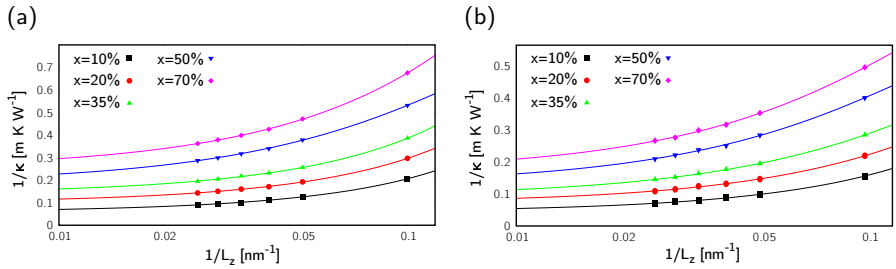

Figure 4.5. **a**: $1/\kappa$ vs. $1/L_z$ and the corresponding quadratic fit provided by Eq. (2.39) for a Ge/Si_xGe_{1-x} SL with $x = 10$, 20, 35, 50 and 70% with a $3:1$ PR. **b**: Same set of data obtained for a Ge/Si_xGe_{1-x} SL with $5:1$ PR. Both sets of a data are obtained for $44.7 \leqslant L_z \leqslant 269.1$ nm

only marginally affected at this concentration, as reported in reference [232]. This could represent an interesting point for a TE device based on Si_xGe_{1-x}. Furthermore, Si_xGe_{1-x} alloy with $x \sim 20\%$ shows the Seebeck coefficient and the power factor ($S^2\sigma$) almost unaffected by the presence of Si, with respect to pure Ge [225]. Figure 4.6a emphasizes also the role of PR: in fact by increasing it from $3:1$ up to $5:1$, i.e. increasing the Ge layer thickness from 3.39 to 5.66 nm, a κ increase of ~ 1.5 was observed, which slightly depends on the stoichiometry.

The role of the period ratio

Driven by these results also smaller values for PR, i.e. $2:1$ and $1:1$, were considered in order to understand how thermal conductivity is affected by further reducing the period ratio. For the reason described above, the investigation was limited to two cases, namely $x = 10\%$ and $x = 20\%$. The results are shown in Fig. 4.6b.

A non-monotonic trend with a minimum for $2:1$ PR corresponding to a Ge layer thickness of 2.26 nm is obtained. This minimum shows a further reduction in thermal conductivity of $\sim 30\%$: if this behavior would be reflected on electronic transport, then this should be the ideal configuration of Ge/Si_xGe_{1-x} SLs for TE applications.

By changing PR from $5:1$ to $2:1$, κ is overall reduced by a factor 2. This result is indeed very promising since, for these Si concentration, a small σ and S reduction is expected. The slight increase in thermal conductivity obtained by

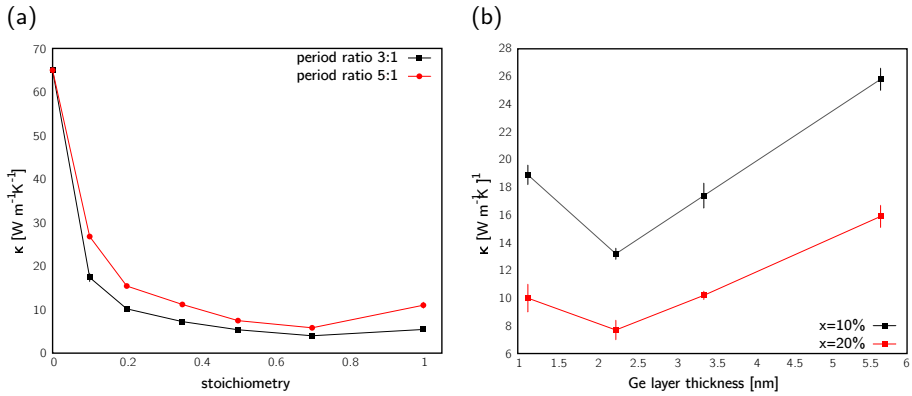

Figure 4.6. **a**: Extrapolated thermal conductivity values as a function of the Si_xGe_{1-x} barrier stoichiometry x for SL with $3:1$ (black squares) and $5:1$ (red dots) PR. **b**: Extrapolated thermal conductivity values for the $Ge/Si_{0.1}Ge_{0.9}$ (black squares) and $Ge/Si_{0.2}Ge_{0.8}$ (red dots) SLs as a function of Ge layer thickness.

further reducing the PR can be explained considering that probably the Ge layer thickness is under the limit of ballistic-like phonon transport, as extensively explained in references [23, 233]. By means of BTE, it has been shown that phonon thermal conductivity in SLs can be modeled by considering two distinct regimes: a wave-like and a ballistic-like one. The difference depends on the SL Ge layer thickness L_{Ge}: if L_{Ge} is greater than the minimum MFP (λ_{min}), then phonons are treated as particles; conversely, if $L_{Ge} < \lambda_{min}$, phonons show a wave-like nature. This could rise to interference phenomena between reflected and transmitted phonons at the interfaces between the SL layers, leading to an overall κ increase.

4.2 SILICON-GERMANIUM INTERFACES

The prediction of the thermal transport properties of a bulk semiconductor material (where the main heat carriers are phonons or, more generally, vibrational modes) usually proceeds through the calculation of its *thermal resistivity* $\mathcal{R}$

(or, equivalently, its inverse quantity κ, namely the thermal conductivity) [234, 235]. While the most fundamental theory to accomplish this task is provided by the BTE [46, 236] (which is now numerically solvable either in the usual single-mode relaxation-time approximation [46, 72] or even exactly [47, 48, 237]), MD simulations [238] represent in fact the most popular tool for computing the thermal transport coefficients, due to their versatility, ease of implementation and comparatively small computational effort. The resistivity is typically evaluated by assuming the Fourier law $\partial T/\partial z = -\mathcal{R}J$ (see also Eq. (2.8)) and by explicitly computing the heat flux J and the temperature gradient $\partial T/\partial z$ in a steady-state condition of thermal transport (for further convenience it is worth remarking that for a sample with total thickness L_z and cross section S the bulk thermal resistance is defined as $R = \mathcal{R}L_z/S$). This approach is largely exploited by non equilibrium MD (NEMD, see Sec. 2.2.2) [105, 239]. Alternatively, the thermal diffusivity $\bar{\kappa} = \kappa/\rho\mathcal{C}_v$ (where ρ and $\mathcal{C}_v$ are the system mass density and specific heat, respectively) is evaluated during the system approach to equilibrium (AEMD, see Sec. 2.2.3) [98]. Finally, equilibrium statistical mechanics offers a direct way to compute thermal conductivity through the general Green-Kubo theory of transport coefficients (EMD, see Sec .2.2.1) [75, 105]. Overall, this panoply of methods allows for computing, in a large variety of (in principle) equivalent ways, the thermal transport coefficients as function of temperature, atomic structure, defect-induced disorder, or chemical composition, thus providing a full characterization of materials thermal properties. It is also possible to include as well quantum features [240–242] if the system is simulated well below its Debye temperature. However, concerns have been raised about the actual reliability of the proposed methods [243].

Heat transport across an interface

The case of heat transport across an interface is intriguingly different and much more subtle [57, 58, 244, 245]. Here a temperature gradient is applied across a HT between two semiconductors which behave differently as for their heat transport properties. Because of this and of interface-specific properties, across the interface region a sudden temperature drop ΔT occurs, giving rise to a TBR R^{TBR} which is phenomenologically described as $R^{TBR} = \Delta T/J$, assuming a steady-state condition. This phenomenon is nowadays widely referred to as Kapitza resistance [58, 244–246], although this expression originally referred to the thermal resistance occurring at the interface when heat flows from a solid into a liquid. While casting the problem in this way could seem

straightforward, actually there are a number of subtleties indeed requiring a deeper understanding, which basically defines the main goal of this section (incidentally, it is worth warning against a widely common abuse of notation: while using the same term "resistance" for both the bulk and interface case, the two quantities have in fact different units: K/W and Km^2/W, respectively).

The role of the interfaces

This issue is a really key feature in nanoscience. In fact, interfaces are everywhere at the scale where most of the present-day semiconductor technology deploys: their role can hardly be underestimated since the fabrication methods of the electronics industry are continuously refined to produce ever smaller devices in the nm size range. In this context, therefore, atomically well-defined interfaces represent the most important structural feature affecting the transfer of energy through thermal exchange. So, the heat flux across interfaces plays a vital role in many front-end applications, including electronics (cooling of nanodevices and optimal control of their thermal budget) [12, 247], information technology (phononics) [248, 249] and energy harvesting/production (superlattices for TE conversion) [19, 20, 103, 225, 250, 251]. In conclusion, exploring heat-related phenomena occurring at semiconductor interfaces will facilitate the precise control of their properties and, ultimately, their best-tailored processing for applications in the above technologies.

Acoustic and Diffuse mismatch models

While the above scenario stands for the need of a detailed understanding of interface thermal properties (possibly including thermal rectification phenomena, as well [252–255]), the theoretical and conceptual paraphernalia usually underlying direct calculations of the TBR is somewhat oversimplified, if not even rudimentary. The most commonly used theory frames, namely the AMM [58, 256] and DMM [58, 257], in fact neglect the actual atomic-scale structure of the interface and also estimate, under the Debye approximation, the phonon dispersion branches as linear. They further assume that the phonon interface scattering is purely elastic, either if it is guessed to be diffusive (DMM) or specular (AMM). None of the assumptions is completely fulfilled by real HT and, therefore, these models fail in predicting quantitatively the TBR in most cases. Occasionally, improved versions of AMM and DMM have been conceived [258–260], including some of the features neglected in the original models, but no major step forward in understanding the underlying physics was reached without including an all-atom treatment of the interface.

A rather different approach is based on lattice dynamics calculations of TBR, where either the spectral density of phonon transmitted across the interface is computed [261] or the phonon interface scattering is calculated directly (see, e.g. Ref. [262] and references therein). This is typically done under the assumption of elastic scattering (i.e. anharmonicities are disregarded) and neglecting the actual junction width. This amounts to approximate the TBR as a "junction thermal resistance"and, therefore, both the left and right material segments emit phonons to the junction, as well as they absorb phonons from it. A corresponding net heat flux can be calculated by following a Landauer-like approach, either by assuming that the phonon distributions are equilibrium (i.e. Bose-Einstein) ones or by assuming non-equilibrium (but bulk-like) expressions for them. Although more fundamental and superior than AMM and DMM (for instance, it directly accounts for quantum effects in the phonon population), even this approach does not provide a satisfactory quantitative prediction of TBR, as found by confronting its predictions for a symmetrically strained Si/Ge interface to the results of a MD simulation with no guess about the phonon scattering events [262]. In addition, in case of non-abrupt interfaces the assumption of specular scattering is questionable. More recently, an anharmonic non-equilibrium Green function approach was developed; this approach overcomes most of the above limitations, but it has been applied to single-molecule junction rather than to solid-solid interfaces [263].

Lattice Dynamics calculations

A third and last approach is entirely based on MD simulations, making no direct use of the phonon language, i.e. not requiring any explicit calculation of phonon frequencies, populations, scattering rates or lifetimes. Basically, the TBR of the HT of interest is described as a series of thermal resistances, corresponding to two materials leads A and B embedding an interface layer, whose morphology is fully defined by the sample preparation stage [214, 264, 265]. The resulting TBR is therefore written as $R^{TBR} = \mathcal{N}[L_z/\kappa^{HT} - l_A/\kappa^A(l_A) - l_B/\kappa^B(l_B)]$, where κ^{HT} is the overall thermal conductivity of the HT of total thickness L_z, while $\kappa^{A,B}(L_{A,B})$ are the thermal conductivities of the leads at their actual thickness $l_{A,B}$. The factor $\mathcal{N} = 1$ or $1/2$ reflects, respectively, the fact that the HT is non-periodic or, rather that periodic conditions are imposed along the z direction. While this approach makes no *a priori* assumptions about the behavior of phonons, it is affected by finite-size effects similar to those ones found in any EMD, NEMD or AEMD

Molecular Dynamics simulations

calculation of transport coefficients [75, 97, 98, 105]. As a matter of fact, a set of three different calculations is required, namely the $\mathfrak{l}$-dependent conductivities of the two materials forming the leads, as well as the overall thermal conductivity of the simulated sample. This could likely result into a heavy computational effort. In any case, the estimated value of TBR actually depends on L_z and, therefore, different calculations must be repeated for increasing L_z so as to properly extrapolate the TBR value for two semi-infinite leads as, outlined, for instance, in Ref. [264]. Furthermore, in some instances the application of the NEMD protocol is problematic because it does not provide a sizable ΔT at the interface from which to compute TBR. In these cases, AEMD has proven to be a valuable alternative [101].

In this section, an alternative formulation of the TBR problem is illustrated, based on the non-equilibrium thermodynamics of transport phenomena as for its theoretical formulation, and non-equilibrium MD as for its actual implementation. This approach combines at best the merits of a general theory to a robust numerical tool which, albeit operating at the true atomic scale, does not require any simplifying assumption about the interface morphology nor about the physics of the scattering of the thermal energy carriers at such boundary. The method also presents a practical advantage, reducing the computational effort.

4.2.1 *Non-equilibrium thermodynamics theory for TBR*

In order to properly define the conceptual framework for a predictive thermodynamical theory of heat transport across an interface, it is useful to consider at first a homogeneous system (not containing any interface), subject to a temperature gradient. It is assumed that no mass or charge transport phenomena occur, as well as chemical reactions, without any loss of generality since the focus is on pure heat transport in solid semiconductor materials. If such a homogeneous system is in a steady-state condition of thermal transport and a linear response regime is assumed, then local equilibrium holds anywhere and, therefore, all thermodynamics equations can be cast in local form and all relevant quantities can be given in units of volume (i.e. as a density). By selecting a volume region in the system, the corresponding change of entropy

Entropy continuity equation

density $\partial s/\partial t$ is given by the sum of the net flow of entropy J_s in and out that volume element and an entropy production term σ provided by any possible source inside the same volume (entropy continuity equation)

$$\frac{\partial s}{\partial t} = -\frac{\partial J_s}{\partial z} + \sigma \tag{4.3}$$

The rate of generation σ is usually expressed in the Onsager form $\sigma = \sum_i J_i X_i$ [266], i.e. as a sum of products between the i-th flux J_i and the corresponding generalized force X_i. Here the index i spans the different transport mechanisms occurring in the system. By using the Gibbs equation $du = T ds$ (where u is the internal energy density and a constant-volume situation is depicted) and the energy balance equation $\partial u/\partial t = -\partial J/\partial z$, Eq. (4.3) is easily transformed into

$$\frac{\partial s}{\partial t} = -\frac{\partial}{\partial z}\left(\frac{J}{T}\right) + J\frac{\partial}{\partial z}\left(\frac{1}{T}\right) \tag{4.4}$$

where T is the temperature. By comparing Eqs. (4.3) and (4.4), the entropy density production term for the case here considered can be immediately identified (no mass or charge transport), as given by the product between the heat flux J and its generalized force $X = \partial(1/T)/\partial z$. Such a force, in principle, is a linear combination of all fluxes J_i occurring in the system. However, in the present case it results $X = \sum_i r_i J_i = rJ$ since, as assumed, no transport phenomena other than the heat current are present. The r_i terms are called Onsager resistivity coefficients: in this context they describe all transport mechanisms and, in particular, r is ascribed to pure heat conduction (in other words, that the non-diagonal resistivity terms r_i would describe the possible coupling of heat to charge and mass transport and, therefore, they are null due to the present assumptions). By inserting in the flux-force equation the explicit form of the generalized force provided by Eq.(4.4), the key result is obtained

$$\frac{\partial}{\partial z}\left(\frac{1}{T}\right) = rJ \tag{4.5}$$

where it is shown by very general arguments that the actual thermodynamic driving force for thermal transport is the gradient of an inverse temperature

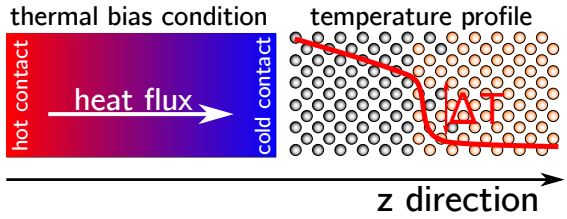

Figure 4.7. Schematic illustration of the appearance of TBR at an interface across which a temperature gradient is established. This cartoon conceptualizes a steady-state condition and, therefore, the temperature profile $T(z)$ far away the interface region is linear (with different slopes at left and right, mimicking an heterojunction between two materials with unlike thermal properties).

[267]. Although somewhat surprising, this result is consistent with the Fourier equation $\partial T/\partial z = -\mathcal{R} J_z$ (normally used in predicting thermal transport features in homogeneous materials) by simply developing the z-derivative of the inverse temperature and obtaining $\partial T/\partial z = -T^2 r J$. This unveils the link between the Onsager r and the ordinary $\mathcal{R}$ thermal resistivity, namely $T^2 r = \mathcal{R}$.

The case of an interface

The application of the above theory to the case of an interface is not trivial, since the system is no longer homogeneous (see Fig. 4.7).

In the following, the prototypical situation of two semi-infinite material leads meeting at a nominal interface will be considered. By selecting any suitable property $P(z)$ having two different values in the bulk-like regions far away from the interface, it is possible to draw its variation along the direction normal to it, as shown in Fig. 4.8, top. This will clearly identify both the left and right interface boundaries (and, therefore, the actual thickness of the interface region) once that it is assumed to define such an interface as that region where $P(z)$ differs from the pure material values (respectively: $P_{\mathtt{left}}$ and $P_{\mathtt{right}}$) by some arbitrary amount. This procedure is named the *Gibbs construction* [266]. For instance, in the case of an interface between two lattice mismatched semiconductors $P(z)$ could be the interplanar lattice constant along z. Alternatively, $P(z)$ could represent the actual content of a dopant, or a given chemical species, or any other structural defect. For a

The Gibbs construction

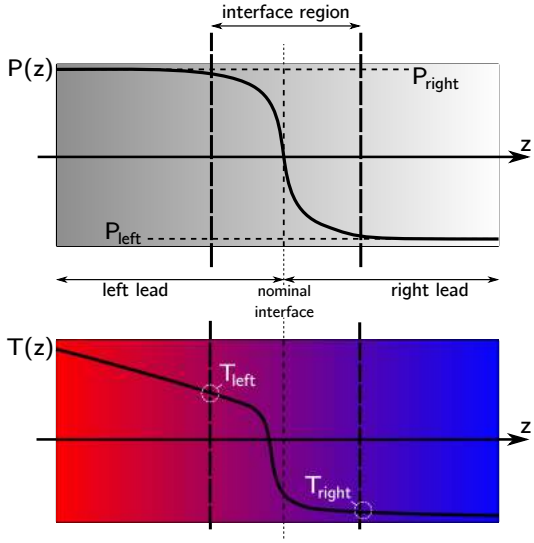

Figure 4.8. Top: Gibbs construction for the definition of the interface; the grey shading mimics the variation of a suitable property $P(z)$ along the growth direction of an HT between unlike leads (where it has values P_{left} and P_{right}, respectively). Bottom: temperature profile $T(z)$ in a steady-state of thermal conduction; the color shading indicates the applied thermal gradients (red: hot region; blue: cold region).

crystalline/amorphous interface $P(z)$ could, finally, represent the local average atomic coordination. As schematically shown in Fig. 4.8, while the $P(z)$ is normally well behaved in the Gibbs interface region, there is in principle no reason for such portion being symmetrically extended into the two facing leads nor to be centered at their nominal interface. The Gibbs construction, therefore, provides a robust definition of the interface which is treated as an *autonomous thermodynamical system* [49,51].

Applying a temperature gradient along z and plotting the temperature profile $T(z)$ once the steady-state regime has been reached, a situation similar to what is pictured in Fig. 4.8 (bottom) is obtained. This figure directly defines

three relevant temperatures in this problem, namely the left T_{left} and right T_{right} temperatures just at the boundaries of the interface region, as well as the interface temperature T_s , defined as the average value in the same volume. This is a quantity easy to compute within a MD simulation using the kinetic energy of the atoms placed in the interface region.

Once that the interface is identified, Eq. (4.3) is recast in the form

$$\frac{\partial s^{int}}{\partial t} = -(J_{s,left} - J_{s,right}) + \sigma^{int} \tag{4.6}$$

where the superscript int indicates an interface quantity, while $J_{s,left}$ and $J_{s,right}$ are the entropy density flux through the left and right boundary of the interface, respectively. By developing the same algebra as in the previous section and exploiting the fact that a steady-state condition of thermal transport is considered, the entropy density production term σ^{int} for the interface reads as

$$\sigma^{int} = J\left(\frac{1}{T_s} - \frac{1}{T_{left}}\right) + J\left(\frac{1}{T_{right}} - \frac{1}{T_s}\right) \tag{4.7}$$

This result is quite interesting since it shows that two different flux-force equations are indeed necessary to correctly describe the interface problem, namely

$$\left(\frac{1}{T_s} - \frac{1}{T_{left}}\right) = r^{left} J \quad , \quad \left(\frac{1}{T_{right}} - \frac{1}{T_s}\right) = r^{right} J \tag{4.8}$$

each one defining its own Onsager resistivity coefficient. Therefore, the total TBR R^{TBR} is in fact a *series of two Onsager resistances*

$$R^{TBR} = T_s^2\left(r^{left} + r^{right}\right) = T_s^2 \frac{1}{J}\left(\frac{1}{T_{right}} - \frac{1}{T_{left}}\right) \tag{4.9}$$

This approach is very clean and robust, since: (i) it is based on very general and elegant thermodynamical arguments; (ii) it does not imply any guess or assumption or approximation about the atomic-scale mechanisms ruling over the thermal energy exchange at the interface; (iii) it does not rely on such a concept as phonon, which only stems from crystals, and therefore can deal with systems lacking of order; (iv) it allows, through the Gibbs construction,

to unambiguously define where the interface indeed occurs and how large it is.

It is worth clarifying the relationship between the standard definition of Kapitza resistance $R^{TBR}_{Kapitza} = (T_{left} - T_{right})/J$ given in the introduction of Sec. 4.2 and the corresponding Onsager definition R^{TBR} provided by the above development. As a matter of fact, Eq. (4.9) can be recast in the form

Relationship with the Kapitza resistance

$$R^{TBR} = R^{TBR}_{Kapitza} \frac{T_s^2}{T_{left} T_{right}} \tag{4.10}$$

where it is clearly shown that the two definitions only differ by the term $T_s^2/T_{left}T_{right}$. It is now convenient to distinguish between the opposite cases of thick and thin interface. When the interface has a non-vanishing width, like in the case of a rough boundary or when interdiffusion of some chemical species indeed occurs, the ratio $T_s^2/T_{left}T_{right}$ may be significantly different from unity since, as explained above, T_s is evaluated through the average kinetic energy of the entire boundary region. Also, if the interface is large enough it could possibly host an additional heat source or a sink, which contributes to the actual value of T_s (definitely no longer related to T_{left} or T_{right} in this configuration). The case of a sharp interface is more subtle. For an infinitesimally thin boundary, it can be assumed with no loss of generality that

$$T_{left} = T_s + \Delta T_{left} \quad \text{and} \quad T_{right} = T_s - \Delta T_{right} \tag{4.11}$$

so that

$$\Delta T = T_{left} - T_{right} = \Delta T_{left} + \Delta T_{right} \tag{4.12}$$

According to Eq. (4.11)

$$T_{right}T_{left} = T_s^2 + T_s(\Delta T_{left} - \Delta T_{right}) - \Delta T_{left}\Delta T_{right} \tag{4.13}$$

and therefore

$$\frac{T_s^2}{T_{left}T_{right}} = \left(1 + \frac{\Delta T_{left} - \Delta T_{right}}{T_s} - \frac{\Delta T_{left}\Delta T_{right}}{T_s^2}\right)^{-1} \sim 1 + \mathcal{O}\left(\frac{\Delta T}{T_s}\right)$$

(4.14)

Equation (4.14) indicates that even in the case of a sharp interface, the factor $T_s^2/T_{left}T_{right}$ is not unity when ΔT is an appreciable fraction of the interface temperature, which in turn falls between T_{left} and T_{right}.

4.2.2 *Addressing TBR through computer experiments*

The numerical implementation of the procedure described in the previous section basically requires a threefold task: (i) the Gibbs construction for the interface; (ii) the set up of a steady state of thermal conduction; and (iii) the evaluation of heat flux in this condition.

The first task is really straightforward and simply requires the calculation of the property $P(z)$. Likely, such a selected property is a structural one and this simply implies that some care must be devoted in preparing the computational sample in a fully relaxed configuration prior to any further calculation.

As for the setting up of a steady-state thermal transport condition, it can be generated by adopting the NEMD framework (see Sec.2.2.2), i.e. by adopting the left and right terminal ends of the system to two heat reservoirs set at different temperatures [75, 105, 214]. By MD simulation, the system is so aged for a long enough time to reach the steady state which is assessed by a constant-in-time temperature profile (see Fig. 4.8, bottom). However, the fact that some details of the profile established across the simulated sample slightly depend on the kind of heat bath used: this, in principle, could somewhat affect the estimation of the temperature drop at the interface (and, therefore, the estimation of T_{left} , T_{right}, and T_s). In general, Langevin thermostatting is recommended since it provides more consistent results with experiments for a large set of simulation parameters [268].

Calculating the heat current

The calculation of the heat current vector is not at all a trivial matter. J is needed in Eq. (4.9) and it is defined, likewise the definition given in Sec.2.2.1, as $J \equiv d/dt(\sum_i \mathbf{r}_i E_i)$, where $\mathbf{r}_i$ is the position i-th and E_i its energy. By using empirical potentials, it is possible to elaborate non equivalent heat current formulas for the same many-body force field, because of the ambiguity in defining the onsite energy E_i . This problem has been recently solved [86] by working out a general pairwise force expression valid for any potential,

which avoids the partition of the potential itself into arbitrary single-particle contributions. The same difficulty in uniquely decomposing an ab initio total energy functional (as typically provided by density functional theory) into individual contributions from each atom is usually reported; however, such a misconception has been eventually clarified and a computable expression of the heat current is now available for ab initio MD calculations [91] as well. A different solution to this problem [214, 269] consists in calculating instead the work W^{hot} and W^{cold} spent by the hot and cold thermostat, respectively, and evaluating the corresponding heat fluxes as $J^{\mathrm{hot,cold}} = (1/S)(\partial W^{\mathrm{hot,cold}}/\partial t)$ (see Sec. 2.2.2), where S is the cross section of the simulated sample. The steady-state condition is now proclaimed when $J^{\mathrm{hot}} = J^{\mathrm{cold}}$ within the accepted numerical error. In this way, there is no need to make use of any atomic-scale formulation for the heat current, which is always preferable.

Whatever solution is adopted to calculate the key ingredients of Eq. (4.9), as many as $\mathcal{O}(10^6)$ MD steps could be needed for reaching the through steady-state condition [214, 269]. Therefore, the direct calculation of R^{TBR} by means of non-equilibrium thermodynamics, while simple in principle, is made non trivial by such a heavy computational demand. Nevertheless, the method outlined previously offers the advantage of requiring the calculation of the relevant quantities just for the HT system, without need to calculate the corresponding properties for the two leads. This translates into a dramatic reduction in the overall computational workload as compared, for instance, to the method based on the treatment of the TBR problem as a series of thermal resistances.

4.2.3 *TBR at the Si/Ge interface*

Thermal transport across Si/Ge HT can be tailored by engineering their superperiodicity [270], as well as the stoichiometry of the barrier layers [200, 271]. As stated earlier in this chapter, while high-frequency phonons are efficiently scattered by Si-Ge alloying, mid- and low-frequency ones are affected by a suitable distribution of Si/Ge interfaces. Overall, this state of affairs makes SiGe superlattices systems with tunable thermal conductivity, a feature useful for the design of TE generators [225, 250, 251] or nanocooling in Si-based

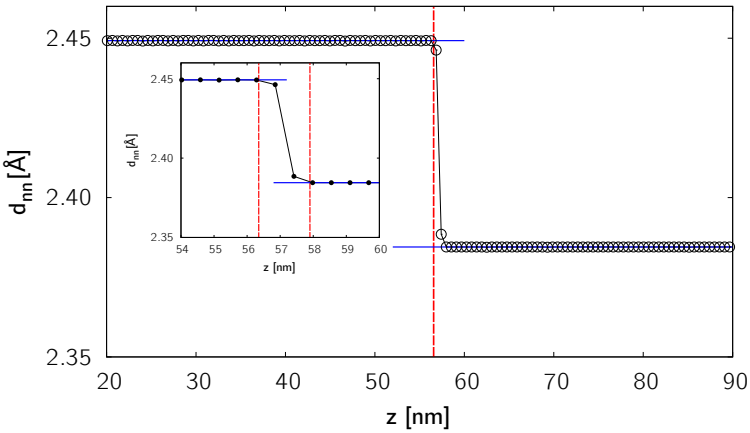

Figure 4.9. The Gibbs construction for an interface between Ge (left) and pseudomorphic Si (right): the nearest neighbors distance d_{nn} is calculated along the growth direction z. The nominal position of the interface (corresponding to the chemical discontinuity) is marked by a vertical red line at $z = 56.567$ nm. The inset provides a magnified view of the interface region, represented as a red shaded area, whose left (at $z = 56.3$ nm) and right (at $z = 58.0$ nm) boundaries are marked by two parallel red lines.

devices [12, 247]. The thermal resistance at the Si/Ge interface represents in this framework the key feature, which is here addressed in order to show the potential of the theory outlined in the previous section in a case of great practical interest. In Fig. 4.9, is reported the Gibbs construction for a planar Si/Ge abrupt interface. Inspired by an experimental work [225], the growth of a (001)-oriented Si/Ge HT on crystalline Ge was modeled; therefore, the in-plane lattice constant was set at $a_0^{Ge} = 5.6567$ Å, namely the bulk-like value predicted for Ge by the adopted Tersoff force field [89]. The cross section of the sample was $5a_0 \times 5a_0$. The Si slab is modeled according to the pseudomorphic growth, meaning that its interplanar spacing is given by Eq. (4.2). After a careful conjugated gradient structural relaxation, the resulting sample length was 108.48 nm. For this configuration, the nearest neighbors distance d_{nn} was calculated along the z direction as an average taken over a passing window as wide as a_0^{Ge}, corresponding for the present case to the property

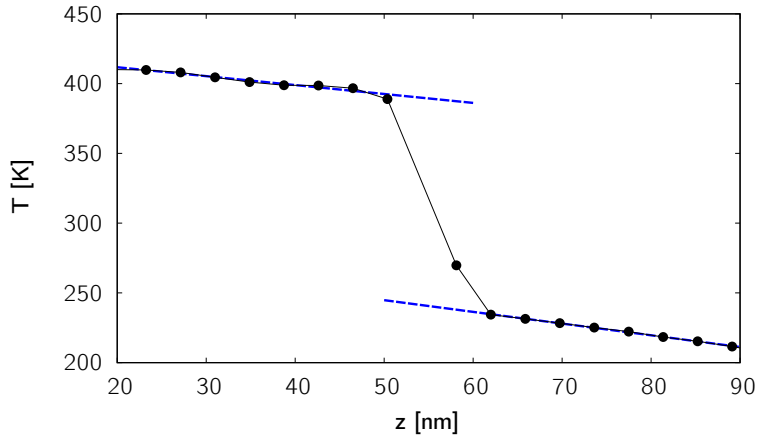

Figure 4.10. Temperature profile calculated for an interface between Ge (left) and pseudomorphic Si (right) in a steady-state condition of thermal transport (the hot and cold thermostats are placed at the Ge and Si ends, respectively, and are set at a nominal $\Delta T = 300K$).

$P(z)$ discussed previously. Far away from the nominal (or, equivalently, chemical) interface, d_{nn} recovers the Ge (left) and p-Si (right) bulk-like values, as expected, while the central segment where such a distance deviated by more than two standard deviations from the reference values was selected as the interface region. This procedure proves that the interface, while chemically abrupt, has in fact a finite thickness of about 17 Å; interestingly enough, it is also observed that the interface region is not symmetrically spread in the two facing leads but, rather, it is almost entirely hosted by the Si one. This is a system where *the chemical interface does not necessarily overlap the thermodynamical one*, as anticipated above. All data needed for computing the TBR are contained in Fig. 4.10 where the corresponding temperature profile is shown, as calculated during a NEMD simulation lasted for 5 ns (the first 2 ns are used to set up the steady-state condition). In particular, the numbers are $T_{left} = 296.8$ K, $T_{right} = 271.7$ K, and $T_s = 284.3$ K; the calculated stationary heat current is $J = 8.32$ GW/m^2 for a nominal temperature offset of 300 K between the hot (Ge side) and cold (Si side) thermostats. Overall, through Eq. (4.9), they provide $R^{TBR} = 3.02$ m^{2}K/GW. This result is nicely consis-

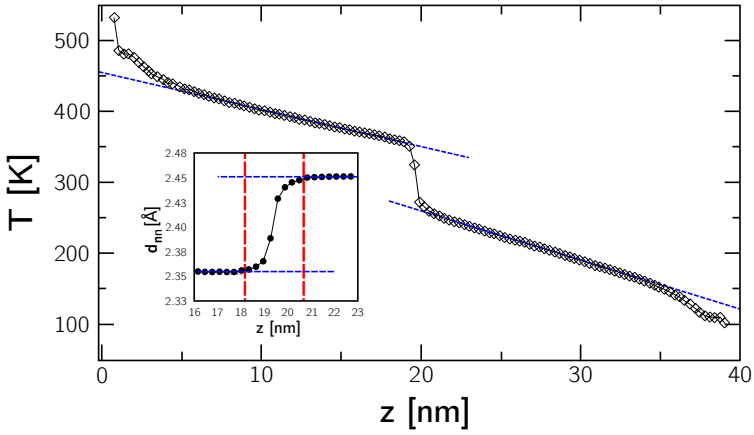

Figure 4.11. Temperature profile calculated for an interface between Ge (left) and pseudomorphic Si (right) in a steady-state condition of thermal transport (the hot and cold thermostats are placed at the Ge and Si ends, respectively, and are set at a nominal $\Delta T = 300K$).

tent with previous calculations [262, 264] based on the more conventional NEMD prediction performed with the same interatomic potential, although in somewhat different structural conditions (in Ref. [43] symmetrically strained interfaces were considered, while in Ref. [262] no interface relaxation was allowed, while clamping atomic planes at the position predicted by continuum elasticity for a pseudomorphic configuration).

The Gibbs construction in a Si/Ge nanowire

The application of the Gibbs construction and the corresponding calculation of the TBR is very robust, since it does not depend on the actual structure of the investigated systems, nor on the thermal bias conditions. In order to prove this, a Si/Ge interface is realized in a nanowire with total length of 40 nm and diameter of 5 nm, where the hot and cold thermostats are coupled to the Si and Ge end, respectively. The nominal temperature offset is now larger, i.e. 400 K. The NW system, at variance with the previous bulk-like interface, can laterally accommodate the lattice mismatch between the component materials and, therefore, a situation inherently different than the pseudmorphic one is here experienced.

Figure 4.11 summarises both the Gibbs construction (see inset) and the resulting temperature profile in the steady state. The resulting TBR is now $R^{TBR} = 2.55$ m^{2}K/GW. The difference with respect to the bulk-like case is easily accounted for by considering that the interface temperature T_s is 284.3 K and 323.4 K for the bulk-like and nanowire system, respectively. The key point here is that, thanks to the Gibbs construction above, the interface corresponds to an autonomous thermodynamical system; therefore, its thermal resistance can be treated as a system variable, only depending upon the interface temperature T_s (calculated, once again, through the Gibbs construction). In other words, as discussed in [272], T_s in fact represents a tunable interface property suitable to fully engineer the thermal resistance at a Si/Ge boundary. Interface alloying, here not considered, provides an additional tool [200, 214, 264].

The present formulation draws a direct link between the Onsager and the phenomenological resistivity and allows to attribute to the interface region its own temperature, making in fact such an interface an autonomous thermodynamical system according to non-equilibrium thermodynamics. While here not addressed, this issue could be important when studying heat transport across an interface in a non-stationary regime and/or for assessing the dependence of boundary resistance upon the local temperature at the interface.

5

SILICON GRADED SYSTEMS

In this chapter, the concept of thermal rectification is explored for bulk-like systems. In particular, by NEMD simulations, the thermal rectification factor R in Si bulk structures containing a gradual distribution of compositional or structural defects is addressed. The reason to select Si for the present investigation is twofold, namely, (i) it has an impact on the emerging phononic nanotechnology quoted above and (ii) it has very well-known thermal properties.

5.1 THERMAL RECTIFICATION IN GRADED SYSTEMS

Thermal rectification [253–255] occurs whenever the heat flux is affected by the actual direction of the thermal gradient applied to the system. The amount of rectification of the heat current is usually quantified by the factor

$$\mathrm{R} = |\mathbf{J}_{\mathrm{fwd}}|/|\mathbf{J}_{\mathrm{rev}}| - 1 \tag{5.1}$$

where $\mathbf{J}_{\mathrm{fwd}}$ and $\mathbf{J}_{\mathrm{rev}}$ are the heat fluxes corresponding to the forward and reverse thermal bias conditions, respectively. The situation is conceptualized for the prototypical configuration corresponding to an interface between two materials A and B. In Fig. 5.1, it is assumed that $\mathbf{J}_{\mathrm{fwd}} > \mathbf{J}_{\mathrm{rev}}$, but the definition of "forward" or "reverse" bias condition is only a matter of convention. While the thermal rectification has been first observed experimentally long ago [273], recently it started attracting an increasing interest since it is a key feature in the emerging nanotechnology referred to as phononics [245, 248, 249]. Here, the generation, control, and manipulation of lattice heat (or, equivalently, phonon flux) are the main tools to engineer devices with functionality similar to their electronic counterparts (like electrical diodes or transistors). As explained in the previous chapter, in most cases of practical interest [245],

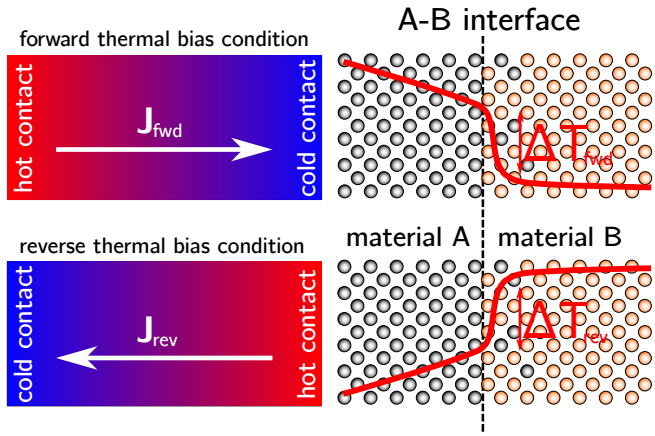

Figure 5.1. Left: schematic representation of the "forward"and "reverse"thermal bias conditions. Rectification occurs whenever $\mathbf{J}_{\mathrm{fwd}} \neq \mathbf{J}_{\mathrm{rev}}$. Right: zoomed interface region where the temperature drop ΔT occurs (full red line), generating localized thermal resistance.

Avoiding interfaces

thermal rectification is observed when two materials with unlike thermal conduction properties are interfaced, as indeed shown in Fig. 5.1. In this configuration, the role played by the sharp interface is crucial: here a temperature drop $\Delta \mathrm{T}_{\mathrm{fwd,rev}}$ occurs in whatever bias condition, giving rise to an interface thermal resistance (ITR) quantified by the ratio $|\Delta \mathrm{T}_{\mathrm{fwd,rev}}|/|\mathbf{J}_{\mathrm{fwd,rev}}|$ as extensively discussed in Refs. [254], [255], and [58]. While ITR is largely referred to in semiconductor systems, also interfacial hybrid systems like metal/superconductor [274] or crystal/polymer [275] junctions have been shown to provide thermal rectification. However, the actual rectifying properties of an interface are affected by many features (structural details, chemical contamination, and interdiffusion to name just a few) which require nontrivial nanofabrication techniques for their government, possibly resulting in a rather difficult technological task to be accomplished.

This scenario suggests that it would be interesting to observe thermal rectification without any localized (i.e., abrupt) temperature drop. This basically requires that such a sharp interface is not present in the rectifying device. In this regard, low-dimensional systems (either model or realistic) prompt several

possible rectifying configurations, such as non-uniform mass loading, suited distributions of defects, and tailored shaping [214, 265, 269, 276–283], where the above combination is actually realized.

5.1.1 *Generating the graded structures*

The NEMD simulations have been performed on the Si tetragonal cells with section $S = (n \times n)a_0^2$ (with $n = 10$ or 13 as indicated below) normal to the (001) direction of heat transport (hereafter named z) and a total length L_z varying in the range of $100 - 350a_0$ (as indicated below). At the left and right extrema of such a simulation cell, two further slabs of thickness $10a_0$ were added and coupled to thermostats (according to th extensively NEMD configuration, Sec.2.2.2). Periodic boundary conditions have been applied along the two directions normal to z. Lattice constant was set to $a_0 = 5.4305$ Å as predicted by the Tersoff potential providing the force field for the present investigation [89]. The simulation cells have been at first filled by a diamond lattice of silicon atoms. Then, a nonuniform dispersion of defects was obtained: (i) by randomly replacing Si atoms with Ge ones, up to a 20% of Ge content, which is the minimum doping corresponding to the maximum reduction of lattice thermal conductivity in a SiGe alloy [103, 231] or (ii) by removing clusters of Si atoms so as to create voids with a random position, size, and shape up to a maximum 31% porosity. In any case, the two thermostatted slabs were not affected by Si→Ge replacements or void generation. This procedure generated a defect distribution characterized by different concentration profiles along the z direction, as shown in Fig. 5.2 (where the thermostatted slabs are not shown for the sake of clarity).

A structural relaxation followed, respectively, (i) through a careful energy minimization by conjugate gradients or (ii) through a high-temperature simulated annealing at 900 K. The latter procedure (implemented over 5×10^5 time step of duration 0.5×10^{-15} s) was indeed required in order to allow for the full reconstruction of dangling bonds created by atom removals. In turn, the reconstruction generates a shell of amorphous matter at the void surface, providing an important source of phonon scattering in nanoporous Si [102] (see also Sec. 3.1). In the case of a SiGe graded alloy, care was also taken of

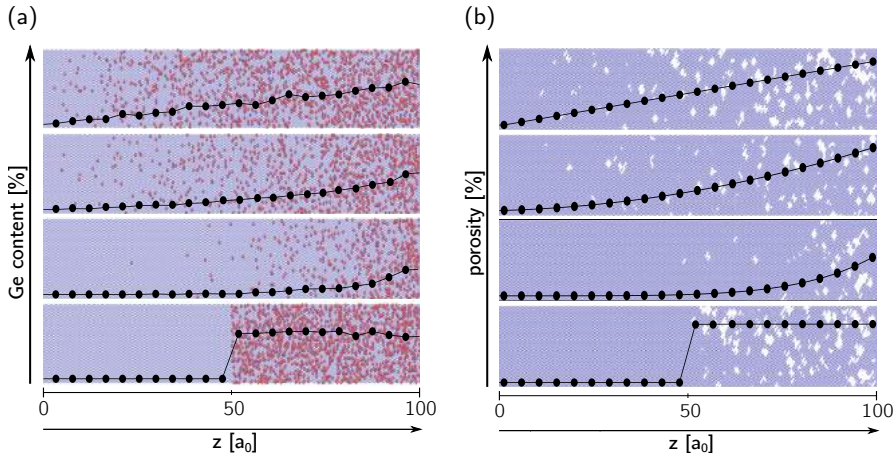

Figure 5.2. **a**: Graded distribution of substitutional Ge defects in a Si lattice. **b**: Graded distribution of pores in a Si lattice. From top to bottom, it is shown a linear, quadratic, exponential, and step-like distribution of defects. Their average concentration is shown by a black dots. Pictures show a $4a_0$-thick longitudinal (xy-plane) section of each sample.

any possible structural relaxation along the z direction due to the Si-Ge lattice mismatch by further performing constant pressure, constant-temperature MD simulations as long as 5×10^5 time steps, each lasting 1.5×10^{-15} s. Since just a very minor variation of the cell length was observed and, in any case, no detectable effect in the calculation of the heat flux (see below), the result here presented are obtained with constant-volume cells. To this aim, fixed boundary conditions were imposed along z by adding one more plane on both sides where atomic positions have been clamped anytime during the simulations. Finally, for the sake of comparison in both cases, it has generated a sharp interface between pure Si and, respectively, a homogeneous SiGe alloy with a 20% of Ge content or a nanoporous Si sample with 31% porosity.

The steady-state

The desired steady state condition where to investigate possible rectification effects was generated (according to the procedure explained in Sec. 2.2.2) in each system by coupling its left and right $10a_0$-thick terminal slabs (see above) to a heat reservoir, respectively, set at $T_h = 700$ K and $T_c = 500$ K

by using Nose-Hoover thermostats. These temperature values guarantee that most part of the system stays above the Si Debye temperature and, therefore, quantum effects play a very minor role. While the initial temperature of each sample was set at the average $(T_h + T_c)/2$ value, the MD simulation was aged until a steady state regime was reached for the selected thermal bias condition (assigned by the relative position of the hot and cold thermostats). Given the very small resulting thermal conductivity, this required as many 3×10^6 or 7×10^6 time steps of MD for the Ge-doped and nanoporous structures, respectively. The simulation was run for further 1×10^6 or 3×10^6, according to the system, in the steady state condition in order to calculate heat fluxes coming out and going in the hot and cold thermostat. By inverting the two thermostats and repeating the calculation, the other heat flux was similarly calculated and, according to Eq. (5.1), the rectification R was eventually obtained. In all samples investigated here, "forward" was the bias condition where the pure silicon part of the system (i.e., the left end in Fig. 5.2), all panels) was set at T_h. All simulations have been executed by using the LAMMPS code [141].

5.1.2 *Achieving rectification*

Table 5.1 summarizes the results obtained for the configurations shown in Fig. 5.2, reporting rectifications in the range of $2.0\% - 3.5\%$ and $1.4\% - 3.2\%$ for Ge and pore distributions; on average, the error in estimating rectification is about 0.45% and 0.32%, respectively. These data provide evidence that not only a rectification is indeed found but also it is ruled over by changing the distribution of Ge atoms or pores along the z direction. Overall, the predicted R is comparable to what was observed in other low-dimensional Si-based systems [284–288] proving that rectification is indeed possible in a bulk-like system lacking sharp interfaces. Interestingly enough, rectifications as small as $3\% - 4\%$ have been indeed measured in the Si-based systems [277]; an even smaller rectification of about $1\% - 2\%$ has been experimentally reported, although in a rather different system as reduced graphene oxide [281]. So, the rectification values predicted in this work should be within the experimental capability of measure.

	Linear	Quadratic	Exponential	Step-like
Ge	2.0%	2.8%	3.5%	2.0%
Pores	1.6%	1.4%	3.2%	1.2%

Table 5.1: Rectification calculated for the graded distributions of Ge atoms or pores shown in Fig. 5.2. On average, the error in estimating rectification is about 0.45% and 0.32%, respectively. For all samples, the temperature offset between the hot and cold thermostats is set at $\Delta T = 200$ K and it is centered at an average temperature of 600 K. Simulation cells have a $13 \times 13 a_0^2$ section and a length $L_z = 100 a_0$.

$\Delta T = 200$ K	$\Delta T = 150$ K	$\Delta T = 100$ K	$\Delta T = 50$ K
3.5%	3.3%	2.8%	2.7%

Table 5.2: Rectification calculated for the graded distributions of Ge atoms with an exponential profile (see Fig. 5.2) as a function of the temperature offset ΔT between the hot and cold thermostats (in all cases, the average temperature is 600 K). On average, the error in estimating rectification is 0.37%. The simulation cells have a section $S = 13 \times 13 a_0^2$ and a length $L_z = 100 a_0$.

Varying the profile of the defect distribution is an effective way to control the resulting R, and the present simulations suggest that the exponential profile turns out to be the most efficient in generating different values for $|\mathbf{J}_{fwd}|$ and $|\mathbf{J}_{rev}|$. This is not, however, the only way to tune rectification features. In fact, the dependence of the rectification on the value of the imposed temperature offset $T_h - T_c = \Delta T$ was calculated, as shown in Table 5.2 for the same $L_z = 100 a_0$ sample containing a graded distribution of Ge defects with similar exponential profile.

Varying the temperature offset

The results are along the expectations: by decreasing the temperature offset between the hot and cold thermostats, the rectification is reduced from 3.5% to 2.7%. On average, the error in estimating the rectification for these systems is 0.37%. However, such a reduction is weak: while the temperature offset was reduced by a factor 4, the calculated rectification is only reduced by

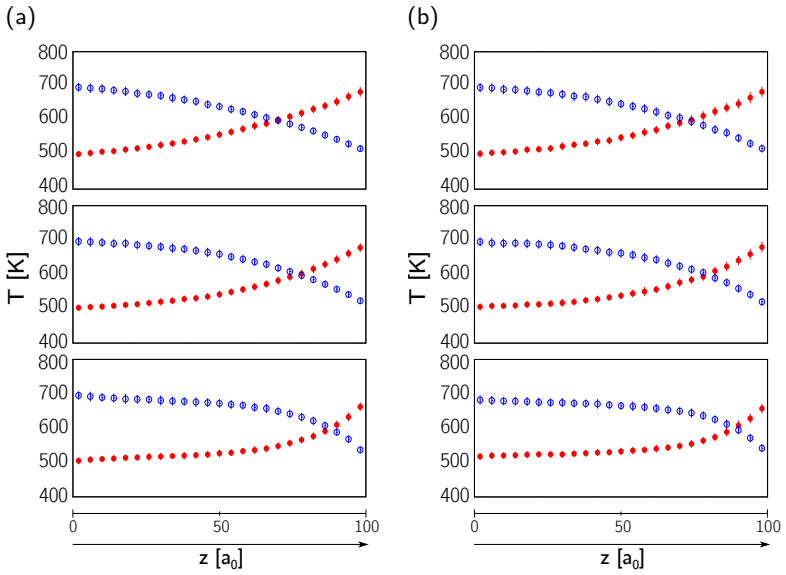

Figure 5.3. **a**: Temperature profiles calculated for the graded distributions of Ge atoms. **b**: Temperature profiles calculated for the graded distributions pores. The profiles are shown in the same order of Fig. 5.2 (the step-like profile is omitted here for sake of clarity). For all systems, which rectification factor are reported in Table 5.1, it has been set $T_h = 700$ K and $T_c = 500$ K. The forward and reverse thermal bias conditions correspond to the empty (blue) and full (red) symbols, respectively. Errors are indicated by vertical bars.

a factor 1.3. This is an interesting result, making clear that the predicted rectification feature is robust. Interestingly enough, the rectification is also affected by varying the absolute temperature of the two thermostats, but still preserving their offset: as a matter of fact, by repeating the calculation for an exponential profile of Ge substitutional defects with $T_h = 900$ K and $T_c = 700$ K, $R = 4.3\%$ was obtained. Such an increased rectification can be attributed to the different average interface temperatures [272].

Another intriguing feature of the rectification phenomena reported here is that they are not paralleled by the onset of any interface temperature

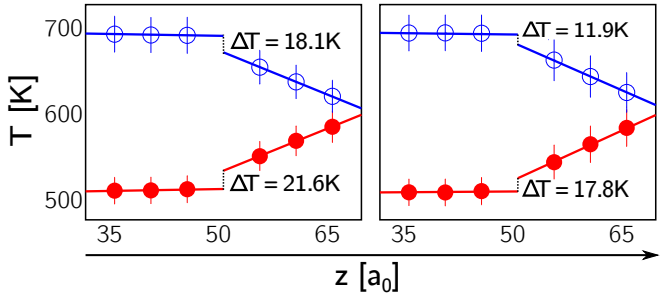

Figure 5.4. Zoomed temperature profiles nearby the interface (positioned at $z = 50a_0$) calculated for a step-like distribution of Ge atoms (left) and pores (right) in the $T_h = 700$ K and $T_c = 500$ K thermostatting condition. The resulting temperature drop ΔT is shown for both the forward (empty blue symbols) and reverse (full red symbols) thermal bias conditions. Errors are indicated by vertical bars.

drop, possibly causing ITR effects. Fig. 5.3 reports the calculated temperature profiles in the steady state conditions for all graded systems shown in Fig. 5.2, both in the forward (open blue symbols) and reverse (red full symbols) thermal bias conditions. The profiles have been obtained by calculating the local temperature of slabs as thin as 2.7 nm aligned along the z direction, over which the atomic velocities have been averaged for 1×10^6 and 3×10^6 time steps, according to the system.

5.1.3 *Nonseparability of thermal conductivity*

The present results can be interpreted in terms of a nonseparable dependence of the thermal conductivity upon the z-coordinate and temperature T which, in turn, defines a non-linear heat transfer regime. Such a non-linear regime is the key feature for rectification, which cannot be simply ascribed to an asymmetric scattering of the heat carriers by defects when inverting the thermal bias. As a matter of fact, the structural inhomogeneity generated by the graded distribution of compositional or structural defects makes the thermal conductivity a function of z. On the other hand, it turns out that the same

quantity is explicitly a function of T as well, since the system is out of equilibrium (although in steady state). In other words, it is taken for granted that each single portion of the system is transmitting heat while experiencing a different local temperature with respect to the temperature of its neighboring regions. This is tantamount to say, that in all investigated samples the function $\kappa = \kappa(z, T)$ is non-separable. In what follows it will be assumed that, contrary to the above conclusion, the thermal conductivity is separable, i.e., it can be written $\kappa(z, T) = f(z)g(T)$, where $f(z)$ and $g(T)$ are known functions. In the steady state condition (whatever thermal bias) investigated here, the heat equation for 1D transport along the z direction,

$$\kappa(z, T)\frac{dT}{dz} = f(z)g(T)\frac{dT}{dz} = -J_z \tag{5.2}$$

can be easily integrated by variable separation since the one-dimensional heat flux J_z is a constant and, therefore

$$\int_{T_l}^{T_r} g(T)dT = -J_z \int_{z_l}^{z_r} \frac{1}{f(z)}dz \tag{5.3}$$

where T_l and T_r are the temperatures of left and right terminal ends of the system, respectively, located at positions z_l and z_r. Equivalently, Eq. (5.3) can be cast in the form

$$J_z = -\frac{\int_{T_l}^{T_r} g(T)dT}{\int_{z_l}^{z^r} \frac{1}{f(z)}dz} \tag{5.4}$$

By inverting the thermal bias condition, the upper and lower limits in the temperature integral are just switched: this will only affect the sign of the heat flux, leaving unaffected its absolute value. This implies a null rectification, i.e., $R = 0$ since $|\mathbf{J}_{fwd}| = |\mathbf{J}_{rev}|$. Therefore, the assumption that $\kappa(z, T) = f(z)g(T)$ is separable has in fact defined a *sufficient condition for no rectification* [283].

This is the key concept that allows to understand these results, providing a rationale for them. Sure enough, the above statement can be logically inverted to say that a nonseparable $\kappa = \kappa(z, T)$ form of the thermal conductivity does represent the *necessary condition for rectification*. This is precisely what is

Necessary condition for rectification

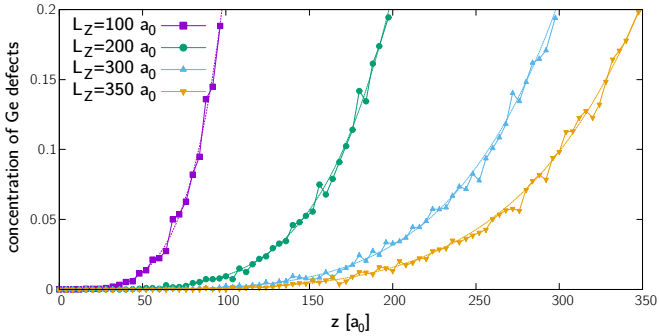

Figure 5.5. Local content of Ge substitutional defects along the direction z of heat transport for four samples with different length L_z. Symbols (connected by thick lines) represent the actual Ge content; thin lines represent a guide to the eye, corresponding to an ideal exponential profile.

exploited by the combination of (i) a graded distribution of defects and (ii) a thermal bias condition. Therefore, the bulk structures here investigated *must rectify* a thermal current: as a matter of fact, their thermal conductivity is a complicated and non-linear convolution given by a z-dependence of the temperature which, in turn, is a function of the local stoichiometry or porosity.

The present picture on rectification is robust since it does not qualitatively depend neither on the nature of the defects (compositional or structural) distributed in the bulk structure nor on their actual distribution profile. It is also found for no matter what thermostatting condition is set: by simulating a graded exponential distribution of Ge defects under two different conditions (namely, $T_h = 700$ K with $T_c = 500$ K and $T_h = 900$ K with $T_c = 700$ K) in both forward and reverse bias, a smooth continuous temperature profile was found in all the samples, similar to that shown in Fig. 5.3. When the same analysis is applied to the systems characterized by a step-like distribution of defects (Fig. 5.2, bottom panels), a small (but definitely non-vanishing) and abrupt temperature offset at the interface was found, as reported in Fig. 5.4. In the case of Ge doping, such an interface temperature drop was estimated to be as large as $\Delta T_{fwd} = 18.1 \pm 2.3$ K and $\Delta T_{rev} = 21.6 \pm 2.6$ K for

$L_z = 100a_0$	$L_z = 200a_0$	$L_z = 300a_0$	$L_z = 350a_0$
4.3%	4.1%	3.6%	3.3%

Table 5.3: Rectification calculated for the graded distributions of Ge atoms with an exponential profile (see Fig. 5.2) as a function of the length L_z of the simulation cell. On average, the error in estimating rectification is 0.75%. In this case, the cross section was reduced to $10 \times 10a_0^2$ for computational convenience. The temperature offset between the hot and cold thermostats is set at $\Delta T = 200$ K and centered at an average temperature of 600 K.

the forward and reverse bias situation, respectively. Similarly, for a step-like distribution of pores $\Delta T_{fwd} = 11.9 \pm 4.2$ K and $\Delta T_{rev} = 17.8 \pm 3.0$ K was obtained, resulting in a more relevant difference between the two thermal bias conditions.

Tuning the gradient of the distribution

Another important issue worth of investigation is how the predicted rectification is affected by the gradient of the defect distribution. To this aim, it was once again selected an exponential profile of Ge substitutional defects which, as in the previous cases, was varied from the minimum 0% to the maximum 20% content over a sample length L_z. However, in this case four different samples with increasing thickness along the direction of heat transport were considered, corresponding to L_z = 100, 200, 300, and $350a_0$, respectively. The resulting defect profiles are shown in Fig. 5.5. The two largest increased lengths correspond to quite a big simulation cell, and therefore, in order to keep the corresponding computational workload sustainable, the sample cross section was reduced to $10 \times 10a_0^2$. This reduction makes unfair the direct comparison with the previously investigated sample with same L_z but larger S, and therefore, the rectification was recalculated for the new section. Results are shown in Table 5.3, indicating that the rectification is predicted to decrease from 4.3% ($L_z = 100a_0$) to 3.3% ($L_z = 350a_0$), i.e., a 3.5 increase of the sample length has reduced rectification by only a factor 1.3. On average, the error in estimating rectification is 0.75%. So, as expected, there is indeed a reduction in the rectification features, but even in this case the dependence on the sample length is weak.

It is hard to assess whether this reduction is due to the increased (because of the increased sample length) scattering of heat carriers or, rather, to the decreased gradient in the defect distribution. In order to further substantiate the argument that the interplay between the sample length and the gradient of the defect distribution is complex, thermal rectification was investigated in one more configuration with $S = 13 \times 13 a_0^2$, $L_z = 100 a_0$ and an exponential profile of Ge substitutional defects which, however, was now varied from 0% to 60% of Ge-content. Interestingly enough in this case, a smaller rectification than reported in Table 5.1 was found, a value in fact very similar to the rectification calculated for the step-like profile. A systematic set of simulations exploring various combinations of length and gradient effects would be needed to fully clarify this issue, which will follow in future works. Finally, by increasing the maximum Ge content of the doped region up to 60%, or by enlarging the $(T_h - T_c)$ difference up to 400 K, or even by reducing the thermostats temperature to $T_h = 400$ K and $T_c = 200$ K (and neglecting possible quantum effects), a full confirmation of the picture outlined above it is found, namely, rectification up to $\sim 5\%$ is always observed in graded bulk structures without any ITR (once again, because of the missing sharp temperature drop anywhere in the system).

Part III

COMPLEX LIQUIDS AND ORGANIC MOLECULES

6

VIBRATIONAL SPECTROSCOPY IN COMPLEX FLUIDS

Contents

VIBRATIONAL spectroscopy, in particular time-resolved pump-probe infrared spectroscopy, is a powerful tool to investigate the dynamics of molecular systems. In particular, hydrogen-bonded (HB) liquids are among the most studied systems, as they exhibit intricate energy dissipation dynamics due to the strong directionality of hydrogen bonds and the complex topology of their network [289, 290].

Hydrogen bond interaction can be probed in detail by exploiting the stretching mode frequency of specific functional groups, for example the hydroxyl groups in liquid alcohols or water [291–294]. Time-resolved one-dimensional nonlinear spectroscopy is based on a pair of laser pulses, which are used to excite the sample, inducing a change in infrared absorption, and to probe the time dependent optical response. Time-resolved dynamical information is obtained by probing the evolution of an excited vibrational state as a function of delay time. Such dynamics are dominated by the dissipation of vibrational energy and by spectral diffusion. Both effects result from anharmonicity and from coupling among vibrational modes. The corresponding molecular transitions probed during the excitation and relaxation processes involve excited states, where the stretching mode is coupled with lower frequency modes via

hydrogen bonding, causing spectral diffusion and non-trivial changes in spectral line shapes and width [295–298]. Furthermore, polarized infrared spectroscopy makes it possible to study the rotational dynamics of such molecules [299–301].

Vibrational spectroscopy in computer experiments

To obtain the underlying molecular-level details of pump probe experiments, vibrational relaxation dynamics has been extensively investigated in computer simulations and several approaches have been proposed. On the one hand, equilibrium simulations have helped in the study of rotational dynamics, by means of autocorrelation functions using the fluctuation-dissipation formalism [302, 303]. On the other hand, non-equilibrium simulations have been already adopted in relaxation processes, providing physical insight on the origin of spectral diffusion in the ultra-fast dynamics of water [304–309].

However, the non-equilibrium approaches proposed so far either were designed *ad hoc* for a specific system [304], or introduced an explicit oscillating electric field potential in the Hamiltonian, the implementation of which poses fundamental and technical issues in systems with periodic boundary conditions [310].

In this chapter, a general approach based on the GLE (previously introduced in Chpt. 2), is proposed to simulate pump-probe processes in non-equilibrium MD simulations. This approach consists of using a non-Markovian thermostat that couples to the to a selected subset of vibrational modes (pump), while the rest of the system remains at the equilibrium temperature. When the thermostat is switched off, the system relaxes to equilibrium, redistributing the excess energy among the other DOF. Such transient regime is monitored (probe) providing quantitative insight into relaxation energy transfer processes at the molecular scale. The method proposed, based on classical MD, lacks the possibility of directly simulating quantum phenomena, but it can still be connected to vibrational energy relaxation rates [311], and it is suitable to simulate long-time thermal relaxation.

6.1 THE "HOTSPOT" THERMOSTAT

6.1.1 *Pumping the system*

While it is possible to define proper conditions for Eqs. (2.43) to sample the canonical ensemble, i.e. to satisfy the fluctuation-dissipation theorem as in Eq. (2.42), the aim is to achieve a non-equilibrium steady state for a finite time. In order to selectively excite a subset of the DOF, one has to use a GLE that does *not* satisfy the fluctuation-dissipation relation. Specifically, a modified version of the so-called δ-thermostat [110] is used, which induces frequency-dependent fluctuations of the momentum in a selected range of vibrational modes, while keeping the remaining ones almost completely frozen. The goal is to reproduce a laboratory set-up where the infrared laser pumps energy into modes at a specific frequency, whereas the other DOF are not coupled directly to the laser source and remain at the equilibrium temperature. To this end a white-noise Langevin thermostat at T_{base}, characterized by a friction parameter γ_{base}, is combined with the δ-thermostat with a target temperature of T_{peak}, acting on a set of given frequencies centered around ω_{peak}.

A memory kernel whose Fourier spectrum combines a white-noise baseline and a Lorentzian shape peak can be obtained with the following parameterization for the matrices $\mathbf{A}_p$ and $\mathbf{D}_p$: *Memory kernel*

$$\mathbf{A}_p = \begin{pmatrix} \gamma_{base} & \sqrt{\frac{\gamma_{peak}\omega_{peak}}{2\pi}} & 0 \\ -\sqrt{\frac{\gamma_{peak}\omega_{peak}}{2\pi}} & \Delta\omega & \omega_{peak} \\ 0 & -\omega_{peak} & 0 \end{pmatrix} \tag{6.1}$$

$$\mathbf{D}_p = \begin{pmatrix} 2T_{base}\gamma_{base} & 0 & 0 \\ 0 & 2T_{peak}\Delta\omega & 0 \\ 0 & 0 & 0 \end{pmatrix}, \tag{6.2}$$

that gives a (friction) memory kernel whose power spectrum reads

$$K(\omega) = 2\gamma_{base} + \frac{\gamma_{peak}}{\pi} \frac{\omega_{peak}\Delta\omega\omega^2}{(\omega^2 - \omega_{peak}^2)^2 + \Delta\omega^2\omega^2}. \tag{6.3}$$

For small $\Delta\omega$, this kernel tends to $\delta(\omega - \omega_{peak})$. Thus, the thermostat will affect the frequencies falling in the interval $\Delta\omega$ centered around the frequency ω_{peak}, injecting energy corresponding to T_{peak}, while the white noise contribution tends to keep the other modes at the target baseline temperature T_{base}. The effect of this "hotspot" thermostat can be predicted analytically, when applied to a harmonic oscillator of frequency $\bar{\omega}$ [111]. Normal modes with $\bar{\omega} \gg \omega_{peak}$ and $\bar{\omega} \ll \omega_{peak}$ equilibrate at the temperature T_{base}. A maximum in temperature is reached for $\bar{\omega} = \omega_{peak}$, which however corresponds to a different temperature than T_{peak}, due to the presence of the white-noise baseline that also interferes with the selected modes. Such maximum temperature T_{max}, for $\bar{\omega} = \omega_{peak}$, can be computed analytically, and it is thus possible to set T_{peak} to

$$T_{peak} = T_{max} - \frac{\gamma_{base}\left(T_{max} - T_{peak}\right)\left[2\pi\Delta\omega\left(\Delta\omega + \gamma_{base}\right) + \gamma_{peak}\omega_{peak}\right]}{\Delta\omega\gamma_{peak}\omega_{peak}}. \tag{6.4}$$

so that, in the harmonic limit, normal modes with frequency ω_{peak} equilibrate at the desired temperature T_{max}. These predictions for the behavior of a "hotspot" thermostat are qualitatively fulfilled in realistic systems, in which vibrational modes are coupled with each other by anharmonicity.

Mode excitation

Figure 6.1 shows the effect of the excitation of the OD stretching mode in deuterated methanol (left panel) and of the OH stretching mode in water (right panel) on the temperature of the D/H species. The temperature T_{base} corresponding to the other atomic species is reported as well. The details of how the kinetic temperatures reported in Fig. 6.1 are computed are given in the next section. In both cases $T_{max} = 400$ K and $T_{base} = 300$ K was chosen. For both examples, after a characteristic transient time, the system reaches a steady-state, in which the species most coupled to the thermostat (D and H) have a higher kinetic energy, while the other atoms, CH_3O atoms in methanol and O atoms in water, equilibrate at $\sim T_{base}$. In the transient time after the

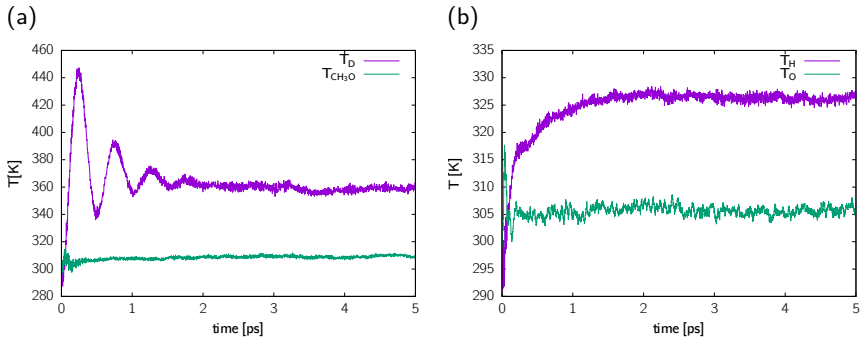

Figure 6.1. **a**: Kinetic temperatures during a "hotspot" thermostatting for deuterated methanol. **b**: Kinetic temperatures during a "hotspot" thermostatting for water. In both cases the purple (green) curve represents the temperature of the excited atoms (the remaining ones) which correspond to deuterium in left panel and hydrogen in right panel.

"hotspot" thermostat is switched on, the two systems respond in different ways. While most of the kinetic energy is effectively transferred to the modes at the target frequency, also the baseline temperature increases, due to the anharmonic coupling among different vibrational modes. In addition, the joint action of a δ-thermostat and of a white-noise Langevin thermostat results in an effective temperature of the excited modes lower than the nominal T_{peak}.

However, T_D in methanol does not correspond exactly to the temperature of the OD stretching that is excited. Using Eq. (6.4) one can tune the interaction between T_{peak} and T_{base} so to achieve the desired mode temperature T_{max}. For example, in the case of methanol, with the parameters used to obtain Fig. 6.1, $T_{peak} = 1460$ K was set to obtain (in the harmonic limit) $T_{max} = 400$ K: the temperature of the stretching mode reported (T_{OD}) reported in Fig. 6.16 turns out very close the one predicted by Eq. (6.4) in the harmonic approximation. Whereas in the general case this harmonic prediction is not exact,an excellent agreement between the predicted T_{max} and the energy resolved on the stretch mode of CH_3OD was observed (see Sec. 6.4, Fig. 6.16)

6.1.2 *Probing the relaxation*

Experimentally the relaxation dynamics that follows the pump phase is probed by a second laser pulse. Vibrational spectra are collected as a function of the time delay of the probe pulse. To model the probe phase the GLE thermostat is switched off and the system evolves in the microcanonical ensemble, so that the energy redistributes among all the DOF, to reach classical equipartition.

During relaxation the kinetic temperature of the excited modes is the most natural quantity to probe. However, further information can be obtained computing the vDOS from the Fourier transform of the velocity autocorrelation function. In order to reproduce the time delay between pump and probe, the NVE trajectory is divided in intervals of the same duration, during which atomic velocities are sampled and the transient vibrational spectrum is computed. This protocol allows to probe the whole range of vibrational frequencies as a function of time, thus monitoring the real time energy diffusion between the different vibrational modes. The hotspot thermalization implies an excess energy in the selected mode, resulting in an enhanced peak intensity in the spectrum that directly reflects the population of the vibrational mode. Relaxation dynamics eventually causes the redistribution of this surplus energy and a change of the intensity of the peaks coupled to the vibrational excited mode.

Transient spectra

The computation of the time-dependent area for peaks centered at a given frequency $\bar{\omega}$

$$A(\bar{\omega}, t) = \int_{\bar{\omega}-\delta\omega}^{\bar{\omega}+\delta\omega} \left[\int_{t_1}^{t_2} \langle \mathbf{v}(t)\mathbf{v}(t+\tau)\rangle e^{-i\omega\tau} d\tau \right] d\omega \tag{6.5}$$

provides time-resolved quantitative information about the dynamics and the characteristic time scale of energy transfer. In what follows vibrational spectra were always calculated considering only the velocities of hydrogen or deuterium atoms, in order to better highlight the dynamics of the vibrational modes of interest.

Although the calculation of power spectra as the Fourier transform of velocity autocorrelation functions is rigorously justified only at equilibrium [120], here it is used to probe non-equilibrium transient regimes. In the following, it is verified that the Green-Kubo formalism provides quantitatively reliable information about the physical properties of systems out of equilibrium, pro-

vided that the chosen time window is long enough to guarantee a suitable statistical accuracy.

6.2 CASE STUDY: METHANOL

As a case study methanol in its liquid phase is considered, since it is a widely studied representative of HB liquids. Hydrogen-bonded liquids are excellent solvents, in part due to the highly dynamic character of the directional interaction associated with the hydrogen bond. A detailed comparison with the experimental case is also presented.

6.2.1 *Simulation details*

Methanol was modeled using the COMPASS force-field [312]: the presence of high-order (cubic and quartic) and cross-coupling terms provides an accurate description of intramolecular interactions. Detailed information about the force-field are given in the Appendix A. Electrostatic interactions are modeled as fixed charges, obtained by fitting the electrostatic potential of an all electron Hartree-Fock calculation performed with a medium-sized basis set $6-31G*$. The fitting was performed using the RESP method [313, 314]. Molecular dynamics simulations are carried out for systems of 216 CH_3OD molecules in a cubic box with periodic boundary conditions with a fixed density $\rho = 0.80$ g/cm^3. All the simulations have been performed using the LAMMPS package [141], in which the equations of motion are integrated with a time step of 0.5 fs. The pump-probe results are obtained by averaging over up to 128 different trajectories.

To simulate the excitation, the GLE thermostat has been applied for 5 ps in order to reach a non-equilibrium steady state. A fully anharmonic force-field results in a transient behavior of the excitation that depends on the details of the system. The dynamics of HB liquids is usually investigated by labeling the highest frequency vibrational mode [291], namely: the OH stretching mode. For the sake of comparison with experimental results [315, 316] it was considered 100% fully deuterated methanol, CH_3OD and the excitation of the OD stretching mode.

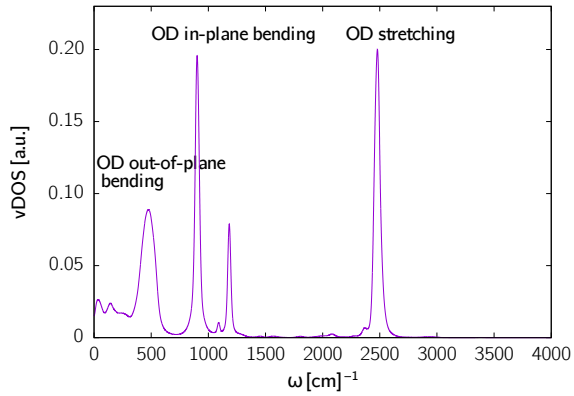

Figure 6.2. vDOS of deuterated methanol CH_3OD.

In the equilibrium vibrational spectrum shown in Fig. 6.2, as stated above, the frequency of the OD stretching mode is centered around $\omega_{peak} = 2477$ cm^{-1}. The power spectrum is calculated considering only deuterium velocities. Interestingly, two peaks not related to the hydroxyl group appear in the spectrum: the first one, around $\omega \sim 1080$ cm^{-1}, corresponds to the CO stretching mode, whereas the other one, centered at $\omega \sim 1200$ cm^{-1}, is the CH_3 rocking mode. The reason for these two additional peaks can be attributed to the functional form for the bonded interactions of the force-field: in addition to the anhamornicity up to the fourth power, COMPASS provides terms for cross-interactions as, for example, a bond-bond and a bond-angle cross term. This explains how the motion of the hydroxyl group cannot be completely decoupled from the effect of other vibrational modes, which involve the surrounding bonds or angles. The vibrational spectra computed here are in good agreement with those obtained by Car-Parrinello simulations [317] as well as with experiments [318].

Thermostat parameters

The colored noise contribution of the thermostat was characterized by $T_{max} = 400$ K, $1/\gamma_{peak} = 0.5$ ps and $\Delta\omega = 1$ cm^{-1}, while the white noise Langevin part was characterized by $T_{base} = 300$ K and $1/\gamma_{base} = 0.5$ ps. Although the excitation is tuned with a narrow width, the response of the mode is broader and a small but noticeable effect on lower frequency modes can be observed (see Fig. 6.1). This feature depends on specific thermostat

settings (see Sec. 6.4), it is the hallmark of the intrinsic coupling between the vibrational modes involving the OD bond and the other modes of the system. Furthermore, T_D is $\sim 10\%$ lower than T_{peak}. As a matter of fact T_D is a measure of the energy of all vibrational modes involving deuterium atoms, including those not affected by the thermostat. Alternatively, one can monitor the kinetic energy of the OD stretching mode, defined from the mode velocity $v_{stretch} = (\mathbf{v}_O - \mathbf{v}_D) \cdot \frac{\mathbf{d}_{OD}}{d_{OD}}$, where $\mathbf{d}_{OD}$ is the vector parallel to the OD bond and d_{OD} its modulus. However, it was verified that the relaxation dynamics of T_D and T_{OD} has the same time scale and the results are reported in the Sec. 6.4.

Eventually, the relaxation is monitored in 50 ps long NVE runs, during which atomic velocities are sampled to compute the kinetic temperature of different atomic species and the vDOS.

6.2.2 *Relaxation mechanisms*

When the GLE thermostat is switched off T_D decreases rapidly as the energy in the OD bond redistributes over the other DOF. The decay time of the temperature fits a simple exponential model

$$T_D(t) = T_D^{eq}(1 + \delta e^{-t/\tau_K}) \ , \tag{6.6}$$

where T_D^{eq} is the temperature of deuterium atoms at the end of the relaxation process (i.e. the equilibrium temperature), δ is a dimensionless factor that quantifies the excess energy at $t = 0$, and τ_K is the decay time, which turns out to be 8.7 ± 0.1 ps. The result is shown in the left panel of Fig. 6.3. To assess the contribution of hydrogen bonding interactions to vibrational relaxation, the pump-probe virtual experiment was repeated switching off the electrostatic interactions. The results reported in the right panel of Fig. 6.3 show that the relaxation dynamics in a non-HB system becomes three to four times slower, thus suggesting that energy redistribution in this system is mainly controlled by intermolecular hydrogen bonding.

Transient vibrational spectra are computed in time windows of 1.5 ps, spanning the relaxation trajectory each 0.5 ps: peak areas have been computed for the three main bands related to the vibrational modes involving the OD bond,

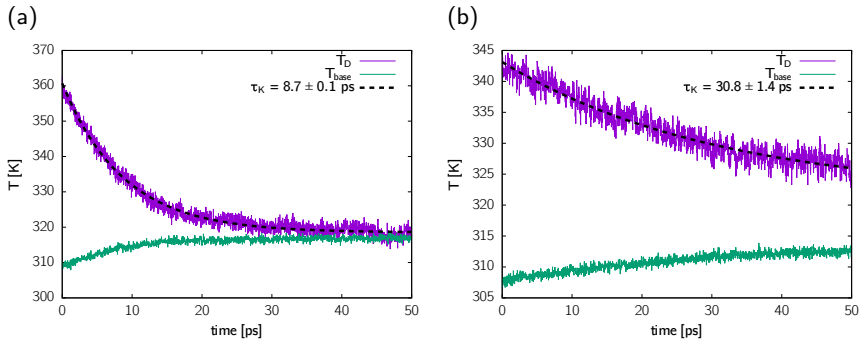

Figure 6.3. Kinetic temperature during the relaxation. **a**: Normal behavior of methanol, the black dashed line is the fit obtained by means of Eq.6.6. **b**: Relaxation of the system when the electrostatic interactions are switched off, leaving the Lennard-Jones interactions as the sole non-bonded interactions.

namely OD stretching, in-plane bending, and out-of-plane bending modes [318, 319]. The result is shown in Fig. 6.4, where areas, computed with Eq. (6.5), are reported in a relative fashion as $A(\bar{\omega}, t) - A_{eq}(\bar{\omega})$ (where $A_{eq}(\bar{\omega})$ is the peak area at the end of the equilibrium process), for the OD stretching mode, and $A(\bar{\omega}, t) - A(\bar{\omega}, 0)$ (where $\bar{\omega}$ is the frequency of the peak and $A(\bar{\omega}, 0)$ is its area right after the excitation) for the bending modes, for a better comprehension. Peak intensities show an exponential trend, which is well fitted by Eq. (6.6), so as to obtain the characteristic time scale of these processes. The area of the excited stretching mode decreases with a lifetime of $\tau_{stretch} = 8.5 \pm 0.5$ ps, which is statistically equivalent to the decay time of the kinetic temperature T_D, thus crossvalidating this analysis. This is a key result, as it justifies *a posteriori* the use of time-correlation functions to calculate response functions, e.g. power spectra, from non-equilibrium trajectories. While this is a rather common practice [305, 306], it often lacks a compelling verification: extensive tests lead to the conclusion that a time window of 1.5 ps is the shortest possible to achieve meaningful results, which also means that it is impossible within this framework to probe faster decay mechanisms by this approach.

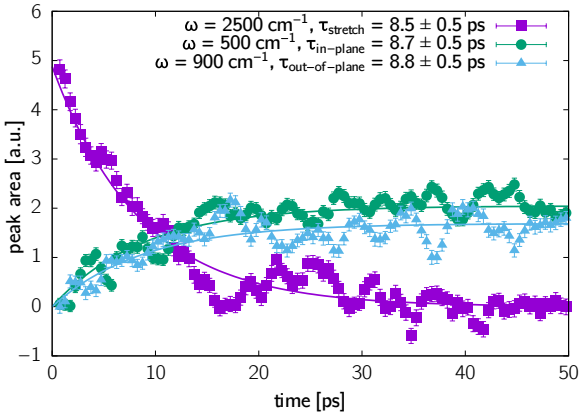

Figure 6.4. Peak areas as function of time as obtained from Eq. (6.5). In y-axis is reported relative intensity for sake of clarity: purple squares show the amount of intensity lost by stretching mode, whereas blue triangles and green circles represent the intensity gained by the bending modes. Dashed lines represent the relative fit.

The dimensionless pre-factor in Eq. (6.6) turns out to be $\delta_{\mathrm{stretch}} = 0.37 \pm 0.01$, which means that the excitation enhances the population of the OD stretching mode by about 37% with respect to the equilibrium population. The dynamics of the low-frequency part of the spectrum shows that energy is transferred in equal amounts to the two bending modes: $\delta_{\mathrm{in-plane}} = 0.14$ and $\delta_{\mathrm{out-of-plane}} = 0.16$. Furthermore the calculated lifetimes show that the transferring process occurs simultaneously, $\tau_{\mathrm{in-plane}} = 8.8 \pm 0.5$ ps and $\tau_{\mathrm{out-of-plane}} = 8.8 \pm 0.5$ ps. The remaining energy contributes to the overall temperature increase of the system, by spreading into the remaining modes of the molecule.

The simulation protocol described above aims at modeling pump-probe spectroscopy [315, 320], but since it is based on classical MD, substantial differences with experiments emerge, stemming from the quantum-mechanical nature of molecular vibrations.In what follows, analogies and differences between modeling and experiments will be highlighted.

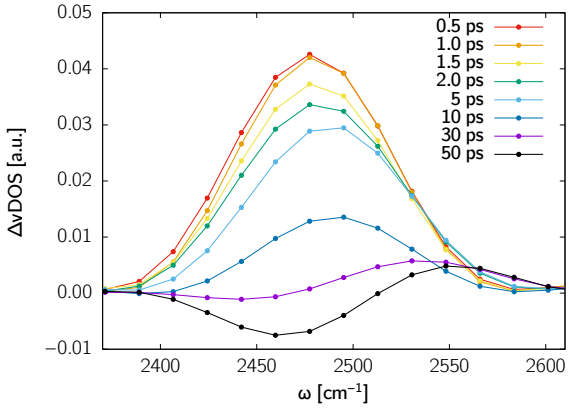

Figure 6.5. Amplitude difference between the non-equilibrium and the equilibrium vDOS at different times: for $t > 5$ ps peak frequency starts shifting and the final configuration ($t = 50$ ps) shows an appreciable contribution at higher frequency and a negative contribution for $2450 \leqslant \omega \leqslant 2550$ cm^{-1}, which is due to the blue shift of the OD stretching bond at higher temperatures. The amplitudes are reported as a difference with respect to a equilibrium configuration at $T = 300$ K, in order to highlight the frequency shift.

Comparison with experiments

The excitation-relaxation process occurring in pump-probe experiments is usually represented as a quantum-mechanical kinetic model, in which a laser pulse excites the target mode from its ground state $|0\rangle$ to its first excited state $|1\rangle$. The population of the excited state relaxes rapidly to an intermediate state $|0^*\rangle$ with a time constant τ^*. In this intermediate state, the excess vibrational energy is not yet fully equilibrated over the system. Eventually this intermediate state relaxes to a heated ground state $|0'\rangle$ with time constant τ_{eq}, as the energy redistributes thermally among all the modes of the system. In HB liquids the higher temperature of the system in the $|0'\rangle$ causes an average weakening of the hydrogen bonds, accompanied by a faster vibration of the OD stretching, i.e. a blue shift of the corresponding band. These processes were analyzed by computing the amplitude difference between the transient vDOS and the equilibrium vDOS at $T = 300$ K (Fig. 6.5).

The excitation from $|0\rangle$ to $|1\rangle$ is purely quantum-mechanical, and classical simulations cannot reproduce its spectral features. In fact, the quantum excitation causes a depopulation of the ground state in favor of the excited state [321], producing an immediate change in the optical absorption spectrum, in which the intensity of the band corresponding to the excitation frequency decreases [322]. This effect, referred to as "bleaching", cannot be observed in a classical MD simulation. Moreover, there are a number of non-thermal processes involved, such as non-Fermi-like distribution of the excited electrons, electronic scattering which cannot be sampled within a classical framework. On the contrary, pumping "colored" energy in an ensemble of coupled classical oscillators "populates" the vibrational modes at the corresponding frequency, therefore enhancing the intensity of the band in the absorption spectrum. At short time scales after the excitation ($t \leqslant 5$ ps) the intensity of the OD stretching band out of equilibrium is indeed higher than that at equilibrium (Fig. 6.5), as a consequence of the excitation of classical OD oscillators with enhanced amplitudes. At later times the differential spectra are characteristic for an equilibrated, heated liquid, with a blue-shifted OD stretching frequency: the spectra display reduced intensity at 2470 cm^{-1} (the absorption maximum before excitation) and enhanced intensity at 2550 cm^{-1}, as heated methanol molecules form weaker hydrogen-bonds (Fig 6.5, $t = 50$ ps).

Assessing the relaxation timescale

Experimentally, the dynamics of the two relaxations occurs over different time scales: the excited state is short-lived and is characterized by a sub-picosecond lifetime; on the other hand the intermediate state relaxes with a longer time constant. Here, the vibrational energy redistribution occurs over longer time scales, since this set-up and analysis tools are not suitable to investigate $\tau < 1$ ps. However, sub-picosecond processes have been investigated in previous theoretical papers for water [304–306], while, according to the state-of-the-art, methanol relaxation has not been studied theoretically. Whereas the differences in the excitation mechanism between experiments and simulations may affect the fast relaxation dynamics from $|1\rangle$ to $|0^*\rangle$, the subsequent thermal energy relaxation from $|0^*\rangle$ to $|0'\rangle$ is essentially classical and can be probed by MD. The time scale calculated for the relaxation of deuterated methanol, 8.5 ps, agrees well with the experimental thermal relaxation time $\tau_{eq} \sim 6.0, 7.0$ ps in Refs. [315, 320]. The small difference may be ascribed to the approximate classical forcefield.

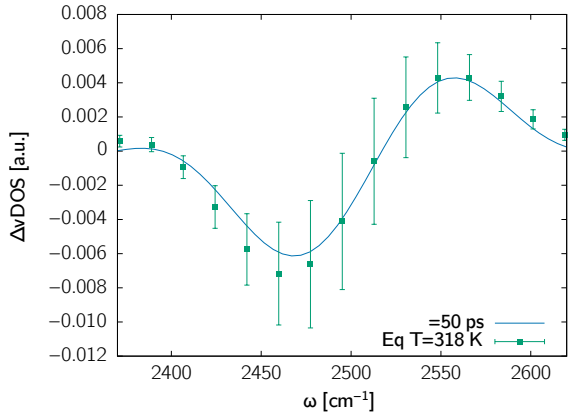

Figure 6.6. Comparison between the spectrum relative to the final configuration ($t = 50$ ps) and the equilibrium vDOS computed at $T = 318$ K. The amplitudes are reported as a difference with respect to a equilibrium configuration at $T = 300$ K, in order to highlight the thermal induced blue shift.

Such an agreement suggests that the underlying relaxation processes at the molecular level unraveled by these simulations are similar to the thermalization that occurs after the depopulation of the excited state of the (quantum) oscillator in experiments. Thus, even though simulated transient spectra show unlike signatures of classical excitations as compared to experiments [315], the good agreement in the time scales ruling the observed phenomena indicates that the simulation accounts for the correct mechanism and rate limiting step of the experimentally observed thermalization dynamics.

By the end of the relaxation, i.e. after 30 ps, the whole energy pumped into the OD stretching is converted into thermal energy. Specifically, with the parameters chosen for the excitation discussed in the previous section, the temperature of the system increases from 300 K to 318 K. The blue shift observed at the end of the relaxation is thermal, as it is suggested by the agreement between the transient spectrum taken at $t = 50$ ps and the vDOS computed at equilibrium for $T = 318$ K (Fig. 6.6),

Furthermore the behavior of the bending modes confirms that the system state at $t = 0$ corresponds to the intermediate state $|0^*\rangle$, in which the vibra-

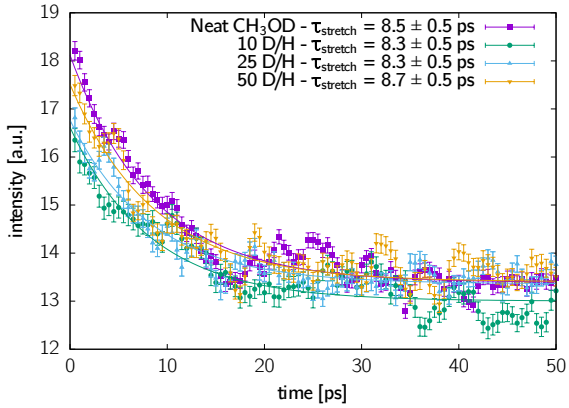

Figure 6.7. Comparison between systems with different isotopic dilution, namely the 10%, 25% and 50% of deuterated molecules. Different intensities correspond to different populations of OD oscillators, but the relaxation time scales are independent on dilution.

tional ground state of the stretching mode is coupled with lower frequency modes [323, 324] determining the main channel for energy redistribution. Interestingly, this relaxation mechanism is independent on the isotopic dilution of the mixture: the same dynamics is observed for different isotopic dilution, 10%, 25% and 50% of deuterated molecules, as showed by Fig. 6.7.

Different peak intensities at $t = 0$ correspond to different mode populations, which depend on the number of oscillators in the system. This is in agreement with previous experimental results [315], showing that the relaxation from the intermediate state does not depend on the isotopic composition of the system. The dependence on the isotopic dilution of the fast relaxation time, instead, is still debated [315, 316, 320].

6.3 CASE STUDY: WATER

The second case study is liquid water. While still a HB liquid, its dynamics is considerably different from that of methanol, since each molecule forms more hydrogen bonds [325, 326].

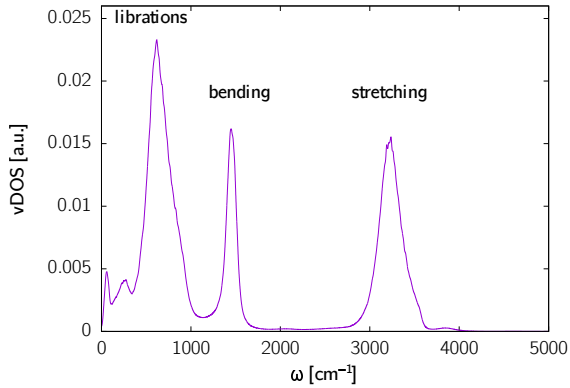

Figure 6.8. vDOS of water calculated from the hydrogen atoms velocity autocorrelation function: the three bands of interest are the OH stretching, a broad band centered at about 3250 cm^{-1}, the bending ($\sim$ 1450 cm^{-1}) and the librations ($\sim$ 650 cm^{-1}).

6.3.1 *Simulation details*

Liquid water is modeled via a force-field fitted to first-principles MD simulations by force-matching [327]. This force-field has shown to accurately reproduce the structural and dynamical properties of water simulated by DFT using the generalized gradient functional by Perdew, Burke and Ernzerhof [328]. Simulations have been performed on a system of 343 molecules in a periodically repeated cell with a density of $\rho = 1.0$ g/cm^3, averaging over 256 statistically independent trajectories.The same GLE thermostat settings as in the methanol case were adopted: the colored excitation was characterized by $T_{mas} = 400$ K, $1/\gamma_{peak} = 0.5$ ps and $\Delta\omega = 1$ cm^{-1}, while the white noise Langevin has $T_{base} = 300$ K and $1/\gamma_{base} = 0.5$ ps. Here the focus is on the OH stretching mode which, gives a broad vibrational band centered at 3211 cm^{-1}, as shown by the vDOS in Figure 6.8. After a 5 ps-long excitation, the system relaxation was monitored for 30 ps.

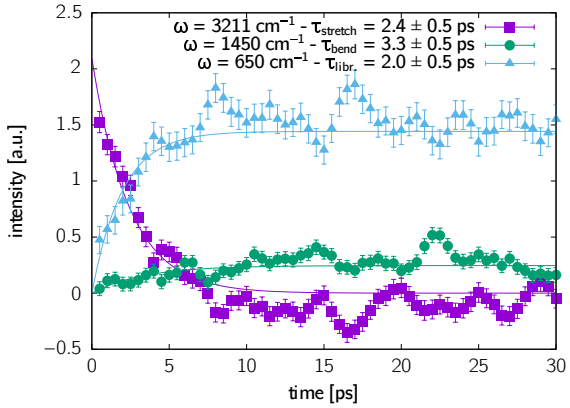

Figure 6.9. Peak areas as function of time as obtained from Eq. (6.5). In y-axis is reported relative intensity, similarly to Fig.6.4. Dashed lines represent the relative fit.

6.3.2 *Relaxation mechanisms*

As mentioned above, the response of water to the thermostat shows a noticeable difference with respect to methanol (Fig. 6.1): frequency-dependent thermalization reaches the steady state in a few hundreds time step. This difference is attributed to the relatively larger number of DOF involved in the excitation, compared to methanol. Since the thermostat forces the excitation over an oscillator surrounded by a number of other oscillators damped by γ_{base}, the difference in the relative number of DOF affects the transient regime prior to the steady state.

The analysis of the transient power spectra highlights further differences between water and methanol. As shown in Fig. 6.9 the decay of the excited OH stretching vibration occurs on a faster time scale with $\tau_{\mathrm{stretch}} = 2.4 \pm 0.5$ ps, which is slower than the experimentally observed equilibration time of ~ 0.7 ps [300]. The slower relaxation observed in simulations may be related to additional relaxation channels, such as Fermi-resonances [329], which classical simulations cannot account for. Notably, τ_{stretch} is significantly faster for water than for methanol. This difference may be traced back to the fact that

water molecules form from 3 to 4 hydrogen bonds [217], while methanol has only 2. Hence, stronger coupling among water molecules and higher connectivity of the hydrogen bonds network provide more channels for vibrational relaxation, leading to shorter relaxation times. Also the relaxation mechanism is different from that of methanol. Fig. 6.9 reports the intensity of the accepting modes, where librations are preferred with respect to bending modes. In fact, the pre-factors in the fitting Eq. (6.6) result in $\delta_{\mathrm{stretch}} = 0.16 \pm 0.01$, $\delta_{\mathrm{bend}} = 0.021 \pm 0.009$ and $\delta_{\mathrm{libr.}} = 0.08 \pm 0.01$, which indicates that most of the energy relaxes into librational modes.

In addition, in water the amount of excess energy that is converted into heat is noticeably larger, thus explaining the higher temperature increase. This energy relaxation time scale of 2.5 ps compares well with experiments that show diffusive rotations in water to occur in $\lesssim 3$ ps [330, 331]. The dynamics of these low frequency modes associates with collective reorientation of the HB network, and the time scale is in agreement with the diffusive rotational dynamics of water.

6.4 TECHNICAL FEATURES

To prove the reliability of the simulation protocol, the thermostat parameters were tested over a reasonable range of values in order to address its reliability in terms of physical prediction and to to identify the range of parameters that give physically meaningful results. As stated in the previous section, the hotspot thermostat has a total of five different tunable parameters: two of them are related to the white noise contribution (standard Langevin equation) and were kept fixed ($\mathrm{T}_{base} = 300\mathrm{K}$ and $1/\gamma_{base} = 0.5$ ps). Hence, each parameter for the colored contribution of the thermostat has been tested separately over the following ranges of value:

- excited mode temperature in the range $320 \leqslant \mathrm{T}_{max} \leqslant 600$ K;
- spectral width in the range $0.1 \leqslant \Delta\omega \leqslant 75$ cm^{-1};
- thermostat friction in the range $0.1 \leqslant 1/\gamma_{peak} \leqslant 5$ ps.

Choosing the GLE parameters within the given range ensures physically meaningful and reproducible results. No appreciable trend was observed in the phys-

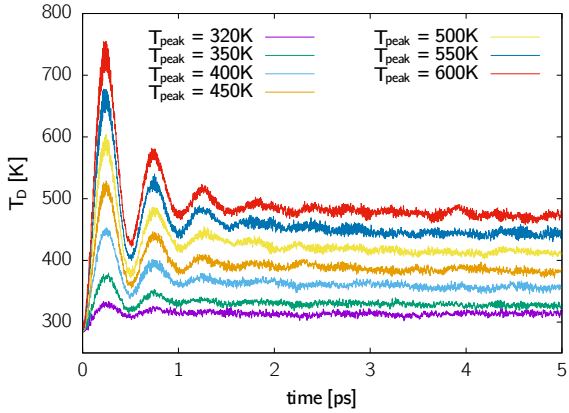

Figure 6.10. Kinetic temperature of deuterium atoms during the excitation phase, for different values of T_{peak}.

ical observable as a function of such parameters, suggesting that the method is solid against the choice of different arbitrary parameters, and it reproduces the correct physics.

The convergence of the results upon the system size was also addressed. The GLE protocol was applied to systems ranging from 27 to 512 molecules. Small systems are affected by finite size effects, and size convergence is reached for systems of 216 molecules or larger.

6.4.1 *Peak temperature*

Changing T_{peak} affects the total amount of energy that the molecules receive from the thermostat. This is clearly shown in Fig. 6.10, where the temperature T_D is plotted during the excitation for different value of T_{peak}.

However, it is worth noting that since the OD oscillators are all coupled via hydrogen bonds, and are interacting with a number of other oscillators (other vibrational modes of the molecule), the efficiency of the frequency dependent thermalization is limited and a small but appreciable temperature rise is observed also for the other DOF. This increase is negligible for $T_{peak} < 400$K and anyway is reasonable (< 10K) for small T_{peak}. Despite this temperature

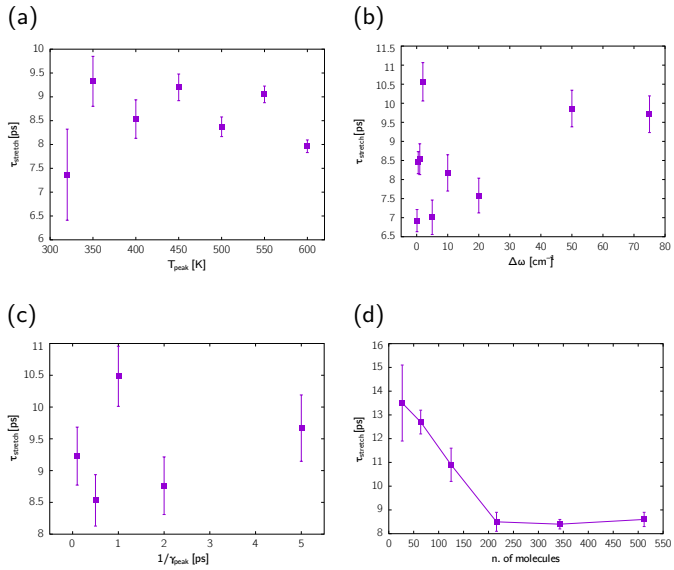

Figure 6.11. **a**: Decay times calculated from OD stretching relaxation decay for different values of T_{peak}. The results are independent from T_{peak}. **b**: Decay times calculated for different values of $\Delta\omega$. The results show no appreciable trend. **c**: Decay times calculated decay for different values of $1/\gamma_{peak}$. The results show no trend. **d**: Decay times calculated for different number of molecules. The results show convergence for systems with a number of molecules $\geqslant 216$.

dependence, the relaxation time for the temperature decays does not show a definite trend, as shown in Fig. 6.11a the relaxation toward the equilibrium does not depend on the amount of energy supplied by the thermostat.

Although the involved mechanism is different, the results is in good agreement with femtosecond infrared spectroscopy experiments, which show that equilibration time τ_{eq}, as shown in the previous section, is independent on the amount of energy to be equilibrated.

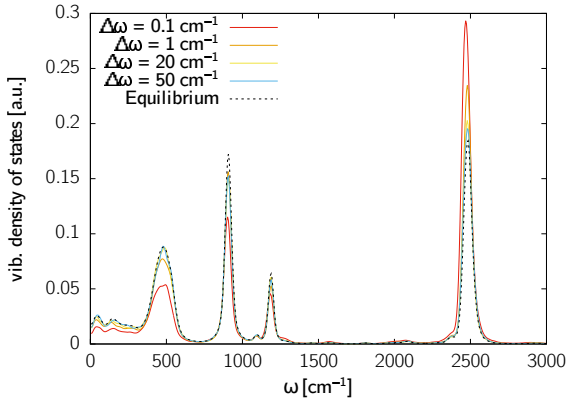

Figure 6.12. Effect of the GLE thermostat spectral width: a narrow excitation results in greater intensity, but can also affect the population of low frequency mode involving the OD bond.

6.4.2 *Spectral width*

The way how $\Delta\omega$ influences the coupling of the thermostat is straightforward: it determines the range of frequencies that are thermostatted at T_{peak}. Fig. 6.12 shows how changing the spectral width of the hotspot thermostat affects the vibrational spectrum: a narrower excitation results in a more efficient coupling between the thermostat and the OD stretching mode, which means an increased population and an enhanced peak of the excited mode.

Furthermore, the lower frequency part of the stretch peak, becomes more populated as the thermostat spectral width decrease. This is related to what happens to low frequency modes involving the deuterium atoms, which are "less populated" after a very narrow excitation, indicating that such a configuration affects appreciably other vibrational modes rather than only the stretching one: the response of the system to the thermostat is wrong, causing T_{base} to increase far above the selected baseline temperature (Fig 6.13).

A reasonable choice is to keep $\Delta\omega > 1$ cm^{-1}, as shown in Fig. 6.13. However no appreciable dependence of $\tau_{stretch}$ on $\Delta\omega$ is observed (Fig. 6.11b).

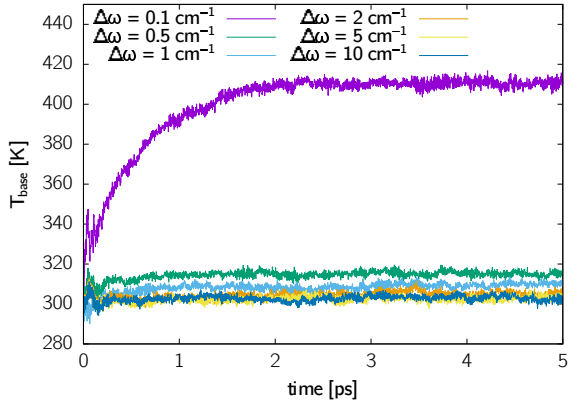

Figure 6.13. Baseline temperature (CH_3 and O atoms) for different value of GLE spectral width. A too narrow affects excessively the dynamics of the other DOF.

6.4.3 *Peak friction*

Finally, $1/\gamma_{\mathrm{peak}}$ is a damping parameter, which determines the coupling between the system and the thermostat: small values of $1/\gamma_{\mathrm{peak}}$, which mean high friction, will result in a strong coupling and wide fluctuations of the kinetic energy, and longer simulation time required to reach the steady state, as show in Fig. 6.14a

Furthermore, reducing considerably $1/\gamma_{\mathrm{peak}}$ value will affect also the sampling efficiency: choosing $1/\gamma_{\mathrm{peak}} < 1/\gamma_{\mathrm{base}}$ will cause a broader response of the system, affecting also vibrational modes with lower frequency involving different atomic species; Fig. 6.14b shows how $1/\gamma_{\mathrm{peak}} = 0.1$ ps determine the baseline temperature to rise up to 335 K, whether $1/\gamma_{\mathrm{peak}} = 1/\gamma_{\mathrm{base}} = 0.5$ ps results in temperature increase for T_{base} lower than < 10 K. However, Fig. 6.11c reports how the relaxation time is not affected, because the vibrational relaxation requires energy exchange with other modes and varying $1/\gamma_{\mathrm{peak}}$ will only change the final equilibrium configuration.

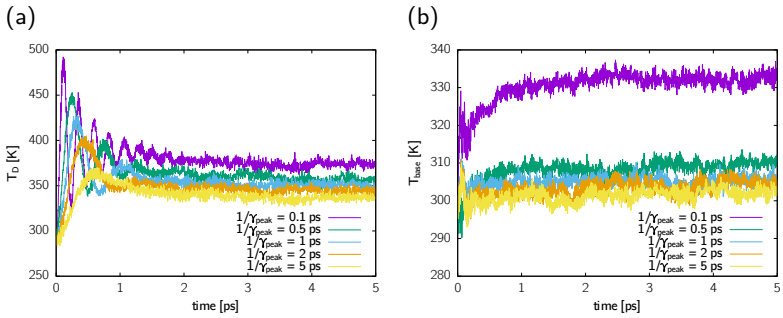

Figure 6.14. **a**: Deuterium atoms response to GLE thermostat for different values of the colored-noise friction parameter: a strong friction results in a highly fluctuating temperature. **b**: Baseline temperature for different values of the friction: the response of the system to strong frictions also perturbs other DOF.

6.4.4 *Size effect*

The GLE protocol was applied to system of increasing size, ranging from 27 molecules (with box size L = 1.2 nm) to 512 molecules (with box size L = 3.4 nm). In this case the set of parameters where chosen as the main simulations in this work $T_{peak} = 400$ K, $\Delta\omega = 1$ cm^{-1}, $1/\gamma_{peak} = 0.5$ ps. For each system size the results have been averaged over 128 different trajectories. The first result that is worth to remark is that the thermostat injects an amount of energy which is independent from the number of molecules, as shown in Fig. 6.15: each molecules has a total energy increase around 0.55 kcal/mol.

The calculated decay time are shown in Fig. 6.11d: increasing the system size reduce the uncertainty because fluctuations are inversely proportional to the number of atoms in the system. Furthermore an appreciable decreasing trend is observed: for the number of molecules $\geqslant 216$, the calculated $\tau_{stretch}$ is unchanged. However, it is necessary to remark that the uncertainty on the decay time here reported is the fit error, while it should be the time interval between each peak area calculation (since it constitutes the shortest time which can be probed by this method). Thus 216 molecules was chosen as a

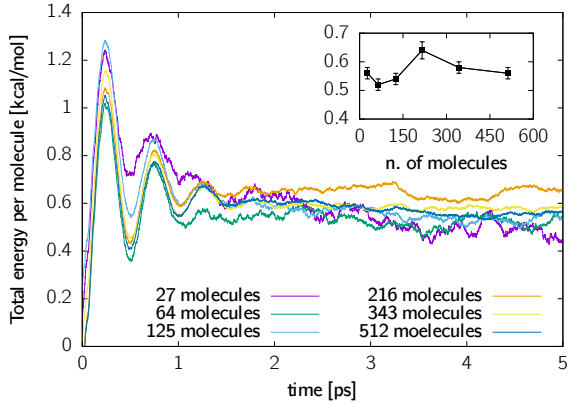

Figure 6.15. Total energy per molecule injected by the thermostat as a function of time, during the excitation phase. The inset shows the average increase of total energy, with respect to the equilibrium configuration, calculated during the steady state.

compromise between an accurate statistical average and a low computational workload.

6.4.5 *Kinetic temperature vs. Mode temperature*

All analysis were performed by considering the kinetic temperature of the atomic species for convenience. Kinetic temperature is a measure of the atomic energies, thus T_D will include all the motions involving deuterium atoms, even those which in principle are not excited by the thermostat. This will result in an effective temperature which is lower than the predicted T_{peak}. In the same way, in considering the temperature T_{CH_3O} for the unperturbed DOF, it is necessary to keep in mind that oxygen atoms carry a fraction of the kinetic energy of the stretching mode resulting hotter than the room temperature.

The exact amount of energy carried by the OD stretching mode can be computed considering the mode velocity

$$\nu_{stretch} = (\mathbf{v}_O - \mathbf{v}_D) \cdot \frac{\mathbf{d}_{OD}}{d_{OD}} \tag{6.7}$$

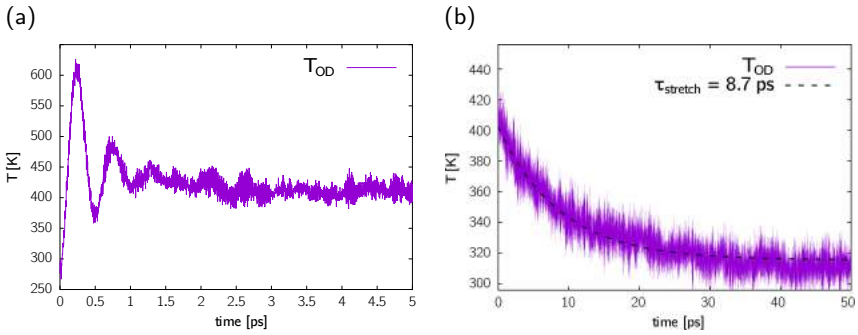

Figure 6.16. **a**: OD stretching mode temperature, computed according to Eq. (6.7), during system excitation. Final temperature is $\langle T_{OD} \rangle = 400$ K. **b**: OD stretching mode temperature, computed according to Eq. (6.7), during system relaxation. The black dashed line is the fit obtained by means of Eq. (6.6).

and by computing the temperature of the mode from its kinetic energy $T_{OD} = \frac{2K_{OD}}{k_B}$. The OD stretching temperature during system excitation is shown in Fig. 6.16a.

The behavior of the mode temperature is basically the same of that reported in Fig. 6.1: after almost 2 ps the system reaches the steady-state. Furthermore, it is easy to verify that the final temperature corresponds exactly to the predicted temperature $T_{peak} = 400$ K. The exponential decay is observed also in this case, providing the same time scale obtained considering the kinetic temperature, as shown in Fig. 6.16b. This further guarantees the accuracy of the analysis performed on the kinetic temperature and on the transient vibrational spectra.

6.5 ASSESSING THE INTERPLAY BETWEEN ENERGY RELAXATION AND THERMAL DIFFUSION IN LIQUID METHANOL

Spectroscopy experiments performed on deuterated liquid methanol by exciting the OD stretch vibration [315], report that even though the vibrational

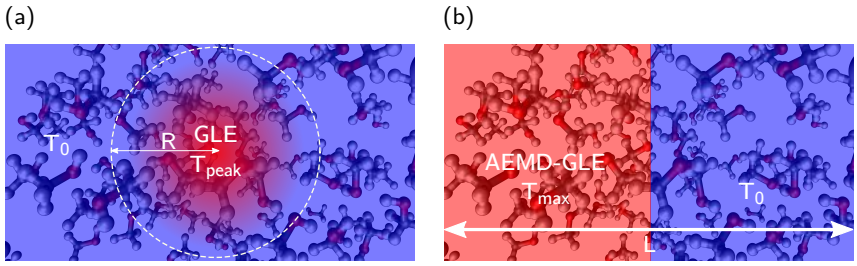

Figure 6.17. **a**: Schematic representation of the radial geometry, where the laser (the GLE thermostat in a MD simulation) excite a specific spot, with radius R, of the sample causing a temperature rise which relaxes according to a spherical symmetry . **b**: 1D set up of the simulation cell, where the GLE thermostat is adopted in the AEMD framework for a system with length L.

excitation has already relaxed, there is a residual memory at long times, where the transient signals are dominated by heating (see above). The locally dissipated energy effectuates spectral changes of the excited OD oscillators. The transient thermal excitation can decay via diffusion of the thermal energy from an initially excited OD group to a unexcited OD group in the vicinity, which depends on the average distance between OD groups in the sample.

A continuum-based model [332–334], which approximate the locally heated OD group by a sphere of radius R having temperature $T + \Delta T_{max}$, while the surrounding bath has a temperature T, correctly describes the trend but predicts a thermal diffusivity eight times lower than the macroscopic values $\bar{\kappa}^{exp.} = 10.1$ Å^2/ps [335]. The disagreement may be related to the fact that, basing on the average distance between oxygen atoms of two neighboring HB molecules ($r^{OO} = 0.28$ nm [336]), the radius of the heated complex in the excited sample was approximated to $R = 0.3$ nm. Hence, adopting a continuum model for such a microscopic level of thermal diffusion may lead to a wrong description of the phenomenon.

The results reported above were obtained by exciting each molecule in the sample, thus each OD bond was influenced by the thermostat. This approach was needed to understand the coupling between the OD stretching mode and

the unexcited vibrational modes. However, in order to investigate the interplay between energy relaxation and thermal diffusion, the GLE excitation needs to be applied locally. In a typical laboratory set-up, the laser hits the sample in a specific spot and, therefore, it excites only a subset of the molecules. Thus a straightforward computational implementation would be a radial configuration, as shown in Fig. 6.17a. Here, the GLE thermostat is applied on the central spot of the sample, in order to investigate the heating effect following the spectral excitation. However, studying thermal diffusion in a radial configuration requires the heat equation Eq. (2.29) to be recast in spherical coordinates

$$\frac{1}{r}\frac{\partial}{\partial r}\left(r\frac{\partial T}{\partial r}\right) = \frac{1}{\bar{\kappa}}\frac{\partial T}{\partial t} \tag{6.8}$$

where $\bar{\kappa} = \kappa/\rho c_v$ is the thermal diffusivity and $T \equiv T(r,t)$ is the time-dependent radial temperature profile. By separating the variables it is easy to verify that the time dependence is the same described for $\Theta(t) \propto \exp(-\alpha^2\bar{\kappa}t)$ in Sec. 2.2.3, while the spatial part of the heat equation requires a solution expressed in terms of spherical Bessel functions of the first and of the second kind $J_1(\alpha r), Y_1(\alpha r)$, which is not easy to implement to fit 'on-the-fly'-computed data of a numerical simulation. Instead, the 1D approach, although conceptually implies a coarser level of approximation, can be easily adopted in this framework. In particular, putting together the AEMD geometry (see Sec. 2.2.3) with the GLE thermostat, as shown in Fig. 6.17b, it is possible to investigate the effect of a local spectral excitation. The initial configuration is a step-like profile

The GLE thermostat in an AEMD configuration

$$T(z,0) = H(z) = \begin{cases} T_{max} = 400 \text{ K} & \text{if } 0 < z < L_z/2 \\ T_0 = 300 \text{ K} & \text{if } L_z/2 < z < L_z \end{cases} \tag{6.9}$$

where the left half of the simulation cell is excited with the GLE thermostat, here implemented with the same settings previously explained (i.e. the excitation of the OD stretching mode), while the right half is left unperturbed at $T_0 \equiv T_{base} = 300$ K, which is also the baseline temperature selected for the unperturbed vibrational modes involving CH_3O atoms. In this case periodic boundary conditions have been applied along the three directions. As usual,

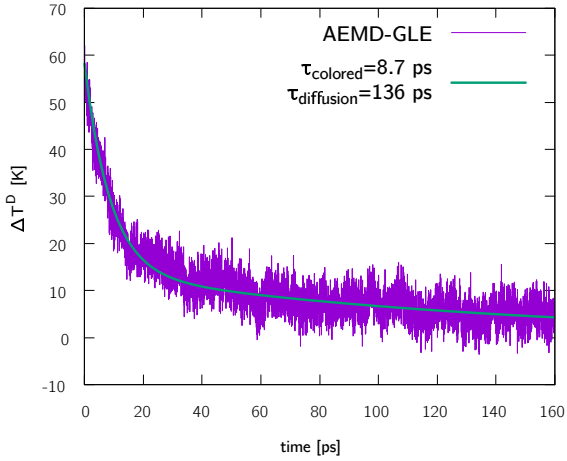

Figure 6.18. Temperature difference as a function of time for a deuterated methanol sample, containing 10368 atoms, with $L_z = 19.95$ nm and a section of 2.44×2.44 nm^2. The green solid line is a fit performed with the two time exponential model of Eq. (6.11), considering $\tau_{colored} = 8.7$ ps, which produces $\tau_{diffusion} = 136$ ps and $\beta = 0.76$.

after the excitation GLE thermostat is switched off and the transient regime is investigated by monitoring the ΔT^D evolution

$$\Delta T^D(t) = \langle T_L^D(t) \rangle - \langle T_R^D(t) \rangle \tag{6.10}$$

i.e. the difference between the deuterium temperature averaged over the excited half of the sample and the deuterium temperature averaged over the unperturbed half. Isolating the temperature of the deuterium atoms helps excluding thermal noise due to the baseline, namely the CH_3O atoms.

A striking difference with respect to the "traditional" AEMD behavior is that $\Delta T^D(t)$ exhibit a two different characteristic times for the exponential decays, which suggests the presence of two different diffusion mechanisms.

Figure 6.18 shows the time dependence of the temperature difference for a sample of deuterated methanol, containing 10368 atoms, with $L_z = 19.95$ nm and a section of 2.44×2.44 nm^2. The trend is characterized by an initial

fast relaxation followed by a slower decay at longer times. It is possible to fit simulation data with a phenomenological relation

$$\Delta T^{D}(t) = \Delta T_0^{D}\left[\beta e^{-t/\tau_{colored}} + (1-\beta)e^{-t/\tau_{diffusion}}\right] \tag{6.11}$$

where ΔT_0^{D} is the temperature difference at $t = 0$ computed for the deuterium atoms between the two regions, β is an dimensional weight parameter, which gives an estimate of the contribution of the two relaxation mechanism, $\tau_{colored}$ is the decay time τ_K already introduced in Eq. (6.6), and $\tau_{diffusion}$ is the characteristic time of the slower relaxation. Hence, the free parameters in the fit functions are the diffusion time $\tau_{diffusion}$ and the β parameter. The interpretation of the temperature behavior is straightforward: the faster relaxation mechanism is the aforementioned vibrational relaxation, which involves the coupling between the excited OD stretching mode and unperturbed modes of the molecule, whether the slower decay is related to the thermal diffusion which follows the vibrational relaxation. The fit produce $\tau_{colored} = 8.7$ ps, $\tau_{diffusion} = 136$ ps and $\beta = 0.76$, indicating that the largest amount of energy is spread out by the vibrational decay. Considering that PBC are imposed and the function used to fit the temperature profile is expressed in terms of the fundamental component of the Fourier series (see Eq. (2.31)), it is reasonable to use the time associated with the heat diffusion to obtain a thermal diffusivity as $\bar{\kappa} = (L_z/2\pi)^2/\tau_{diffusion}$. For the simulation cell corresponding to Fig. 6.18, the thermal diffusion time produces $\bar{\kappa} = 7.4$ Å^2/ps.

The interplay between vibrational relaxation and heat diffusion

It is interesting to focus on the relation between the two relaxation mechanisms. To this aim, several simulation cells of increasing size have been realized, spanning the interval $4.0 \leqslant L_z \leqslant 74.3$ nm. The AEMD-GLE was used to determine the two relaxation times by adopting the aforementioned approach, producing the results reported in Fig. 6.19a and b. These results are obtained by performing a configurational average over several independent simulations, ranging from 160 replicas for the smallest sample to 4 replicas for the largest one. As expected, the thermal relaxation times increases with system size. Indeed, the diffusion time accounts for the time needed to relax the thermal excitation along the sample and larger systems require longer times. However, the thermal diffusivity shows a growing trend which tends to saturate after $\sim 20-30$ nm. Interestingly enough, the value obtained for thermal diffusivity is in very good agreement with Green-Kubo obtained values. Diffusivity

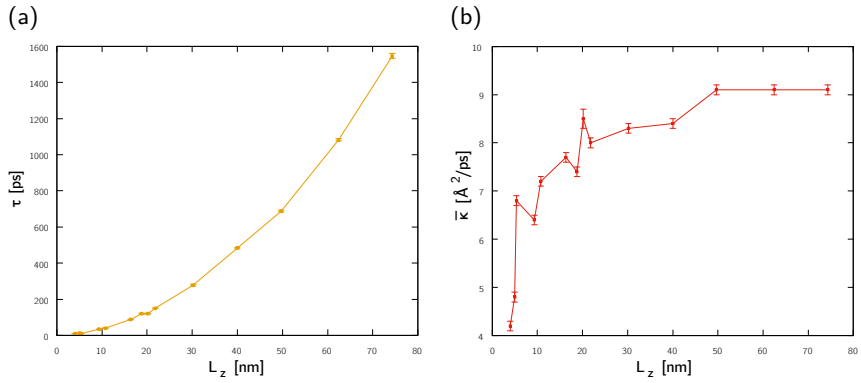

Figure 6.19. **a**: Heat diffusion times $\tau_{\text{diffusion}}$ as a function of system length. **b**: Corresponding diffusivity computed with the obtained $\tau_{\text{diffusion}}$ and the respective system length L_z.

values shown in Fig. 6.20 are calculated by considering the thermal conductivity values determined by Green-Kubo calculations (see Sec. 2.2.1) and using the relation $\bar{\kappa} = \kappa/\rho c_v$, with $c_v = 85.8$ J/mol K [337]. These values are in excellent agreement with experimentally determined thermal conductivity $\bar{\kappa}^{exp.} = 10.1$ Å^2/ps [335], providing that the model adopted for describing the molecule is correct.

In order to explain the weak size-dependence observed in Fig. 6.19b, the behavior of β can be helpful. Figure 6.21 shows a size dependence also for the β parameter, which suggest different contribution of the two relaxation mechanism for different time scales. From Figs. 6.19b and 6.21 it is argued that the heat diffusion occurs on a very different time scale than the vibrational relaxation. However, if the size involved in the process are too small, it is not possible to disentangle the two mechanisms: for $L_z \lesssim 20$ nm, both channel decays contributes the to thermal redistribution ($\beta \sim 0.5$), whereas for larger system the major contribution comes from the vibrational relaxation. Despite the higher amount of energy carried, the vibrational relaxations is very fast since it occurs thanks to the coupling between the excited OD stretching mode and the unexcited OD bending modes and the CH_3 modes as well. The

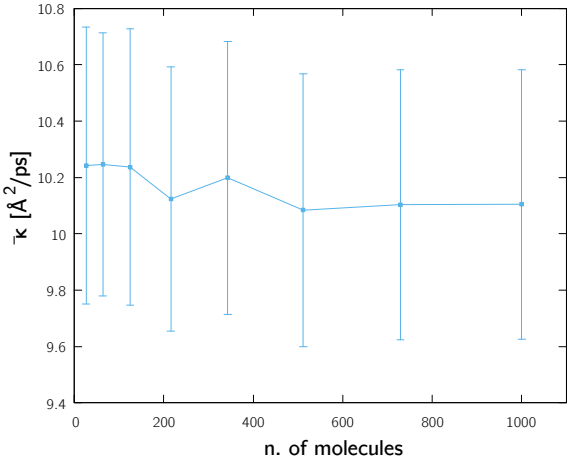

Figure 6.20. Thermal diffusivity calculated with Green-Kubo for increasing system size, reported as a function of the number of molecules in the simulation cell. Green-Kubo run were performed on cubic cell containing 3^3, 4^3, 5^3, 6^3, 7^3, 8^3, 9^3 and 10^3 molecules, carefully optimized and relaxed to their equilibrium volumes, prior to the thermal conductivity calculation.

coupling between the two processes implies that on short length scales, which means short time scales, heat transfer occurs when the vibrational excitation has not fully decayed. This results in an amount of energy to relax considerably larger than that competing to those lengths and resulting in a less efficient transport mechanism. Consequently, a continuum-based model could not be able to catch the full picture, as highlighted by the AEMD-GLE approach which, however, can investigate spectrally resolved excitations over a suitable range of system size.

As extensively explained in this chapter, detailed informations can be extracted from transient vDOS, hence further analysis will focus on a deep investigation of the transient vDOS in the two regions of the sample, in order to highlight microscopic mechanism from a spectral point of view occurring during the two decay relaxation.

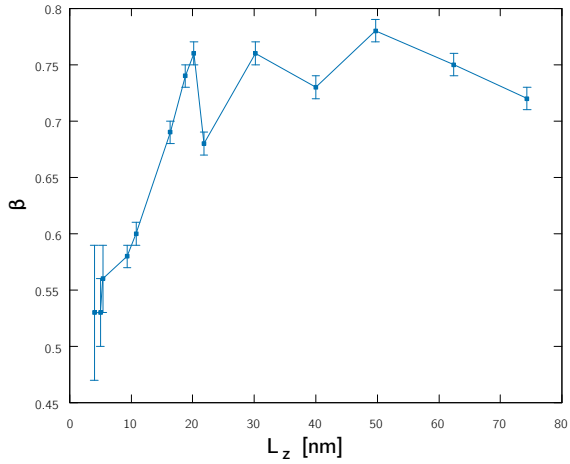

Figure 6.21. β parameters obtained by means of Eq. (6.11) as a function of system length.

7

ORGANIC GLASSES

Contents

Glasses can be conceptually considered as fluids systems that lost their ability to flow. As a matter of facts, from a structural point of view a glass is practically indistinguishable from the liquid phase prior to its formation. Glassy materials combine the disordered structure of a liquid with the mechanical properties of a solid.

Upon cooling below the freezing point T_m, molecular motion slows down. Figure 7.1 illustrates the temperature dependence of a liquid volume (or enthalpy) at constant pressure. If the liquid is cooled sufficiently fast, crystallization can be avoided and "supercooled liquid" regime is achieved, that is a metastable phase in which molecules will rearrange so slowly that they cannot adequately sample configurations in the available time allowed by the cooling rate [339, 340]. This characteristic *relaxation time* can increase of several order of magnitude up to $10^2 - 10^3$ seconds and the rate of change of volume or enthalpy with respect to temperature decreases abruptly (but continuously) to a value comparable to that of a crystalline solid. The temperature at which these changes occur is referred to as the glass transition temperature T_g. Typical laboratory cooling rates vary from 0.1 to 100 K/min, considerably slower than the rates achievable in computer simulations. The slower a liquid is cooled, the longer the time available for configurational sampling at each temperature, and hence the colder it becomes before falling out of liquid-state equilibrium. Consequently, T_g increases with cooling rate [341,

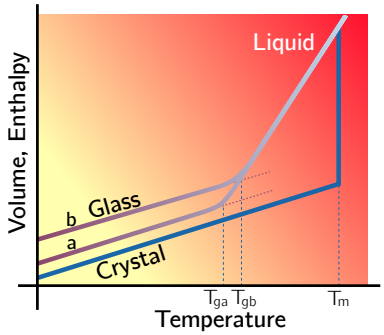

Figure 7.1. Temperature dependence of a liquid volume V or enthalpy H at constant pressure. T_m is the melting temperature. A slow cooling rate produces a glass transition at T_{ga}; faster cooling rate leads to a glass transition at T_{gb}. The thermal expansion coefficient and the isobaric heat capacity change abruptly but continuously at T_g. [338]

342]. The properties of a glass, therefore, depend on the process by which it is formed.

Glassy systems can be described in terms of a potential energy landscape, with thermodynamics and kinetics controlled by the minima and barriers on the landscape, respectively [338–340]. Many important issues could be addressed if liquids or glasses with very low energies could be created [88, 339, 343, 344]. For example, it might be possible to definitively understand the Kauzmann entropy crisis [345–347]. Boltzmann's entropy formula reads as

$$S(N, V, E) = k_B \ln \Omega \tag{7.1}$$

where S is the entropy, k_B is Boltzmann constant, Ω is the number of microstates accessible to N particles with fixed energy E in a volume V. Because Ω cannot be less than one, the entropy cannot be negative. When a crystal is cooled sufficiently slowly, it approaches a unique state of lowest energy, and hence its entropy approaches zero as $T \to 0$. If the entropy of a supercooled liquid were to become smaller than that of the stable crystal at the Kauzmann temperature, its entropy would eventually become negative upon further cooling. This impossible scenario represents *de facto* an entropy crisis.

The importance of organic glasses

Organic glasses are important for a wide range of scientific and technological processes [348]. Their utilization in organic electronics applications such as organic light-emitting devices (OLEDs) [349] is no longer a lab curiosity but rather a mature technology for high-performance displays [349, 350]. However, solid-state lightning applications that require high brightness are still to be realized due to the insufficient thermal stability of the organic materials. Thermal stress and degradation [351], together with the fact that the luminance and lifetime of OLEDs decreases when operated at high temperatures [352], are widely reported facts. In this respect, an appropriate understanding of thermal transport may help designing materials with tailored heat dissipation characteristics to minimize heat accumulation in OLEDs [353, 354] or to reduce heat flow while increasing charge transport in search for potential thermoelectric applications [355–358]. Their semiconductor nature and the low thermal conductivities make them suitable candidates to improve the thermoelectric figure-of-merit ZT. Most of the previous studies in this direction have been reported for polymer-based devices and fewer on small molecule organic semiconductors [359].

A striking discovery in the field of glasses showed that vapor deposition can bypass these kinetic restrictions and produce glassy materials that have extraordinary energetic and kinetic stability and unusually high densities. This was demonstrated for two organic glass formers: 1,3-bis-(1-naphthyl)-5-(2-naphthyl)benzene (TNB) ($T_g = 347$ K) and indomethacin (IMC) ($T_g = 315$ K) [360].

Ultrastable organic glasses

Physical vapor deposition has been shown to be a suitable tool to tailor the properties of the deposited layers, not only for organic semiconductors [361, 362], but also for many other small organic molecules [363–368]. When the deposition conditions, basically substrate temperature and growth rate, are properly set, glasses with exceptional thermodynamic and kinetic stability [361, 363, 364, 369], high densities [362, 370–372], low heat capacities [365, 373], low water uptake [374] or high moduli [375] can be obtained. These glasses, dubbed ultrastable, are currently gaining widespread attention within the glass community, and a recent report demonstrates the improved packing of these glasses can yield to outstanding improvements in OLEDs efficiency [376]. An interesting feature of some vapor-deposited organic glasses is that molecules can have average spatial orientations that differ from the random

distribution of an isotropic glass. Recent studies have started to focus on the molecular orientation in those materials and its influence on the efficiency of OLEDs [377]. The existence of molecular packing anisotropy in vapor-deposited organic semiconductor thin film glasses was first identified by Lin et al. [378]. Yokoyama and coworkers [379, 380] studied the degree of orientation depending on the molecular aspect ratio of the molecule and the deposition conditions. Dalal et al. [361] performed dichroism and birefringence measurements on several organic semiconductors, and proposed the ratio between the deposition temperature and the glass transition temperature, T_{dep}/T_g, to be the primary parameter affecting the molecular orientation. In particular, it has been shown that the lower the substrate temperature during growth, the higher the tendency towards horizontal orientation. This tunable molecular orientation provides new opportunities to tailor the electrical, thermal and optical properties of the glassy materials.

Thermal properties of organic glasses

Many previous studies have focused on the electronic transport properties of organic glasses and crystals, since this is a key parameter for the use of these materials in optoelectronic devices [381]. On the contrary, thermal conductivity measurements in small molecule organic glasses remains largely unexplored and only few studies are reported [382, 383]. In general, it is well known that increasing disorder has a remarkable effect on the thermal conductivity. For an inorganic material, such as silicon, the thermal conductivity varies from 150 W $m^{-1}K^{-1}$ in bulk Si to around 1.4 W $m^{-1}K^{-1}$ for the disordered material [384, 385]. This low value is frequently understood through the theory of the minimum thermal conductivity where atomic vibrations with mean free paths of the order of the interatomic distance contribute to heat transport [386]. In organic materials the van der Waals (vdW) interactions between molecules have a remarkable effect on heat propagation and disorder plays a comparatively less dramatic effect on the thermal conductivity compared to their crystalline counterparts. However, the current understanding of heat conduction in organic glasses is limited by the largely incomplete knowledge about the actual mechanisms ruling over thermal energy exchange in these systems and how the glass atomic-scale morphology affects transport. Measurements on thin-film organic crystals although more abundant also lack a proper understanding of how crystal anisotropy may affect thermal transport along and perpendicular to the molecular chain. The growth of large crys-

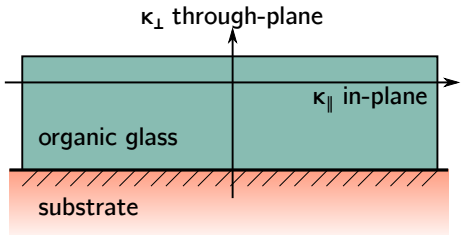

Figure 7.2. Schematic representation of a deposited organic glass, reporting the concept of in-plane and through-plane thermal conductivity. The in-plane thermal conductivity $\kappa_{\parallel}$ is defined as the average of the thermal conductivity values along the direction parallel to the substrate. Similarly, the through-plane thermal conductivity $\kappa_{\perp}$ is the thermal conductivity along the direction perpendicular to the substrate.

tals to minimize the strong influence of grain size on phonon transport is a requirement to unveil the role of crystal anisotropies in heat flow propagation. Ac-calorimetry was previously used to extract the thermal diffusivity of rubrene layers [387]. The thermal anisotropy ratio defined as the relative difference between *in-plane* and *through-plane* conductivity, $(\kappa_{\parallel} - \kappa_{\perp})/\kappa_{\perp}$ (see Fig. 7.2), was larger than 100% indicating poor thermal transport across the phenyl groups of the rubrene molecules. On the contrary measurements on 6,13-Bis(triisopropylsilylethynyl)pentacene, TIPSpn, show the through-plane thermal diffusivity is larger than the in-plane one due to an excellent π-orbital overlap [388]. The role of thermal anisotropy has been already addressed in polymeric samples [389] where rubbing or stretching has been used to produce the alignment of the backbone of the polymer along the fiber direction. In this case, the conductivity along the axis of the polymeric chain can be up to 20 times higher than in the perpendicular direction [390].

In this chapter it is reported how, by tuning the molecular orientation in glassy films of an organic semiconductor, such as toluene and TPD, the thermal anisotropy ratio can be modified to nearly 30%. The achievement of substantial thermal anisotropy in small molecule thin-film glasses is counter-intuitive since structural disorder should lower the anisotropy ratio. Here it is provided evidence that the change of thermal conductivity is mainly driven

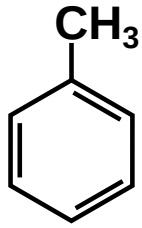

Figure 7.3. Schematic representation of the toluene molecule.

by the molecular packing anisotropy in the glass and that thermal transport along the N-N backbone of TPD molecule is strongly preferred with respect to the perpendicular direction due to a stronger molecular interaction in the former.

7.1 TOLUENE GLASSY FILM

As a validation for these simulation protocols, toluene (C_7H_8, with $T_g = 117$ K) was selected as a model material because of its simple chemical structure and its well-characterized glassy behavior [391]. The actual molecular structure of toluene was at first generated and fully relaxed using the following computational set-up. The toluene molecule, shown in Fig. 7.3, is modeled according to the CVFF force field [392], where crosscoupling terms between the various bonded terms provide an accurate description of intramolecular interactions. The non-bonded interactions are in turn described by a superposition of a Lennard-Jones potential (addressed to describing the vdW contribution) and of a Coulomb term as follows

$$\sum_{i,j}\left(\frac{A}{r_{ij}^{12}}-\frac{B}{r_{ij}^{6}}\right)+\sum_{i,j}\frac{q_i q_j}{r_{ij}} \tag{7.2}$$

where the sum is performed over all the pairs of non-bonded atoms. The Lennard-Jones term is truncated by a cut-off set at 10.0 Å, while a particle-particle particle-mesh solver approach is adopted to solve the electrostatic problem in the reciprocal space. Coulomb interactions are calculated by assuming fixed charges, as previously obtained by fitting the electrostatic potential

of an all-electron Hartree-Fock calculation performed with a medium-sized basis set $6-31G^*$. The fitting was performed using the RESP method. [313, 314]

7.1.1 *Generating a glass by quenching-from-the-melt*

The simulation cell adopted for the quenching-from-the-melt protocol was obtained by replicating the molecule in the three directions: a system containing 1000 molecules (15000 atoms) of toluene was obtained by replicating the molecule $10 \times 10 \times 10$ times, then a NPT simulation was performed to optimize the density at ambient temperature and pressure. Afterwards a simulated NVT annealing was carried out at 550 K (well above toluene melting temperature of $T_m = 178$ K) for 300 ps.

The quenching-from-the-melt procedure

Toluene glasses were obtained by unconstrained quenching-from-the-melt: the previously prepared liquid system was quenched to 10 K at four different cooling rate of $10^{-3} - 10^{0}$ K/fs (very slow for simulations, but still much higher than typical experimental rates). The potential-energy landscapes are sampled by minimization of the potential energy: configurations were then saved on-the-fly during cooling every 18 K and further aged for 50 ps at that temperature. Local-energy minimization was performed for a subset of configurations generated at each temperature (see Fig. 7.4b) and finally the *inherent structure energy* E_{IS} is computed through accurate configurational averages [88, 393–396]. The inherent structure is the structure corresponding to the minimum energy at that temperature and, consequently, the E_{IS} is the energy related to that configuration. Since at any given temperature the energy landscape is characterized by a large number of minima, the role of the inherent structure energy is to identify the global minimum of the energy landscape associated to that temperature.

Inherent structure energy of toluene

Figure 7.4a shows the temperature-dependent average inherent structure energy of toluene ordinary glasses prepared at different cooling rates. Three different regions can be distinguished in the plot:

1. the high temperature region, in which E_{IS} decreases progressively with temperature but it is weakly dependent on it: at high temperature the system explores a broad range of minimum energies, as shown for $T =$

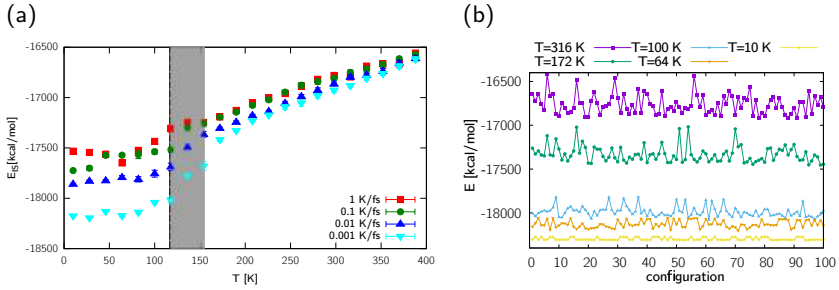

Figure 7.4. **a**: Average per-particle inherent-structure energy for toluene ordinary glasses prepared by cooling the liquid at different rates. Each point of the plot represents a configurational average performed over 50 inherent structure. **b**: Individual minimum energies for the configurations at cooling rate 10^{-3} K/fs. At high and intermediate temperatures, these individual energies cover a broad range. At low temperatures the sampled energies become narrowly distributed around the average values.

316 K and T = 172 K in Fig. 7.4b. Dynamics is dominated by free diffusion and sufficient kinetic energy to sample the entire landscape, characterized by shallow minima. This behavior is basically independent from the cooling rate;

2. the glass transition region, in which the energy landscape becomes sharply and starts being populated by deeper minima and higher barriers. The energy landscape, in principle, changes strongly with temperature and so does E_{IS}. This is strictly verified for the slowest cooling rates, while 1 K/fs seems to be too high to accurately sample the energy landscape;

3. the low temperature region, where system gets trapped in a minimum of the energy landscape corresponding to a specific glassy configuration. Lowering the temperature, the sampling is progressively biased towards lower energies, that become more narrowly distributed around the average values, as shown for T = 64 K and T = 10 K in Fig. 7.4b. Similarly

to what found in the high temperature region, E_{IS} is temperature independent.

From the slope change of $E_{IS}(T)$ between the two last regions, it is possible to determine the glass transition temperature for toluene which results $T_g = 118$, in very good agreement with the experimental value of $T_g^{exp} = 117$ K.

7.1.2 *Generating anisotropic samples*

In order to search for anisotropy-related features in thermal transport, samples with some in-plane preferential alignment of molecular axis were generated. A simulation cell with 1000 toluene carefully relaxed molecules were obtained by a super-imposed orientational order: they were placed on a regular 2D xy grid and piled-up along the z direction. The system was gently relaxed at low temperature by performing NVT dynamics for 200 ps. Finally, a NPT simulated annealing was carried out: samples were heated up to the target temperature, with a cooling rate of 10^{-4} K/fs and then further equilibrated for 200 ps. The resulting samples show almost identical structural features; Fig. 7.5a compares the density of the two toluene samples (quenched-from-the-melt and anisotropic), showing that the latter is slightly less dense, while Fig. 7.5b shows the radial distribution function calculated for both samples: the structure is almost the same, guaranteeing an overall amorphous structure for the anisotropic system, despite an additional peaks in the $C-C$ radial distribution function due to the local order and an over-coordination of the anisotropic sample beyond intramolecular distances.

7.1.3 *The role of anisotropy in thermal transport*

For each system thermal conductivity was calculated for different temperature, spanning from low temperatures far below the corresponding glass transition to values beyond T_g. Thermal conductivity was calculated using the Green-Kubo method (see Sec. 2.2.1): the advantage of this approach lies in the fact that, since heat current is a vector, calculating the contribution to thermal conductivity in the three directions is straightforward. In other words: just one calculation allows for predicting thermal transport either along the direction

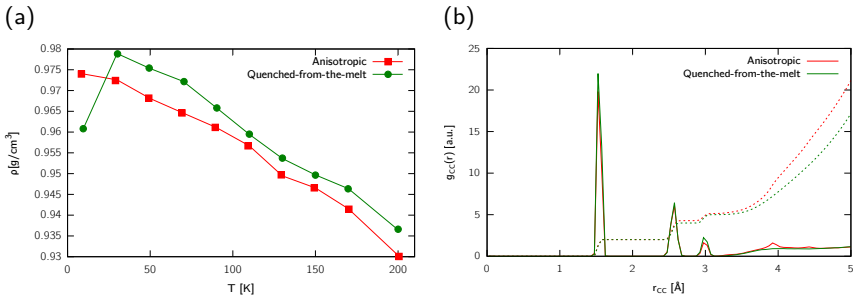

Figure 7.5. **a**: Density of the toluene samples as a function of temperature: the obtained values are in excellent agreement with experimental reported ones ($\rho^{exp} = 0.87$ g/cm^3 at T $= 300$ K). **b**: Radial distribution function obtained considering only carbon atoms: the dashed lines represent the integrated values over the distance of the $g_{C-C}(r)$ function, showing a long range over-coordination of the anisotropic samples..

of preferential alignment and normal to it. This allows for the assessment of any possible anisotropic behavior.

Thermal conductivity for toluene has been investigated for temperatures ranging from 10K to 200K: the system was equilibrated by NVT dynamics at the operative temperature for 20 ps, then was aged in the microcanonical ensemble for further 200 in order to achieve the convergence of the heat current autocorrelation function. Finally thermal conductivity values were averaged over the last 50 ps of simulation. Figure 7.6a shows the temperature-dependent thermal conductivity for the quenched-from-the-melt toluene: as expected, by reaching the glassy state through a cooling process, a completely isotropic system is produced; accordingly, the corresponding contribution to thermal conductivity from the x, y, and z component of the heat current is basically just the same. This is in sharp contrast to what found for the "aligned glass" case, reported in Fig. 7.6b.

Thermal anisotropy of toluene

Simulation results clearly show the thermal conductivity in the in-plane "parallel" direction (i.e. the xy-plane) is appreciably higher with respect to the through-plane direction (z). At very low temperatures the difference is rather high, reducing with increasing temperature, as expected: as a matter

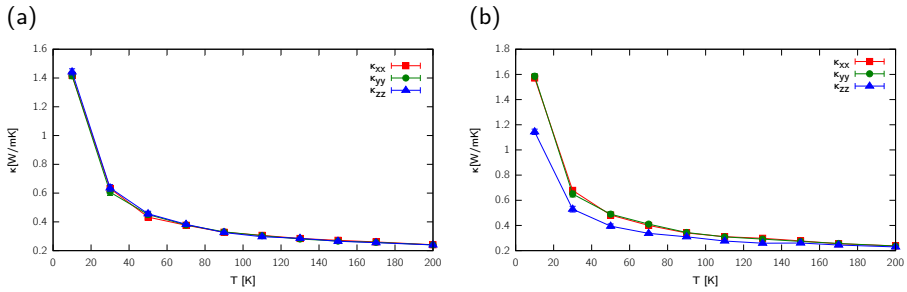

Figure 7.6. **a**: Thermal conductivity along the three directions as a function of temperature for a quenched-from-the-melt toluene sample. **b**: Thermal conductivity along the three directions as a function of temperature for an anisotropic toluene sample.

of fact, the temperature breaks the alignment of the molecules in the xy-plane. Alignment is still appreciable provided that $T < T_g$. Beyond this value the system completely loses its anisotropy and thermal conductivity approach the value of quenched-from-the-melt samples.

Figure 7.7 shows a comparison between the two situations, by plotting the *relative difference* $\Delta\kappa_\perp$ between the in-plane and the through-plane thermal conductivity defined as

$$\Delta\kappa_\perp = \frac{\kappa_\parallel - \kappa_\perp}{\kappa_\parallel} \tag{7.3}$$

where $\kappa_\perp$ is the thermal conductivity along the through-plane direction and $\kappa_\parallel = \langle \kappa_{in-plane} \rangle \equiv (\kappa_{xx} + \kappa_{yy})/2$ is the average conductivity in the xy-plane.

Thermal conductivity obtained for quenched samples is represented as a straight line at $\Delta\kappa_\perp = 0$ with its corresponding standard deviation (grey shaded area). In this case the difference is between in-plane and through-plane conductivity is centered at ~ 0. The difference in thermal conductivity values can be explained by considering the ordering of the molecules: the interactions between the toluene molecules in the through-plane direction is governed mostly by the $\pi - \pi$ interactions due to the stacking of the molecules while

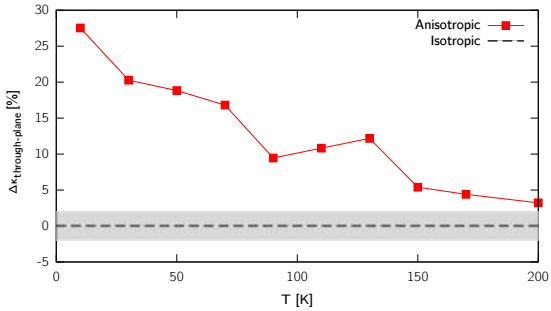

Figure 7.7. Relative variation of the through-plane thermal conductivity computed as $(\kappa_{\parallel} - \kappa_{\perp})/\kappa_{\parallel}$. The black dashed lines refers to the average value of the isotropic sample which averages to zero and the grey shaded area accounts for the uncertainty due to the numerical noise.

the in-plane directions are ruled by much more stronger interactions (bonded interactions dominate with respect to the vdW between sigma orbitals, which however is stronger than that occurring between π ones.).

A tentative explanation of how thermal transport is influenced by anisotropy in toluene is given in Fig. 7.8a, which shows the vDOS of toluene in the regions of C-H stretching computed at T = 10 K. The blue curve is the vDOS of the quenched toluene, which can be taken as a reference: the vDOS computed for the in-plane direction shows a higher contribution in correspondence of the C-H stretching at 2970 cm^{-1} (the peak centered a 2900 cm^{-1} is referred to the C-H stretching of the methyl group). This suggests that greater number of C-H oscillator are contributing to the vibrational properties of the system. The other significant contribution to the vibrational properties of the system comes from the C-H bending modes (either of the ring or of the methyl group) shown in Fig. 7.8b: the intensity of the peak for in-plane directions is appreciably higher than the through-plane one. The peak at higher frequency shows a lower contribution for the in-plane direction: this is related to the C-C stretching mode which however is not fundamental since the overall contribution to the vibrational spectrum is rather low.

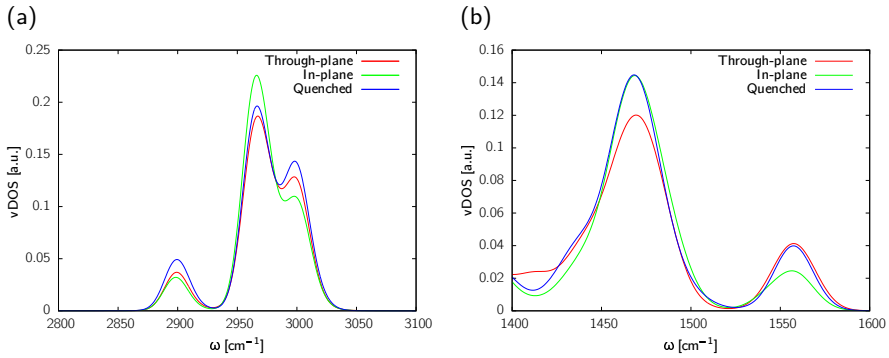

Figure 7.8. **a**: Vibrational density of state calculated for the toluene sample in the C-H stretching region for the isotropic and for the anisotropic sample. **b**: vDOS calculated for the toluene sample in the C-H bending region for the isotropic and for the anisotropic sample. In both case, for the anisotropic sample the contribution coming from the in-plane and the through-plane motion are distinguished.

7.2 TPD GLASSY FILMS

Toluene glass served as a validation for the cooling protocol and the glass modeling but also provided evidence that anisotropy can play a crucial role in thermal conductivity of organic glasses. In fact, despite its small size and its symmetric structure, the super-imposed planar alignment results in a less efficient energy transfer between the through-plane DOF.

A very well-known glass former, among the organic glasses, is the TPD molecule, already subject of investigation for stability issues [361, 395], which has a slightly elongated structure, shown in Fig. 7.9, and which is worth of investigating in order to highlight the mechanisms leading to orientational anisotropy.

The same energy minimization and geometry optimization followed for toluene was adopted in this case: the CVFF force field was adopted and the fixed partial charges were obtained by fitting the electrostatic potential of an

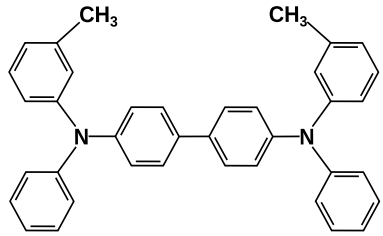

Figure 7.9. Schematic representation of the TPD molecule.

all-electron Hartree-Fock calculation performed with a medium-sized basis set $6-31G*$.

7.2.1 *The role of the substrate*

Toluene structure is characterized by a planar geometry, which is also preserved in vacuum performed simulations. TPD molecule, however, in vacuum tends to assume a twisted configuration which introduces complications in realizing an anisotropic structure with a preferred in-plane alignment. Thus, it is necessary to exploit the role of the substrate to enforce anisotropy. A $20a_0 \times 20a_0 \times 5a_0$ silicon substrate is realized, where $a_0 = 5.4305$ Å is equilibrium silicon lattice constant for Tersoff potential [89]. Two kind of anisotropic samples are realized: samples which will be referred to as *xy-ISO* and samples referred to as *ANIS*. Both are characterized by a preferential in-plane molecular orientation, where the referencez-plane is in any case the substrate surface: this feature has been obtained by enforcing the planar alignment of molecular axis during the sample preparation. A first layer of 47 molecules is placed on top of the substrate, followed by a geometry optimization and a low temperature (T = 1 K) annealing for 100 ps. However, the two systems differ in that the in-plane alignment is totally random in the xy-ISO sample or further enforced to align to the x direction for the ANIS sample, respectively. As for xy-ISO samples, in fact, there was no in-plane order, while in the ANIS samples molecular axes were mainly oriented along an in-plane direction. This procedure was then repeated piling up to 16 layers: at each step the whole structure was very carefully relaxed. This effectively generated a 6.9 nm-thick film of 752 TPD

Planar anisotropy

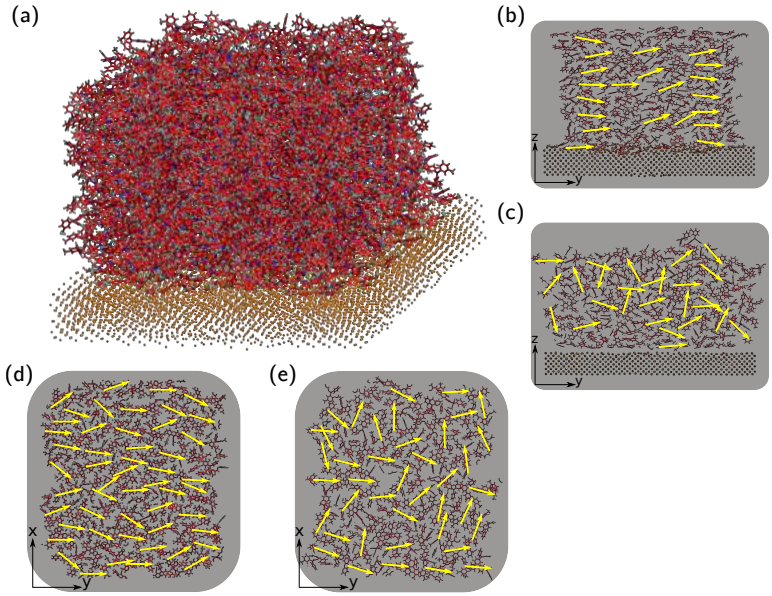

Figure 7.10. **a**: perspective view of the simulated TPD film deposited on Si substrate. **b** and **c**: side view of, respectively, xy-ISO and ISO samples. **d** and **e**: top view of, respectively, ANIS and xy-ISO samples. Yellow arrows represent the orientation of the molecule backbone, reflecting the anisotropy of the systems.

molecules, which resulted aligned parallel to the substrate. Eventually, the final sample was gently heated up (at 10^{-4} K/fs rate) and then equilibrated (400 ps + 100 ps) at the measurement temperature, obtaining a density in the range $1.080 - 1.085$ g/cm^3, for the ANIS samples, and $1.069 - 1.079$ g/cm^3 for the xy-ISO. As for the isotropic case, which will be referred to as *ISO*, the xy-ISO sample was used as starting configuration: the deposited film was heated up to 900 K during a 300 ps-long NVT run, and then annealed at that temperature for further 500 ps. This allowed the TPD film to completely lose its previous anisotropic structure. The molecular orientation was carefully monitored on-the-fly to control that a fully isotropic sample was indeed forming. The TPD film was then cooled (at 10^{-4} K/fs rate) and the equili-

brated at the measurement temperature, resulting into a density in the range $1.059 - 1.065$ g/cm^3. Representative views of the structures are shown in Fig. 7.10. In short, the sequence (ISO)-(xy-ISO)-(ANIS) provides an increasing character of molecular anisotropy.

7.2.2 *Anisotropic thermal conductivity*

The absolute values of thermal conductivity are appreciably larger than those obtained experimentally, $\kappa^{ISO} \backsimeq 0.85$ W m^{-1}K^{-1} in comparison to $\kappa^{exp} \backsimeq 0.15$ W m^{-1}K^{-1} at $T = 300$ K.

This is related to the adopted force-field, which description of intra- and intermolecular forces often can represent an approximation, especially for molecules with such complicate geometry. However, molecular simulations are a powerful tool to provide trend and relative values: for sake of comparison, thermal conductivity values are normalized to the value obtained at $T = 320$ K such as $(\kappa_{xx} + \kappa_{yy} + \kappa_{zz})/\kappa_{T=320K} = 1$, the closest value to the glass transition temperature, which for TPD results $T_{TPD}^{exp} = 333$ K.

The resulting picture is fully consistent with experimental evidence [397]: Fig. 7.11 shows the thermal conductivity of the three sets of TPD along the different directions and it is clear how the system with anisotropy transport heat along the x direction with respect to the ISO sample.

In addition, the xyISO sample is characterized by a higher thermal conductivity along the y than the ANIS sample: the latter system in fact has a preferential alignment of the molecule backbone and this suggest that, in the direction perpendicular to the backbone, the intermolecular interactions are poorly conductive. Interesting enough, the ISO sample shows higher values along the z direction due to the enforced planar stacking parallel to the substrate of the xyISO and ANIS case.

As shown in Fig. 7.12a, which reports the relative difference $\Delta\kappa_{in-plane} = (\kappa_{xx} - \kappa_{yy})/\kappa_{xx}$ between the in-plane conductivity, thermal transport is highly influenced by the molecular orientation, since $\Delta\kappa_{in-plane}$ value for the ANIS sample is found to be around 10% and it is temperature independent while the xyISO sample shows values very close to zero as expected for an isotropic configuration, although some fluctuation is still

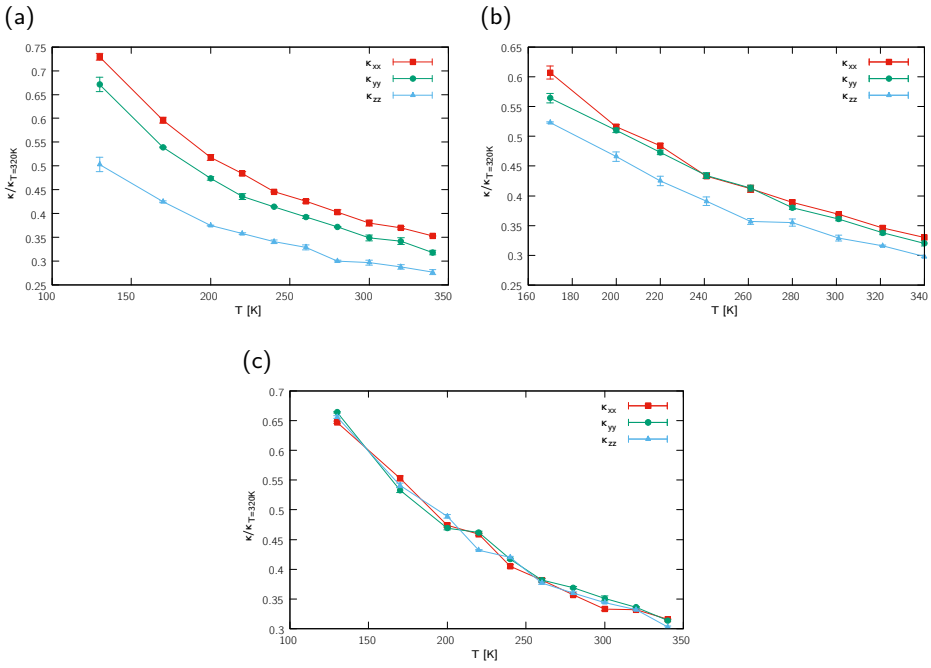

Figure 7.11. **a**: Thermal conductivity values for the ANIS sample, normalized at $\kappa^{ANIS}_{T=320K} = 0.46$ W m^{-1}K^{-1}. The anisotropic character of the sample is reflected on the behavior of thermal transport in the three directions, highest values are obtained for the x direction along which all the molecules in the system are aligned. **b**: Thermal conductivity values for the xyISO sample, normalized at $\kappa^{xyISO}_{T=320K} = 0.56$ W m^{-1}K^{-1}. In this case, despite some fluctuation which could be reducing performing configurational average, the x and y directions are characterized by the same value of thermal conductivity because the molecules are randomly oriented in the xy-plane. **c**: Thermal conductivity values for the ISO sample, normalized at $\kappa^{ISO}_{T=320K} = 0.85$ W m^{-1}K^{-1}. All the three directions have the same efficiency in transferring heat.

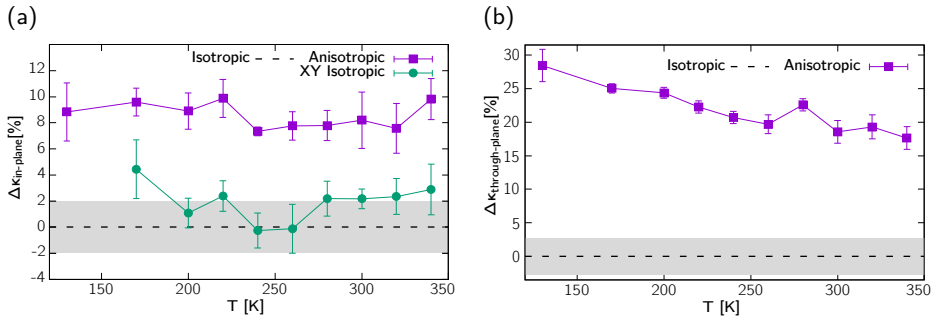

Figure 7.12. **a**: Relative variation of the in-plane thermal conductivity for the three system investigated. The ANIS sample is characterized by an appreciable difference which is basically temperature independent, while for the xy-ISO sample $\Delta\kappa_{in-plane}$ averages to a value close to zero as expected, due to the random orientation of the molecules in the xy-plane. **b**: Relative variation of the through-plane thermal conductivity. The results for the ANIS sample show how the geometry of the TPD molecule is much more anisotropic with respect to the toluene one.

present. Similarly, the through-plane difference calculated according to Eq. (7.3) (Fig. 7.12b), assumes high values with a weak, but still appreciable, temperature dependence. Thus the substrate drives molecules to organize in-plane and the consequence of the more complicated geometry of TPD molecule is that the anisotropy features are preserved at relatively high temperature, unlike the toluene case.

7.2.3 *Molecular orientation*

A useful interpretation for thermal conductivity results is provided by an in-depth analysis of the molecular orientation. The spatial orientation of TPD molecules can be unambiguously specified by defining two vectors, namely: (i) the vector lying along the direction linking the nitrogen atoms of the molecule (hereafter labeled as NN-vector), shown in Fig. 7.13a, and (ii) the vector identifying thez-plane of the molecule (hereafter labeled as planar vector). This

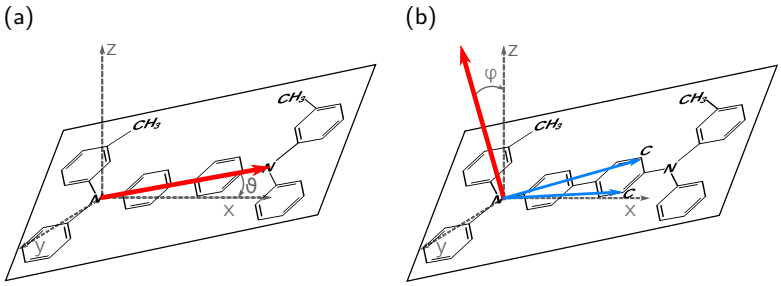

Figure 7.13. **a**: Projection of the NN-vector along x,y,z directions. **b**: Orientation of the planar vector. The two vectors are represented by a red arrow.

latter is defined by considering the vector product between the two vectors joining one nitrogen atom to two carbon atoms of the opposite aromatic ring of the TPD backbone, as reported in Fig. 7.13b. The distribution of the angles that vectors (i) and (ii) form with the three Cartesian coordinates (x, y, z) will provide informations on the overall molecular orientations in the sample (the Cartesian coordinates are defined as reported in Fig. 7.10. In Fig. 7.14 a thorough comparison between the ANIS and xyISO samples is performed by considering the orientation of the NN-vector (Fig. 7.14a, b and c); the ANIS and ISO samples are in turn compared by considering the orientation of the planar vector (Fig. 7.14d, e and f). All data are calculated at T = 280 K. It is possible to extract quite a few information. The angular distribution of the NN-vector in the ANIS sample is highly peaked for $\cos\theta_x = \pm 1$ which explains the higher efficiency of thermal transport along x direction. On the other hand, the xyISO sample shows a much flatter distribution due to its random orientation in the xy-plane (see Fig. 7.14a). Furthermore, the ANIS sample shows a (broad) distribution around $\cos\theta_y = 0$, which is a fingerprint of a preferential normal orientation of the molecules with respect to the y direction. Again, for the xyISO sample, the distribution is much flatter and contains non-zero values for a greater range of $\cos\theta_y$ values (see Fig. 7.14b). Both samples show a distribution peaked around $\cos\theta_z = 0$, confirming the $\pi - \pi$ stacking along the z direction: this reflects in a less efficient thermal transport (see Fig. 7.14c). Another interesting features is that ANIS sample

Angular distributions

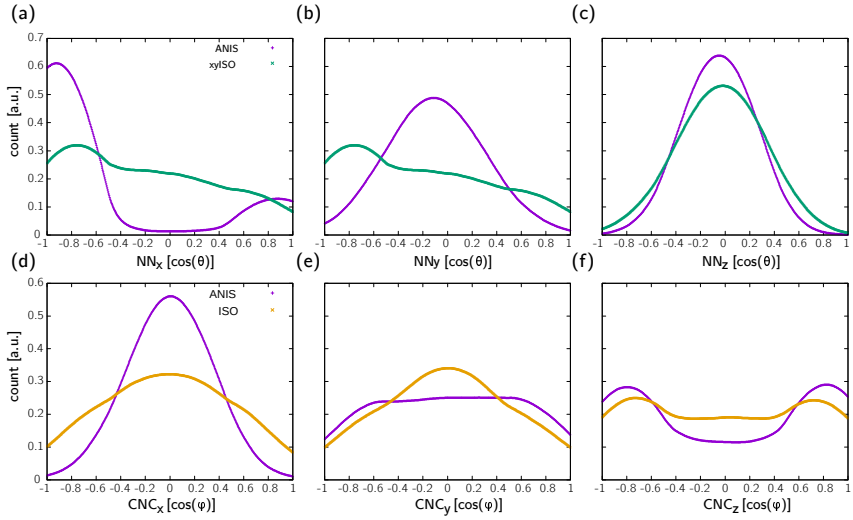

Figure 7.14. **a**, **b** and **c**: Orientation of the NN-vector for the ANIS (purple curve) and xyISO samples (green curve). **d**, **e** and **f**: Orientation of the planar vector for the ANIS (purple curve) and ISO samples (yellow curve).

shows a distribution peaked around $\cos\varphi_x = 0$, suggesting that molecules are on planar vector average parallel to the xy-plane and aligned along x. On the other hand, the ISO sample shows a broad and flatter distribution due to a random orientation of the planar vector (see Fig. 7.14d). The ANIS sample also show a flat distribution, corresponding to a randomly tilted orientation of the molecular$z$-plane with respect to y. This does not affect thermal transport since for such a system thermal conduction preferentially occurs along the x direction. The ISO sample has roughly the same distribution shown for $\cos\varphi_x = 0$ (see Fig. 7.14e). Finally, the distribution for z component (describing the orientation with respect to the substrate$z$-plane) is peaked at $\cos\varphi_z = \pm 1$ for the ANIS sample, accounting for a preferential stacking arrangement along the z direction. The same distribution for the ISO sample, in turn, is almost flat, as a consequence of the isotropy of the system. The small shoulders at $\cos\varphi_z = \pm 1$ are relative to the molecules directly attached to the substrate and to the molecules in the last z-plane of the TPD film, since they preserve an overall planar arrangement (see Fig. 7.14f).

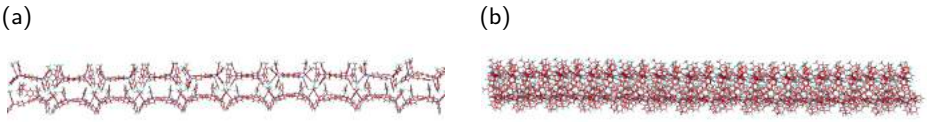

Figure 7.15. **a**: Structure realized organizing the TPD molecule along the backbone direction. **b**: Structure realized piling up the molecule along the $\pi-\pi$ stacking direction.

7.3 A PHENOMENOLOGICAL MODEL FOR TPD THERMAL CONDUCTANCE

Anisotropic thermal transport suggests that different heat flows are experienced by molecules oriented along the backbone direction or through $\pi-\pi$ stacking, which occurs in the normal-to-backbone direction. To validate the idea that thermal transport is preferred along the backbone direction of molecular chains two different quasi-1D structures were simulated: (i) a linear bundle of TPD molecules aligned along the N-N axis and (ii) a line-up of TPD molecules aligned along the direction of $\pi-\pi$ bonding. Such configurations are shown in Fig. 7.15 and hereafter will be referred to as backbone stacking or $\pi-\pi$ stacking, respectively. A structural unit containing $2\times2\times2$ TPD molecules is replicated along either backbone or $\pi-\pi$ stacking directions. The resulting structures were equilibrated with a low temperature NVT dynamics followed by a NPT relaxation for a total simulation time of 200 ps. The simulation cell was relaxed only along the direction of 1D alignment. Due to the TPD geometry, the $\pi-\pi$ configuration results more packed than the backbone chain and the same number of molecules produced a shorter $\pi-\pi$ stacking configuration. Both pseudo-1D samples were prepared with the same density, namely: $\rho_{\text{backbone}} = 0.83$ g/cm^3 and $\rho_{\pi-\pi\text{ stacking}} = 0.84$ g/cm^3.

7.3.1 *Stacking vs. backbone*

Thermal conductivity for these structures was calculated by means of AEMD method (see Sec. 2.2.3). The results can be interpreted in terms of a different

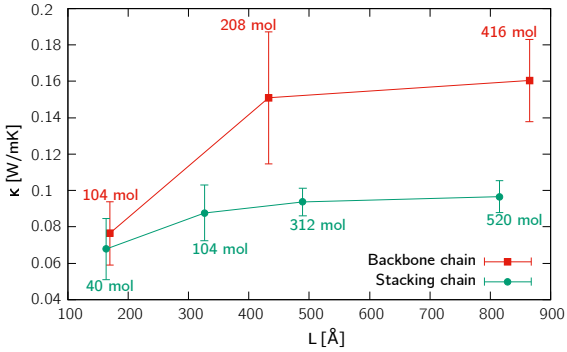

Figure 7.16. Thermal conductivity as a function of length for the quasi-1D structures.

efficiency in transmitting heat carriers, depending on the direction of the heat flow with respect to the molecular orientation. Figure 7.16 reports the thermal conductivity versus length for the linear chains. The overall trend shows a saturation for increasing length and confirms that the direction perpendicular to the backbone is detrimental for heat transport. Present simulations intelligibly reported a 70% higher thermal conductivity for the backbone configuration. Moreover, a much larger number of TPD molecules is needed to reach the "bulk", definitely confirming a less efficient transport mechanism along the $\pi - \pi$ direction.

7.3.2 *Intermolecular interactions*

In order to explain this result, the interaction strength between molecules in both 1D arrangements as function of the inter-molecular spacing was calculated. More specifically, the average intermolecular distance $\langle r_{inter} \rangle$ was varied in the range $4.75\text{Å} \leqslant r_{inter} \leqslant 7.5\text{Å}$ and the corresponding configurational energy has been computed as shown in Fig. 7.17. Such a potential energy nearby the equilibrium distance is basically harmonic, while at smaller/higher distances the onset of anharmonic behavior is observed, as expected. A parabolic fitting near the minimum yields the effective force constants char-

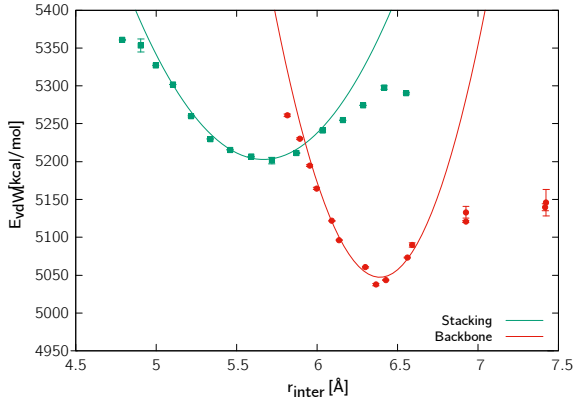

Figure 7.17. Configurational energy due to vdW interactions as a function of the intermolecular distance.

acterizing the intermolecular coupling within a simple spring-and-ball picture. The quadratic fit for both set of data is a function of the form

$$E(r) = K(r - r_0)^2 + E_0 \tag{7.4}$$

where K is the spring constant and E_0 is the energy minimum located at a r_0. The obtained values are $K_{backbone} = 824.7$ kcal/molÅ^2, $r_{backbone} = 6.39$ Å and $E_{0,backbone} = 5047.2$ kcal/mol, for the backbone configuration and $K_{stacking} = 312.7$ kcal/molÅ^2, $r_{stacking} = 5.67$ Å and $E_{0,stacking} = 5202.8$ kcal/mol for the stacking configuration. Consistently with the adopted picture, it can be argued that a stiffer effective spring value translates into a more efficient thermal conduction, according to the following twofold heuristic argument. In general, thermal conductivity is proportional to the group velocity of heat carriers: since a larger force constant causes a steeper vibrational branch, this reflects into a higher group velocity. On the other hand, heat current basically represents the energy transferred by a flux of carriers corresponding to atomic vibrations: the higher the force constant, the higher the vibrational energy, the higher the energy of such heat carriers. The thermal anisotropy reported here qualitatively agrees with observations in aligned polymers systems where an increase in the strength of intermolecular forces leads to an enhancement of the thermal conductivity [389]. The in-plane and

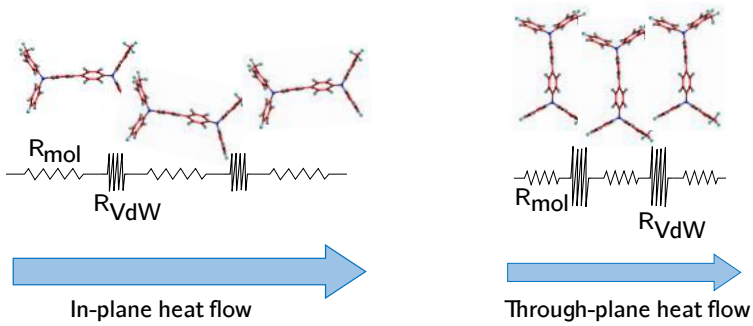

Figure 7.18. Schematics of thermal resistance network in the in-plane direction (left) and the through-plane direction (right). R_{VdW} accounts for the strength of the intermolecular interactions and R_{mol} represents the intramolecular thermal resistance.

TPD as a thermal resistive network

through-plane conductance can be estimated considering that the molecules and vdW interactions form a thermal resistive network, as shown in Fig. 7.18. The interface thermal resistance (ITR), corresponding somehow to the coupling between neighboring molecules that are joined through weak vdW interactions, is assumed to dominate thermal transport if the molecule and the vdW interactions can be seen as a thermal resistive network. A stronger molecular interaction is represented by a lower ITR (higher thermal interface conductance) and the intermolecular $\pi-\pi$ stacking entails higher thermal resistance between molecules.

The total thermal resistance can be written as the sum of the two series resistances $R_T = R_{T,mol} + R_{T,VdW} = N_{mol}R_{mol} + N_{VdW}R_{VdW}$, where N_{mol} and N_{VdW} are the number of molecular and vdW units and R_{mol} and R_{VdW} the individual resistances associated to each unit, respectively. Writing the above R_T in terms of the individual conductivities

$$R_T = N_{mol}\frac{L_{mol}}{\kappa_{mol}} + N_{VdW}\frac{L_{VdW}}{\kappa_{VdW}} \tag{7.5}$$

with L_{mol} and L_{VdW} being the lengths of the single units. Therefore, it is possible to write the total conductance (along a specific direction) as

$$G_T = \frac{\kappa}{L} = \frac{1}{R_T} = \frac{\kappa_{mol}\kappa_{VdW}}{\kappa_{VdW}N_{mol}L_{mol} + \kappa_{mol}N_{VdW}L_{VdW}} \tag{7.6}$$

where L is the total thickness and κ is the computed thermal conductivity (along a specific direction). Assuming that the conductance is dominated by an ITR due to vdW interactions, it is correct to write $\kappa_{mol} \gg \kappa_{VdW}$ leading to a simplified expression

$$G_T \simeq \frac{\kappa_{mol}\kappa_{VdW}}{\kappa_{mol}N_{VdW}L_{VdW}} = \frac{G_{VdW}}{N_{VdW}} \tag{7.7}$$

Putting together Eqs. (7.6) and (7.7), an expression of the thermal interface conductance for the interatomic interactions is obtained

$$G_{VdW} = \kappa\frac{N_{VdW}}{L} = \frac{\kappa}{L_{mol} + L_{VdW}} \tag{7.8}$$

G_{VdW} stands for the conductance of an individual unit (the interface thermal conductance due to vdW interactions). The average distance between molecules $L_{mol} + L_{VdW}$ in the in-plane and through-plane directions is calculated from the simulated XRD profiles, reported in Fig. 7.19 and compared to the values derived by Gujral et al. [398] that used XRD to evaluate the structure of a TPD sample deposited at 260 K. i.e. with molecules on average oriented parallel to the substrate surface. XRD patterns were calculated for both the ANIS and xyISO samples at $T = 300$ K and estimated according to the procedure described in [399] and implemented in LAMMPS, with an incident wavelength $\lambda = 1.541$ Å as used in similar GIWAXS studies [400, 401]. The XRD patterns were calculated by considering only the nitrogen atoms belonging to different TPD molecules. This choice allowed to unveil the interchain structural features discarding the intramolecular peaks. The simulated average distances are $2\pi/Q \sim 4.50$ Å (4.58 Å) and 5.9 Å (6.0 Å) in the through-plane, i.e. the z-plane, and in-plane, i.e. the xy-plane, respectively, for the ANIS (xyISO) sample. Experimentally the distance between molecules in the through-plane direction is well defined by the low-angle XRD peak located at $Q \simeq 1.4$ Å^{-1} that gives 4.5 Å. The value associated to the xy-plane is more difficult to evaluate since several low-angle peaks or shoulders appear at 1.2, 1.0 and 0.75 Å^{-1}. A rough averaging gives a mean distance value around 6 Å. The agreement between simulated and experimental data support the suitability of the simulated structure. According to Fourier law the heat flux J is proportional to the temperature difference ΔT through $J = G\Delta T$,

Simulated X-ray diffraction

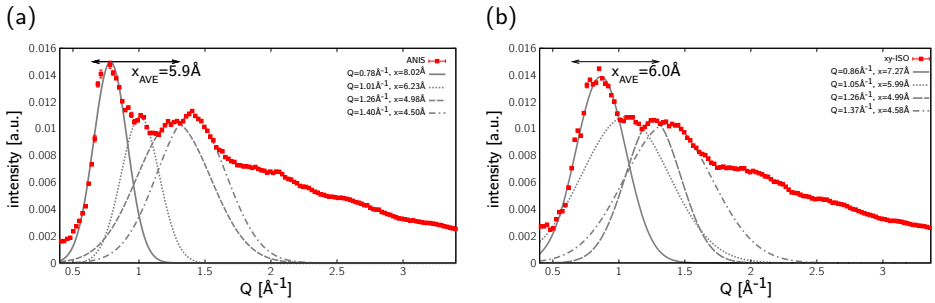

Figure 7.19. **a**: XRD diffraction pattern of the ANIS sample. **b**: XRD diffraction pattern of the xyISO sample. The major contribution is located around 1.4 Å^{-1} and is associated with the planar stacking of the molecules since it correspond to the typical distance in the $\pi - \pi$ stacking configurations. The other peaks at lower angles are relative to the different orientation of the molecule in-plane and an amplitude-weighted average produces a distance around 6 Å. Red squared symbols correspond to the calculated profile, while black lines provide a Gaussian fit for the different peaks.

where G is the thermal conductance. Considering the in-plane and through-plane values of the thermal conductivity obtained for the experimental samples [397] at T = 300 K, i.e. $\kappa_{\parallel} = 0.175$ W m^{-1}K^{-1} and $\kappa_{\perp} = 0.110$ W m^{-1}K^{-1}, the results are $G_{VdW,\parallel} \simeq 292$ MW m^{-2}K^{-1} and $G_{VdW,\perp} \simeq 240$ MW m^{-2}K^{-1}. Given the inherent disorder of the samples the evaluated conductance should be considered as an average contribution to the thermal boundary conductance of the various vdW interactions between different entities of nearest-neighbor molecules and therefore cannot be directly compared to the directional force constants evaluated previously. A comparison to previous works provides significantly lower than those reported for metal/dielectric interfaces, approximately 1 GW m^{-2}K^{-1} and comparable to the calculated thermal interface conductance between different crystallographic orientations in crystalline dinaphtho$[2,3-b:2,3-f]$thieno$[3,2-b]$thiophene (DNTT) that ranges between $150-300$ MW m^{-2}K^{-1} [402] or to the interface between myoglobin proteins that amounts to 301 MW m^{-2}K^{-1} at 320 K [403]. The data for TPD lies between those of organic–organic interfaces such as cop-

per phthalocyanine (CuPc)–fullerene (C_60) interfaces, (400 MW $m^{-2}K^{-1}$) and organic/inorganic interfaces such as pentacene/metal (10 MW $m^{-2}K^{-1}$) [404] or CuPc-Au (20 MW $m^{-2}K^{-1}$) that is purely a VdW-like interaction [405].

8

CONCLUSIONS

A glimpse on the vast field of nanoscale thermal transport was given in this thesis. The investigation of thermal properties of materials is strongly stimulated by the countless applications and technological implications of thermal managements at the nanoscale. As a matter of fact the target of this work is twofold. On the one hand, several theoretical tools have been considered and addressed on every detail, and some of them have been here implemented for the first time (e.g the AEMD method or the "hotspot" based on the GLE). As already pointed out, the computational techniques adopted aim at accomplishing similar tasks but under different point of views. EMD approach, despite its slow convergence, proved itself a reliable tool when dealing with anisotropic structures, relating the anisotropic thermal transport to morphological features. Moreover, the convergence issue is overcome when the system under investigation has no long-range order. NEMD, instead, exploits a non-equilibrium steady-state configuration which has revealed a successful strategy in the calculation of heat fluxes to compute thermal rectification. Finally, methods involving the transient regime, such as AEMD and GLE-MD, require a time evolution analysis of the sample thermal state: such an approach relieve of the long simulation times needed for EMD and NEMD approach, thus allowing the investigation of very large system or with a high degree of complexity at the nanoscale.

On the other hand, a manifold of different nanostructured materials have been thoroughly probed, each of them as representative of a state-of-the-art issue in nanoscale thermal transport. In Chapter 3, the role of morphological defects and dimensionality in nanostructured silicon was addressed. Nanoporous silicon is a key material for a large number of applications, such as thermal insulation and photovoltaic conversion. Thus, understanding how point and extended defects, as well as dimensionality, can affect or enhance its perfor-

mance is of paramount importance. Chapter 4 focused on silicon-germanium nanostructures and on the interface between the two semiconductors: superlattices represent a promising strategy for thermoelectric conversion, since the possibility of introducing phonon barriers (in terms of silicon concentration and period ratio) has the twofold consequence of reducing thermal conductivity without appreciably affecting electronic transport properties, and devising a nanostructure which is mostly composed by germanium (which is cheaper and more easily synthesizable than silicon). Moreover, an alternative and more precise way of determining the interface thermal resistance is proposed: interface plays a central role in nanoscience and a rigorous estimate could be profitable for all those production processes acting in the submicron and nanometer regime. Chapter 5, instead, brings together nanovoids and germanium as a substitutional defect to realize graded architectures in order to achieve rectification in bulk semiconductors avoiding interfaces. Such a construction could be crucial for possible building blocks of an information technology based on phonon management at the nanoscale. This chapter concludes the first part of the thesis, which was related to semiconductor based nanostructures. The second part starts with Chapter 6, addressing the role of hydrogen bonds in vibrational spectroscopy and the relation between energy diffusion and thermal dissipation after a spectral excitation. Here, theoretical transient method could serve as a support to vibrational spectroscopy experiment in order to elucidate the microscopic mechanism of relaxation underlying such phenomena. Finally, in Chapter 7 the interplay between molecular anisotropy and thermal transport is extensively explored in organic glasses such as toluene and TPD, in order to come up with possible strategies for future developments to implement small molecule thin films for its use in thermoelectric-based applications.

In conclusion, the field of nanoscale thermal transport is still evolving, beside its huge extension and its countless applications. In this context, the possibility of performing computer simulations at different length and time scale and with different levels of accuracy, represents a precious and essential support for experimental investigations and fabrication processes, which constantly aims at improving device efficiency and minimizing energy losses.

The contents presented in this thesis has already been (partly or entirely) published on the following publications

- Chapter 3 is based on the following papers
  R. Dettori et al. "Model for thermal conductivity in nanoporous silicon from atomistic simulations." *Phys. Rev. B* 91.5 (2015), 054305
  X. Cartoixà et al. "Thermal transport in porous Si nanowires from approach-to-equilibrium molecular dynamics calculations." *Appl. Phys. Lett.* 109.1 (2016), 013107
  B. Lorenzi et al. "Phonon scattering in silicon by multiple morphological defects: A multiscale analysis." Accepted. 2018

- Chapter 4 is based on the following papers
  R. Dettori, C. Melis, and L. Colombo. "Si_xGe_{1-x} alloy as efficient phonon barrier in Ge/Si superlattices for thermoelectric applications." *Eur. Phys. J. B* 88.1 (2015), 27
  R. Dettori et al. "Thermal boundary resistance in semiconductors by non-equilibrium thermodynamics." *Adv. Phys. X* 1.2 (2016), 246–261

- Chapter 5 is based on the following paper
  R. Dettori et al. "Thermal rectification in silicon by a graded distribution of defects." *J. App. Phys.* 119.21 (2016), 215102

- Chapter 6 is based on the following paper
  R. Dettori et al. "Simulating Energy Relaxation in Pump-Probe Vibrational Spectroscopy of Hydrogen-Bonded Liquids." *J. Chem. Theory Comput.* 13.3 (2017), 1284–1292

- Chapter 7 is based on the following paper
  J. Ràfols-Ribé et al. "Evidence of thermal transport anisotropy in stable glasses of vapour deposited organic molecules." Accepted. 2018

and it has been presented at the following conferences

- Sep 21, 2016 – Invited talk to "E-MRS 2016 Fall Meeting" (Warsaw University of Technology, Poland)

titled "Thermal rectification in silicon by a graded distribution of defects"

- Sep 29, 2015 – Contributed talk to "FISMAT 2015, Italian National Conference on Condensed Matter Physics", (University of Palermo, Italy) titled "Thermal diffusion and colored energy dissipation in hydrogen bonded liquids"
- May 23, 2017 – Two poster contributions to "E-MRS 2017 Spring Meeting", (Convention Centre of Strasbourg, France)
- Jun 10, 2015 – Poster contribution to "Mainz Materials Simulation Days 2015 - Non-Equilibrium Processes in Soft Matter" (Mainz, Germany)
- Feb 24, 2015 – Poster contribution to "Son et Lumière: from microphotonics to nanophononics", (École de Physique des Houches, Les Houches, France)

Part IV

APPENDIX

A

MOLECULAR DYNAMICS

Contents

Molecular dynamics (MD) is a computational method, based on statistical mechanics, widely used to compute the time evolution of a set of interacting atoms by integrating Newton equation of motion. By means of MD it is possible to calculate equilibrium and transport properties of a classical many-body system, since the motion of the particles constituting the system obeys to the laws of classical mechanics [238]. In this appendix a brief outline of the MD framework will be given.

A.1 BASIC STRUCTURE

The complete description of a many-body system requires the solution of the time-dependent Schrödinger equation including both the electronic (with coordinates $\mathbf{r}_j = \mathbf{r}_1, \mathbf{r}_2, \ldots, \mathbf{r}_{N_e}$) and the nuclear (with coordinates $\mathbf{R}_i = \mathbf{R}_1, \mathbf{R}_2, \ldots, \mathbf{R}_{N_n}$) DOF

$$H(\mathbf{R}_i, \mathbf{r}_j)\Psi(\mathbf{R}_i, \mathbf{r}_j) = E\Psi(\mathbf{R}_i, \mathbf{r}_j) \tag{A.1}$$

where the Hamiltonian operator is given by

$$\begin{aligned} H(\mathbf{R}_i, \mathbf{r}_j) =& \mathbf{T}_n(\mathbf{R}_i) + \mathbf{U}_{nn}(\mathbf{R}_i) + \\ &+ \mathbf{T}_e(\mathbf{r}_j) + \mathbf{U}_{ee}(\mathbf{r}_j) + \mathbf{U}_{en}(\mathbf{R}_i, \mathbf{r}_j) \end{aligned} \tag{A.2}$$

Here, the labels e and n are referred respectively to nuclei and electrons; $i = 1, \ldots, N_n$ and $j = 1, \ldots, N_e$, where N_n and N_e are the number of electrons and nuclei respectively. $\mathbf{T}_n$ and $\mathbf{T}_e$ operators represent the kinetic energy of nuclei and electrons; $\mathbf{U}_{nn}$ is the operator representing the potential energy of the nucleus-nucleus interactions, $\mathbf{U}_{ee}$ stands for the electron-electron interactions and $\mathbf{U}_{en}$ for the electron-nucleus interactions. However, Eq. (A.1) cannot be solved exactly for systems with more than two electrons. Due to the mass difference between nuclei and electrons, the Born-Oppenheimer or *adiabatic* approximation can be adopted to treat separately their motion: it is in fact assumed that the electrons can instantaneously adapt their wavefunction to the nuclear positions and thus the nuclei appear as "frozen" in the electronic reference frame. This allows to cast Eq. (A.1) into two separate equation, one for electrons depending parametrically on nuclear coordinates

$$H_e(\mathbf{R}_i, \mathbf{r}_j)\psi\mathbf{R}_i, \mathbf{r}_j) = E_e(\mathbf{R}_i)\psi\mathbf{R}_i, \mathbf{r}_j) \tag{A.3}$$

and a second equation for the nuclei

$$[T_n(\mathbf{R}_i) + E_e(\mathbf{R}_i)]\phi(\mathbf{R}_i) = E\phi(\mathbf{R}_i) \tag{A.4}$$

where the eigenvalue $E_e(\mathbf{R}_i)$, obtained from Eq. (A.3), acts as a potential energy for the nuclear motion. Quantum effects on nuclear motion can be neglected, due to their large mass, and this enables to treat them as classical particles, satisfying Newton equation of motion. It is then possible to obtain the total force $\mathbf{F}_i$ acting on i-th particle

$$\mathbf{F}_i = -\nabla_{\mathbf{R}_i} U(\mathbf{R}_i) \tag{A.5}$$

where $U(\mathbf{R}_i)$ contains both the effects of the other nuclei and of the electrons. With this approach it is possible to compute a mechanical trajectory $\mathbf{R}_i = \mathbf{R}_i(t)$, provided that the instantaneous particle positions are computable at each time t. When dealing with condensed-matter systems, trajectories are typically generated within a periodically repeated simulation cell, containing the full set of N particles. Therefore, it is investigated the trajectory of any given particle or its periodic image, in case it migrates through cell boundary. Periodic boundary conditions (PBCs), concept illustrated in Fig. A.1a, minimize the absolute number of particles to deal with and avoid the presence of

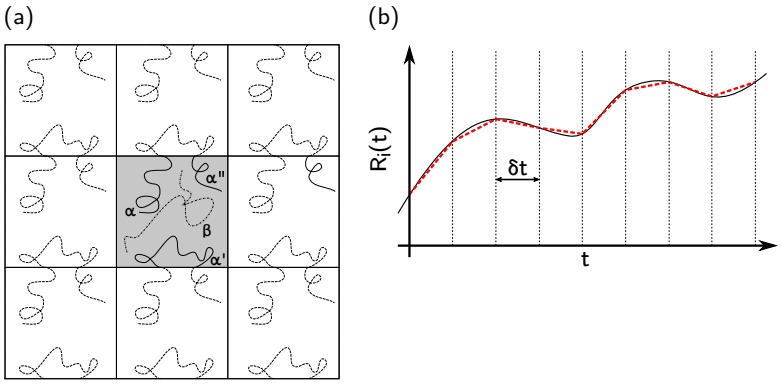

Figure A.1. **a**: Two-dimensional example of periodic boundary conditions. The full-line trajectory α migrates through the simulation cell (central panel) boundaries; dashed lines represent its periodic images. The dash-dotted trajectory β, instead, is completely contained inside the simulation cell so it is not necessary to apply PBC. **b**: Discretization of the particle trajectory by means of the introduction of the time step, the time unit in MD simulations.

free surfaces created by simulation cell truncation at the boundaries. Furthermore, it is possible to simulate ensembles with a constant number of particles.

The discretization of the time evolution

To implement Eq. (A.5) in a computer simulation, it is necessary to introduce the discretization of the time evolution. This is achieved by defining a time step δt, representing the unit of time interval, and by further assuming that the force $\mathbf{F}_i$ is constant over δt. This results in a linear and uniformly accelerated motion throughout δt, as shown in Fig. A.1b. The value of the time step depends on the investigated system: in most application it is of the order of 10^{-15} s. A good rule of thumb for this choice states that the optimal time step should be at least $10-20$ times smaller than the period associated to the highest frequency vibrational mode, in order to allow a correct sample of the vibrational spectrum of the system. For example, crystalline silicon has the highest frequency vibrational mode at $\nu \sim 16$ THz, corresponding to a period of $\tau \sim 6 \times 10^{-14}$ s; thus a good choice is a time step of $\delta t = 2$ fs,

which has always produced reliable results (see Chpt. 3, 4 and 5). On the other hand, in the case of organic or hydrogen bonded molecules, the highest frequency modes are always associated to hydrogen atoms. Indeed, in liquid deuterated methanol it is found that CH stretching modes are characterized by $\bar{\nu} \simeq 3000$ cm^{-1}, while for water, the OH stretching mode has 3500 cm^{-1}. This results in an oscillation period ranging of about $\tau = 9 - 11 \times 10^{-15}$ s, therefore the best compromise is $\delta t = 0.5$ fs (see Chpt. 6 and 7). In general, the smaller the values of δt, the more accurate the numerical solution of Newton's equations of motions, but too small time steps will results in a computational waste of time. Instead, too large time steps will cause a wrong sampling of the particles trajectories due to the particle motions during the time step itself (linear motion and constant acceleration).

The equations of motion

The corresponding equations of motion are formulated according to second-order Newton dynamics

$$\begin{aligned} \mathbf{R}_i(t+\delta t) &= \mathbf{R}_i(t) + \dot{\mathbf{R}}_i(t)\delta t + \frac{1}{2}\ddot{\mathbf{R}}_i(t)\delta t^2 \\ \dot{\mathbf{R}}_i(t+\delta t) &= \dot{\mathbf{R}}_i(t) + \ddot{\mathbf{R}}_i(t)\delta t \end{aligned} \qquad \text{(A.6)}$$

with the particle acceleration computed according to the interaction model

$$\ddot{\mathbf{R}}_i(t) = \frac{1}{M_i}\mathbf{F}_i(t) = -\frac{1}{M_i}\nabla_{\mathbf{R}_i} U(\mathbf{R}_1(t), \mathbf{R}_2(t), \ldots, \mathbf{R}_N)(t) \qquad \text{(A.7)}$$

where M_j is the particle mass. From this formulation it is possible to set up a first *iterative scheme* to generate the time evolution of a set of particle with a computer simulation

1. define an initial atomic configuration (i.e. assign atomic positions and velocities)
2. compute interatomic forces according to the initial configuration
3. update atomic positions and velocities according to Eq. (A.6)
4. go to step (2) and iterate once more the loop

Such a procedure is the core of a MD simulation.

A.2 GENERATION OF PARTICLE TRAJECTORIES

The overall reliability of the MD method critically depends on the generation of accurate and stable particle trajectories. A crucial point is the algorithm adopted to integrate Newton equations of motion. One of the most common integration scheme is the so-called velocity-Verlet (VV) algorithm [408], a prototypical example of numerical integration scheme by finite difference methods. This scheme involves a multiple-step procedure. Firstly, the particle positions $\mathbf{R}_i(t)$ are updated to time $t + \delta t$ following Eq. (A.6), while the atomic velocities are computed after a half time step $t + (1/2)\delta t$ according to

$$\dot{\mathbf{R}}_i(t + \frac{1}{2}\delta t) = \dot{\mathbf{R}}_i(t) + \frac{1}{2}\ddot{\mathbf{R}}_i(t)\delta t \tag{A.8}$$

Then, accelerations are re-computed at time $t + \delta t$ and particle velocities are eventually updated to time $t + \delta t$

$$\dot{\mathbf{R}}_i(t + \delta t) = \dot{\mathbf{R}}_i(t + \frac{1}{2}\delta t) + \frac{1}{2}\ddot{\mathbf{R}}_i(t + \delta t)\delta t \tag{A.9}$$

This method is correct to the order of δt^4

The VV algorithm is simple and its numerical implementation is straightforward. Furthermore, is stable and allows to use relatively long time steps ($10^{-15} \leqslant \delta t \leqslant 10^{-14}$ s) providing an optimal conservation of the mechanical time-invariant quantities. A variety of different algorithms other than VV for the present Hamiltonian formulation of the MD method are indeed available, which allows for a combination with hybrid Monte Carlo methods or developed for MD simulations performed within the Car-Parrinello method [409–414].

A.3 THE INTERACTION SCHEME

Another key element in MD runs is the interaction potentials. A good interactions scheme should be accurate (it should provide an accurate estimate of total energy and its derivatives), reliable (it should be obtained starting from physical and chemical characteristics of the system under investigation), transferable (it should be capable of handling the system under arbitrary conditions of temperatures, pressure, state of aggregation, etc.)

Model potential MD

The simplest approach for the construction of the potential U, consists in formally developing the total potential as a sum of two-body terms $U^{(2)}$, three-body terms $U^{(3)}$, ..., N-body terms $U^{(N)}$

$$U(\mathbf{R}_1(t), \mathbf{R}_2(t), \ldots, \mathbf{R}_N) = \sum_{i>l} U^{(2)}(\mathbf{R}_i, \mathbf{R}_l) + \\ + \sum_{i>l>m} U^{(3)}(\mathbf{R}_i, \mathbf{R}_l, \mathbf{R}_m) + \ldots \tag{A.10}$$

According to the very nature of the interatomic bond treated in the investigation, the series is arrested to a given order. For example, a rough but effective approximation to treat simple metals is to consider only the two body terms, while to study materials characterized by directional and covalent bonds it is necessary to consider also the third order term. A great number of interatomic potentials have been developed for almost every kind of material, including long range interactions (i.e. considering Coulombic interaction) for ionic and polar compounds. A quick overview of the interatomic potentials adopted in this thesis is given in Appx. B.

The explicit form for each functional $U^{(2)}, U^{(3)}, \ldots, U^{(N)}$ is assumed under specific physical-chemical considerations of the investigated system, and also for numeric convenience. These functionals depend upon empirical parameters which need to be fitted to correctly reproduce system properties. In the case of short-range interactions, it is possible to optimize the calculation of the forces acting on each particles limiting the evaluation of the potential to the only particles lying within a cut-off radius. The empirical character allows to appreciably improve simulation performances, since computational workload scales (for short-range potentials) as $m \times N$, where m is the average number of nearest neighbor for each of N particles constituting the simulation cell. In this way it is possible to treat systems with a large number of particles (up to 10^7 atoms) for long simulation times (up to tens of nanoseconds). However, the empirical character strongly limits the transferability of the force field, which is usually realized *ad-hoc* for the investigated system.

First Principles MD

An alternative approach consists in a more fundamental level of description. According to the aforementioned Born-Oppenheimer approximation and to the

one-electron approximation, the total energy of an ionic system (nuclei+core electrons) together with valence electrons can be expressed as

$$U(\mathbf{R}_1(t), \mathbf{R}_2(t), \ldots, \mathbf{R}_N) = U_{ee} + U_{ei} + U_{ii} \tag{A.11}$$

where i and e indicates ions and electrons, respectively. In order to compute this expression, it is necessary to know electronic energies ε_n and wavefunctions ψ. Once that they are known by solving numerically the single-electron Schrödinger equation, the total potential energy U can be written as

$$U = 2\sum_{n}^{occ} \varepsilon_n + U_{ii} - U_{ee} \tag{A.12}$$

where the sum is performed over the energies of the occupied states (the factor 2 accounts for the spin degeneracy) and the $-U_{ee}$ contributions corrects the double counting of the electron-electron interactions in the first term. Then, by applying the Hellmann-Feynman theorem it is possible to obtain the interparticle forces within a full quantum mechanical picture of particle interactions. In this framework, which is called *first principles molecular dynamics* (FPMD), the most computationally expensive steps are

- the Schrödinger equation solution
- the self-consistent evaluation of U_{ee}

The resulting CPU workload typically scales as N^3 with a large prefactor, strongly limiting the number of addressable particle in a typical FPMD run ($\leqslant 10^2$ particles).

Semi-empirical MD

An approximation of the first-principles approach is represented by the tight-binding (TB) picture. Accordingly, the electron wavefunction ψ are expanded as linear combinations of atomic orbitals $\{\phi_{l\alpha}\}$

$$\psi = \sum_{l\alpha} c^n_{l\alpha} \phi_{l\alpha} \tag{A.13}$$

where l is the quantum number index and α identifies the crystal basis atom of position $\mathbf{d}_\alpha$. The matrix elements $\langle \phi_{l'\beta} | \, h \, | \phi_{l\alpha} \rangle$ of the single-electron Hamiltonian are then treated as disposable constants to be fitted, instead of

computed self-consistently. The result is a *semi-empirical molecular dynamics* (SEMD) scheme with improved accuracy and transferability with respect to model potential MD. The computational workload is dramatically reduced with respect to FPMD simulations since no self-consistency is required. However, it is still significantly heavy and the overall procedure scales as N^2, due to the tight-binding matrix diagonalization, making SEMD simulations typically performed on systems containing many as several hundreds particles.

B

INTERATOMIC POTENTIALS

Contents

Force field methods ignore the electronic motions and calculate the energy of a system as a function of the nuclear positions (and velocities) only. MD is thus invariably used to perform calculations on systems containing significant numbers of atoms. In some cases force fields can provide answers that are as accurate as even the highest-level quantum mechanical calculations, in a fraction of the computer time. However, MD cannot of course provide properties that depend upon the electronic distribution in a molecule. The validity of these methods relies on several assumptions. One of these is the already mentioned Born-Oppenheimer approximation, without which it would be impossible to contemplate writing the energy as a function of the nuclear coordinates at all. Transferability is a key attribute of a force field, for it enables a set of parameters developed and tested on a relatively small number of cases to be applied to a much wider range of problems. Moreover, parameters developed from data on small molecules can be used to study much larger molecules such as polymers.

In this appendix will be proposed a quick overview about the force-fields and the model potentials adopted in this thesis. In particular, for nanostructured semiconductors the Tersoff [89, 415] and the EDIP [142, 416] were adopted, while for organic molecules the COMPASS [312] and the CVFF [392] force-field have been the best choice due to molecular complexity.

B.1 TERSOFF

In real systems, the strength of each bond depends on the local environment, i.e. an atom with many neighbors forms weaker bonds than an atom with few neighbors. Thus, Tersoff developed a pair potential the strength of which depends on the environment. The form of the energy E, as a function of the atomic coordinates, reads as

$$E = \sum_i E_i = \frac{1}{2} \sum_{i \neq j} V_{ij} \tag{B.1}$$

with

$$V_{ij} = f_C(r_{ij})[f_R(r_{ij}) + b_{ij} f_A(r_{ij})] \tag{B.2}$$

where the potential energy is decomposed into a site energy E_i and a bonding energy V_{ij}, r_{ij} is the distance between the atoms i and j, f_A and f_R are the attractive and repulsive pair potential respectively

$$\begin{aligned} f_R(r) &= A \exp(-\lambda_1 r) \\ f_A(r) &= -B \exp(-\lambda_2 r) \end{aligned} \tag{B.3}$$

and f_C is a smooth cutoff function

$$f_C(r) = \begin{cases} 1, & r < R - D \\ \frac{1}{2} - \frac{1}{2} \sin\left[\frac{\pi}{2}(r - R)/D\right], & R - D < r < R + D \\ 0, & r > R + D \end{cases} \tag{B.4}$$

The parameters R and D are not systematically optimized but are chosen so as to include the first-neighbor shell only for several selected high-symmetry bulk structure of silicon, namely for Si_2, graphite, diamond, simple cubic, and face-centered cubic structures. The f_C function, thus, decreases from 1 to 0 in the range $R - D < r < R + D$. The main feature of this potential is the b_{ij} term, since the idea is that the strength of each bond depends upon the local environment and is lowered when the number of neighbors is relatively high. Such a dependence is expressed by the explicit form of b_{ij} appearing in

Eq.(B.3), which can increase or decrease the attractive force relatively to the repulsive one, according to the environment, such that

$$\begin{aligned} b_{ij} &= \frac{1}{(1+\beta^n \zeta_{ij}^n)^{1/2n}} \\ \zeta &= \sum_{k\neq i,j} f_C(r_{ij}) g(\theta_{ijk}) \exp\left[\lambda_3^3 (r_{ij}-r_{ik})^3\right] \\ g(\theta) &= 1 + \frac{c^2}{d^2} - \frac{c^2}{[d^2+(\cos\theta-\cos\theta_0)^2]} \end{aligned} \tag{B.5}$$

The term ζ_{ij} define the effective coordination number of atom i, i.e. the number of nearest neighbors, taking in account the atomic environment, thus the relative distance of two neighbors $r_{ij}-r_{ik}$ and the bond-angle θ. The function $g(\theta)$ has a minimum for $\cos(\theta_0)$, d determines the sharpness of the angle dependence, and c expresses the strength of the angular effect.

This potential and the parameters were chosen to fit theoretical and experimental data obtained for the cohesive energy of several high-symmetry bulk structures previously mentioned, the lattice constant and bulk modulus of the silicon lattice in the diamond configuration. Later it was parametrized also for carbon [417].

B.2 EDIP

The Environment Dipendent Interatomic Potential (EDIP) is an efficient and realistic model for interatomic forces in covalent solids and liquids which incorporates recent theoretical advances in understanding the environment-dependence of (sigma) chemical bonding in condensed phases [416, 418]. The parameterization for silicon [142] provided significantly reliable results when tested for bulk phases (amorphous, liquid, crystal elasticity, thermal expansion,...), defects (point defects, stacking faults, dislocations,...) and phase transitions (crystal phases, amorphous, liquid).

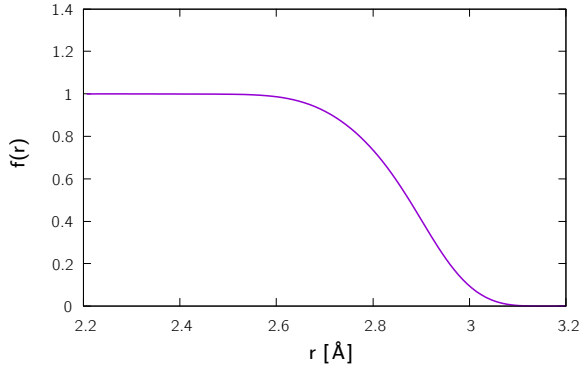

Figure B.1. $f(r)$ function determining the contribution of each neighbor to the effective coordination number Z.

Configurational energy can be expressed as a sum of site energy (as explained for Tersoff potential) $E = \sum_i E_i$, each containing a two body and a three body term

$$E_i = \sum_{j \neq i} V_2(R_{ij}, Z_i) + \sum_{j \neq i} \sum_{k \neq i, k > j} V_3(\mathbf{R}_{ij}, \mathbf{R}_{ik}, Z_i) \tag{B.6}$$

where $V_2(R_{ij}, Z_i$ is an interaction term between atoms i and j and represents pairwise bond, while $V_3(\mathbf{R}_{ij}, \mathbf{R}_{ik}, Z_i)$ is the interaction term between atoms i, j and k, centered on the i-th atom and represents angular forces. Both interactions depend on the local environment of the i-th atom by means of its effective coordination number, defined as

$$Z_i = \sum_{m \neq i} f(R_{im}) \tag{B.7}$$

where $f(R_{im})$ is a cutoff function, which measures the contribution of m-th neighbor to the i-th atom coordination number in terms of R_{im}. Such a function is shown in Fig. B.1 and reads as

$$f(r) = \begin{cases} 1, & r < c \\ \exp\left(\dfrac{\alpha}{1 - x^{-3}}\right), & c < r < a \\ 0, & r > a \end{cases} \tag{B.8}$$

where $x = (r - c)/(a - c)$. A neighbor of atom i at a distance $r < c$ is considered a full neighbor, while the neighbors between c and a give only a partial contribution to Z_i. The cutoffs are constrained to reproduce the coordinations of important crystal structures, e. g. $Z_i = 4$ is the diamond lattice.

The two body term includes an attractive and a repulsive term

$$V_2(r, Z) = A \left[\left(\frac{B}{r} \right)^{\rho} - p(Z) \right] \exp \left(\frac{\sigma}{r - a} \right) \tag{B.9}$$

which go to zero at the cutoff $r = a$ with all derivatives continuous. The bond strength adapts to changes in the local atomic environment. The coordination dependence introduces an asymmetry, $V_2(R_{ij}, Z_i) \neq V_2(R_{ji}, Z_i)$, similar to the Tersoff potential in that the strength of the attractive force is controlled by a bond order function $p(Z)$ that depends on the local coordination. Theoretical calculations showed the weakening of the attractive interaction and the corresponding increase in bond length for increasing coordination [416, 418, 419]. Such theoretical dependence is captured by a Gaussian function [416]

$$p(Z) = \exp\left(-\beta Z^2\right) \tag{B.10}$$

The three-body term contains radial and angular factors

$$V_3(\mathbf{R}_{ij}, \mathbf{R}_{ik}, Z_i) = g(R_{ij}) g(R_{ik} h(l_{ijk}, Z_i) \tag{B.11}$$

where $l_{ijk} = \cos\theta_{ijk} = \mathbf{R}_{ij} \cdot \mathbf{R}_{ik} / R_{ij} R_{ik}$. The radial function has the form [88]

$$g(r) = \exp\left(\frac{\gamma}{r - a} \right) \tag{B.12}$$

and goes to zero smoothly at the cutoff distance a. The angular function $h(l, Z)$ is strongly dependent on the local coordination through two functions $\tau(Z)$ and $Q(Z)$ that control the equilibrium angle and the strength of the interaction, respectively

$$h(l, Z) = \lambda \left\{ \left(1 - \exp\left[-Q(Z)(l + \tau(Z))^2\right]\right) + \eta Q(Z) l + \tau(Z))^2 \right\} \tag{B.13}$$

with $Q(Z) = Q_0 \exp(-\mu Z)$, which controls the strength of angular forces as a function of coordination, and $\tau(Z) = -l_0(Z) = -\cos\theta_0(Z)$, which controls the equilibrium angle $\theta_0(Z)$ of the three-body interaction as a function of coordination.

A variation of Z_i causes a variation in the two-body and three-body interactions, resulting in a dependence of Z_i from equilibrium distance between atoms and from bond angles. An increase of coordination number weakens the bonds and thus reduces their equilibrium length. At the same time, an increase of Z_i causes a reduction in bond angles.

In summary, this implementation of EDIP for bulk silicon has 13 adjustable parameters: A, B, ρ, β, σ, a, c, λ, η, γ, Q_0, μ and α. The functional form already contains informations about chemical bonding in bulk silicon taken directly from theoretical studies, mostly of ideal crystal structures. The adjustable parameters provide the necessary freedom to extrapolate these bonding dependences for defect structures strictly outside the theoretical input,

B.3 COMPASS

Condensed-phase Optimized Molecular Potentials for Atomistic Simulation Studies (COMPASS) [312, 420–423] is a member of the consistent family of force fields (CFF91, PCFF, CFF), which are closely related second-generation force fields. They were parameterized against a wide range of experimental observables for organic compounds containing H, C, N, O, S, P, halogen atoms and ions, alkali metal cations, and several biochemically important divalent metal cations. Moreover, they present a broad coverage of organic polymers, (inorganic) metals, and zeolites. COMPASS is the first force field that has been parameterized and validated using condensed phase properties in addition to various and empirical data for molecules in isolation. Consequently, this force field enables accurate and simultaneous prediction of structural, conformational, vibrational, and thermo-physical properties for a broad range of molecules in isolation and in condensed phases.

The COMPASS functional form includes high-order (cubic and quartic) force constants and off-diagonal cross-coupling terms. The force field parametrization is able to describe, using the same functional form, organic as well as

inorganic materials [312, 424]. The functional forms are the same as those used in consistent force-fields (CFF)[425] and are given by

$$\begin{aligned} E_{total} &= E_b + E_\theta + E_\phi + E_\chi + \\ &+ E_{b,b'} + E_{b,\theta} + E_{b,\phi} + E_{\theta,\phi} + \\ &+ E_{\theta,\theta'} + E_{\theta,\theta',\phi} + E_q + E_{vdW} \end{aligned} \tag{B.14}$$

where:

$$\begin{aligned} E_b &= \sum_b \left[k_2(b-b_0)^2 + k_3(b-b_0)^3 + k_4(b-b_0)^4\right] \\ E_\theta &= \sum_\theta \left[k_2(\theta-\theta_0)^2 + k_3(\theta-\theta_0)^3 + k_4(\theta-\theta_0)^4\right] \\ E_\phi &= \sum_\phi \left[k_1(1-\cos\phi) + k_2(1-\cos 2\phi) + k_3(1-\cos 3\phi)\right] \\ E_\chi &= \sum_\chi k_2\chi^2 \\ E_{b,b'} &= \sum_{b,b'} k(b-b_0)(b'-b_0') \\ E_{b,\theta} &= \sum_{b,\theta} k(b-b_0)(\theta-\theta_0) \\ E_{b,\phi} &= \sum_{b,\phi} (b-b_0)\left[k_1\cos\phi + k_2\cos 2\phi + k_3\cos 3\phi\right] \\ E_{\theta,\phi} &= \sum_{\theta,\phi} (\theta-\theta_0)\left[k_1\cos\phi + k_2\cos 2\phi + k_3\cos 3\phi\right] \\ E_{\theta,\theta'} &= \sum_{\theta,\theta'} k(\theta-\theta_0)(\theta'-\theta_0') \\ E_{\theta,\theta',\phi} &= \sum_{\theta,\theta',\phi} k(\theta-\theta_0)(\theta'-\theta_0')\cos\phi \\ E_q &= \sum_{ij} \frac{q_i q_j}{r_{ij}} \end{aligned} \tag{B.15}$$

and

$$E_{vdW} = \sum_{ij} \epsilon_{ij}\left[2\left(\frac{r_{ij}^0}{r_{ij}}\right)^9 - 3\left(\frac{r_{ij}^0}{r_{ij}}\right)^6\right] \tag{B.16}$$

with the following combining rules

$$r_{ij}^0 = \left(\frac{(r_i^0)^6 + (r_j^0)^6}{2} \right)^{1/6} \quad \epsilon_{ij} = 2\sqrt{\epsilon_i \cdot \epsilon_j} \left(\frac{(r_i^0)^3 \cdot (r_j^0)^3}{(r_i^0)^6 \cdot (r_j^0)^6} \right) \tag{B.17}$$

The functions are divided into two types: valence terms including diagonal ($E_{b,b'}$, $E_{\theta,\theta'}$) and off-diagonal cross-coupling terms ($E_{b,\theta}$, $E_{b,\phi}$, $E_{\theta,\phi}$, $E_{\theta,\theta',\phi}$), and non-bonded interaction terms. The valence terms represent internal coordinates of bond (b), angle (θ), torsion angle (ϕ), and out-of-plane angle (χ), while the cross-coupling terms include combinations of two or three internal coordinates. The cross-coupling terms are important for the prediction of vibrational frequencies as well as structural variations associated with conformational changes. In Eq. (B.15) the subscript 0 indicates the reference values of the bond, angle, dihedral angle and out-of-plane angle, while k, k_1, k_2, k_3, k_4 are the force constants estimated by quantum mechanical calculations. Terms involving explicit internuclear distances, r, represent non-bonded interactions which are composed by a E_{vdW} Lennard Jones (LJ) 9-6 function for the vdW term and a E_q Coulombic function for an electrostatic interaction.

B.4 CVFF

The Consistent-Valent Force Field (CVFF) is a generalized valence force field [392]. Parameters are provided for amino acids, water, and a variety of other functional groups.

The analytic form of the energy expression used in CVFF is given by E_{total}

$$
\begin{aligned}
E_{total} = & \sum \left\{ D_b \left[1 - \exp -\alpha(b - b_0)\right]^2 - D_b \right\} + \\
& + \frac{1}{2} \sum H_0 (\theta - \theta_0)^2 + \\
& + \frac{1}{2} \sum H_0 (1 + s \cos n\phi) + \frac{1}{2} \sum H_\chi \chi^2 + \\
& + \sum \sum F_{bb'} (b - b_0)(b' - b'_0) \\
& + \sum \sum F_{\theta\theta'} (\theta - \theta_0)(\theta' - \theta'_0) + \\
& + \sum \sum F_{b\theta} (b - b_0)(\theta - \theta_0) \\
& + \sum F_{\phi\theta\theta'} \cos\phi (\theta - \theta_0)(\theta' - \theta'_0) + \\
& + \sum \sum F_{\chi\chi'} \chi\chi' \\
& + \sum_{ij} \epsilon_{ij} \left[2 \left(\frac{r^0_{ij}}{r_{ij}} \right)^9 - 3 \left(\frac{r^0_{ij}}{r_{ij}} \right)^6 \right] + \sum_{ij} \frac{q_i q_j}{r_{ij}}
\end{aligned}
\tag{B.18}
$$

The terms in Eq. (B.18) represent the energies required to deform the internal coordinates (which are labeled as b, θ, ϕ, and χ) from their unstrained standard values, denoted by the subscript 0, or the energies of non-bonded interactions (which are the same as in the case of the COMPASS force field). The terms in Eq. (B.18) are illustrated schematically in Fig. B.2. Terms 1-4 are commonly referred to as the diagonal terms of the valence force field and represent the energy of deformation of bond lengths, bond angles, torsion angles, and out-of-plane interactions, respectively. Note that a Morse potential (Term 1) is used for the bond-stretching term. The Morse form is computationally more expensive than the harmonic form.

Terms 5-9 are off-diagonal (or cross) terms and represent couplings between deformations of internal coordinates. For example, Term 5 describes the coupling between stretching of adjacent bonds. These terms are required to accurately reproduce experimental vibrational frequencies and, therefore, the dynamical properties of molecules. In some cases, they revealed to be important in accounting for structural deformations. However, cross terms can

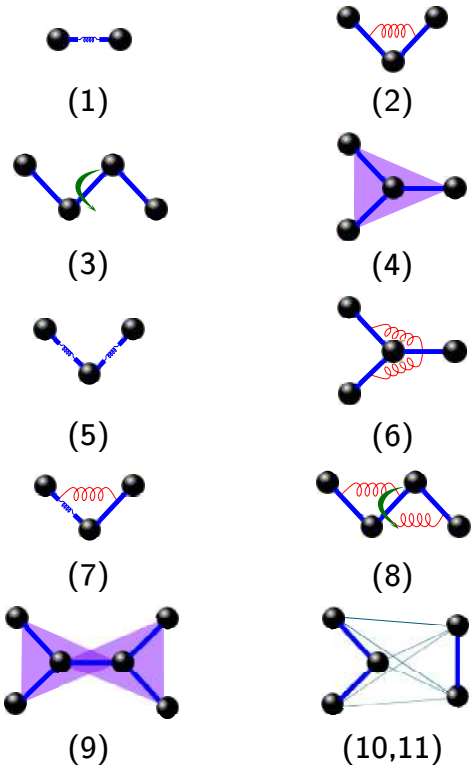

Figure B.2. Graphic illustration of terms in CVFF.

become unstable when the structure is far from a minimum. Terms 10-11 describe the non-bonded interactions. Term 10 represents the vdW interactions with a Lennard-Jones function. Term 11 is the Coulombic representation of electrostatic interactions. In the CVFF force field, hydrogen bonds are a natural consequence of the standard vdW and electrostatic parameters, and special hydrogen bond functions do not improve the fit of CVFF to experimental data [426–428].

The parameters D_b, H_o, H_ϕ, H_χ, $F_{bb'}$, $F_{\theta\theta'}$, $F_{b\theta}$, $F_{\phi\theta\theta'}$ and $F_{\chi\chi'}$ are the force constants for the corresponding intramolecular deformations, ϵ_{ij} and r_{ij}^0 are the parameters for the non-bonded repulsive and dispersive interactions, and q_i are the partial charges carried by each atom.

BIBLIOGRAPHY

[1] R. R. Schaller. "Moore's law: past, present and future." *IEEE Spectrum* 34.6 (1997), 52–59 (cit. on p. 3).

[2] United States Environmental Protection Agency. *Sources of Greenhouse Gas Emissions*. 2015. URL: https://www.epa.gov/ghgemissions/sources-greenhouse-gas-emissions (cit. on p. 3).

[3] M. Aspelmeyer, T. J. Kippenberg, and F. Marquardt. "Cavity optomechanics." *Rev. Mod. Phys.* 86.4 (2014), 1391–1452 (cit. on p. 4).

[4] S. Hermelin, S. Takada, M. Yamamoto, S. Tarucha, A. D. Wieck, L. Saminadayar, C. Bäuerle, and T. Meunier. "Electrons surfing on a sound wave as a platform for quantum optics with flying electrons." *Nature* 477 (2011), 435 (cit. on p. 4).

[5] R. P. G. McNeil, M. Kataoka, C. J. B. Ford, C. H. W. Barnes, D. Anderson, G. A. C. Jones, I. Farrer, and D. A. Ritchie. "On-demand single-electron transfer between distant quantum dots." *Nature* 477 (2011), 439 (cit. on p. 4).

[6] C. Rossignol, N. Chigarev, M. Ducousso, B. Audoin, G. Forget, F. Guillemot, and M. C. Durrieu. "In Vitro picosecond ultrasonics in a single cell." *Appl. Phys. Lett.* 93.12 (2008), 123901 (cit. on p. 4).

[7] Jean Baptiste Joseph Fourier. *The Analytical Theory of Heat*. First English Edition. 1878 (cit. on p. 4).

[8] E. W. Montroll. "Size Effect in Low Temperature Heat Capacities." *J. Chem. Phys.* 18.2 (1950), 183–185 (cit. on p. 5).

[9] H. P. Baltes and E. R. Hilf. "Specific heat of lead grains." *Solid State Commun.* 12.5 (1973), 369 –373. ISSN: 0038-1098 (cit. on p. 5).

[10] D. G. Cahill, W. K. Ford, K. E. Goodson, G. D. Mahan, A. Majumdar, H. J. Maris, R. Merlin, and S. R. Phillpot. "Nanoscale thermal transport." *J. Appl. Phys.* 93.2 (2003), 793–818 (cit. on p. 5).

[11] M. Kazan, G. Guisbiers, S. Pereira, M. R. Correia, P. Masri, A. Bruyant, S. Volz, and P. Royer. "Thermal conductivity of silicon bulk and nanowires: Effects of isotopic composition, phonon confinement, and surface roughness." *J. Appl. Phys.* 107.8 (2010), 083503 (cit. on p. 5).

[12] E. Pop. "Energy dissipation and transport in nanoscale devices." *Nano Res.* 3.3 (2010), 147–169 (cit. on pp. 6, 104, 114).

[13] Z. Yan, G. Liu, J. M. Khan, and A. A. Balandin. "Graphene quilts for thermal management of high-power GaN transistors." *Nat. Commun.* 3 (2012), 827 (cit. on p. 6).

[14] D. M. Rowe. *CRC Handbook of Thermoelectrics*. Taylor & Francis Group, 1995 (cit. on p. 6).

[15] D. M. Rowe. *Thermoelectrics Handbook: Macro to Nano*. Taylor & Francis Group, 20055 (cit. on p. 6).

[16] G. Nolas, J. Sharp, and H. J. Goldsmid. *Thermoelectrics: Basic Principles and New Materials Developments*. Springer, 2001 (cit. on p. 6).

[17] X. Zhang and L. D. Zhao. "Thermoelectric materials: Energy conversion between heat and electricity." *J. Materiomics* 1.2 (2015), 92 –105 (cit. on p. 7).

[18] G. J. Snyder and E. S. Toberer. "Complex thermoelectric materials." *Nat. Mater.* 7 (2008), 105 (cit. on p. 7).

[19] A. J. Minnich, M. S. Dresselhaus, Z. F. Ren, and G. G. Chen. "Bulk nanostructured thermoelectric materials: current research and future prospects." *Energy Environ. Sci.* 2.5 (2009), 466–479 (cit. on pp. 7, 104).

[20] M. S. Dresselhaus, G. Chen, M. Y. Tang, R. Y. Yang, H. Lee, D. Z. Wang, Z. F. Ren, J. P. Fleurial, and P. Gogna. "New Directions for Low-Dimensional Thermoelectric Materials." *Adv. Mater.* 19.8 (2007), 1043–1053 (cit. on pp. 7, 104).

[21] B.C. Sales, D. Mandrus, and R. K. R. K. Williams. "Filled Skutterudite Antimonides: A New Class of Thermoelectric Materials." *Science* 272.5266 (1996), 1325–1328 (cit. on p. 7).

[22] L. D. Hicks and M. S. Dresselhaus. "Effect of quantum-well structures on the thermoelectric figure of merit." *Phys. Rev. B* 47.19 (1993), 12727–12731 (cit. on p. 8).

[23] B. Yang and G. Chen. "Partially coherent phonon heat conduction in superlattices." *Phys. Rev. B* 67.19 (2003), 195311 (cit. on pp. 8, 102).

[24] R. Venkatasubramanian, E. Siivola, T. Colpitts, and B. O'Quinn. "Thin-film thermoelectric devices with high room-temperature figures of merit." *Nature* 413.24 (2001), 597–602 (cit. on pp. 8, 93, 94).

[25] *Advances in 1-D and 2-D thermoelectric materials*. 1999 (cit. on p. 8).

[26] J. Zou and A. Balandin. "Phonon heat conduction in a semiconductor nanowire." *J. App. Phys.* 89.5 (2001), 2932–2938 (cit. on pp. 8, 68).

[27] Y. M. Lin and M. S. Dresselhaus. "Thermoelectric properties of superlattice nanowires." *Phys. Rev. B* 68.7 (2003), 075304 (cit. on p. 8).

[28] Sebastian Volz. *Thermal nanosystems and nanomaterials*. Ed. by Sebastian Volz. 1st ed. Vol. 118. Topics in Applied Physics. Springer-Verlag Berlin Heidelberg, 2009 (cit. on pp. 8, 10).

[29] Sebastian Volz. *Microscale and nanoscale heat transfer*. Ed. by Sebastian Volz. 1st ed. Vol. 107. Topics in Applied Physics. Springer, 2007 (cit. on p. 8).

[30] A. I. Hochbaum, R. Chen, R. D. Delgado, W. Liang, E. C. Garnett, M. Najarian, A. Majumdar, and P. Yang. "Enhanced thermoelectric performance of rough silicon nanowires." *Nature* 451 (2008), 163 (cit. on pp. 8, 67, 76).

[31] R. Chen, A. I. Hochbaum, P. Murphy, J. Moore, P. Yang, and A. Majumdar. "Thermal Conductance of Thin Silicon Nanowires." *Phys. Rev. Lett.* 101.10 (2008), 105501 (cit. on p. 8).

[32] D. Li, Y. Wu, P. Kim, L. Shi, P. Yang, and A. Majumdar. "Thermal conductivity of individual silicon nanowires." *Appl. Phys. Lett.* 83.14 (2003), 2934–2936 (cit. on p. 8).

[33] M. P. Zaitlin, L. M. Scherr, and A. C. Anderson. "Boundary scattering of phonons in noncrystalline materials." *Phys. Rev. B* 12.10 (1975), 4487–4492 (cit. on p. 8).

[34] D. G. Cahill. "Thermal conductivity measurement from 30 to 750 K: the 3ω method." *Rev. Sci. Instrum.* 61.2 (1990), 802–808 (cit. on p. 8).

[35] D. G. Cahill and R. O. Pohl. "Thermal conductivity of amorphous solids above the plateau." *Phys. Rev. B* 35.8 (1987), 4067–4073 (cit. on p. 8).

[36] D. G. Cahill, M. Katiyar, and J. R. Abelson. "Thermal conductivity of a-Si:H thin films." *Phys. Rev. B* 50.9 (1994), 6077–6081 (cit. on p. 8).

[37] T. Tong and A. Majumdar. "Reexamining the 3ω technique for thin film thermal characterization." *Rev. Sci. Instrum.* 77.10 (2006), 104902 (cit. on p. 8).

[38] D. G. Cahill and T. H. Allen. "Thermal conductivity of sputtered and evaporated SiO2 and TiO2 optical coatings." *Appl. Phys. Lett.* 65.3 (1994), 309–311 (cit. on p. 9).

[39] S. M. Lee and D. G. Cahill. "Heat transport in thin dielectric films." *J. Appl. Phys.* 81.6 (1997), 2590–2595 (cit. on pp. 9, 10).

[40] T. Borca-Tasciuc et al. "Thermal conductivity of symmetrically strained Si/Ge superlattices." *Superlattices Microstruct.* 28.3 (2000), 199 –206 (cit. on pp. 9, 94).

[41] Y. S. Ju, K. Kurabayashi, and K. E. Goodson. "Thermal characterization of anisotropic thin dielectric films using harmonic Joule heating." *Thin Solid Films* 339.1 (1999), 160 –164 (cit. on p. 9).

[42] Y. S. Ju and K. E. Goodson. "Phonon scattering in silicon films with thickness of order 100 nm." *Appl. Phys. Lett.* 74.20 (1999), 3005–3007 (cit. on pp. 9, 77).

[43] M. M. Rojo, O. Caballero Calero, A. F. Lopeandia, J. Rodriguez-Viejo, and M. Martín-Gonzalez. "Review on measurement techniques of transport properties of nanowires." *Nanoscale* 5.23 (2013), 11526–11544 (cit. on p. 9).

[44] M. Soini, I. Zardo, E. Uccelli, S. Funk, G. Koblmller, A. Fontcuberta i Morral, and G. Abstreiter. "Thermal conductivity of GaAs nanowires studied by micro-Raman spectroscopy combined with laser heating." *Appl. Phys. Lett.* 97.26 (2010), 263107 (cit. on p. 9).

[45] G. S. Doerk, C. Carraro, and R. Maboudian. "Single Nanowire Thermal Conductivity Measurements by Raman Thermography." *ACS Nano* 4.8 (2010), 4908–4914 (cit. on p. 9).

[46] J. M. Ziman. *Electrons and Phonons: The Theory of Transport Phenomena in Solids*. Oxford University Press, 2001, p. 568 (cit. on pp. 10, 20, 57, 79, 80, 87, 91, 103).

[47] M. Omini and A. Sparavigna. *Il Nuovo Cim. D* 19 (1997), 1537 (cit. on pp. 10, 21, 103).

[48] G. Fugallo, M. Lazzeri, L. Paulatto, and F. Mauri. "*Ab initio* variational approach for evaluating lattice thermal conductivity." *Phys. Rev. B* 88.4 (2013), 045430 (cit. on pp. 10, 21, 103).

[49] A. Cepellotti, G. Fugallo, L. Paulatto, M. Lazzeri, F. Mauri, and N. Marzari. "Phonon hydrodynamics in two-dimensional materials." *Nat. Commun.* 6 (2015), 6400 (cit. on pp. 10, 21).

[50] K. Y. Lee, B. Esmaeili, B. Zealley, and Masanori M. Mishima. "Direct interaction between centralspindlin and PRC1 reinforces mechanical resilience of the central spindle." *Nat. Commun.* 6 (2015), 7290 (cit. on p. 10).

[51] R. Landauer. "Electrical resistance of disordered one-dimensional lattices." *Phil. Mag.* 21.172 (1970), 863–867 (cit. on p. 10).

[52] N. Mingo and L. Yang. "Phonon transport in nanowires coated with an amorphous material: An atomistic Green's function approach." *Phys. Rev. B* 68.24 (2003), 245406 (cit. on pp. 10, 16).

[53] W. Zhang, T. S. Fisher, and N. Mingo. "Simulation of Interfacial Phonon Transport in Si-Ge Heterostructures Using an Atomistic Green's Function Method." *J. Heat Transfer* 129.4 (2006), 483–491 (cit. on p. 10).

[54] N. Mingo. "Anharmonic phonon flow through molecular-sized junctions." *Phys. Rev. B* 74.12 (2006), 125402 (cit. on p. 10).

[55] J. S. Wang, J. Wang, and N. Zeng. "Nonequilibrium Green's function approach to mesoscopic thermal transport." *Phys. Rev. B* 74.3 (2006), 033408 (cit. on p. 10).

[56] S. Xiong, J. Ma, S. Volz, and T. Dumitrică. "Thermally-Active Screw Dislocations in Si Nanowires and Nanotubes." *Small* 10.9 (2014), 1756–1760 (cit. on p. 10).

[57] P. L. Kapitza. *J. Phys. U.S.S.R.* 4.181 (1941) (cit. on pp. 10, 103).

[58] E. T. Swartz and R. O. Pohl. "Thermal boundary resistance." *Rev. Mod. Phys.* 61.3 (1989), 605–668 (cit. on pp. 10, 103, 104, 120).

[59] A. J. C. Ladd, B. Moran, and W. G. Hoover. "Lattice thermal conductivity: A comparison of molecular dynamics and anharmonic lattice dynamics." *Phys. Rev. B* 34.8 (1986), 5058–5064 (cit. on p. 10).

[60] S. Volz, J. B. Saulnier, M. Lallemandl, B. Perrin, P. Depondt, and M. Mareschal. "Transient Fourier-law deviation by molecular dynamics in solid argon." *Phys. Rev. B* 54.1 (1996), 340–347 (cit. on p. 10).

[61] P. Hohenberg and W. Kohn. "Inhomogeneous Electron Gas." *Phys. Rev.* 136.3B (1964), B864–B871 (cit. on p. 16).

[62] W. Kohn and L. J. Sham. "Self-Consistent Equations Including Exchange and Correlation Effects." *Phys. Rev.* 140.4A (1965), A1133–A1138 (cit. on p. 16).

[63] S. Baroni, S. de Gironcoli, A. Dal Corso, and P. Giannozzi. "Phonons and related crystal properties from density-functional perturbation theory." *Rev. Mod. Phys.* 73.2 (2001), 515–562 (cit. on p. 16).

[64] P. B. Allen and J. L.Feldman. "Thermal conductivity of disordered harmonic solids." *Phys. Rev. B* 48.17 (1993), 12581–12588 (cit. on p. 16).

[65] R. Peierls. "Zur kinetischen Theorie der Weleitung in Kristallen." *Ann. Phys. (Berl.)* 395.8 (1929), 1055–1101 (cit. on p. 17).

[66] N. W. Ashcroft and N. D. Mermin. *Solid State Physics*. Brooks Cole, Cengage Learning, 1976, p. 461 (cit. on pp. 17, 36, 57, 58, 78).

[67] M. T. Dove. *Structure and Dynamics: An Atomic View of Materials*. Oxford Master Series in Condensed Matter Physics, Vol. 1. Oxford University Press, USA, 2002 (cit. on p. 17).

[68] G. P. Srivastava. *The Physics of Phonons*. Taylor & Francis Group, New York, U.S.A, 1990 (cit. on pp. 19, 20).

[69] J. E. Turney, E. S. Landry, A. J. H. McGaughey, and C. H. Amon. "Predicting phonon properties and thermal conductivity from anharmonic lattice dynamics calculations and molecular dynamics simulations." *Phys. Rev. B* 79.6 (2009), 064301 (cit. on pp. 19, 20).

[70] G. Lehmann and M. Taut. "On the Numerical Calculation of the Density of States and Related Properties." *Phys. Status Solidi B* 54.2 (1972), 469–477 (cit. on p. 20).

[71] P. G. Klemens. "The thermal conductivity of dielectric solids at low temperatures (Theoretical)." *Proc. Royal Soc. A* 208.1092 (1951), 108–133 (cit. on p. 20).

[72] J. Callaway. "Model for Lattice Thermal Conductivity at Low Temperatures." *Phys. Rev.* 113.4 (1959), 1046–1051 (cit. on pp. 21, 84, 103).

[73] G. Fugallo, A. Cepellotti, L. Paulatto, M. Lazzeri, N. Marzari, and F. Mauri. "Thermal Conductivity of Graphene and Graphite: Collective Excitations and Mean Free Paths." *Nano Lett.* 14.11 (2014), 6109–6114 (cit. on p. 21).

[74] S. Lee, D. Broido, K. Esfarjani, and G. Chen. "Hydrodynamic phonon transport in suspended graphene." *Nat. Commun.* 6 (2015), 6290 (cit. on p. 21).

[75] Y. He, I. Savić, D. Donadio, and G. Galli. "Lattice thermal conductivity of semiconducting bulk materials: atomistic simulations." *Phys. Chem. Chem. Phys.* 14.47 (2012), 16209–16222 (cit. on pp. 21, 103, 106, 112).

[76] G. Galli and M. Parrinello. "Ab-Initio Molecular Dynamics: Principles and Practical Implementation." In: *Computer Simulation in Materials Science: Interatomic Potentials, Simulation Techniques and Applications*. Ed. by M. Meyer and V. Pontikis. Dordrecht: Springer Netherlands, 1991, pp. 283–304 (cit. on p. 21).

[77] M. E. Tuckerman, J. P. Ungar, T. von Rosenvinge, and M. L. Klein. "Ab Initio Molecular Dynamics Simulations." *J. Phys. Chem.* 100.31 (1996), 12878–12887 (cit. on p. 21).

[78] L. Colombo. "Tight-binding molecular dynamics: a primer." 28.10 (2005), 59 (cit. on p. 21).

[79] M. Finnis. *Interatomic Forces in Condensed Matter*. Oxford Series on Materials Modelling. Oxford University Press, 2004 (cit. on p. 21).

[80] D. A. McQuarrie. *Statistical Mechanics*. Harper & Row, 1976 (cit. on pp. 22, 23).

[81] M. E. Tuckerman. *Statistical Mechanics: Theory and Molecular Simulation*. Oxford University Press, USA, 2010 (cit. on p. 22).

[82] R. Kubo. "Statistical-Mechanical Theory of Irreversible Processes. I. General Theory and Simple Applications to Magnetic and Conduction Problems." *J. Phys. Soc. Jap.* 12.6 (1957), 570–586 (cit. on p. 23).

[83] M. S. Green. "Markoff Random Processes and the Statistical Mechanics of Time-Dependent Phenomena. II. Irreversible Processes in Fluids." *J. Chem. Phys.* 22.3 (1954), 398–413 (cit. on p. 23).

[84] J. M. Luttinger. "Theory of Thermal Transport Coefficients." *Phys. Rev.* 135.6A (1964), A1505–A1514 (cit. on p. 23).

[85] R. Vogelsang, C. Hoheisel, and G. Ciccotti. "Thermal conductivity of the Lennard-Jones liquid by molecular dynamics calculations." *J. Chem. Phys.* 86.11 (1987), 6371–6375 (cit. on p. 23).

[86] Z. Fan, L. F. C. Pereira, H. Wang, J. Zheng, D. Donadio, and A. Harju. "Force and heat current formulas for many-body potentials in molecular dynamics simulations with applications to thermal conductivity calculations." *Phys. Rev. B* 92.9 (2015), 094301 (cit. on pp. 24, 112).

[87] R. J. Hardy. "Energy-Flux Operator for a Lattice." *Phys. Rev.* 132.1 (1963), 168–177 (cit. on p. 24).

[88] F. H. Stillinger and T. A. Weber. "Computer simulation of local order in condensed phases of silicon." *Phys. Rev. B* 31.8 (1985), 5262–5271 (cit. on pp. 24, 25, 166, 171, 211).

[89] J. Tersoff. "Modeling solid-state chemistry: Interatomic potentials for multicomponent systems." *Phys. Rev. B* 39.8 (1989), 5566–5568 (cit. on pp. 24, 114, 121, 178, 207).

[90] D. W. Brenner. "Empirical potential for hydrocarbons for use in simulating the chemical vapor deposition of diamond films." *Phys. Rev. B* 42.15 (1990), 9458–9471 (cit. on p. 24).

[91] A. Marcolongo, P. Umari, and S. Baroni. "Microscopic theory and quantum simulation of atomic heat transport." *Nat. Phys.* 12 (2016), 80–84 (cit. on pp. 25, 113).

[92] L. Ercole, A. Marcolongo, P. Umari, and S. Baroni. "Gauge Invariance of Thermal Transport Coefficients." *J. Low Temp. Phys.* 185.1 (2016), 79–86 (cit. on p. 25).

[93] C. Carbogno, R. Ramprasad, and M. Scheffler. "*Ab Initio* Green-Kubo Approach for the Thermal Conductivity of Solids." *Phys. Rev. Lett.* 118.17 (2017), 175901 (cit. on p. 25).

[94] C. L. Yaws. *Handbook of thermal conductivity, Volume 1: Organic Compounds C1 to C4*. Library of physico-chemical property data. Gulf Pub. Co, 1997 (cit. on p. 26).

[95] R. Dettori, C. Melis, R., and L. Colombo. "Thermal rectification in silicon by a graded distribution of defects." *J. App. Phys.* 119.21 (2016), 215102 (cit. on pp. 30, 195).

[96] F. Muller-Plathe. "A simple nonequilibrium molecular dynamics method for calculating the thermal conductivity." *J. Chem. Phys.* 106.14 (1997), 6082–6085 (cit. on pp. 31, 33).

[97] P. K. Schelling, S. R. Phillpot, and P. Keblinski. "Comparison of atomic-level simulation methods for computing thermal conductivity." *Phys. Rev. B* 65.14 (2002), 144306 (cit. on pp. 31, 32, 38, 52, 74, 106).

[98] C. Melis, R. Dettori, S. Vandermeulen, and L. Colombo. "Calculating thermal conductivity in a transient conduction regime: theory and implementation." *Eur. Phys. J. B* 87.96 (2014) (cit. on pp. 33, 37, 50–52, 69, 82, 103, 106).

[99] H. Zaoui, P. L. Palla, F. Cleri, and E. Lampin. "Length dependence of thermal conductivity by approach-to-equilibrium molecular dynamics." *Phys. Rev. B* 94.5 (2016), 054304 (cit. on pp. 33, 50).

[100] E. Lampin, P. L. Palla, P. A. Francioso, and F. Cleri. "Thermal conductivity from approach-to-equilibrium molecular dynamics." *J. Appl. Phys.* 114.3 (2013), 033525 (cit. on pp. 33, 50).

[101] E. Lampin, Q. H. Nguyen, P. A. Francioso, and F. Cleri. "Thermal boundary resistance at silicon-silica interfaces by molecular dynamics simulations." *Appl. Phys. Lett.* 100.13 (2012), 131906 (cit. on pp. 33, 36, 106).

[102] R. Dettori, C. Melis, X. Cartoixà, R. Rurali, and L. Colombo. "Model for thermal conductivity in nanoporous silicon from atomistic simulations." *Phys. Rev. B* 91.5 (2015), 054305 (cit. on pp. 37, 67, 68, 72, 82, 121, 195).

[103] C. Melis and L. Colombo. "Lattice Thermal Conductivity of $Si_{1-x}Ge_x$ Nanocomposites." *Phys. Rev. Lett.* 112.6 (2014), 065901 (cit. on pp. 37, 82, 100, 104, 121).

[104] G. Barbarino, C. Melis, and L. Colombo. "Intrinsic thermal conductivity in monolayer graphene is ultimately upper limited: A direct estimation by atomistic simulations." *Phys. Rev. B* 91.3 (2015), 035416 (cit. on pp. 37, 82).

[105] D.P. Sellan, E. S. Landry, J. E. Turney, A. J. H. McGaughey, and C. H. Amon. "Size effects in molecular dynamics thermal conductivity predictions." *Phys. Rev. B* 81.21 (2010), 214305 (cit. on pp. 38, 52, 59, 103, 106, 112).

[106] X. Xu et al. "Length-dependent thermal conductivity in suspended single-layer graphene." *Nat, Commun.* 5.3689 (2014) (cit. on p. 38).

[107] M. Ceriotti, G. Bussi, and M. Parrinello. "Colored-Noise Thermostats à la Carte." *J. Chem. Theory Comput.* 6.4 (2010), 1170–1180 (cit. on pp. 39, 42, 43).

[108] M. Ceriotti, G. Bussi, and M. Parrinello. "Langevin Equation with Colored Noise for Constant-Temperature Molecular Dynamics Simulations." *Phys. Rev. Lett.* 102.4 (2009), 020601 (cit. on pp. 39, 43).

[109] M. Ceriotti, G. Bussi, and M. Parrinello. "Nuclear quantum effects in solids using a colored-noise thermostat." *Phys. Rev. Lett.* 103.3 (2009), 030603 (cit. on pp. 39, 42, 43).

[110] M. Ceriotti and M. Parrinello. "The δ-thermostat: selective normal-modes excitation by colored-noise Langevin Dynamics." *Procedia Computer Sci.* 1.1 (2010), 1607–1614 (cit. on pp. 39, 43, 135).

[111] M. Ceriotti. "A novel framework for enhanced molecular dynamics based on the generalized Langevin equation." PhD thesis. ETH Zürich, 2010 (cit. on pp. 39, 43, 136).

[112] R. Dettori, M. Ceriotti, J. Hunger, C. Melis, L. Colombo, and D. Donadio. "Simulating Energy Relaxation in Pump-Probe Vibrational Spectroscopy of Hydrogen-Bonded Liquids." *J. Chem. Theory Comput.* 13.3 (2017), 1284–1292 (cit. on pp. 39, 195).

[113] S. Nosé. "A unified formulation of the constant temperature molecular dynamics methods." *J. Chem. Phys.* 81.1 (1984), 511–519 (cit. on p. 39).

[114] W. G. Hoover. "Canonical dynamics: Equilibrium phase-space distributions." *Phys. Rev. A* 31.3 (1985), 1695–1697 (cit. on p. 39).

[115] G. J. Martyna, M. L. Klein, and M. Tuckerman. "Nosé-Hoover chains: The canonical ensemble via continuous dynamics." *J. Chem. Phys.* 97.4 (1992), 2635–2643 (cit. on p. 39).

[116] H. C. Andersen. "Molecular dynamics simulations at constant pressure and/or temperature." *J. Chem. Phys.* 72.4 (1980), 2384–2393 (cit. on p. 40).

[117] H. Tanaka, K. Nakanishi, and N. Watanabe. "Constant temperature molecular dynamics calculation on Lennard-Jones fluid and its application to water." *J. Chem. Phys.* 78.5 (1983), 2626–2634 (cit. on p. 40).

[118] T. Schneider and E. Stoll. "Molecular-dynamics study of a three-dimensional one-component model for distortive phase transitions." *Phys. Rev. B* 17.3 (1978), 1302–1322 (cit. on p. 40).

[119] J. C. Mattingly, A. M. Stuart, and D. J. Higham. "Ergodicity for SDEs and approximations: locally Lipschitz vector fields and degenerate noise." *Stoch. Process. Appl.* 101.2 (2002), 185 –232 (cit. on p. 40).

[120] R. Zwanzig. *Non-equilibrium Statistical Mechanics*. 198 Madison Avenue, New York, New York 10016: Oxford University Press, 2001, pp. 18–21 (cit. on pp. 41, 43, 138).

[121] H. Nyquist. "Thermal Agitation of Electric Charge in Conductors." *Phys. Rev.* 32 (1928), 110–113 (cit. on p. 41).

[122] H. B. Callen and T. A. Welton. "Irreversibility and Generalized Noise." *Phys. Rev.* 83 (1951), 34–40 (cit. on p. 41).

[123] H. Mori. "A Continued-Fraction Representation of the Time-Correlation Functions." *Prog. Theor. Phys.* 34.3 (1965), 399–416 (cit. on p. 41).

[124] F. Marchesoni and P. Grigolini. "On the extension of the Kramers theory of chemical relaxation to the case of nonwhite noise." *J. Chem. Phys.* 78.10 (1983), 6287 (cit. on p. 41).

[125] J. Łuczka. "Non-Markovian stochastic processes: Colored noise." *Chaos* 15.2 (2005), 026107 (cit. on p. 41).

[126] Y. He, D. Donadio, J. Lee, J. C. Grossman, and G. Galli. "Thermal Transport in Nanoporous Silicon: Interplay between Disorder at Mesoscopic and Atomic Scales." *ACS Nano* 5.3 (2011), 1839–1844 (cit. on pp. 47, 48, 52, 58).

[127] Á. Miranda-Durán, X. Cartoixà, M. Cruz Irisson, and R. Rurali. "Molecular Doping and Subsurface Dopant Reactivation in Si Nanowires." *Nano Lett.* 10.9 (2010), 3590–3595 (cit. on p. 47).

[128] E. Garrone, F. Geobaldo, P. Rivolo, G. Amato, L. Boarino, M. Chiesa, E. Giamello, R. Gobetto, P. Ugliengo, and A. Viale. "A Nanostructured Porous Silicon Near Insulator Becomes Either a p- or an n-Type Semiconductor upon Gas Adsorption." *Adv. Mater.* 17.5 (2005), 528–531 (cit. on p. 47).

[129] V. Lehmann and U. Gösele. "Porous silicon formation: A quantum wire effect." *Appl. Phys. Lett.* 58.8 (1991), 856–858 (cit. on p. 47).

[130] A. G. Nassiopoulou and G. Kaltsas. "Porous Silicon as an Effective Material for Thermal Isolation on Bulk Crystalline Silicon." *Phys. Status Solidi A* 182.1 (2000), 307–311 (cit. on p. 47).

[131] J. H. Lee, J. C. Grossman, J. Reed, and G. Galli. "Lattice thermal conductivity of nanoporous Si: Molecular dynamics study." *App. Phys. Lett.* 91.22 (2007), 223110 (cit. on pp. 47, 48).

[132] M. J. Sailor. *Fundamentals of Porous Silicon Preparation*. Wiley-VCH Verlag GmbH & Co. KGaA, 2011, pp. 1–42 (cit. on pp. 48, 50).

[133] A. Drost, P. Steiner, H. Moser, and W. Lang. "Thermal conductivity of porous silicon." *Sens. Mat.* 7.2 (1995), 111 (cit. on pp. 48, 63).

[134] U. Bernini, P. Maddalena, E. Massera, and A. Ramaglia. "Thermal characterization of porous silicon via thermal wave interferometry." *Opt. Commun.* 168.1 (1999), 305 –314 (cit. on p. 48).

[135] G. Gesele, J. Linsmeier, V. Drach, J. Fricke, and R. Arens-Fischer. "Temperature-dependent thermal conductivity of porous silicon." *J. Phys. D: Appl. Phys.* 30.21 (1997), 2911 (cit. on pp. 48, 63).

[136] J. Tang, H. T. Wang, D. H. Lee, M. Fardy, Z. Huo, T. P. Russell, and P. Yang. "Holey Silicon as an Efficient Thermoelectric Material." *Nano Lett.* 10.10 (2010), 4279–4283 (cit. on pp. 48, 67).

[137] J. H. Lee, G. A. Galli, and J. C. Grossman. "Nanoporous Si as an Efficient Thermoelectric Material." *Nano Lett.* 8.11 (2008), 3750–3754 (cit. on p. 48).

[138] A. Eucken. "Heat transfer in ceramic refractory materials: Calculation from thermal conductivities of constituents." *Ceram. Abstr.* 11 (1932), 576 (cit. on pp. 48, 55).

[139] A. Eucken. *Ceram. Abstr.* 12 (1933), 231 (cit. on pp. 48, 55).

[140] J. Rouquerol, D. Avnir, D. H. Everett, C. Fairbridge, M. Haynes, N. Pernicone, J. D. F. Ramsay, K. S. W. Sing, and K. K. Unger. "Guidelines for the Characterization of Porous Solids." In: *Characterization of Porous Solids III*. Ed. by J. Rouquerol, F. Rodrìguez-Reinoso, K. S. W. Sing, and K. K. Unger. Studies in Surface Science and Catalysis 87. Elsevier, 1994, pp. 1–9 (cit. on p. 49).

[141] Steve Plimpton. "Fast Parallel Algorithms for Short-Range Molecular Dynamics." *J. Comp. Phys.* 117.1 (1995), 1 –19 (cit. on pp. 51, 71, 123, 139).

[142] J. F. Justo, M. Z. Bazant, E. Kaxiras, V. V. Bulatov, and S. Yip. "Interatomic potential for silicon defects and disordered phases." *Phys. Rev. B* 58.5 (1998), 2539–2550 (cit. on pp. 51, 71, 82, 207, 209).

[143] A. S. Henry and G. Chen. "Spectral Phonon Transport Properties of Silicon Based on Molecular Dynamics Simulations and Lattice Dynamics." *J. Comput. Theor. Nanosci.* 5.2 (2008), 141–152 (cit. on p. 52).

[144] P. E. Hopkins, P. T. Rakich, R. H. Olsson, I. F. El-kady, and L. M. Phinney. "Origin of reduction in phonon thermal conductivity of microporous solids." *App. Phys. Lett.* 95.16 (2009), 161902 (cit. on p. 52).

[145] R. H. Tarkhanyan and D. G. Niarchos. "Reduction of thermal conductivity in porous "gray "materials." *APL Mater.* 2.7 (2014), 076107 (cit. on p. 55).

[146] V. Jean, S. Fumeron, K. Termentzidis, S. Tutashkonko, and D. Lacroix. "Monte Carlo simulations of phonon transport in nanoporous silicon and germanium." *J. Appl. Phys.* 115.2 (2014), 024304 (cit. on p. 55).

[147] David Song and Gang Chen. "Thermal conductivity of periodic microporous silicon films." *Appl. Phys. Lett.* 84.5 (2004), 687–689 (cit. on pp. 55, 76).

[148] F. X. Alvarez, D. Jou, and A. Sellitto. "Pore-size dependence of the thermal conductivity of porous silicon: A phonon hydrodynamic approach." *Appl. Phys. Lett.* 97.3 (2010), 033103 (cit. on p. 56).

[149] J. Fang and L. Pilon. "Scaling laws for thermal conductivity of crystalline nanoporous silicon based on molecular dynamics simulations." *J. Appl. Phys.* 110.6 (2011), 064305 (cit. on p. 56).

[150] I. Sumirat, Y. Ando, and S. Shimamura. "Theoretical consideration of the effect of porosity on thermal conductivity of porous materials." *J. Porous Mater.* 13.3 (2006), 439–443 (cit. on p. 58).

[151] A. Ould-Abbas, M. Bouchaour, and N. Sari. "Study of Thermal Conductivity of Porous Silicon Using the Micro-Raman Method." *Open J. Phys. Chem.* 02.01 (2012), 1–6 (cit. on p. 63).

[152] S. Périchon, V. Lysenko, B. Remaki, D. Barbier, and B. Champagnon. "Measurement of porous silicon thermal conductivity by micro-Raman scattering." *J. Appl. Phys.* 86.8 (1999), 4700–4702 (cit. on p. 63).

[153] G. Benedetto, L. Boarino, and R. Spagnolo. "Evaluation of thermal conductivity of porous silicon layers by a photoacoustic method." *Appl. Phys. A* 64.2 (1997), 155–159 (cit. on p. 63).

[154] L. Yang, Q. Zhai, H. Jiang, L. Han, J. Wang, and E. Wang. "A light transmission technique for pore size measurement in track-etched membranes." *Chem. Commun.* 49.97 (2013), 11415–11417 (cit. on p. 64).

[155] W. Lu and C. M Lieber. "Semiconductor nanowires." *J. Phys. D: Appl. Phys.* 39.21 (2006), R387 (cit. on p. 67).

[156] R. Rurali. "Colloquium: Structural, electronic, and transport properties of silicon nanowires." *Rev. Mod. Phys.* 82.1 (2010), 427–449 (cit. on p. 67).

[157] L. T. Canham. "Silicon quantum wire array fabrication by electrochemical and chemical dissolution of wafers." *Appl. Phys. Lett.* 57.10 (1990), 1046–1048 (cit. on p. 67).

[158] L. Deyu, W. Yiying, K. Philip, S. Li, Y. Peidong, and M. Arun. "Thermal conductivity of individual silicon nanowires." *Appl. Phys. Lett.* 83.14 (2003), 2934–2936 (cit. on p. 67).

[159] A. I. Boukai, Y. Bunimovich, J. Tahir-Kheli, J. K. Yu, W. A. Goddard III, and J. R. Heath. "Silicon nanowires as efficient thermoelectric materials." *Nature* 451 (2008), 168 (cit. on pp. 67, 76).

[160] X. Zianni, V. Jean, K. Termentzidis, and D. Lacroix. "Scaling behavior of the thermal conductivity of width-modulated nanowires and nanofilms for heat transfer control at the nanoscale." *Nanotechnology* 25.46 (2014), 465402 (cit. on p. 67).

[161] Y. Qu, H. Zhou, and X. Duan. "Porous silicon nanowires." *Nanoscale* 3.10 (2011), 4060–4068 (cit. on p. 67).

[162] M. Ge, J. Rong, X. Fang, and C. Zhou. "Porous Doped Silicon Nanowires for Lithium Ion Battery Anode with Long Cycle Life." *Nano Lett.* 12.5 (2012), 2318–2323 (cit. on p. 67).

[163] A. Najar, J. Charrier, P. Pirasteh, and R. Sougrat. "Ultra-low reflection porous silicon nanowires for solar cell applications." *Opt. Express* 20.15 (2012), 16861–16870 (cit. on p. 67).

[164] H. B. G. Casimir. "Note on the conduction of heat in crystals." *Physica* 5.6 (1938), 495 –500 (cit. on p. 68).

[165] T. Feng, B. Qiu, and X. Ruan. "Coupling between phonon-phonon and phonon-impurity scattering: A critical revisit of the spectral Matthiessen's rule." *Phys. Rev. B* 92.23 (2015), 235206 (cit. on pp. 68, 79).

[166] J. E. Turney, A. J. H. McGaughey, and C. H. Amon. "In-plane phonon transport in thin films." *J. App. Phys.* 107.2 (2010), 024317 (cit. on p. 69).

[167] M. Luisier. "Thermal transport and Matthiessen's rule in ultra-scaled Si nanowires." *App. Phys. Lett.* 103.11 (2013), 113103 (cit. on pp. 69, 73, 79).

[168] J. M. Weisse, A. M. Marconnet, D. R. Kim, P. M. Rao, M. A. Panzer, K. E. Goodson, and X. Zheng. "Thermal conductivity in porous silicon nanowire arrays." *Nanoscale Res. Lett.* 7.1 (2012), 554 (cit. on p. 69).

[169] T. Zhang, S. Wu, R. Zheng, and G. Cheng. "Significant reduction of thermal conductivity in silicon nanowire arrays." *Nanotechnology* 24.50 (2013), 505718 (cit. on p. 69).

[170] J. M. Larkin and A. J. H. McGaughey. "Thermal conductivity accumulation in amorphous silica and amorphous silicon." *Phys. Rev. B* 89.14 (2014), 144303 (cit. on p. 71).

[171] S. Plimpton, A. Thompson, S. Moore, and A. Kohlmeyer. *LAMMPS - Large-scale Atomic/Molecular Massively Parallel Simulator*. URL: http://lammps.sandia.gov/ (cit. on p. 71).

[172] P. B. Allen, J. L. Feldman, J. Fabian, and F. Wooten. "Diffusons, locons and propagons: Character of atomie yibrations in amorphous Si." *Philos. Mag. B* 79.11-12 (1999), 1715–1731 (cit. on p. 73).

[173] C. Oligschleger and J. C. Schön. "Simulation of thermal conductivity and heat transport in solids." *Phys. Rev. B* 59.6 (1999), 4125–4133 (cit. on p. 74).

[174] K. T. Regner, D. P. Sellan, Z. Su, C. H. Amon, A. J. H. McGaughey, and J. A. Malen. "Broadband phonon mean free path contributions to thermal conductivity measured using frequency domain thermoreflectance." *Nat. Commun* 4 (2013), 1640 (cit. on p. 74).

[175] J. Michalski. "Thermal conductivity of amorphous solids above the plateau: Molecular-dynamics study." *Phys. Rev. B* 45.13 (1992), 7054–7065 (cit. on p. 74).

[176] F. Yang and C. Dames. "Mean free path spectra as a tool to understand thermal conductivity in bulk and nanostructures." *Phys. Rev. B* 87.3 (2013), 035437 (cit. on pp. 76, 78, 80).

[177] M. Nomura, Y. Kage, D. Müller, D. Moser, and O. Paul. "Electrical and thermal properties of polycrystalline Si thin films with phononic crystal nanopatterning for thermoelectric applications." *Appl. Phys. Lett.* 106.22 (2015), 223106 (cit. on p. 76).

[178] Z. Wang, J. E. Alaniz, W. Jang, J. E. Garay, and C. Dames. "Thermal Conductivity of Nanocrystalline Silicon: Importance of Grain Size and Frequency-Dependent Mean Free Paths." *Nano Lett.* 11.6 (2011), 2206–2213 (cit. on pp. 76, 77, 84, 85, 90).

[179] C. Hua and A. J. Minnich. "Importance of frequency-dependent grain boundary scattering in nanocrystalline silicon and silicon-germanium thermoelectrics." *Semicond. Sci. Technol.* 29.12 (2014), 124004 (cit. on pp. 76, 77, 84).

[180] J. Ma, B. R. Parajuli, M. G. Ghossoub, A. Mihi, J. Sadhu, P. V. Braun, and S. Sinha. "Coherent Phonon-Grain Boundary Scattering in Silicon Inverse Opals." *Nano Lett.* 13.2 (2013), 618–624 (cit. on p. 76).

[181] J. Fang, C. B. Kang, Y. Huang, S. H. Tolbert, and L. Pilon. "Thermal Conductivity of Ordered Mesoporous Nanocrystalline Silicon Thin Films Made from Magnesium Reduction of Polymer-Templated Silica." *J. Phys. Chem. C* 116.23 (2012), 12926–12933 (cit. on p. 76).

[182] D. G. Cahill and R. O. Pohl. "Lattice Vibrations and Heat Transport in Crystals and Glasses." *Annu. Rev. Phys. Chem.* 39.1 (1988), 93–121 (cit. on p. 77).

[183] P. Jiang, L. Lindsay, and Y. K. Koh. "Role of low-energy phonons with mean-free-paths > 0.8 μm in heat conduction in silicon." *J. Appl. Phys.* 119.24 (2016), 245705 (cit. on pp. 77, 80).

[184] M. T. Dunham, B. Lorenzi, S. C. Andrews, A. Sood, M. Asheghi, D. Narducci, and K. E. Goodson. "Enhanced phonon scattering by nanovoids in high thermoelectric power factor polysilicon thin films." *Appl. Phys. Lett.* 109.25 (2016), 253104 (cit. on pp. 77, 89, 90, 92).

[185] L. Weber and E. Gmelin. "Transport properties of silicon." *Appl. Phys. A* 53.2 (1991), 136–140 (cit. on p. 77).

[186] M. Asheghi, Y. K. Leung, S. S. Wong, and K. E. Goodson. "Phonon-boundary scattering in thin silicon layers." *Appl. Phys. Lett.* 71.13 (1997), 1798–1800 (cit. on p. 77).

[187] Z. Z. Aksamija and I. Knezevic. "Anisotropy and boundary scattering in the lattice thermal conductivity of silicon nanomembranes." *Phys. Rev. B* 82.4 (2010), 045319 (cit. on p. 77).

[188] W. Liu and M. Asheghi. "Thermal conduction in ultrathin pure and doped single-crystal silicon layers at high temperatures." *J. Appl. Phys.* 98.12 (2005), 123523 (cit. on p. 77).

[189] D. Narducci, G. Cerofolini, M. Ferri, F. Suriano, F. Mancarella, L. Belsito, S. Solmi, and A. Roncaglia. "Phonon scattering enhancement in silicon nanolayers." *J. Mater. Sci.* 48.7 (2013), 2779–2784 (cit. on p. 77).

[190] S. K. Bux, R. G. Blair, P. K. Gogna, H. Lee, G. Chen, M. S. Dresselhaus, R. B. Kaner, and J. P. Fleurial. "Nanostructured Bulk Silicon as an Effective Thermoelectric Material." *Adv. Funct. Mater.* 19.15 (2009), 2445–2452 (cit. on p. 78).

[191] T. Claudio, N. Stein, D. G. Stroppa, B. Klobes, M. M. Koza, P. Kudejova, N. Petermann, H. Wiggers, G. Schierning, and R. P. Hermann. "Nanocrystalline silicon: lattice dynamics and enhanced thermoelectric properties." *Phys. Chem. Chem. Phys.* 16.47 (2014), 25701–25709 (cit. on pp. 78, 85).

[192] N. Neophytou, X. Zianni, H. Kosina, S. Frabboni, B. Lorenzi, and D. Narducci. "Simultaneous increase in electrical conductivity and Seebeck coefficient in highly boron-doped nanocrystalline Si." *Nanotechnology* 24.20 (2013), 205402 (cit. on p. 78).

[193] D. Narducci, B. Lorenzi, X. Zianni, N. Neophytou, S. Frabboni, G. Gazzadi, A. Roncaglia, and F. Suriano. "Enhancement of the power factor in two-phase silicon-boron nanocrystalline alloys." *Phys. Status Solidi A* 211.6 (2014), 1255–1258 (cit. on pp. 78, 92).

[194] D. Narducci, S. Frabboni, and X. Zianni. "Silicon de novo: energy filtering and enhanced thermoelectric performances of nanocrystalline silicon and silicon alloys." *J. Mater. Chem. C* 3.47 (2015), 12176–12185 (cit. on pp. 78, 92).

[195] N. S. Bennett, N. M. Wight, S. R. Popuri, and J. W. G. Bos. "Efficient thermoelectric performance in silicon nano-films by vacancy-engineering." *Nano Energy* 16.Supplement C (2015), 350 –356 (cit. on p. 78).

[196] Z. Aksamija. "Lattice Thermal Transport in Si-based Nanocomposites for Thermoelectric Applications." *J. Electron. Mater.* 44.6 (2015), 1644–1650 (cit. on p. 78).

[197] X. Cartoixà, R. Dettori, C. Melis, L. Colombo, and R. Rurali. "Thermal transport in porous Si nanowires from approach-to-equilibrium molecular dynamics calculations." *Appl. Phys. Lett.* 109.1 (2016), 013107 (cit. on pp. 79, 90, 195).

[198] K. Esfarjani, G. Chen, and H. T. Stokes. "Heat transport in silicon from first-principles calculations." *Phys. Rev. B* 84.8 (2011), 085204 (cit. on pp. 80, 84).

[199] L. Brambilla, L., V. Rosato, and F. Cleri. "Solid-liquid interface velocity and diffusivity in laser-melt amorphous silicon." *Appl. Phys. Lett.* 77.15 (2000), 2337–2339 (cit. on p. 82).

[200] R. Dettori, C. Melis, and L. Colombo. "Si_xGe_{1-x} alloy as efficient phonon barrier in Ge/Si superlattices for thermoelectric applications." *Eur. Phys. J. B* 88.1 (2015), 27 (cit. on pp. 82, 113, 117, 195).

[201] K. R. Hahn, C. Melis, and L. Colombo. "Structural, Vibrational, and Thermal Properties of Nanocrystalline Graphene in Atomistic Simulations." *J. Phys. Chem. C* 120.5 (2016), 3026–3035 (cit. on p. 82).

[202] K. R. Hahn, C. Melis, and L. Colombo. "Thermal transport in nanocrystalline graphene investigated by approach-to-equilibrium molecular dynamics simulations." *Carbon* 96.Supplement C (2016), 429–438 (cit. on p. 82).

[203] S. Das Sarma and F. Stern. "Single-particle relaxation time versus scattering time in an impure electron gas." *Phys. Rev. B* 32.12 (1985), 8442–8444 (cit. on p. 83).

[204] J. Yang and T. Caillat. "Thermoelectric Materials for Space and Automotive Power Generation." *MRS Bulletin* 31.3 (2006), 224?229 (cit. on p. 84).

[205] R. Tubino, L. Piseri, and G. Zerbi. "Lattice Dynamics and Spectroscopic Properties by a Valence Force Potential of Diamondlike Crystals: C, Si, Ge, and Sn." *J. Chem. Phys.* 56.3 (1972), 1022–1039 (cit. on p. 85).

[206] V. Chiloyan, J. Garg, K. Esfarjani, and G. Chen. "Transition from near-field thermal radiation to phonon heat conduction at sub-nanometre gaps." *Nat. Commun.* 6.6755 (2015) (cit. on p. 87).

[207] M. Asheghi, K. Kurabayashi, R. Kasnavi, and K. E. Goodson. "Thermal conduction in doped single-crystal silicon films." *J. Appl. Phys.* 91.8 (2002), 5079–5088 (cit. on p. 89).

[208] B. Lorenzi, D. Narducci, R. Tonini, S. Frabboni, G. C. Gazzadi, G. Ottaviani, N. Neophytou, and X. Zianni. "Paradoxical Enhancement of the Power Factor of Polycrystalline Silicon as a Result of the Formation of Nanovoids." *J. Electron. Mater.* 43.10 (2014), 3812–3816 (cit. on pp. 90, 92).

[209] B. Lorenzi, S. Frabboni, G. Gazzadi, R. Tonini, G. Ottaviani, and D. Narducci. "Nanovoid Formation and Dynamics in He+-Implanted Nanocrystalline Silicon." *J. Electron. Mater.* 43.10 (2014), 3852–3856 (cit. on pp. 90, 92).

[210] D. Narducci, E. Selezneva, G. Cerofolini, S. Frabboni, and G. Ottaviani. "Impact of energy filtering and carrier localization on the thermoelectric properties of granular semiconductors." *J. Solid State Chem.* 193.Supplement C (2012). Solid State Chemistry and Materials Science of Thermoelectric Materials, 19 –25 (cit. on p. 92).

[211] M. H. Elsheikh, D. A. Shnawah, M. F. M. Sabri, S. B. M. Said, M. H. Hassan, M. B. A. Bashir, and M. Mohamad. "A review on thermoelectric renewable energy: Principle parameters that affect their performance." *Renew. Subst. Energ. Rev.* 30.Supplement C (2014), 337 –355 (cit. on p. 93).

[212] L. D. Hicks and M. S. Dresselhaus. "Thermoelectric figure of merit of a one-dimensional conductor." *Phys. Rev. B* 47.24 (1993), 16631–16634 (cit. on p. 93).

[213] B. Yang and G. Chen. "Experimental Studies on Thermal Conductivity of Thin Films and Superlattices." In: *Thermal Conductivity: Theory, Properties and Applications*. Ed. by T. M. Tritt. Springer, Boston, MA, 2004 (cit. on p. 93).

[214] R. Rurali, X. Cartoixà, and L. Colombo. "Heat transport across a SiGe nanowire axial junction: Interface thermal resistance and thermal rectification." *Phys. Rev. B* 90.4 (2014), 041408 (cit. on pp. 93, 105, 112, 113, 117, 121).

[215] T. C. Harman, P. J. Taylor, M. P. Walsh, and B. E. LaForge. "Quantum Dot Superlattice Thermoelectric Materials and Devices." *Science* 297.5590 (2002), 2229–2232. eprint: http://science.sciencemag.org/content/297/5590/2229.full.pdf (cit. on pp. 93, 94).

[216] G. Chen. "Thermal conductivity and ballistic-phonon transport in the cross-plane direction of superlattices." *Phys. Rev. B* 57.23 (1998), 14958–14973 (cit. on p. 94).

[217] I. C. Lin, A. P. Seitsonen, I. Tavernelli, and U. Rothlisberger. "Structure and Dynamics of Liquid Water from ab Initio Molecular Dynamics-Comparison of BLYP, PBE, and revPBE Density Functionals with and without van der Waals Corrections." *J. Chem. Theory Comput.* 8.10 (2012), 3902–3910 (cit. on pp. 94, 150).

[218] Y. K. Koh, Y. Cao, D. G. Cahill, and D. Jena. "Heat-Transport Mechanisms in Superlattices." *Adv. Funct. Mater.* 19.4 (2009), 610–615 (cit. on p. 94).

[219] G. Chen and C. L. Tien. "Thermal conductivities of quantum well structures." *J. Thermophys. Heat Transf.* 7.2 (1993), 311–318 (cit. on p. 94).

[220] Z. Chen, J. Yang, P. Zhuang, M. Chen, J. Zhu, and Y. Chen. "Thermal conductivity measurement of InGaAs/InGaAsP superlattice thin films." *Chin. Sci. Bull.* 51.23 (2006), 2931–2936 (cit. on p. 94).

[221] Y. Chen, D. Li, Juekuan Yang, Yonghua Wu, Jennifer R. Lukes, and Arun Majumdar. "Molecular dynamics study of the lattice thermal conductivity of Kr/Ar superlattice nanowires." *Physica B: Condensed Matter* 349.1 (2004), 270 –280 (cit. on p. 94).

[222] Y. Chen, D. Liand J. R. Lukes, Z. Ni, and M. Chen. "Minimum superlattice thermal conductivity from molecular dynamics." *Phys. Rev. B* 72.17 (2005), 174302 (cit. on p. 94).

[223] I. Savić, D. Donadio, F. Gygi, and G. Galli. "Dimensionality and heat transport in Si-Ge superlattices." *Appl. Phys. Lett.* 102.7 (2013), 073113 (cit. on p. 94).

[224] S. Chakraborty, C. A. Kleint, A. Heinrich, C. M. Schneider, J. Schumann, M. Falke, and S. Teichert. "Thermal conductivity in strain symmetrized Si/Ge superlattices on Si(111)." *Appl. Phys. Lett.* 83.20 (2003), 4184–4186 (cit. on pp. 94, 99).

[225] L. Ferre Llin et al. "The cross-plane thermoelectric properties of p-Ge/Si0.5Ge0.5 superlattices." *Appl. Phys. Lett.* 103.14 (2013), 143507 (cit. on pp. 94, 95, 99, 101, 104, 113, 114).

[226] T. H. Geballe and G. W. Hull. "Seebeck Effect in Germanium." *Phys. Rev.* 94.5 (1954), 1134–1140 (cit. on pp. 95, 99).

[227] M. Peressi, L. Colombo, R. Resta, S. Baroni, and A. Baldereschi. "Structural and electronic properties of strained Si/GaAs heterostructures." *Phys. Rev. B* 48.16 (1993), 12047–12052 (cit. on p. 95).

[228] Chris G. Van de Walle. "Band lineups and deformation potentials in the model-solid theory." *Phys. Rev. B* 39.3 (1989), 1871–1883 (cit. on p. 95).

[229] F. Schäffler. "Silicon-Germanium ($Si_{1-x}Ge_x$)." In: *Properties of Advanced Semiconductor Materials: GaN, AlN, InN, BN, SiC, SiGe*. Ed. by M. E. Levinshtein, S. L. Rumyantsev, and M. S. Shur. John Wiley & Sons, Inc., 2001 (cit. on p. 96).

[230] K. Moriguchi and A. Shintani. "Verification of Tersoff's Potential for Static Structural Analysis of Solids of Group-IV Elements." *Jpn. J. Appl. Phys.* 37.2R (1998), 414 (cit. on p. 96).

[231] J. Garg, N. Bonini, B. Kozinsky, and N. Marzari. "Role of Disorder and Anharmonicity in the Thermal Conductivity of Silicon-Germanium Alloys: A First-Principles Study." *Phys. Rev. Lett.* 106.4 (2011), 045901 (cit. on pp. 100, 121).

[232] G. Busch and O. Vogt. "Electrical conductivity and hall effect of Ge-Si alloys." *Helv. Phys. Acta* 33.5 (1960) (cit. on pp. 100, 101).

[233] M. V. Simkin and G. D. Mahan. "Minimum Thermal Conductivity of Superlattices." *Phys. Rev. Lett.* 84.5 (2000), 927–930 (cit. on p. 102).

[234] T.L. Bergman, A.S. Lavine, F.P. Incropera, and D.P. Dewitt. *Fundamentals of Heat and Mass Transfer*. John Wileys & Sons, 2002 (cit. on p. 103).

[235] J.H. Lienhard IV and J.H. Lienhard V. *A heat transfer textbook*. Phlogiston Press, Cambridge, 2006 (cit. on p. 103).

[236] G. Fugallo and L. Colombo. "Calculating lattice thermal conductivity: a synopsis." *Phys. Scr.* (2017). in press (cit. on p. 103).

[237] D. A. Broido, M. Malorny, G. Birner, Natalio Mingo, and D. A. Stewart. "Intrinsic lattice thermal conductivity of semiconductors from first principles." *Appl. Phys. Lett.* 91.23 (2007), 231922 (cit. on p. 103).

[238] D. Frenkel and B. Smit. *Understanding Molecular Simulations - From Algoritms to Applications*. Academic Press, San Diego, 1996 (cit. on pp. 103, 199).

[239] P. Jund and R. Jullie. "Molecular-dynamics calculation of the thermal conductivity of vitreous silica." *Phys. Rev. B* 59.21 (1999), 13707–13711 (cit. on p. 103).

[240] J. S. Wang. "Quantum Thermal Transport from Classical Molecular Dynamics." *Phys. Rev. Lett.* 99.16 (2007), 160601 (cit. on p. 103).

[241] H. Dammak, Y. Chalopin, M. Laroche, M. Hayoun, and J. J. Greffet. "Quantum Thermal Bath for Molecular Dynamics Simulation." *Phys. Rev. Lett.* 103.19 (2009), 190601 (cit. on p. 103).

[242] J. L. Barrat and D. Rodney. "Portable Implementation of a Quantum Thermal Bath for Molecular Dynamics Simulations." *J. Stat. Phys.* 144.3 (2011), 679–689 (cit. on p. 103).

[243] O. N. Bedoya-Martínez, J. L. Barrat, and D. Rodney. "Computation of the thermal conductivity using methods based on classical and quantum molecular dynamics." *Phys. Rev. B* 89.1 (2014), 014303 (cit. on p. 103).

[244] G. L. Pollack. "Kapitza Resistance." *Rev. Mod. Phys.* 41.1 (1969), 48–81 (cit. on p. 103).

[245] D. G. Cahill et al. "Nanoscale thermal transport. II. 2003-2012." *Appl. Phys. Rev.* 1.1 (2014), 011305 (cit. on pp. 103, 119).

[246] A. Antidormi and L. Colombo. "Lattice Thermal Boundary Resistance." In: *Handbook of Materials Modeling*. Ed. by W. Andreoni and S. Yip. Springer, Boston, MA, 2017. in press (cit. on p. 103).

[247] J. Chen, G. Zhang, and B. Li. "Thermal contact resistance across nanoscale silicon dioxide and silicon interface." *J. Appl. Phys.* 112.6 (2012), 064319 (cit. on pp. 104, 114).

[248] N. Li, J. Ren, L. Wang, G. Zhang, P. Hänggi, and B. Li. "*Colloquium*: Phononics: Manipulating heat flow with electronic analogs and beyond." *Rev. Mod. Phys.* 84.3 (2012), 1045–1066 (cit. on pp. 104, 119).

[249] S. Volz et al. "Nanophononics: state of the art and perspectives." *Eur. Phys. J. B* 89.1 (2016), 15 (cit. on pp. 104, 119).

[250] P. Chen et al. "Evolution of thermal, structural, and optical properties of SiGe superlattices upon thermal treatment." *Phys. Status Solidi A* 213.3 (2016), 533–540 (cit. on pp. 104, 113).

[251] P. Ferrando-Villalba et al. "Tailoring thermal conductivity by engineering compositional gradients in $Si_{1?x}Ge_x$ superlattices." *Nano Res.* 8.9 (2015), 2833–2841 (cit. on pp. 104, 113).

[252] M. Terraneo, M. Peyrard, and G. Casati. "Controlling the Energy Flow in Nonlinear Lattices: A Model for a Thermal Rectifier." *Phys. Rev. Lett.* 88.9 (2002), 094302 (cit. on p. 104).

[253] B. Li, L. Wang, and G. Casati. "Thermal Diode: Rectification of Heat Flux." *Phys. Rev. Lett.* 93.18 (2004), 184301 (cit. on pp. 104, 119).

[254] N.A. Roberts and D.G. Walker. "A review of thermal rectification observations and models in solid materials." *Int. J. Therm. Sci.* 50.5 (2011), 648 –662 (cit. on pp. 104, 119, 120).

[255] C. Dames. "Solid-State Thermal Rectification With Existing Bulk Materials." *J. Heat Transfer.* 131.6 (2009), 061301 (cit. on pp. 104, 119, 120).

[256] I. M. Khalatnikov. *Zh. Eksp. Teor. Fiz.* 22.687 (1952) (cit. on p. 104).

[257] W. A. Little. "The transport of heat between dissimilar solids at low temperatures." *Can. J. Phys.* 37.3 (1959), 334–349 (cit. on p. 104).

[258] T. Beechem, S. Graham, P. Hopkins, and P. Norris. "Role of interface disorder on thermal boundary conductance using a virtual crystal approach." *Appl. Phys. Lett.* 90.5 (2007), 054104 (cit. on p. 104).

[259] P. E. Hopkins, J. C. Duda, S. P. Clark, C. P. Hains, T. J. Rotter, L. M. Phinney, and G. Balakrishnan. "Effect of dislocation density on thermal boundary conductance across GaSb/GaAs interfaces." *Appl. Phys. Lett.* 98.16 (2011), 161913 (cit. on p. 104).

[260] R. S. Prasher, P. E. Phelan, and E. Patrick. "A Scattering-Mediated Acoustic Mismatch Model for the Prediction of Thermal Boundary Resistance." *J. Heat Transf.* 123.1 (2000), 105–112 (cit. on p. 104).

[261] D. A. Young and H. J. Maris. "Lattice-dynamical calculation of the Kapitza resistance between fcc lattices." *Phys. Rev. B* 40.6 (1989), 3685–3693 (cit. on p. 105).

[262] E. S. Landry and A. J. H. McGaughey. "Thermal boundary resistance predictions from molecular dynamics simulations and theoretical calculations." *Phys. Rev. B* 80.16 (2009), 165304 (cit. on pp. 105, 116).

[263] L. A. Zotti, M. Bürkle, F. Pauly, W. Lee, K. Kim, W. Jeong, Y. Asai, P. Reddy, and J. C. Cuevas. "Heat dissipation and its relation to thermopower in single-molecule junctions." *New J. Phys* 16.1 (2014), 015004 (cit. on p. 105).

[264] K. R. Hahn, M. Puligheddu, and L. Colombo. "Thermal boundary resistance at Si/Ge interfaces determined by approach-to-equilibrium molecular dynamics simulations." *Phys. Rev. B* 91.19 (2015), 195313 (cit. on pp. 105, 106, 116, 117).

[265] X. Cartoixà, L. Colombo, and R. Rurali. "Thermal Rectification by Design in Telescopic Si Nanowires." *Nano Lett.* 15.12 (2015), 8255–8259 (cit. on pp. 105, 121).

[266] S. Kjelstrup and D. Bedeaux. "Thermodynamic Relations for Heterogeneous Systems." In: *Non-Equilibrium Thermodynamics of Heterogeneous Systems*. World Scientific, 2011 (cit. on pp. 107, 108).

[267] C. Kittel and H. Kroemer. *Thermal Physics*. W.H. Freeman Publisher, New York, 1980 (cit. on p. 108).

[268] J. Chen, G. Zhang, and B. Li. "Molecular Dynamics Simulations of Heat Conduction in Nanostructures: Effect of Heat Bath." *J. Phys. Soc. Jpn* 79.7 (2010), 074604 (cit. on p. 112).

[269] C. Melis, G. Barbarino, and L. Colombo. "Exploiting hydrogenation for thermal rectification in graphene nanoribbons." *Phys. Rev. B* 92.24 (2015), 245408 (cit. on pp. 113, 121).

[270] S. M. Lee, D. G. Cahill, and R. Venkatasubramanian. "Thermal conductivity of Si-Ge superlattices." *Appl. Phys. Lett.* 70.22 (1997), 2957–2959 (cit. on p. 113).

[271] G. Zhang and B. Li. "Impacts of doping on thermal and thermoelectric properties of nanomaterials." *Nanoscale* 2.7 (2010), 1058–1068 (cit. on p. 113).

[272] R. Rurali, L. Colombo, X. Cartoixà, O. Wilhelmsen, T. T. Trinh, D. Bedeaux, and S. Kjelstrup. "Heat transport through a solid-solid junction: the interface as an autonomous thermodynamic system." *Phys. Chem. Chem. Phys.* 18 (2016), 13741–13745 (cit. on pp. 117, 125).

[273] C. Starr. "The Copper Oxide Rectifier." *Physics* 7.1 (1936), 15–19 (cit. on p. 119).

[274] M. J. Martínez-Pérez, A. Fornieri, and F. Giazotto. "Rectification of electronic heat current by a hybrid thermal diode." *Nat. Nanotechnol.* 10 (2015), 303 (cit. on p. 120).

[275] M. Hu, P. Keblinski, and B. Li. "Thermal rectification at silicon-amorphous polyethylene interface." *Appl. Phys. Lett.* 92.21 (2008), 211908 (cit. on p. 120).

[276] N. Yang, N. Li, L. Wang, and B. Li. "Thermal rectification and negative differential thermal resistance in lattices with mass gradient." *Phys. Rev. B* 76.2 (2007), 020301 (cit. on p. 121).

[277] C. W. Chang, D. Okawa, A. Majumdar, and A. Zettl. "Solid-State Thermal Rectifier." *Science* 314.5802 (2006), 1121–1124 (cit. on pp. 121, 123).

[278] G. Wu and B. Li. "Thermal rectifiers from deformed carbonnanohorns." *J. Phys. Cond. Mat.* 20.17 (2008), 175211 (cit. on p. 121).

[279] N. Yang, G. Zhang, and B. Li. "Carbon nanocone: A promising thermal rectifier." *Appl. Phys. Lett.* 93.24 (2008), 243111 (cit. on p. 121).

[280] J. Hu, X. Ruan, and U. P. Chen. "Thermal Conductivity and Thermal Rectification in Graphene Nanoribbons: A Molecular Dynamics Study." *Nano Lett.* 9.7 (2009), 2730–2735 (cit. on p. 121).

[281] H. Tian, D. Xie, Y. Yang, T. L. Ren, G. Zhang, Y. F. Wang, C. J. Zhou, P. G. Peng, L. G. Wang, and L. T. Liu. "A Novel Solid-State Thermal Rectifier Based On Reduced Graphene Oxide." *Sci. Rep.* 2 (2012), 523 (cit. on pp. 121, 123).

[282] L. Medrano Sandonas, R. Gutierrez, A. Dianat, and G. Cuniberti. "Engineering thermal rectification in MoS2 nanoribbons: a non-equilibrium molecular dynamics study." *RSC Adv.* 5.67 (2015), 54345–54351 (cit. on p. 121).

[283] D. B. Go and M. Sen. "On the Condition for Thermal Rectification Using Bulk Materials." *J. Heat Transfer* 132.12 (2010), 124502–124502–4 (cit. on pp. 121, 127).

[284] X. Zhang, M. Hu, and D. Tang. "Thermal rectification at silicon/horizontally aligned carbon nanotube interfaces." *J. Appl. Phys.* 113.19 (2013), 194307 (cit. on p. 123).

[285] M. Schmotz, J. Maier, E. Scheer, and P. Leiderer. "A thermal diode using phonon rectification." *New Journal of Physics* 13.11 (2011), 113027 (cit. on p. 123).

[286] S. Ju and X. Liang. "Thermal rectification and phonon scattering in asymmetric silicon nanoribbons." *J. Appl. Phys.* 112.2 (2012), 024307 (cit. on p. 123).

[287] S. Ju and X. Liang. "Thermal rectification and phonon scattering in silicon nanofilm with cone cavity." *J. Appl. Phys.* 112.5 (2012), 054312 (cit. on p. 123).

[288] M. Criado-Sancho, F. X. Alvarez, and D. Jou. "Thermal rectification in inhomogeneous nanoporous Si devices." *J. Appl. Phys.* 114.5 (2013), 053512 (cit. on p. 123).

[289] C. J. Fecko, J. D. Eaves, J. J Loparo, A. Tokmakoff, and P. L. Geissler. "Ultrafast Hydrogen-Bond Dynamics in the Infrared Spectroscopy of Water." *Science* 301.5640 (2003), 1698–1702 (cit. on p. 133).

[290] I. Josefssonm, S. K. Eriksson, N. Ottosson, G.Öhrwall, H. Siegbahn, A. Hagfeldt, H. Rensmo, and O. Björneholm M. Odelius. "Collective hydrogen-bond dynamics dictates the electronic structure of aqueous I3-." *Phys. Chem. Chem. Phys.* 15.46 (2013), 20189–20196 (cit. on p. 133).

[291] H. J. Bakker and J. L. Skinner. "Vibrational Spectroscopy as a Probe of Structure and Dynamics in Liquid Water." *Chem. Rev.* 110.3 (2010), 1498–1517 (cit. on pp. 133, 139).

[292] R. Laenen, G. M. Gale, and N. Lascoux. "IR Spectroscopy of Hydrogen-Bonded Methanol: Vibrational and Structural Relaxation on the Femtosecond Time Scale." *J. Phys. Chem. A* 103.50 (1999), 10708–10712 (cit. on p. 133).

[293] K. L. Vodopyanov. "Saturation studies of H20 and HDO near 3400 cm-1 using intense picosecond laser pulses." *J. Chem. Phys.* 94.8 (1991), 5389–5393 (cit. on p. 133).

[294] A. Luzar and D. Chandler. "Hydrogen-bond kinetics in liquid water." *Nature* 379.6560 (1996), 55–57 (cit. on p. 133).

[295] C. P. Lawrence and J. L. Skinner. "Vibrational spectroscopy of HOD in liquid D2O. III. Spectral diffusion, and hydrogen-bonding and rotational dynamics." *J. Chem. Phys.* 118.264 (2003), 264–272 (cit. on p. 134).

[296] K. Ohno, M. Okimura, N. Akaib, and Y. Katsumoto. "The effect of cooperative hydrogen bonding on the OH stretching-band shift for water clusters studied by matrix-isolation infrared spectroscopy and density functional theory." *Phys. Chem. Chem. Phys.* 7.16 (2005), 3005–3014 (cit. on p. 134).

[297] F. Li and J. L. Skinner. "Infrared and Raman line shapes for ice Ih. II. H2O and D2O." *J. Chem. Phys.* 133.24 (2010), 244504 (cit. on p. 134).

[298] L. Shi, S. M. Gruenbaum, and J. L. Skinner. "Interpretation of IR and Raman Line Shapes for H2O and D2O Ice Ih." *J. Phys. Chem. B* 116.47 (2012), 13821–13830 (cit. on p. 134).

[299] M. L. Cowan, B. D. Bruner, N. Huse, J. R. Dwyer, B. Chugh, E. T. J. Nibbering, T. Elsaesser, and R. J. D. Miller. "Ultrafast memory loss and energy redistribution in the hydrogen bond network of liquid H2O." *Nature* 434 (2005), 199–202 (cit. on p. 134).

[300] K. Ramasesha, L. De Marco, A. Mandal, and A. Tokmakoff. "Water vibrations have strongly mixed intra- and intermolecular character." *Nat. Chem.* 5.11 (2013), 935–940 (cit. on pp. 134, 149).

[301] S. T. van der Post and H. J. Bakker. "Femtosecond Mid-Infrared Study of the Reorientation of Weakly Hydrogen-Bonded Water Molecules." *J. Phys. Chem. B* 8.118 (2014), 8179–8189 (cit. on p. 134).

[302] A. A. Vartia, K. R. Mitchell-Koch, G. Stirnemann, D. Laage, and W. H. Thompson. "On the Reorientation and Hydrogen-Bond Dynamics of Alcohols." *J. Phys. Chem. B* 115.42 (2011), 12173–12178 (cit. on p. 134).

[303] M. Długosz and J. M. Antosiewicz. "Evaluation of Proteins Rotational Diffusion Coefficients from Simulations of Their Free Brownian Motion in Volume-Occupied Environments." *J. Chem. Theory Comput.* 10.1 (2014), 481–491 (cit. on p. 134).

[304] Y. Nagata, S. Yoshimune, C. Hsieh, J. Hunger, and M. Bonn. "Ultrafast Vibrational Dynamics of Water Disentangled by Reverse Nonequilibrium Ab Initio Molecular Dynamics Simulations." *Phys. Rev. X* 5.2 (2015), 021002 (cit. on pp. 134, 145).

[305] T. Yagasaki and S. Saito. "A novel method for analyzing energy relaxation in condensed phases using nonequilibrium molecular dynamics simulations: Application to the energy relaxation of intermolecular motions in liquid water." *J. Chem. Phys.* 134.18 (2011), 184503 (cit. on pp. 134, 142, 145).

[306] T. Yagasaki, Junichi Ono, and S. Saito. "Ultrafast energy relaxation and anisotropy decay of the librational motion in liquid water: A molecular dynamics study." *J. Chem. Phys.* 131.16 (2009), 164511 (cit. on pp. 134, 142, 145).

[307] T. Hasegawa and Y. Tanimura. "Calculating fifth-order Raman signals for various molecular liquids by equilibrium and nonequilibrium hybrid molecular dynamics simulation algorithm." *J. Chem. Phys.* 125.7 (2006), 074512 (cit. on p. 134).

[308] T. Hasegawa and Y. Tanimura. "Nonequilibrium molecular dynamics simulations with a backward-forward trajectories sampling for multidimensional infrared spectroscopy of molecular vibrational modes." *J. Chem. Phys.* 128.6 (2006), 064511 (cit. on p. 134).

[309] H. Ito and Y. Tanimura. "Simulating two-dimensional infrared-Raman and Raman spectroscopies for intermolecular and intramolecular modes of liquid water." *J. Chem. Phys.* 144.7 (2016), 074201 (cit. on p. 134).

[310] R. D. King-Smith and D. Vanderbilt. "Theory of polarization of crystalline solids." *Phys. Rev. B* 47.3 (1993), 1651–1654 (cit. on p. 134).

[311] J. L. Skinner and K. Park. "Calculating Vibrational Energy Relaxation Rates from Classical Molecular Dynamics Simulations: Quantum Correction Factors for Processes Involving Vibration-Vibration Energy Transfer." *J. Phys. Chem. B* 105.28 (2001), 6716–6721 (cit. on p. 134).

[312] H. Sun. "COMPASS: An ab Initio Force-Field Optimized for Condensed-Phase Applications Overview with Details on Alkane and Benzene Compounds." *J. Phys. Chem. B* 102.38 (1998), 7338–7364 (cit. on pp. 139, 207, 212, 213).

[313] C. I. Bayly, P. Cieplak, W. D. Cornell, and P. A. Kollman. "A Well-Behaved Electrostatic Potential Based Method Using Charge Restraints For Determining Atom-Centered Charges: The RESP Model." *J. Chem. Phys.* 97.40 (1993), 10269–10280 (cit. on pp. 139, 171).

[314] W. D. Cornell, P. Cieplak, C. I. Bayly, and P. A. Kollman. "Application of RESP charges to calculate conformational energies, hydrogen bond energies, and free energies of solvation." *J. Am. Chem. Soc.* 115.21 (1993), 9620–9631 (cit. on pp. 139, 171).

[315] K. Mazur, M. Bonn, and J. Hunger. "Hydrogen Bond Dynamics in Primary Alcohols: A Femtosecond Infrared Study." *J. Phys. Chem. B* 119.4 (2015), 1558–1566 (cit. on pp. 139, 143, 145–147, 157).

[316] D. J. Shaw, M. R. Panman, and S. Woutersen. "Evidence for Cooperative Vibrational Relaxation of the NH-, OH-, and OD-Stretching Modes in Hydrogen-Bonded Liquids Using Infrared Pump-Probe Spectroscopy." *Phys. Rev. Lett.* 103.22 (2009), 227401 (cit. on pp. 139, 147).

[317] M. Pagliai, G. Cardini, R. Righini, and V. Schettino. "Hydrogen bond dynamics in liquid methanol." *J. Chem. Phys.* 119.13 (2003) (cit. on p. 140).

[318] M. Falk and E. Whalley. "Infrared Spectra of Methanol and Deuterated Methanols in Gas, Liquid and Solid Phases." *J. Chem. Phys.* 34.5 (1961), 1554–1568 (cit. on pp. 140, 142).

[319] C. Tanaka, K. Kuratani, and S. Mizushima. "In-plane normal vibrations of methanol." *Spectrochim. Acta* 9.4 (1957), 265–269 (cit. on p. 142).

[320] A. J. Lock, S. Woutersen, and H. J. Bakker. "Ultrafast Energy Equilibration in Hydrogen-Bonded Liquids." *J. Phys. Chem. A* 105.8 (2001), 1238–1243 (cit. on pp. 143, 145, 147).

[321] Y. L. A. Rezus and H. J. Bakker. "On the orientational relaxation of HDO in liquid water." *J. Chem. Phys.* 123.11 (2005), 114502 (cit. on p. 145).

[322] W. Demtröder. *Laser Spectroscopy*. Springer Berlin Heidelberg, 2008 (cit. on p. 145).

[323] J. Finzi, F. E. Hovis, V. N. Panfilov, P. Hess, and C. B. Moore. "Vibrational relaxation of water vapor." *J. Chem. Phys.* 67.9 (1977), 4057–4061 (cit. on p. 147).

[324] H. Nienhuys, S. Woutersen, R. A. van Santen, and H. J. Bakker. "Mechanism for vibrational relaxation in water investigated by femtosecond infrared spectroscopy." *J. Chem. Phys.* 111.4 (1999), 1494–1500 (cit. on p. 147).

[325] P. Wernet, D. Nordlund, U. Bergmann, M. Odelius M. Cavalleri, H. Ogasawara, L . Å. Näslund, T. K. Hirsch; L. Ojamäe, P. Glatzel, L. G. M. Pettersson, and A. Nilsson. "The Structure of the First Coordination Shell in Liquid Water." *Science* 304.5673 (2004), 995–999 (cit. on p. 147).

[326] J. D. Smith, C. D. Cappa, K. R. Wilson, B. M. Messer, R. C. Cohen, and R. J. Saykally. "Energetics of Hydrogen Bond Network Rearrangements in Liquid Water." *Science* 306.5697 (2004), 851–853 (cit. on p. 147).

[327] S. Fritsch, R. Potestio, D. Donadio, and Kurt Kremer. "Nuclear Quantum Effects in Water: A Multiscale Study." *J. Chem. Theory Comput.* 10.2 (2014), 816–824 (cit. on p. 148).

[328] J. P. Perdew, K. Burke, and M. Ernzerhof. "Generalized Gradient Approximation Made Simple." *Phys. Rev. Lett.* 78.7 (1997), 1396–1396 (cit. on p. 148).

[329] S. T. van der Post, C. S. Hsieh, M. Okuno, Y. Nagata, H. J. Bakker, M. Bonn, and J. Hunger. "Strong frequency dependence of vibrational relaxation in bulk and surface water reveals sub-picosecond structural heterogeneity." *Nat. Commun.* 6 (2015), 8384 (cit. on p. 149).

[330] H. Nienhuys, R. A. van Santen, and H. J. Bakker. "Orientational relaxation of liquid water molecules as an activated process." *J. Chem. Phys.* 112.4 (2000), 8487–8494 (cit. on p. 150).

[331] R. Laenen, C. Rauscher, and A. Laubereau. "Local Substructures of Water Studied by Transient Hole-Burning Spectroscopy in the Infrared: Dynamics and Temperature Dependence." *J. Phys. Chem. B* 102.46 (1998), 9304–9311 (cit. on p. 150).

[332] L. Liu, J. Hunger, and H. J. Bakker. "Energy Relaxation Dynamics of the Hydration Complex of Hydroxide." *J. Phys. Chem. A* 115.51 (2011), 14593–14598 (cit. on p. 158).

[333] J. Hunger, T. Sonnleitner, L. Liu, R. Buchner, M. Bonn, and H. J. Bakker. "Hydrogen-Bond Dynamics in a Protic Ionic Liquid: Evidence of Large-Angle Jumps." *J. Phys. Chem. Lett.* 3.20 (2012), 3034–3038 (cit. on p. 158).

[334] G. Seifert, T. Patzlaff, and H. Graener. "Size Dependent Ultrafast Cooling of Water Droplets in Microemulsions by Picosecond Infrared Spectroscopy." *Phys. Rev. Lett.* 88.14 (2002), 147402 (cit. on p. 158).

[335] M. L. Williams. "CRC Handbook of Chemistry and Physics, 76th edition." *Occup. Environ. Med.* 53.7 (1996), 504–504 (cit. on pp. 158, 162).

[336] I. F. Williamo Kuo, C. J. Mundy, M. J. McGrath, and J. Ilja Siepmann. "Structure of the Methanol Liquid-Vapor Interface: A Comprehensive Particle-Based Simulation Study." *J. Phys. Chem. C* 112.39 (2008), 15412–15418 (cit. on p. 158).

[337] T. Katayama. "Heats of mixing, liquid heat capacities and enthalpy, concentration charts for methanol-water and isopropanol-water systems." *Kagaku Kogaku* 26 (1962), 361–372 (cit. on p. 162).

[338] Pablo G. P. G. Debenedetti and F. H. Stillinger. "Supercooled liquids and the glass transition." *Nature* 410 (2001), 259 (cit. on p. 166).

[339] D. Turnbull. "Under what conditions can a glass be formed?" *Contemporary Physics* 10.5 (1969), 473–488 (cit. on pp. 165, 166).

[340] C. A. Angell. "Structural instability and relaxation in liquid and glassy phases near the fragile liquid limit." *J. Non-Cryst. Solids* 102.1 (1988). Proceedings of the Ninth University Conference on Glass Science, 205 –221 (cit. on pp. 165, 166).

[341] C. T. Moynihan, P. B. Macedo, C. J. Montrose, P. K. Gupta, M. A. DeBolt, J. F. Dill, B. E. Dom, P. W. Drake, and A. J. Easteal et al. "Thermodynamic and transport properties of liquids near the glass transition temperature. Structural relaxation in vitreous materials." In: *The Glass Transition and the Nature of the Glassy State*. Ed. by M. Goldstein and R. Simha. Vol. 279. New York Academy of Sciences, 1976 (cit. on p. 165).

[342] R. Brüning and K. Samwer. "Glass transition on long time scales." *Phys. Rev. B* 46.18 (1992), 11318–11322 (cit. on p. 165).

[343] M. D. Ediger, C. A. Angell, and S. R. Nagel. "Supercooled Liquids and Glasses." *J. Phys. Chem.* 100.31 (1996), 13200–13212 (cit. on p. 166).

[344] W. Kauzmann. "The Nature of the Glassy State and the Behavior of Liquids at Low Temperatures." *Chemical Reviews* 43.2 (1948), 219–256 (cit. on p. 166).

[345] F. Simon. "er den Zustand der unterkhlten Flüssigkeiten und Gläser." *Zeitschrift für anorganische und allgemeine Chemie* 203.1 (1931), 219–227 (cit. on p. 166).

[346] P. G. Wolynes. "Aperioidic crystals: Biology, Chemistry and Physics in a fugue with stretto." *AIP Conference Proceedings* 180.1 (1988), 39–65 (cit. on p. 166).

[347] P. G. Wolynes. "Entropy Crises in Glasses and Random Heteropolymers." *J Res. Natl. Inst. Stand. Technol.* 102.2 (1997), 187–194 (cit. on p. 166).

[348] C. A. Angell. "Formation of Glasses from Liquids and Biopolymers." *Science* 267.5206 (1995), 1924–1935. eprint: http://science.sciencemag.org/content/267/5206/1924.full.pdf (cit. on p. 167).

[349] B. Geffroy, P. le Roy, and C. Prat. "Organic light-emitting diode (OLED) technology: materials, devices and display technologies." *Polymer International* 55.6 (2006), 572–582 (cit. on p. 167).

[350] S. Reineke, M. Thomschke, B. Lüssem, and K. Leo. "White organic light-emitting diodes: status and perspective." *Rev. Mod. Phys.* 85.3 (2013), 1245–1293 (cit. on p. 167).

[351] J. R. Sheats, H. Antoniadis, M. Hueschen, W. Leonard, J. Miller, R. Moon, D. Roitman, and A. Stocking. "Organic Electroluminescent Devices." *Science* 273.5277 (1996), 884–888 (cit. on p. 167).

[352] X. Zhou, J. He, L. S. Liao, M. Lu, X. M. Ding, X. Y. Hou, X. M. Zhang, X. Q. He, and S. T. Lee. "Real-Time Observation of Temperature Rise and Thermal Breakdown Processes in Organic LEDs Using an IR Imaging and Analysis System." *Adv. Mater.* 12.4 (2000), 265–269 (cit. on p. 167).

[353] S. Chung, J. H. Lee, J. Jeong, J. J. Kim, and Y. Hong. "Substrate thermal conductivity effect on heat dissipation and lifetime improvement of organic light-emitting diodes." *Appl. Phys. Lett.* 94.25 (2009), 253302 (cit. on p. 167).

[354] X. Wang, K. D. Parrish, J. A. Malen, and P. K. L. Chan. "Modifying the thermal conductivity of small molecule organic semiconductor thin films with metal nanoparticles." *Sci. Rep.* 5 (2015), 16095 (cit. on p. 167).

[355] O. Bubnova, Z. U. Khan, A. Malti, S. Braun, M. Fahlman, M. Berggren, and X. Crispin. "Optimization of the thermoelectric figure of?merit?in the conducting polymer poly(3,4-ethylenedioxythiophene)." *Nat. Mater.* 10 (2011), 429 EP (cit. on p. 167).

[356] Q. Zhang, Y. Sun, W. Xu, and D. Zhu. "Organic Thermoelectric Materials: Emerging Green Energy Materials Converting Heat to Electricity Directly and Efficiently." *Adv. Mater.* 26.40 (2014), 6829–6851 (cit. on p. 167).

[357] T. A. Lin et al. "Sky-Blue Organic Light Emitting Diode with 37Quantum Efficiency Using Thermally Activated Delayed Fluorescence from Spiroacridine-Triazine Hybrid." *Adv. Mater.* 28.32 (2016), 6976–6983 (cit. on p. 167).

[358] D. Mendels and N. Tessler. "Drift and Diffusion in Disordered Organic Semiconductors: The Role of Charge Density and Charge Energy Transport." *J. Phys. Chem. C* 117.7 (2013), 3287–3293 (cit. on p. 167).

[359] K. P. Pernstich, B. Rössner, and B. Batlogg. "Field-effect-modulated Seebeck coefficient in organic semiconductors." *Nat. Mater.* 7 (2008), 321 (cit. on p. 167).

[360] S. F. Swallen, K. L. Kearns, M. K. Mapes, Y. S. Kim, R. J. McMahon, M. D. Ediger, T. Wu, L. Yu, and S. Satija. "Organic Glasses with Exceptional Thermodynamic and Kinetic Stability." *Science* 315.5810 (2007), 353–356 (cit. on p. 167).

[361] S. S. Dalal, D. M. Walters, I. Lyubimov, J. J. de Pablo, and M. D. Ediger. "Tunable molecular orientation and elevated thermal stability of vapor-deposited organic semiconductors." *Proc. Natl. Acad. Sci. U.S.A.* 112.14 (2015), 4227–4232 (cit. on pp. 167, 168, 177).

[362] D. M. Walters, R. Richert, and M. D. Ediger. "Thermal stability of vapor-deposited stable glasses of an organic semiconductor." *J. Chem. Phys.* 142.13 (2015), 134504 (cit. on p. 167).

[363] K. L. Kearns, S. F. Swallen, M. D. Ediger, T. Wu, and L. Yu. "Influence of substrate temperature on the stability of glasses prepared by vapor deposition." *J. Chem. Phys.* 127.15 (2007), 154702 (cit. on p. 167).

[364] E. Leon-Gutierrez, A. Sepulveda, G. Garcia, M. T. Clavaguera-Mora, and J.Rodriguez-Viejo. "Stability of thin film glasses of toluene and ethylbenzene formed by vapor deposition: an in situ nanocalorimetric study." *Phys. Chem. Chem. Phys.* 12.44 (2010), 14693–14698 (cit. on p. 167).

[365] M. Ahrenberg, Y. Z. Chua, K. R. Whitaker, H. Huth, M. D. Ediger, and C. Schick. "In situ investigation of vapor-deposited glasses of toluene and ethylbenzene via alternating current chip-nanocalorimetry." *J. Chem. Phys.* 138.2 (2013), 024501 (cit. on p. 167).

[366] S. L. L. M. Ramos, M. Oguni, K. Ishii, and H. Nakayama. "Character of Devitrification, Viewed from Enthalpic Paths, of the Vapor-Deposited Ethylbenzene Glasses." *J. Phys. Chem. B* 115.49 (2011), 14327–14332 (cit. on p. 167).

[367] C. Rodríguez-Tinoco, M. Gonzalez-Silveira, J. Rls-Ribé, G. Garcia, and J. Rodrez-Viejo. "Highly stable glasses of celecoxib: Influence on thermo-kinetic properties, microstructure and response towards crystal growth." *J. Non-Cryst. Solids* 407.Supplement C (2015), 256 –261 (cit. on p. 167).

[368] K. R. Whitaker, M. Tylinski, M. Ahrenberg, C. Schick, and M. D. Ediger. "Kinetic stability and heat capacity of vapor-deposited glasses of o-terphenyl." *J. Chem. Phys.* 143.8 (2015), 084511 (cit. on p. 167).

[369] K. L. Kearns, S. F. Swallen, M. D. Ediger, Y. Sun, and L. Yu. "Calorimetric Evidence for Two Distinct Molecular Packing Arrangements in Stable Glasses of Indomethacin." *J. Phys. Chem. B* 113.6 (2009), 1579–1586 (cit. on p. 167).

[370] S. S. Dalal, Z. Fakhraai, and M. D. Ediger. "High-Throughput Ellipsometric Characterization of Vapor-Deposited Indomethacin Glasses." *J. Phys. Chem. B* 117.49 (2013), 15415–15425 (cit. on p. 167).

[371] K. Ishii, H. Nakayama, S. Hirabayashi, and R. Moriyama. "Anomalously high-density glass of ethylbenzene prepared by vapor deposition at temperatures close to the glass-transition temperature." *Chem. Phys. Lett.* 459.1 (2008), 109–112 (cit. on p. 167).

[372] S. S. Dalal, A. Sepúlveda, G. K. Pribil, Z. Fakhraai, and M. D. Ediger. "Density and birefringence of a highly stable α, α, β-trisnaphthylbenzene glass." *J. Chem. Phys.* 136.20 (2012), 204501 (cit. on p. 167).

[373] Y. Z. Chua, M. Ahrenberg, M. Tylinski, M. D. Ediger, and C. Schick. "How much time is needed to form a kinetically stable glass? AC calorimetric study of vapor-deposited glasses of ethylcyclohexane." *J. Chem. Phys.* 142.5 (2015), 054506 (cit. on p. 167).

[374] K. J. Dawson, K. L. Kearns, M. D. Ediger, M. J. Sacchetti, and G. D. Zografi. "Highly Stable Indomethacin Glasses Resist Uptake of Water Vapor." *J. Phys. Chem. B* 113.8 (2009), 2422–2427 (cit. on p. 167).

[375] K. L. Kearns, T. Still, G. Fytas, and M. D. Ediger. "High-Modulus Organic Glasses Prepared by Physical Vapor Deposition." *Adv. Mater.* 22.1 (2010), 39–42 (cit. on p. 167).

[376] J. Ràfols Ribé. "Organic Vapour-Deposited Stable Glasses: From Fundamental Thermal Properties to High-Performance Organic Light Emitting Diodes." PhD thesis. Universitat Autònoma de Barcelona, 2017 (cit. on p. 167).

[377] T. D. Schmidt, T. Lampe, M. R. D. Sylvinson, P. I. Djurovich, M. E. Thompson, and W. Brütting. "Emitter Orientation as a Key Parameter in Organic Light-Emitting Diodes." *Phys. Rev. Appl.* 8.3 (2017), 037001 (cit. on p. 168).

[378] H. W. Lin, C. L. Lin, H. H. Chang, Y. T. Lin, C. C. Wu, Y. M. Chen, R. T. Chen, Y. Y. Chien, and K. T. Wong. "Anisotropic optical properties and molecular orientation in vacuum-deposited ter(9,9-diarylfluorene)s thin films using spectroscopic ellipsometry." *J. Appl. Phys.* 95.3 (2004), 881–886 (cit. on p. 168).

[379] D. Yokoyama, A. Sakaguchi, M. Suzuki, and C. Adachi. "Enhancement of electron transport by horizontal molecular orientation of oxadiazole planar molecules in organic amorphous films." *Appl. Phys. Lett.* 95.24 (2009), 243303 (cit. on p. 168).

[380] D. Yokoyama. "Molecular orientation in small-molecule organic light-emitting diodes." *J. Mater. Chem.* 21.48 (2011), 19187–19202 (cit. on p. 168).

[381] S. Fratini, S. Ciuchi, D. Mayou, G. Trambly de Laissardière, and A. Troisi. "A map of high-mobility molecular semiconductors." *Nat. Mater.* 16 (2017), 998 (cit. on p. 168).

[382] N. Kim, B. Domercq, S. Yoo, A. Christensen, B. Kippelen, and S. Graham. "Thermal transport properties of thin films of small molecule organic semiconductors." *Appl. Phys. Lett.* 87.24 (2005), 241908 (cit. on p. 168).

[383] N. Lu, L. Li, N. Gao, and M. Liu. "A unified description of thermal transport performance in disordered organic semiconductors." *Org. Electron.* 41.Supplement C (2017), 294 –300 (cit. on p. 168).

[384] C. J. Glassbrenner and G. A. Slack. "Thermal Conductivity of Silicon and Germanium from 3°K to the Melting Point." *Phys. Rev.* 134.4A (1964), A1058–A1069 (cit. on p. 168).

[385] D. G. Cahill, M. Katiyar, and J. R. Abelson. "Thermal conductivity of a-Si: H thin films." *Phys. Rev. B* 50.9 (1994), 6077–6081 (cit. on p. 168).

[386] D. G. Cahill and R. O. Pohl. "Heat flow and lattice vibrations in glasses." *Solid State Commun.* 70.10 (1989), 927 –930 (cit. on p. 168).

[387] H. Zhang and J. W. Brill. "Interlayer thermal conductivity of rubrene measured by ac-calorimetry." *J. Appl. Phys.* 114.4 (2013), 043508 (cit. on p. 169).

[388] H. Zhang, Y. Yao, Marcia M. Payne, J. E. Anthony, and J. W. Brill. "Thermal diffusivities of functionalized pentacene semiconductors." *Appl. Phys. Lett.* 105.7 (2014), 073302 (cit. on p. 169).

[389] K. Kurabayashi, M. Asheghi, M. Touzelbaev, and K. E. Goodson. "Measurement of the thermal conductivity anisotropy in polyimide films." *J. Microelectromech. Syst.* 8.2 (1999), 180–191 (cit. on pp. 169, 187).

[390] V. Singh et al. "High thermal conductivity of chain-oriented amorphous polythiophene." *Nat. Nanotechnol.* 9 (2014), 384 (cit. on p. 169).

[391] K. L. Ngai and M. Paluch. "Classification of secondary relaxation in glass-formers based on dynamic properties." *J. Chem. Phys.* 120.2 (2004), 857–873 (cit. on p. 170).

[392] P. Dauber-Osguthorpe, V. A. Roberts, D. J. Osguthorpe, J. Wolff, M. Genest, and A. T. Hagler. "Structure and energetics of ligand binding to proteins: Escherichia coli dihydrofolate reductase-trimethoprim, a drug-receptor system." *Proteins* 4.1 (1988), 31–47 (cit. on pp. 170, 207, 214).

[393] S. Singh, M. D. Ediger, and J. J. de Pablo. "Ultrastable glasses from in silico vapour deposition." *Nat. Mater.* 12 (2013), 139 (cit. on p. 171).

[394] J. HelfferichI. LyubimovD. ReidaandJ. J. de Pablo. "Inherent structure energy is a good indicator of molecular mobility in glasses." *Soft Matter* 12.27 (2016), 5898–5904 (cit. on p. 171).

[395] I. Lyubimov, L. Antony, D. M. Walters, D. Rodney, M. D. Ediger, and J. J. de Pablo. "Orientational anisotropy in simulated vapor-deposited molecular glasses." *J. Chem. Phys.* 143.9 (2015), 094502 (cit. on pp. 171, 177).

[396] S. Sastry, P. G. Debenedetti, and F. H. Stillinger. "Signatures of distinct dynamical regimes in the energy landscape of a glass-forming liquid." *Nature* 393 (1998), 554 (cit. on p. 171).

[397] J. Ràfols-Ribé, R. Dettori, P. Ferrando-Villalba, M. Gonzalez-Silveira, L. Abad, A. Lopeandía, L. Colombo, and J. Rodríguez-Viejo. "Evidence of thermal transport anisotropy in stable glasses of vapour deposited organic molecules." Accepted. 2018 (cit. on pp. 180, 190, 195).

[398] A. Gujral, K. A. O'Hara, M. F. Toney, M. L. Chabinyc, and M. D. Ediger. "Structural Characterization of Vapor-Deposited Glasses of an Organic Hole Transport Material with X-ray Scattering." *Chem. Mater.* 27.9 (2015), 3341–3348 (cit. on p. 189).

[399] S. P. Coleman, D. E. Spearot, and L. Capolungo. "Virtual diffraction analysis of Ni [0 1 0] symmetric tilt grain boundaries." *Model. Simul. Mater. Sci. Eng.* 21.5 (2013), 055020 (cit. on p. 189).

[400] C. M. Palumbiny, F. Liu, T. P. Russell, A. Hexemer, C. Wang, and P. Müller-Buschbaum. "The Crystallization of PEDOT:PSS Polymeric Electrodes Probed In Situ during Printing." *Adv. Mater.* 27.22 (2015), 3391–3397 (cit. on p. 189).

[401] J. F. Franco-Gonzalez and I. V. Zozoulenko. "Molecular Dynamics Study of Morphology of Doped PEDOT: From Solution to Dry Phase." *J. Phys. Chem. B* 121.16 (2017), 4299–4307 (cit. on p. 189).

[402] X. Wang, J. Zhang, Y. Chen, and P. K. L. Chan. "Molecular dynamics study of thermal transport in a dinaphtho[$2,3-b:2',3'-f$]thieno[$3,2-b$]thiophene (DNTT) organic semiconductor." *Nanoscale* 9.6 (2017), 2262–2271 (cit. on p. 190).

[403] D. M. Leitner. "Thermal Boundary Conductance and Thermal Rectification in Molecules." *J. Phys. Chem. B* 117.42 (2013), 12820–12828 (cit. on p. 190).

[404] J. Epstein, W. L. Ong, C. J. Bettinger, and J. A. Malen. "Temperature Dependent Thermal Conductivity and Thermal Interface Resistance of Pentacene Thin Films with Varying Morphology." *ACS Appl. Mater. Interfaces* 8.29 (2016), 19168–19174 (cit. on p. 191).

[405] Y. Jin, S. Nola, K. P. Pipe, and M. Shtein. "Improving thermoelectric efficiency in organic-metal nanocomposites via extra-low thermal boundary conductance." *J. Appl. Phys.* 114.19 (2013), 194303 (cit. on p. 191).

[406] B. Lorenzi, R. Dettori, M. Dunham, C. Melis, R. Tonini, L. Colombo, A. Sood, K. Goodson, and D. Narducci. "Phonon scattering in silicon by multiple morphological defects: A multiscale analysis." Accepted. 2018 (cit. on p. 195).

[407] R. Dettori, C. Melis, X. Cartoix, R. Rurali, and L. Colombo. "Thermal boundary resistance in semiconductors by non-equilibrium thermodynamics." *Adv. Phys. X* 1.2 (2016), 246–261 (cit. on p. 195).

[408] W. C. Swope, H. C. Andersen, P. H. Berens, and K. R. Wilson. "A computer simulation method for the calculation of equilibrium constants for the formation of physical clusters of molecules: Application to small water clusters." *J. Chem. Phys.* 76.1 (1982), 637–649 (cit. on p. 203).

[409] M. Tuckerman, B. J. Berne, and G. J. Martyna. "Reversible multiple time scale molecular dynamics." *J. Chem. Phys.* 97.3 (1992), 1990–2001 (cit. on p. 203).

[410] H. Kamberaj, R. J. Low, and M. P. Neal. "Time reversible and symplectic integrators for molecular dynamics simulations of rigid molecules." *J. Chem. Phys.* 122.22 (2005), 224114 (cit. on p. 203).

[411] M. E. Tuckerman and M. Parrinello. "Integrating the Car-Parrinello equations. I. Basic integration techniques." *J. Chem. Phys.* 101.2 (1994), 1302–1315 (cit. on p. 203).

[412] M. E. Tuckerman and M. Parrinello. "Integrating the Car-Parrinello equations. II. Multiple time scale techniques." *J. Chem. Phys.* 101.2 (1994), 1316–1329 (cit. on p. 203).

[413] J. Hutter, M. Tuckerman, and M. Parrinello. "Integrating the Car-Parrinello equations. III. Techniques for ultrasoft pseudopotentials." *J. Chem. Phys.* 102.2 (1995), 859–871 (cit. on p. 203).

[414] R. Car and M. Parrinello. "Unified Approach for Molecular Dynamics and Density-Functional Theory." *Phys. Rev. Lett.* 55.22 (1985), 2471–2474 (cit. on p. 203).

[415] J. Tersoff. "New empirical approach for the structure and energy of covalent systems." *Phys. Rev. B* 37.12 (1988), 6991–7000 (cit. on p. 207).

[416] M. Z. Bazant, E. Kaxiras, and J. F. Justo. "Environment-dependent interatomic potential for bulk silicon." *Phys. Rev. B* 56.14 (1997), 8542–8552 (cit. on pp. 207, 209, 211).

[417] J. Tersoff. "Empirical Interatomic Potential for Carbon, with Applications to Amorphous Carbon." *Phys. Rev. Lett.* 61.25 (1988), 2879–2882 (cit. on p. 209).

[418] M. Z. Bazant and E. Kaxiras. "Modeling of Covalent Bonding in Solids by Inversion of Cohesive Energy Curves." *Phys. Rev. Lett.* 77.21 (1996), 4370–4373 (cit. on pp. 209, 211).

[419] A. E. Carlsson, P. A. Fedders, and C. W. Myles. "Generalized embedded-atom format for semiconductors." *Phys. Rev. B* 41.2 (1990), 1247–1250 (cit. on p. 211).

[420] H. Sun, P. Ren, and J.R. Fried. "The COMPASS force field: parameterization and validation for phosphazenes." *Comput. Theor. Polym. Sci.* 8.1 (1998), 229 –246 (cit. on p. 212).

[421] S. W. Bunte and H. Sun. "Molecular modeling of energetic materials: the parametrization and validation of nitrate esters in the COMPASS force field." *J. Phys. Chem. B* 104.11 (2000), 2477–2489 (cit. on p. 212).

[422] J. Yang, Y. Ren, A. Tian, and Huai H. Sun. "COMPASS Force Field for 14 Inorganic Molecules, He, Ne, Ar, Kr, Xe, H_2, O_2, N_2, NO, CO, CO_2, NO_2, CS_2, and SO_2, in Liquid Phases." *J. Phys. Chem. B* 104.20 (2000), 4951–4957 (cit. on p. 212).

[423] M. Waldman and A.T. Hagler. "New combining rules for rare gas van der waals parameters." *J. Comput. Chem.* 14.9 (1993), 1077–1084 (cit. on p. 212).

[424] H. Heinz, R. A. Vaia, B. L. Farmer, and R. R. Naik. "Accurate Simulation of Surfaces and Interfaces of Face-Centered Cubic Metals Using 12-6 and 9-6 Lennard-Jones Potentials." *J. Phys. Chem. C* 112.44 (2008), 17281–17290 (cit. on p. 213).

[425] S. O. Jonsdottir and K. Rasmussen. "The consistent force field. Part 6: an optimized set of potential energy functions for primary amines." *New J. Chem.* 24.4 (2000), 243–247 (cit. on p. 213).

[426] S. Lifson, A. T. Hagler, and P. Dauber. "Consistent force field studies of intermolecular forces in hydrogen-bonded crystals. 1. Carboxylic acids, amides, and the C==O···H– hydrogen bonds." *J. Am. Chem. Soc.* 101.18 (1979), 5111–5121 (cit. on p. 216).

[427] T. A. Hagler, S. Lifson, and P. P. Dauber. "Consistent force field studies of intermolecular forces in hydrogen-bonded crystals. 2. A benchmark for the objective comparison of alternative force fields." *J. Am. Chem. Soc.* 101.18 (1979), 5122–5130 (cit. on p. 216).

[428] T. A. Hagler, P. Dauber, and S. Lifson. "Consistent force field studies of intermolecular forces in hydrogen-bonded crystals. 3. The C==O···H–O hydrogen bond and the analysis of the energetics and packing of carboxylic acids." *J. Am. Chem. Soc.* 101.18 (1979), 5131–5141 (cit. on p. 216).